4-2016

Coupled orbit-attitude mission design in the circular restricted three-body problem

Davide Guzzetti

Graduate School Form
30 Updated 12/26/2015

PURDUE UNIVERSITY
GRADUATE SCHOOL
Thesis/Dissertation Acceptance

This is to certify that the thesis/dissertation prepared

By Davide Guzzetti

Entitled
COUPLED ORBIT-ATTITUDE MISSION DESIGN IN THE CIRCULAR RESTRICTED THREE-BODY PROBLEM

For the degree of Doctor of Philosophy

Is approved by the final examining committee:

KATHLEEN C. HOWELL
Chair

DENGFENG SUN

JAMES M. LONGUSKI

MICHELE R. LAVAGNA

To the best of my knowledge and as understood by the student in the Thesis/Dissertation Agreement, Publication Delay, and Certification Disclaimer (Graduate School Form 32), this thesis/dissertation adheres to the provisions of Purdue University's "Policy of Integrity in Research" and the use of copyright material.

Approved by Major Professor(s): KATHLEEN C. HOWELL

Approved by: WEINONG WAYNE CHEN 04/25/2016

Head of the Departmental Graduate Program Date

COUPLED ORBIT-ATTITUDE MISSION DESIGN

IN THE CIRCULAR RESTRICTED THREE-BODY PROBLEM

A Dissertation

Submitted to the Faculty

of

Purdue University

by

Davide Guzzetti

In Partial Fulfillment of the

Requirements for the Degree

of

Doctor of Philosophy

May 2016

Purdue University

West Lafayette, Indiana

To the Joy.

ACKNOWLEDGMENTS

I shall first and foremost thank my family and friends oversea. Thank you for enduring my physical distance and keeping me always in your thoughts and hearts: you remain the strongest foundation for all my achievements. Comforted by a safe landing where to return, my journey across the Pillar if Hercules has been made easier.

Next, my gratitude moves toward Professor Kathleen Howell, for the several opportunities she entrusted me with. I am extremely thankful for each chance she gave me to growth professionally and personally, and for sharing her passion and guidance. As an outstanding mentor and researcher as Professor Howell is, I hope to be able to continue my collaboration with her. I would additionally like to thank Professor Michèle Lavagna, Professor James Longuski, and Professor Dengfeng Sun to serve in my committee.

While pursuing my degree, I also had the great privilege to interact with professional realities outside of the grad school at Purdue University. Mr. Davide Folta at Goddard Space Flight Center, Dr. Diane Craig Davis at Johnson Space Center, and the team lead by prof. Michèle Lavagna at Politecnico di Milano deserve special recognition. I have truly enjoyed their collaboration, and I greatly value the sharing of their expertise.

I also must thank all of the past and current members of my research group, that have offered their support (in a technical sense as well) and friendship. It has been an honor and an inspiration to be part of this sparkling group. I wish everyone to achieve the success you deserve.

Finally, I own thanks to the generosity of the following institutions that have provided financial assistance throughout my years at Purdue University: the Purdue College of Engineering, the School of Aeronautics and Astronautics, the NASA Goddard Space Flight Center with grants NNX13AM17G and NNX13AH02G, and the NASA Johnson Space Center with grant NNX13AK60.

TABLE OF CONTENTS

LIST OF TABLES

LIST OF FIGURES

Figure Page

Figure Page

Figure Page

ABSTRACT

Guzzetti, Davide PhD, Purdue University, May 2016. Coupled Orbit-Attitude Mission Design in the Circular Restricted Three-Body Problem. Major Professor: Kathleen C. Howell.

Trajectory design increasingly leverages multi-body dynamical structures that are based on an understanding of various types of orbits in the Circular Restricted Three-Body Problem (CR3BP). Given the more complex dynamical environment, mission applications may also benefit from deeper insight into the attitude motion. In this investigation, the attitude dynamics are coupled with the trajectories in the CR3BP. In a highly sensitive dynamical model, such as the orbit-attitude CR3BP, periodic solutions allow delineation of the fundamental dynamical structures. Periodic solutions are also a subset of motions that are bounded over an infinite time-span (assuming no perturbing factors), without the necessity to integrate over an infinite time interval. Euler equations of motion and quaternion kinematics describe the rotational behavior of the spacecraft, whereas the translation of the center of mass is modeled in the CR3BP equations. A multiple shooting and continuation procedure are employed to target orbit-attitude periodic solutions in this model. Application of Floquet theory, Poincaré mapping, and grid search to identify initial guesses for the targeting algorithm is described. In the Earth-Moon system, representative scenarios are explored for axisymmetric vehicles with various inertia characteristics, assuming that the vehicles move along Lyapunov, halo as well as distant retrograde orbits. A rich structure of possible periodic behaviors appears to pervade the solution space in the coupled problem. The stability analysis of the attitude dynamics for the selected families is included. Among the computed solutions, marginally stable and slowly diverging rotational behaviors exist and may offer interesting mission applications. Additionally, the solar radiation pressure is included and a fully coupled orbit-attitude model

is developed. With specific application to solar sails, various guidance algorithms are explored to direct the spacecraft along a desired path, when the mutual interaction between orbit and attitude dynamics is considered. Each strategy implements a different form of control input, ranging from instantaneous reorientation of the sail pointing direction to the application of control torques, and it is demonstrated within a simple station keeping scenario.

1. INTRODUCTION

Worldwide, space agencies are increasingly exploiting multi-body dynamical structures for their most advanced missions, with several trajectory proposals fundamentally based on an understanding of the Circular Restricted Three-Body Problem (CR3BP). These missions comprise astronomical observatories [1–3], deep-space human habitats or staging infrastructures [4], solar sails, as well as repositioned natural bodies [5, 6]. Improving the pointing accuracy of telescopes, safely docking to space stations, maneuvering a solar sail, or reconstructing the orientation history of captured asteroids are possible challenges in developing the capability to control and predict the attitude motion in more complex dynamical environments. The spacecraft attitude history may also constrain the thrusting direction, thus, limiting the options for maneuvers [7].

When the attitude dynamics is coupled to a multi-body orbital regime, the spacecraft may also manifest complex rotational behaviors. Within the set of chaotic responses that is typical in a multi-body system, buried fundamental dynamical structures are also apparent, ones that may aid in mission design when the attitude dynamics is incorporated. Periodic or quasi-periodic structures may potentially support ACS (Attitude Control System) operational modes for continuous data acquisition or communications, with coarse pointing requirements. A subset of the center subspace might be employed for safe-mode or long-term configurations. For example, an asteroid or a space station placed in a marginally stable subspace associated with the attitude modes is more likely to avoid tumbling in the long-term. Manifold structures may guide large attitude slews. Natural orbit-attitude dynamics may be leveraged to improve a solar sail guidance strategy. There is, therefore, justified interest to better understand the attitude dynamics when it is coupled to the CR3BP regime.

1.1 Problem Definition

From a general perspective, this investigation aims at a better understanding of the orbit-attitude mechanisms within the CR3BP for future applications to mission design. Specifically, the coupled dynamical behavior for a spacecraft travelling along a known CR3BP periodic orbit is the main focus. Fully nonlinear periodic orbits within the CR3BP are employed as a viable approximation for the actual spacecraft trajectory, and, possibly, describe a mission scenario more accurately than artificially fixing the vehicle at a specific spatial location or adopting linear models. The orbit-attitude dynamics within the CR3BP are first explored along two strands that may, eventually, yield promising mission applications:

1. The prediction of bounded attitude oscillatory motions (or librations) as a function of the reference orbit, initial attitude configuration, and spacecraft topology.

2. The utilization of an orbit-attitude coupling device, such as a solar sails, to maintain the vicinity of a reference orbit.

For example, applications such as deep-space stations or redirected asteroids would benefit from naturally bounded rotational motions, especially on a long-term mission horizon. Additionally, a bounded attitude libration may also facilitate the control of astronomical observatories and similar types of vehicle. Finally, more efficient station keeping strategies and novel mission scenarios may become available if the propellant budget is significantly reduced by implementing solar sail powered orbital maneuvering.

1.1.1 The Orbit-Attitude Bounded Librations Problem

There are a series of questions that naturally arise in the attempt to predict bounded attitude librations along a reference orbit, for example: which combinations of reference orbit and spacecraft geometry yield a bounded rotational motion? Or, given a spacecraft geometry and a reference trajectory, which initial orientation and rotational rates yield a nondiverging solution, if any? Are there sets of particular solutions that may aid the construction of bounded solutions? If so, how are such solutions identified and computed? Finally, to what degree of fidelity are those solutions valid? These, and other questions generally lead to the characterization of the solution space, which is, however, nontrivial, as no closed form solution is available for the orbit-attitude problem within the CR3BP (and neither there exist for the orbital problem alone). Reliance on numerical techniques is, therefore, a necessity. To address the questions posed by the "bounded librations problem", which describes one of the two general goals for this investigation, the following objectives are, first, identified:

- Develop techniques to identify, in representative scenarios, bounded attitude solutions along reference periodic orbits in the form of orbit-attitude periodic motions.

- Develop algorithms to compute orbit-attitude periodic solutions.

- Preliminarily characterize the stability of the orbit-attitude periodic solutions and their linkage to bounded responses.

Periodic solutions are a subset of bounded motions, that delineate fundamental dynamical structures for the problem. It seems, therefore, reasonable to begin the investigation of bounded motions from periodic orbit-attitude solutions. Other forms of bounded response may also exist in vicinity of a periodic motion. As is generally true for trajectories in the CR3BP, such coupled orbit-attitude solutions are expected to transition to higher-fidelity models with various degrees of success. Nonetheless, the challenges in recognizing ordered and predictable behaviors in higher-fidelity models is also largely acknowledged. Orbit-attitude periodic solutions from a simplified coupled model may be the stepping stone to identify, and leverage, potential natural behavior in the actual – more dynamically complex – operational environment.

1.1.2 The Orbit-Attitude Solar Sailing Problem

A coupled orbit-attitude approach to mission design may offer the possibility to employ orbit-attitude coupling devices to guide a spacecraft along a desired path. That possibility is the second main topic explored in this discussion. Currently, flat solar sails are likely the most practical means to supply orbit-attitude maneuvering capability: the attitude of a sail relative to the incoming photon flux determines the magnitude and the direction of the force experienced by the sail itself, and, therefore, may ultimately influence the orbital motion. These devices potentially enable nearly-zero-cost station keeping strategies, as many of the actuators for attitude control do not use propellant or only necessitate a significantly small fraction of the overall DV budget. Then, is it possible to demonstrate their utilization in a coupled orbit-attitude dynamical model? Are orbit-attitude steering laws efficacious? Can natural orbit-attitude dynamics aid the practical implementation for a guidance strategy? What control inputs are available within a coupled orbit-attitude design, and how the guidance approach changes? To start the development for a framework able to address those general questions, the following specific objectives are recognized:

- Develop algorithms to construct solar sail pointing sequences able to maintain the vehicle in vicinity of the reference orbit.
- Assess the effectiveness for the proposed guidance strategies on a short-term time window.
- Preliminarily explore benefits and limitations for each strategy.

Developing effective techniques to control orbit-attitude coupling devices is a key factor to incorporate a coupled orbit-attitude model into the design process, and potentially enable alternative, more efficient, missions.

1.2 Summary of Previous Contributions

1.2.1 Attitude Dynamics and Periodic Solutions in the Circular Restricted Three-Body Problem

Within the CR3BP, the earliest investigations from Kane, Marsh and Robinson consider the attitude stability of different satellite configurations, assuming that the spacecraft is artificially maintained precisely at the equilibrium points [8, 9]. Successive studies introduce Euler parameters, i.e., quaternions, and Poincaré maps to explore the dynamics of a single body, one that remains fixed at the Lagrangian points [10,11]. The effects of the gravity torque along libration point orbits are examined by Wong, Patil and Misra for a single rigid vehicle in the Sun-Earth system [12]. Wong, Patil and Misra select Lyapunov and halo orbits for their investigation, and assume reference trajectories that are expressed in linear form; consequently, the results are acknowledged to apply to relatively small orbits close to the equilibrium points. Incorporating another simplification of the CR3BP, i.e., the Hill problem, Sanjurjo-Rivo et al. numerically reproduce the coupled orbit-attitude dynamics of a large dumbell satellite on halo and vertical orbits in the Earth-Moon system [13]. The application of Hill equations is limited to the vicinity of the smallest body in the system, when such a primary has practically negligible mass compared to the other attractor. Assuming that the spacecraft is in fast rotation, the attitude dynamics can be decoupled from the orbital dynamics by averaging the equations of motion over the "fast" angle [13]. Under this condition, it is demonstrated that incorporating sufficiently elongated structures may impact the stability of halo and L_2 vertical orbits in the Hill problem [14]. Later, Guzzetti et al. numerically investigate the coupled orbit and attitude equations of motion using the Lyapunov family as reference orbits and without simplifications of the CR3BP nonlinear dynamics, but the rotation of the vehicle is limited to the orbital plane [15, 16]. Guzzetti et al. also incorporate solar radiation pressure and simple flexible bodies in the investigation. The full three-dimensional coupled motion is explored by Knutson and Howell for a spacecraft comprised of multiple bodies in nonlinear Lyapunov and halo reference orbits [17, 18]. Both Knutson and Guzzetti dedicate significant effort to identify conditions that determine bounded attitude solutions relative to the rotating frame in the CR3BP along nonlinear reference trajectories. Attitude maps are proven useful to recognize the orbital characteristics and the body inertia properties that enable the spacecraft to maintain its initial orientation with respect the rotating frame [19, 20]. Additionally, Meng, Hao and Chen analyze the case of a dual-spin satellite in halo orbits and, employing a semi-analytical expansion of the gravity torque, identify the main frequency components of the subsequent motion [21].

Along with stability diagrams at the equilibrium points, mapping techniques and frequency analysis, periodic solutions may contribute to the understanding of the attitude dynamics when it is coupled to the CR3BP. In this investigation, solutions are sought that are simultaneously periodic in both the orbital and attitude states, when viewed in the rotating frame in the CR3BP. From the orbital dynamics perspective only, periodic orbits are one of the most successful approaches to the circular restricted three-body problem, which lacks a closed form analytical solution. Poincaré first indicated periodic solutions as the primary means of understanding the CR3BP [22]. However, at the time, the search of periodic orbits was significantly limited by the numerical capabilities, to the extent that a prominent investigator, such as Forest Moulton believed that certain periodic solutions are "practically impossible" to compute [23]. With the advent of artificial calculators, such concern is gone, as numerical procedures grant easy access to several types of periodic solutions [24, 25]. To date, many periodic orbits or their neighbouring dynamical structures have been successfully exploited for space mission applications in both the Sun-Earth [26] and Earth-Moon [7] system. Catalogs of periodic and quasi-periodic orbits have been compiled to better understand the dynamical behaviour [27] and to guide mission design within the context of a given three-body system [28–30]. Most recently, the possibility to identify and compute an attitude periodic motion that is coupled to an existing CR3BP periodic orbit, has also been demonstrated [31, 32]. Within a multi-body regime, coupled orbit-attitude periodic structures enlarge the current design space, and add options that may support certain mission applications. Following the introduction of coupled orbit-attitude periodic solutions within the CR3BP, Bucci explores the application of a coupled periodic motion to a large space structure that is located in a distant retrograde orbit, and offers an analysis of the perturbations induced by the solar radiation pressure and spacecraft flexibility to the reference CR3BP orbit-attitude periodic solution [33].

Periodic solutions are typically generated by numerically correcting an initial guess to meet specific boundary conditions, which include the continuity between the final and initial states. Physical symmetries or integrals of the motion may also be leveraged to enforce periodicity. Even with the current computational capabilities, the convergence of algorithms for periodic orbits depends significantly on the accuracy of the initial guess and the implementation of the targeting scheme. In this investigation, viable methods to obtain precise initial guesses and effectively solve for periodicity are explored in the coupling of orbit and attitude. Several numerical schemes are available to solve boundary values problems. Because of its simplicity and adaptability, single shooting is frequently applied to orbital mechanics in the CR3BP [34]. The Two-Point Boundary Value Problem (TPBVP) is converted to an Initial Value Problem (IVP), where the selected initial states are iteratively updated, on the basis of a Newton approach, until the constraints at the final time are satisfied within a given tolerance, i.e., differential corrections. If the single shooting is employed in combination with specific symmetry features of the motion, then it is obviously limited to solutions that share those symmetries [34]. A direct extension of the single shooting scheme is to target multiple states along the path, rather than only the final states. This method, also known as multiple shooting, is introduced by Keller to solve general TPBVP's [35] and is now largely applied to the computation of periodic orbits [36–38]. A common implementation of multiple shooting, denoted as parallel shooting, requires all the design variables to be simultaneously corrected to target the complete set of constraints along the path at each iteration. An alternative multiple shooting algorithm is the, so called, two level corrector, that was originally developed in astrodynamics to compute quasi-periodic motions [39] and introduced a nested level of iterations to converge on a subset of the constraint vector by adjusting a subset of the free variables. This method is currently also applied to periodic and non-periodic trajectories to impose various path constrains to the baseline trajectory [40]. Finally, specific parameters of the periodic solution may be varied to form other periodic solutions that belong to the same dynamical family. This continuation process can be based on the direct modification of the natural parameters or using the direction tangent to the null space of the monodromy matrix associated to the reference periodic solution. The latter algorithm is denoted pseudo-arclength continuation and, in some applications, benefits from a more general and robust formulation than the natural parameter continuation [41].

1.2.2 Solar Sailing

Solar sails are originally envisioned as an alternative propulsion mechanism for transfers within the solar system. In this context, the minimum-time optimal problem is usually examined for transfers from the Earth to other interplanetary destinations. The path control may be implemented as a continuous-time law [42,43], which requires constant maneuvering of the sail pointing direction throughout the trajectory. Within the CR3BP, Waters and McInnes utilize a continuous control scheme in combination with the natural manifolds to transfer a spacecraft to a parking orbit in vicinity of the L_1 Lagrangian point [44]. The complexity of a continuous-time steering law can be reduced by dividing the trajectory into a finite number of arcs and assuming a fixed attitude relative to the Sun-sail line along each segment. Following this idea, Otten and McInnes discretize the true minimum-time solution into segments with fixed orientation; the solution is, then, no longer optimal, but it is significantly easier to implement [45]. Rather than discretizing the continuous solution, the optimal discrete problem may be solved as a sequence of control arcs, that fix the sail pointing direction relative to the Sun-sail line. Mengali and Quarta adopted this approach and further restrict the control set to a finite number of possible sail orientations during the transfer [46]. When a spacecraft is assumed to maintain a fixed orientation along each control arc, with respect to a relative or inertial reference, the guidance strategy is also referred as Turn and Hold (TnH) strategy. Besides transfers, it is well understood that solar sails enable a variety of displaced non-Keplerian orbits, that would not otherwise be accessible with solely chemical propulsion [47–49]. For these types of orbit, conic sail geometries are proposed as a possible means to achieve coarse passive orbit stabilization via a prescribed attitude configuration [50]; the investigation of such a mechanism naturally incorporates a coupled orbit-attitude model [51]. Alternatively, non-Keplerian displaced orbits may be maintained via classical forms of active control for the solar sail pointing direction [52].

Novel operational orbits are also possible in the CR3BP when the solar radiation pressure is incorporated and the sail is properly oriented. Solutions are developed for both autonomous, e.g., Sun-Earth, and non-autonomous, e.g., Earth-Moon, systems [53–55]. In an autonomous system, the source of radiation is fixed relative to the rotating frame, within the assumptions for the CR3BP, thus, the equations of motion are not explicitly a function of time. The orbits enabled by solar sailing may display unusual regimes of motion: see, for instance, trajectories proposed by Simo and C.R. McInnes [56], or by Wawrzyniak and Howell [57, 58]. Solar sail orbits also arise from a modification for the original dynamical structure within the CR3BP. For example, the Richardson approximation for CR3BP halo orbits may be adjusted to incorporate the solar radiation pressure; then, a set of halo orbits, equivalent to the natural CR3BP, may be computed [59–61]. Obviously, the greater the force exerted by the solar sail, the more a family of modified solutions deviates from the classical form within the CR3BP [61]. A solar sail may also be employed to maintain the vicinity of a reference orbit by controlling the attitude configuration, and, therefore, without the direct utilization of chemical propulsion. Several well-known approaches, such as, linearized optimal control [62, 63], Hamiltonian structure-preserving stabilization [64] or look-ahead strategies [65, 66] are generally applicable to the station keeping problem for a solar sail. Similar to transfer design, these control design approaches for station keeping may be used in combination with either an infinite (e.g., continuous-time scheme) or finite (e.g., Turn and Hold) set of control variables. Regardless of the nature for the control law, the control input is typically determined by the orientation of the solar sail, which is defined in terms of some angles or as a pointing vector. However, the attitude dynamics are not directly incorporated into the design process; the solar sail rotation history is afterwards reconstructed on the bases of the pointing sequence produced by the controller.

Along with steering techniques and trajectory design, several important applications for solar sails have been proposed. Geostorm is, for example, a mission concept that is largely discussed throughout the scientific community [67]. MacDonald [68] and Johnson [69] both supply a critical analysis for the most significant mission concepts that have been considered for solar sails. However, despite the clear interest in adopting solar sails, to date, only two missions have flown and implemented this technology. The Japanese test mission IKAROS is the first demonstration of flight operations in deep space for solar sails [70]. A similar objective is also accomplished by NanoSail-D, that is a cubesat satellite [71]. One possible follow-up missions is currently Sunjammer.[1] Sunjammer is a technology mission demonstrator being developed by LGarde Inc, that targets the vicinity of the sub-L_1 Lagrangian point within the Sun-Earth system. Trajectory design studies and higher fidelity sail models are on-going investigations [72]. One among the technical difficulties preventing a wider implementation of photon propulsion is certainly the challenge to store and deploy sails large enough to supply the desired level of acceleration. A sail is most likely constituted of a thin deformable surface; after deployment, achieving and maintaining an adequate level of stiffness for the sail structure is non-trivial. In the IKAROS mission, the entire sail is spinned at about 2 rpm to leverage the centrifugal force and artificially produce stiffness. This method is simple and effective, however, it poses

[1]As January 2016, this mission is currently cancelled.

another difficulty that is well described by Wie [73, 74]: because of high moments of inertia (due to the large dimension for the reflective sail area) and a possible fast spin rate, conventional attitude actuators may be inadequate to supply the control authority necessary to steer the sail. As an alternative, the solar radiation pressure may be leveraged to generate the desired control moments. In IKAROS, a belt of Liquid Crystal devices is embedded in the sail and a net control moment is possible by varying the local reflectivity of the surface. Another strategy, explored within the design for Sunjammer, consists of small reflective vanes located at the tips of the sail; the vanes are actively oriented to provide a three-axis attitude control. Turning rates are problematic as well. Because a sail is highly deformable, an upper limit on the reorientation angular velocities may also exist. High turn rates may, in fact, distort the geometry of the sails and yield potential damages. Thus, as many of the advantages provided by solar sailing may be, to a certain degree, limited by the capability to reorient the solar sail, an investigation for its coupled orbit-attitude dynamics is justified. A collection of articles that more exhaustively review the current advances and challenges in solar sailing is published by MacDonald [75].

1.3 Present Work

In this investigation, the CR3BP is expanded to incorporate coupled orbit-attitude dynamics, both natural and artificial. First a general coupled orbit-attitude dynamical model for a rigid, monolithic, spacecraft is formulated. Simplifying assumptions on the coupling effects are introduced to allow the establishment for an initial framework of solutions. Yet, the model is sufficiently complex to reveal some of the challenges associated with an actual vehicle and mission application.

Within the process of designing an attitude profile for a space mission, a great effort is typically devoted to limit, or control, the spacecraft natural librations. Spacecraft tumbling is, in most scenarios, not desirable, or even critically endangering the mission success. Natural bounded attitude librations are not necessarily trivial to identify within an intrinsically chaotic dynamics, such as that corresponding to the coupled orbit-attitude CR3BP. In this discussion, bounded librations are constructed in the form of orbit-attitude periodic solutions. Motions that exhibit natural periodic behavior, as observed from a rotating frame, in both the orbit and attitude components are a novel contribution to the exploration of the CR3BP. Numerical procedures to precisely compute an orbit-attitude periodic solution along a known periodic reference trajectory are discussed. The success for the numerical methods adopted, largely depends on the accuracy for the initial guess. Then, several approaches are proposed for obtaining a proper initial guess for an orbit-attitude periodic response, starting from well-known dynamical systems techniques, such as Floquet theory or Poincaré mapping. Non-trivial orbit-attitude periodic behaviors are successfully identified and accurately computed for librations along Lyapunov, halo, and distant retrograde orbits. Evidence that orbit-attitude behaviors also exist for a large variety of spacecraft mass distributions and initial configurations is manifest from the available solutions. Natural periodic motions not only supply a reference for possible bounded librations but may also allow other fundamental dynamical structures, e.g., manifolds or quasi-periodic torii, to emerge, ones that may eventually yield a new dynamical approach to attitude operations.

Alternative forms of trajectory control to direct the spacecraft along a desired orbital path may also develop from a mutual interaction between the orbit and attitude dynamics, such as in the case of solar sailing. Accordingly, the orbit-attitude framework is applied to a simple solar sail application. As a contribution of this work, various types of control input are explored to maneuver the sailcraft. Classical steering strategies, such as a Turn and Hold approach, are discussed within the context of a coupled orbit-attitude regime, and other types of guidance, that necessarily depend on the inclusion of the vehicle rotational dynamics, are introduced. Each guidance strategy is applied to a simplified station keeping scenario, that serves as a stepping stone for more complex applications.

The organization of this study is as follows:

- Chapter 2. System Models - In this chapter, the equations of motion are derived for the CR3BP, a general attitude problem, and for the coupled orbit-attitude dynamics within the CR3BP. Equilibrium and periodic solutions within the CR3BP are discussed. Orbit-attitude coupling effects induced by higher order gravitation components and solar radiation pressure are presented.

- Chapter 3. Numerical Targeting Schemes - Linear variational equations and the associated state transition matrix are formulated for the orbit-attitude dynamics. These equations are employed within the numerical solution for a two-boundary value problem, that may reflect the existence of periodicity conditions (e.g., bounded librations problem) or the targeting of a desired final state along a reference orbit (e.g., solar sailing problem). Ultimately, the two-boundary problem is transformed into an initial value problem, that is solved via differential correction. A multiple shooting formulation that implements Newton-Raphson updates is the principal numerical scheme for the computation of both orbit-attitude periodic solutions and solar sail trajectories. Additionally, two methods for the numerical continuation of a solution are presented, and applied for the creation of families for similar orbit-attitude behaviors.

- Chapter 4. Bounded Librations: Identification of Orbit-Attitude Periodic Solutions by Floquet Theory - Following the definition of a numerical strategy to precisely compute orbit-attitude periodic solutions, the application of Floquet theory for the identification of a viable initial guess is discussed. An elementary orbit-attitude periodic motion for an axysimmetric spacecraft is employed as an initial reference. The stability for this elementary motion is explored for various reference periodic orbits, including Lyapunov and distant retrograde orbits. Modification of the vehicle inertia properties is also considered. A variation of the stability structure may indicate the existence of a distinct periodic solution nearby the reference. In fact, various non-elementary orbit-attitude periodic solutions are revealed. The analysis of representative non-elementary orbit-attitude periodic motions is included.

- Chapter 5. Bounded Librations: Identification of Orbit-Attitude Periodic Solutions by Poincaré mapping - In this chapter the possibility to recognize an orbit-attitude periodic solution via an ordered structure that emerges on a Poincaré map is explored. An algorithm to automatically detect the existence of ordered patterns onto a Poincaré mapping, and facilitate the analysis of several surface of sections is investigated. The automatic identification algorithm is based on statistics that relates to the distribution of returns to the surface of section. A large campaign of Poincaré map simulations, that is enabled by the automatic identification algorithm, encompasses several reference periodic orbits and spacecraft mass distributions. The analysis of representative orbit-attitude periodic motions, that are revealed by the Poincaré maps, is included.

- Chapter 6. Bounded Librations: Identification of Orbit-Attitude Periodic Solutions by Grid Search - Previous research has demonstrated that regions of orbit-attitude bounded motion, in terms of selected system parameters, may emerge on a grid search map. A grid search map is basically a visual summary of several simulations, that are generated for different configurations of the selected parameters. A possible link between an area of bounded motion on a grid search map and the existence of an orbit-attitude periodic solution within that region, is demonstrated. Upon the understanding of that connection, a representative family of orbit-attitude periodic behaviors is revealed along L_1 halo orbits.

- Chapter 7. Solar Sailing: Maneuvering Strategies - It is reasonable to regard a solar sail as an orbit-attitude coupling device, that enables a change in the vehicle attitude configuration to guide the orbital path. Considering such a capability, different guidance strategies are formulated. Each guidance law is developed within a coupled orbit-attitude regime, and leverages a distinct control input, one that first influences the spacecraft orientation. Thus, an instantaneous solar sail pointing realignment, an external control torque, and a relative angular momentum vector, may be supplied by internal rotors, are explored as control inputs.

- Chapter 8. Solar Sailing: Application to a Simple Station Keeping Scenario in the Sun-Earth System - The guidance strategies discussed in the previous chapter, are implemented in a simple station keeping scenario for an ideal, flat solar sail. Given selected orbits within the modified L_1 halo family for the Sun-Earth system, each strategy is applied to correct an initial error in position and velocity, and target a desired final state along the nominal orbit. This elementary test offers some of the challenges associated with controlling the solar sail pointing direction to steer the vehicle orbital path within a coupled orbit-attitude model, and can easily be extended to reflect more complex operational scenarios.

- Chapter 9: Concluding Remarks - A summary for the main results of this investigation and recommendations for future work are included here.

2. SYSTEM MODELS

2.1 Relevant Notation Convention

The following list supplies basic guidelines on relevant notation convention that is adopted throughout this document:

- Vector quantities are denoted in bold, e.g. $\boldsymbol{v}$. The modulus corresponding to the vector $\boldsymbol{v}$, is $||\boldsymbol{v}|| = v$. The vector basis for $\boldsymbol{v}$ may be specified as $\underset{\hat{a}}{\boldsymbol{v}}$, which explicitly indicates that $\boldsymbol{v}$ is written in the $\hat{a}$-frame.

- An unit vector is denoted by the hat notation, $\widehat{\bullet}$. For example, $\hat{\boldsymbol{v}}$ indicates a vector with unitary module, $v = 1$.

- To describe the rotation of a final $\hat{a}'$-frame relatively to an initial $\hat{a}$-frame, the corresponding direction cosine matrix is written as $\underset{\hat{a}'\cdot\hat{a}}{A}$. Other vector quantities that describe characteristics of the $\hat{a}'$-frame with respect to the $\hat{a}$-frame, are written as ${}^{a}\boldsymbol{v}^{a'}$.

- A partial derivative of a vector $\boldsymbol{v}$ with respect to a vector quantity $\boldsymbol{x}$, $\dfrac{\partial \boldsymbol{v}}{\partial \boldsymbol{x}}$, is written as $\boldsymbol{v}_{/\boldsymbol{x}}$. The same notation applies to scalar quantities.

- the time derivative $\dfrac{d\boldsymbol{v}}{dt}$ is expressed with the Newton's notation, $\dot{\boldsymbol{v}}$.

2.2 Orbital Dynamics

This work explores orbit-attitude dynamics for a spacecraft that is moving in a non-keplerian regime. Specifically, the underlying model for the vehicle orbital dynamics is the Circular Restricted Three Body Problem (CR3BP). Coupling forces may be particular relevant in this regime that, in certain locations, such as the vicinity of certain equilibrium points, is characterized by highly nonlinear and sensitive dynamics. It follows that, the identification of solutions that are relevant to mission design is challenging for this problem.

2.2.1 The Circular Restricted Three-Body Problem

Consider three masses that interact gravitationally. The two more massive bodies P_1, and P_2, define the primary attractors, and are also simply referred as primaries; the third body P_3 may represent a particle of interest, such as a spacecraft or a natural object within the same celestial system. The motion of three particles under mutual gravitational influence may be directly described by Newton's second law. For certain practical scenarios, the motion of the particle of interest P_3 is, however, the only dynamics relevant. In such a case, it may be advantageous to introduce a series of simplifying assumptions that preserve some fundamental underlying multi-body dynamics, and increase the tractability of the general three-body problem. This simplification of the model is practical and useful in several applications. Thus, the following assumptions are considered:

- The primaries P_1 and P_2 are spheres with uniform mass density.
- The particle of interest P_3 possesses negligible mass compared to the bodies P_1 and P_2, and does not affect their motion.
- The primaries P_1 and P_2 travel along circular orbits around their common center of mass.
- The body P_1 is more massive than the body P_2.

The resulting model is commonly known as the Circular Restricted Three-Body Problem (CR3BP), and largely presented in orbital mechanics literature [76–78]. As the bodies P_1 and P_2 follow a known circular trajectory, it is possible to define a synodic frame that is fixed relative to the primaries. This synodic frame originates at the baricenter for the P_1-P_2 system and rotates with constant angular velocity Ω relative to an inertial reference. The angular velocity Ω equals the mean motion of the system P_1-P_2. The geometry of the CR3BP is conveniently rendered within a synodic rotating frame, or simply, rotating frame. When expressed in terms of this rotating frame, the dynamical equations for the CR3BP possess, in fact, an analytical integral of the motion. Let $(\hat{\boldsymbol{x}}, \hat{\boldsymbol{y}}, \hat{\boldsymbol{z}})$ be the unit vectors that define the rotating frame, such that $\hat{\boldsymbol{z}}$ is normal to primaries orbital plane, and let $(\hat{\boldsymbol{X}}, \hat{\boldsymbol{Y}}, \hat{\boldsymbol{Z}})$ be the vector basis for the inertial reference frame, as depicted in Figure 2.1. The inertial and rotating frame are aligned at $t = 0$. Conventionally, the primaries lie on the x-axis for the synodic frame. Finally, the system is normalized with the following quantities appearing as unit: the total system mass m, the distance between the two attractor centers, the angular frequency Ω of the circular motion for the P_1-P_2 system, and the universal constant of gravity G. Length, velocity and time are converted as follows

$$
\begin{aligned}
\text{[Length]} \quad & \ell' = L\ell \\
\text{[Velocity]} \quad & v' = \frac{L}{T}v \\
\text{[Time]} \quad & t' = \frac{T}{2\pi}t \quad ,
\end{aligned}
$$

where the primed quantities are dimensional, and the unprimed variables are normalized; L is the dimensional distance between P_1 and P_2, and T is the orbital period of P_1 and P_2. Such quantities are tabled for different systems in [79]. Consequent to the normalization process, only one parameter describes the dynamics for the CR3BP, which is

$$\mu = \frac{m_2}{m_1 + m_2} \quad , \tag{2.1}$$

defined as the ratio between the P_2 mass and the total mass for the system $m_1 + m_2$. The mass parameter, μ, also defines the position in non-dimensional units for the primaries within the rotating frame: recalling $m_1 > m_2$, the primary P_1 is located in $(-\mu, 0, 0)$ and the body P_2 is at $(1 - \mu, 0, 0)$.

Expressing the Newton's second law of motion in the rotating frame via a nondimensional framework, and introducing a potential function, U, for the gravitational

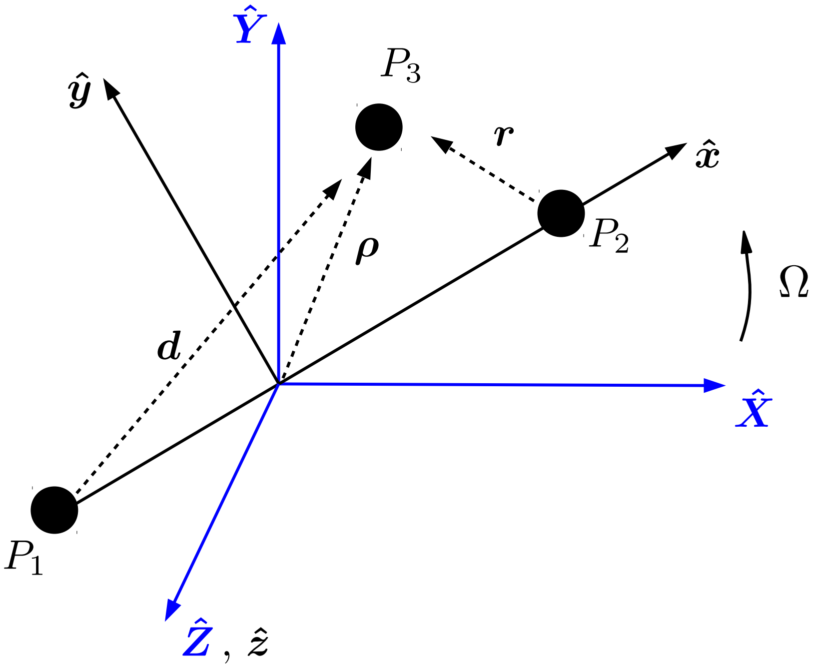

Figure 2.1. Geometry of the R3BP.

pull exerted by both P_1 and P_2, the relative acceleration for the particle P_3 is produced by

$$\ddot{\boldsymbol{\rho}} + 2\boldsymbol{n} \times \dot{\boldsymbol{\rho}} + \boldsymbol{n} \times (\boldsymbol{n} \times \boldsymbol{\rho}) + \dot{\boldsymbol{n}} \times \boldsymbol{\rho} = \frac{\partial U}{\partial \boldsymbol{\rho}} \tag{2.2}$$

where $\boldsymbol{\rho} = x\hat{\boldsymbol{x}} + y\hat{\boldsymbol{y}} + z\hat{\boldsymbol{z}}$ is the position vector for the particle of interest written in the rotating frame, and $\boldsymbol{n} = \Omega\hat{\boldsymbol{z}} = 1\hat{\boldsymbol{z}}$ is the nondimensional angular velocity of the rotating frame relative to the inertial frame. Following the assumptions for the CR3BP, the nondimensional equations of motion generally presented by Eq. (2.2), reduce to

$$\begin{cases} \ddot{x} &= 2\dot{y} + U^*_{/x} \\ \ddot{y} &= -2\dot{x} + U^*_{/y} \\ \ddot{z} &= U^*_{/z} \quad , \end{cases} \tag{2.3}$$

where $U^*(x,y,z) = \frac{1}{2}(x^2+y^2)+\frac{1-\mu}{d}+\frac{\mu}{r}$ is a modified expression for the gravitational potential function, or also known as pseudo-potential. The distances from P_1 and P_2 are respectively denoted by

$$d = \sqrt{(x+\mu)^2 + y^2 + z^2}\ , \quad r = \sqrt{(x-1+\mu)^2 + y^2 + z^2} \quad .$$

The system in Eq. (2.3) is autonomous (i.e., time does not explicitly appear within the dynamical equations), and there exist a known analytical integral, named Jacobi constant, that is $JC = 2U^* - (\dot{x}^2 + \dot{y}^2 + \dot{z}^2)$. By its definition, increasing the Jacobi constant reflects a decrease for the energy of P_3 within the rotating frame.

2.2.2 Libration Points

In certain locations within the configuration space defined by the rotating frame, the gravitational force and the apparent centrifugal force mutually balance, yielding zero relative acceleration on the particle of interest, P_3. A particle, such as a spacecraft, that is at rest at those locations will ideally preserve its state of equilibrium. The position of such equilibrium points, indicated by the vector $\boldsymbol{\rho}_{eq}$, may be identified as the zero for the gradient of the pseudo-potential function, $\nabla U^*(\boldsymbol{\rho}_{eq}) = 0$. Referencing Figure 2.2, the equilibrium points are usually divided into two groups:

- three equilibrium solutions lie on the x-axis of the rotating frame, and are named collinear points. Specifically, the point between the two attractors is labelled L_1; the point beyond the smaller primary, along the positive x direction, is L_2; the equilibrium preceding P_1 along the x-axis, is denoted L_3.

- two equilibrium solutions display an unit distance (in non-dimensional units) from both the primary bodies. As each of these two points forms an equilateral triangle with P_1 and P_2, they are known as the equilateral points L_4 (positive y coordinate) and L_5 (negative y coordinate).

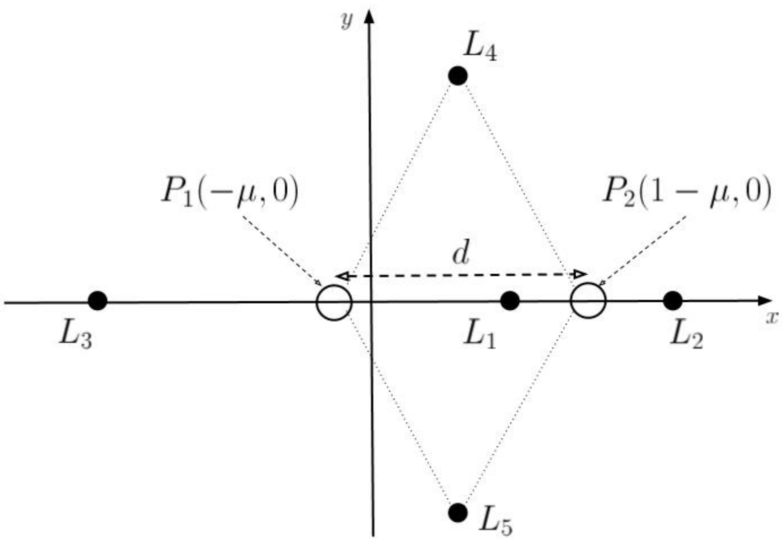

Figure 2.2. Geometry of the equilibrium points.

To determine the location for the L_4, and L_5 equilibria, consider that the function $U^*(d, r)$ has the same critical points as the function $U^*(x, y, z)$, when $y \neq 0$, and $z = 0$ [79]. Employing the pseudo-potential function $U^*(d, r)$ yields

$$\begin{cases} U^*_{/d} = & -(1-\mu)d + \dfrac{(1-\mu)}{d^2} & = 0 \\ U^*_{/r} = & -\mu r + \dfrac{\mu}{r^2} & = 0 \quad . \end{cases} \tag{2.4}$$

The unique solution for Eq. (2.4) is $d = r = 1$, which produces an equilateral equilibrium configuration for P_1, P_2, and P_3, as in Figure 2.2. The collinear equilibria are, instead, rendered by the critical points for

$$U^*(x, 0, 0) = -\frac{1}{2}x^2 - \frac{1-\mu}{|x+\mu|} - \frac{\mu}{|x+\mu-1|} \quad . \tag{2.5}$$

The computation for $dU^*(x, 0, 0)/dx = 0$ yields a quintic equation after simplification. Selecting the equilibrium points L_i , $i = 1, 2$, such quintic expression is the polynomial

$$\gamma_i^5 \mp (3-\mu)\gamma_i^4 + (3-2\mu)\gamma_i^3 - \mu\gamma_i^2 \pm 2\mu\gamma_i - \mu = 0 \quad , \tag{2.6}$$

where γ_i is the positive distance of the equilibrium point L_i from the nearest primary (i.e., the body P_2 for $i = 1, 2$). In Eq. (2.6) the upper signs are used for γ_1, the lower sings for γ_2. The roots for Eq. (2.6) are not available in closed form, but numerical schemes, such as the Newton's method, may be employed. The substitution of γ_i to the x coordinate improves the robustness of a numerical approach to the solution of Eq. (2.6). A good initial guess may be also obtained with a series expansion [78], such as

$$\gamma_1 = r_h(1 - \frac{1}{3}r_h - \frac{1}{9}r_h^2 + \ldots) \quad , \tag{2.7}$$

and

$$\gamma_2 = r_h(1 + \frac{1}{3}r_h - \frac{1}{9}r_h^2 + \ldots) \quad , \tag{2.8}$$

with $r_h = (\mu/3)^{1/3}$. The equilibrium points, both equilateral and collinear, are also called Lagrangian points (as a tribute to the contribution of Lagrange to the identification of L_4 and L_5), or librations points (in correlation to the possible existence of nearby periodic behaviors).

2.2.3 Periodic Orbits in the CR3BP

Periodic orbits are another relevant set of solutions for Eq. (2.3) within the CR3BP. A periodic orbit is such that any arbitrary state, along the trajectory, as defined relatively to a given reference, recurs at intervals. The minimum time span between the recurrence of a selected state is named minimal period of the orbit, or simply period. If the dynamical flow associated to a given set of equations of motion, e.g., Eq. (2.3), is $\phi(\boldsymbol{x}, t)$, then, any state $\boldsymbol{x}_0$ that belongs to the periodic orbit, Γ, satisfies

$$\boldsymbol{x}_0 = \phi(\boldsymbol{x}_{\mathbf{0}}, P) \quad \text{for} \quad \boldsymbol{x}_0 \in \Gamma \quad , \tag{2.9}$$

where $t = P$ is, in fact, the period of the orbit. The relationship in Eq. (2.9) is also satisfied for any multiple integer of the period, P. The existence of periodic behaviors also depends on the definition of the system state description. Recall that, the equations of motion for the CR3BP are typically written within the rotating frame, as in Eq. (2.3). Accordingly, periodic motions are naturally observed in position and velocity as defined within the rotating frame. A trajectory periodic within the rotating frame, does not necessarily retain its periodicity when transitioned to a different set of coordinates, such as an inertial frame. Obviously, the concept of periodicity can be applied to any dynamical system, consistently with the definition for its state variables.

There exist an infinite number of periodic orbits that permeates the solution space for the CR3BP. Periodic orbits may be organized into families. Members of the same family share the continuous variation of certain parameters and generally display similar motion patterns. Families of periodic orbits within the Earth-Moon system that have been utilized or proposed for mission applications include, for example, L_1/L_2 Lyapunov orbits (Figure 2.3), L_1/L_2 halo orbits (Figure 2.4), Distant Retrograde Orbits (DRO) (Figure 2.5). Considering the Earth-Moon system, more details on the currently well-established periodic solutions within the CR3BP, their classification and characterization are available in [80]. A periodic trajectory may be obtained by targeting symmetry conditions at the final state, which is located half-way along the orbit, or, directly solving for the continuity between the initial and final state after one period. Several numerical schemes for the precise computation of periodic orbit are discussed in [81].

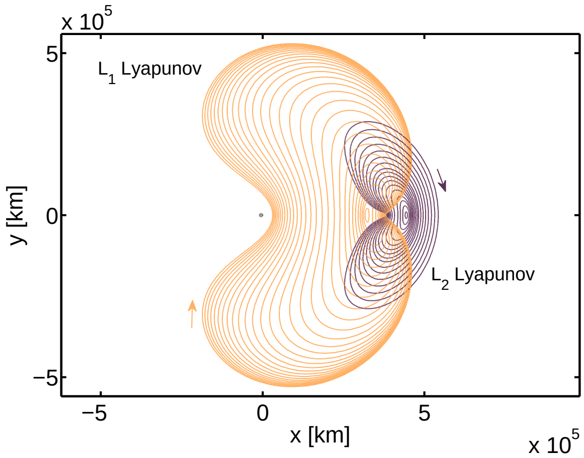

Figure 2.3. Lyapunov type periodic orbits within the Earth-Moon system (rotating frame).

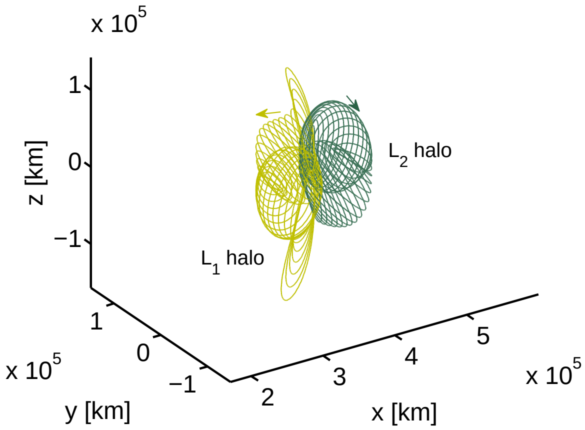

Figure 2.4. Halo type periodic orbits within the Earth-Moon system (rotating frame).

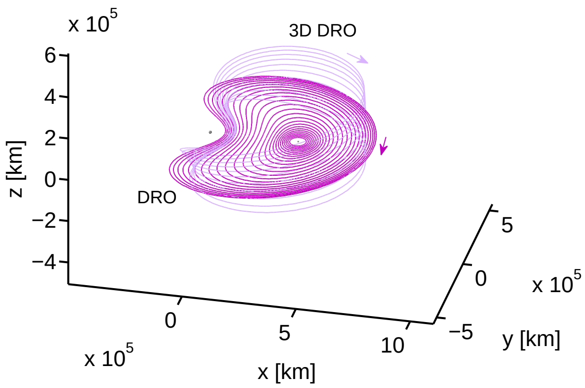

Figure 2.5. DRO type periodic orbits within the Earth-Moon system (rotating frame).

2.2.4 Gravity on a Rigid Body Exerted by a Particle

Within the assumptions for the CR3BP, the model for the body of interest, P_3, is equivalent to a mass-point. When orbit-attitude dynamics are considered, the finite extension for P_3 is necessarily introduced. In general, the resultant gravity force on a particle, and on an extended body are naturally different. Let a rigid body with mass m experience the gravitational pull of a particle P_i with mass m_i, as illustrated in

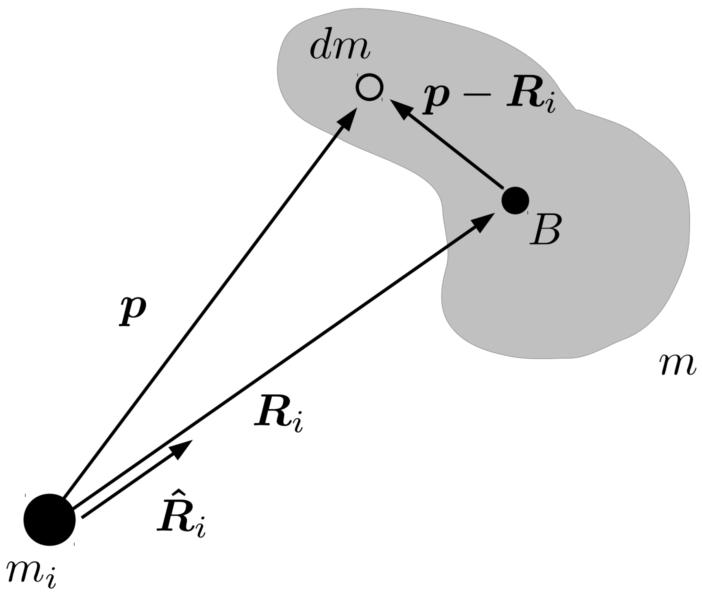

Figure 2.6. Gravity force exerted by a particle on a rigid body schematics.

Figure 2.6. The precise expression for the gravity force that is applied on m because of m_i is

$$\boldsymbol{F}_i = -Gm_i \int_m \boldsymbol{p}(\boldsymbol{p}\cdot\boldsymbol{p})^{-3/2} dm \quad , \tag{2.10}$$

where $\boldsymbol{p}$ denotes the position vector of an infinitesimal mass, dm, relative to the selected primary, P_i, and G is the universal gravitational constant. When more attracting particles exist within the system, as for the CR3BP, the total force on the rigid body is simply the summation of each individual contribution, that is computed using Eq. (2.10). A useful form for Eq. (2.10) can be obtained by replacing the vector $\boldsymbol{p}$ with the vector $\boldsymbol{R}_i$, defined as $\boldsymbol{R}_i = R_i\hat{\boldsymbol{R}}_i$, which describes the position of the body center of mass, B, relative to the primary P_i, and yields

$$\boldsymbol{F}_i = -\frac{Gm_i m}{R_i^2}\left[\hat{\boldsymbol{R}}_i + \sum_{j=2}^{\infty} \boldsymbol{f}^{(j)}\right] \quad . \tag{2.11}$$

In Eq. (2.11), the resultant force is separated in two contributions: first, the force directed along the radial direction, $\hat{\boldsymbol{R}}_i$, and equivalent to a mass-point located at the body center of mass; second, a collection of terms, $\boldsymbol{f}^{(j)}$, that are proportional to ascending powers $(|\boldsymbol{p} - \boldsymbol{R}_i|/\boldsymbol{R}_i)^j$, and reflect the body finite mass distribution [82].

When the summation for the terms $\boldsymbol{f}^{(j)}$ is zero, the gravity force configuration acting on the body is identical to a point-mass model. A mass distribution that displays such a property, is named centrobaric. For a body that is small compared to the distance from the primary, such that $(|\boldsymbol{p} - \boldsymbol{R}_i|/\boldsymbol{R}_i) << 1$, every component of the series proportional to a power for $(|\boldsymbol{p} - \boldsymbol{R}_i|/\boldsymbol{R}_i)^j$ higher than the second order is, typically, neglected. The remaining second order term is a function of the body inertia tensor about the center of mass, I, as

$$\boldsymbol{f}^{(2)} = \frac{1}{mR_i^2}\left\{\frac{3}{2}\left[Tr(I) - 5\hat{\boldsymbol{R}}_i \cdot I \cdot \hat{\boldsymbol{R}}_i\right]\hat{\boldsymbol{R}}_i + 3I \cdot \hat{\boldsymbol{R}}_i\right\} \quad ; \tag{2.12}$$

recall that, m is the mass of the body, and $\hat{\boldsymbol{R}}_i$ is a unit vector that aligns along the line from P_i to B. Accordingly, an expression for the gravity force, approximated for a small body that is distant from the primary, is supplied by

$$\boldsymbol{F}_i \approx -\frac{Gm_i m}{R_i^2}\left[\hat{\boldsymbol{R}}_i + \boldsymbol{f}^{(2)}\right] \quad . \tag{2.13}$$

The vector $\boldsymbol{f}^{(2)}$ is not generally parallel to the direction $\hat{\boldsymbol{R}}_i$, consequently, the resultant gravity force does not align with the line from the primary to the body center of mass. Previous studies report that, perturbations other than the second order gravity expansion $\boldsymbol{f}^{(2)}$, e.g., the solar radiation pressure, appear more relevant for small bodies (characteristic length less than 100 m) in vicinity of the libration points [15]. Therefore, to possibly facilitate the identification of fundamental orbit-attitude dynamical structures for a small spacecraft, the components of the gravitational force that corresponds to $\boldsymbol{f}^{(2)}$ (or any higher order term) are not included in the orbital model, as they are negligible compared to other types of orbital perturbation.

2.2.5 Solar Radiation Pressure

In determining the path evolution for a spacecraft that travels at a significant distance from any gravitational attractor, for example stationing near a libration point or rendering other types of motion within the CR3BP, the Solar Radiation Pressure (SRP) may be an important addition to the point-mass gravitational force model.

The solar radiation pressure is an expression for the exchange of linear momentum between incoming photons from the Sun and a material surface that is immersed into such a flux. This interaction generates a net force on the surface that may disturb the nominal trajectory, or may also be exploited as an alternative propulsion mechanism, e.g., solar sail applications. Assuming an opaque surface, three types of phenomena may occur after the collision of the photons flux with the surface: specular reflection, diffuse reflection and absorption. Each type of interaction produces an infinitesimal force on the infinitesimal local impact area, dA,

$$d\boldsymbol{F}_a = Pc_a \cos\alpha \hat{\boldsymbol{\ell}}_1 \, dA \qquad \alpha \in [-\pi/2, \pi/2] \tag{2.14}$$

$$d\boldsymbol{F}_d = Pc_d \left(\frac{2}{3} \cos\alpha \hat{\boldsymbol{u}} + \cos\alpha \hat{\boldsymbol{\ell}}_1 \right) dA \qquad \alpha \in [-\pi/2, \pi/2] \tag{2.15}$$

$$d\boldsymbol{F}_s = 2Pc_s \cos^2\alpha \hat{\boldsymbol{u}} \, dA \qquad \alpha \in [-\pi/2, \pi/2] \tag{2.16}$$

where the subscripts a, d, s, denote the absorbed, diffusively reflected and specularly reflected radiation, respectively; P is the time-average radiation pressure at a given distance from the Sun, $d_\odot$, which is derived from a reference value at one Astronomical Unit (AU) $P_0 = 1358\text{W/m}^2$ as

$$P = \frac{P_0}{(d_\odot[AU])^2} \quad , \tag{2.17}$$

with $d_\odot$ expressed in astronomical units; α is the angle between the incident photons direction $\hat{\boldsymbol{\ell}}_1$ and the local surface normal $\hat{\boldsymbol{u}}$, defined by

$$\cos\alpha = \hat{\boldsymbol{\ell}}_1 \cdot \hat{\boldsymbol{u}} \quad ; \tag{2.18}$$

the coefficients c_a, c_d, c_s represent the percentage of the incoming flux that is absorbed, diffusively reflected and specularly reflected, respectively. These percentages are not necessarily constant throughout the surface, but they satisfy the following relationship at any point

$$c_s + c_d + c_a = 1 \quad . \tag{2.19}$$

Integrating over the total surface area, A, the sum of the infinitesimal actions in Eq. (2.14)-(2.16) and substituting Eq. (2.19), yields the total force produced by the solar radiation pressure

$$\boldsymbol{F}_{\text{SRP}} = P \int_A \left[(1 - c_s)\hat{\boldsymbol{\ell}}_1 + 2\left(c_s(\hat{\boldsymbol{\ell}}_1 \cdot \hat{\boldsymbol{u}}) + \frac{1}{3}c_d \right) \hat{\boldsymbol{u}} \right] (\hat{\boldsymbol{\ell}}_1 \cdot \hat{\boldsymbol{u}})\, dA \quad . \tag{2.20}$$

The integration of Eq. (2.20) is elementary for a flat surface (illustrated in Figure 2.7) with constant coefficients, and it is further simplified by including solely specular reflection, resulting in

$$\boldsymbol{F}^{SRP} = PAc_s(\hat{\boldsymbol{\ell}}_1 \cdot \hat{\boldsymbol{u}})^2 \hat{\boldsymbol{u}} \quad , \tag{2.21}$$

The expression in Eq. (2.21) may also describe the force produced by an ideal solar sail, i.e., flat and perfectly reflective.

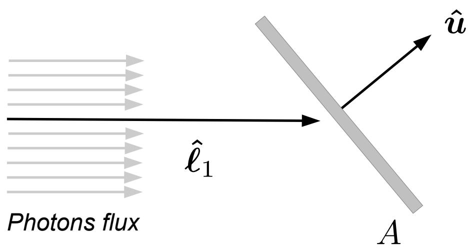

Figure 2.7. Solar radiation pressure on a flat surface schematics.

2.3 Attitude Dynamics

In this investigation, the prediction, and possibly the control, for a space vehicle orientation in the three-dimensional space is incorporated within the CR3BP framework. The discipline that typically concerns a spacecraft rotational motion is referred as attitude dynamics. Attitude dynamics proceeds from the definition for a kinematical description that represents the vehicle orientation relative to some reference frame, to the formulation of equations of motion that render the body orientation evolution in time. Basic concepts, that are employed to construct the orbit-attitude dynamical framework, are discussed in the following sections.

2.3.1 Rotational Kinematics

There exist several representations to render a rigid body orientation relative to a given observer, but, at minimum, three variables are required within any description [82]. Some parameter combinations within a minimum set may, however, produce the identical, actual, spacecraft orientation. A vehicle attitude configuration that does not uniquely correspond to a set of the selected kinematical variables is referred as a singularity. Adding additional parameters may aid in removing certain singularities. Note that, any non-minimal set is accompanied by additional constraint equations, that are appropriate to restore the correct number of independent variables. Three attitude descriptors are principally employed in this work as detailed below.

Direction Cosine Matrix

The matrix formalism offers a simple means of relating one coordinate frame to another. Consider the transformation from some initial frame, identified by the tern of unit vectors $(\hat{\boldsymbol{a}}_1, \hat{\boldsymbol{a}}_2, \hat{\boldsymbol{a}}_3)$, to some final frame, defined by the unit vectors $(\hat{\boldsymbol{a}}'_1, \hat{\boldsymbol{a}}'_2, \hat{\boldsymbol{a}}'_3)$. The initial and final frame may be simply referred as $\hat{a}$-frame and $\hat{a}'$-frame. Then, the rotation from the $\hat{a}$-frame to the $\hat{a}'$-frame may be written as

$$\begin{bmatrix} \hat{\boldsymbol{a}}'_1 \\ \hat{\boldsymbol{a}}'_2 \\ \hat{\boldsymbol{a}}'_3 \end{bmatrix} = \underset{\hat{a}'\cdot\hat{a}}{A} \begin{bmatrix} \hat{\boldsymbol{a}}_1 \\ \hat{\boldsymbol{a}}_2 \\ \hat{\boldsymbol{a}}_3 \end{bmatrix} \quad , \tag{2.22}$$

where

$$\underset{\hat{a}'\cdot\hat{a}}{A} = \begin{bmatrix} A_{11} & A_{12} & A_{13} \\ A_{21} & A_{22} & A_{23} \\ A_{31} & A_{32} & A_{33} \end{bmatrix} \quad . \tag{2.23}$$

is the Direction Cosine Matrix (DCM). The elements that comprise the DCM may be employed as a nine-parameter set to deduce the orientation of the $\hat{a}'$-frame with respect to the $\hat{a}$-frame, in fact,

$$\begin{aligned} \hat{a}'_1 &= A_{11}\hat{a}_1 + A_{12}\hat{a}_2 + A_{13}\hat{a}_3 \\ \hat{a}'_2 &= A_{21}\hat{a}_1 + A_{22}\hat{a}_2 + A_{23}\hat{a}_3 \\ \hat{a}'_3 &= A_{31}\hat{a}_1 + A_{32}\hat{a}_2 + A_{33}\hat{a}_3 \quad . \end{aligned} \tag{2.24}$$

The direction cosine matrix, $\underset{\hat{a}'\cdot\hat{a}}{A}$, is equivalent to a rotation matrix that changes the vector basis for a given vector, $\boldsymbol{v}$, from the $\hat{a}$-frame to the $\hat{a}'$-frame, simply

$$\underset{\hat{a}'}{\boldsymbol{v}} = \underset{\hat{a}'\cdot\hat{a}}{A}\ \underset{\hat{a}}{\boldsymbol{v}} \quad , \tag{2.25}$$

where, in fact, $\underset{\hat{a}}{\boldsymbol{v}}$ is some vector written in the initial set of coordinates and $\underset{\hat{a}'}{\boldsymbol{v}}$ denotes the same vector, but expressed in the final reference frame. As a rotation matrix, direction cosine elements must satisfy the following constraint equations

$$\underset{\hat{a}'\cdot\hat{a}}{A}^T \underset{\hat{a}'\cdot\hat{a}}{A} = \mathbb{I} \quad . \tag{2.26}$$

Direction cosine matrices are particularly useful to transform vector, or tensor, quantities among different reference frames, ones that may be introduced in this investigation.

Quaternion

The quaternion, also known as Euler parameters, is a set of 4 scalar variables that is commonly employed in numerical simulations for attitude motion. The quaternion formalism is, in fact, free of trigonometric functions, and a limited number of operations are involved in the representation of successive rotations. Additionally, it is always possible to avoid any singularity during the transformation process from a given direction cosine matrix to the corresponding quaternion set. The quaternion four-dimensional vector, ${}^{a}\boldsymbol{q}^{a'} = \begin{bmatrix} q_1 & q_2 & q_3 & q_4 \end{bmatrix}^T$, that describes the orientation of some final frame, denoted with a', relative to some initial frame, denoted with a, is defined as

$$ {}^{a}\boldsymbol{q}^{a'} = \begin{bmatrix} \hat{\boldsymbol{\lambda}} \sin(\theta/2) \\ \cos(\theta/2) \end{bmatrix} \quad , \tag{2.27} $$

where $\hat{\boldsymbol{\lambda}}$ is the Euler axis of rotation, such that,

$$ \hat{\boldsymbol{\lambda}} = \underset{\hat{a}'\cdot\hat{a}}{A} \hat{\boldsymbol{\lambda}} \quad , $$

and θ is the Euler angle, such that,

$$ \cos(\theta) = \frac{1}{2}\left(Tr\left(\underset{\hat{a}'\cdot\hat{a}}{A}\right) - 1\right) \quad . $$

The Euler axis and angle render the transformation from $\hat{a}$ to $\hat{a}'$ as a simple rotation about an axis $\hat{\boldsymbol{\lambda}}$ by an angle θ. The quaternion group includes one more variable than the minimum-set and, consequently, one constraint equation is necessary, which is

$$ {}^{a}\boldsymbol{q}^{a'} \cdot {}^{a}\boldsymbol{q}^{a'} = 1 \quad . \tag{2.28} $$

A direction cosine matrix from the $\hat{a}$-frame to the $\hat{a}'$-frame is expressed in terms of a quaternion vector as

$$ \underset{\hat{a}'\cdot\hat{a}}{A} = \begin{bmatrix} q_1^2 - q_2^2 - q_3^2 + q_4^2 & 2(q_1q_2 + q_3q_4) & 2(q_1q_3 - q_2q_4) \\ 2(q_1q_2 - q_3q_4) & -q_1^2 + q_2^2 - q_3^2 + q_4^2 & 2(q_2q_3 + q_1q_4) \\ 2(q_1q_3 + q_2q_4) & 2(q_2q_3 - q_1q_4) & -q_1^2 - q_2^2 + q_3^2 + q_4^2 \end{bmatrix} \quad . \tag{2.29} $$

Vice-versa, the quaternion vector that represents the rotation from the $\hat{a}$-frame to the $\hat{a}'$-frame is constructed from the corresponding direction cosine matrix using one of the following sets of equations

$$ \left\{ \begin{aligned} q_1 &= \frac{1}{4q_4}(A_{23} - A_{32}) \\ q_2 &= \frac{1}{4q_4}(A_{31} - A_{13}) \\ q_3 &= \frac{1}{4q_4}(A_{12} - A_{21}) \\ q_4 &= \frac{1}{2}(1 + A_{11} + A_{22} + A_{33})^{\frac{1}{2}} \end{aligned} \right. \qquad \left\{ \begin{aligned} q_1 &= \frac{1}{2}(1 + A_{11} - A_{22} - A_{33})^{\frac{1}{2}} \\ q_2 &= \frac{1}{4q_1}(A_{12} + A_{21}) \\ q_3 &= \frac{1}{4q_1}(A_{13} + A_{31}) \\ q_4 &= \frac{1}{4q_1}(A_{23} - A_{32}) \end{aligned} \right. \tag{2.30} $$

$$\begin{cases} q_2 = \dfrac{1}{2}(1 - A_{11} + A_{22} - A_{33})^{\frac{1}{2}} \\ q_1 = \dfrac{1}{4q_2}(A_{12} + A_{21}) \\ q_3 = \dfrac{1}{4q_2}(A_{23} + A_{32}) \\ q_4 = \dfrac{1}{4q_2}(A_{31} - A_{13}) \end{cases} \quad \begin{cases} q_3 = \dfrac{1}{2}(1 - A_{11} - A_{22} + A_{33})^{\frac{1}{2}} \\ q_1 = \dfrac{1}{4q_3}(A_{13} + A_{31}) \\ q_2 = \dfrac{1}{4q_3}(A_{23} + A_{32}) \\ q_4 = \dfrac{1}{4q_3}(A_{12} - A_{21}) \end{cases} \tag{2.31}$$

As a common good practice, the set of equations for the inverse transformation is chosen such that, the maximum quaternion vector component appears at the denominator in Eq. (2.30)-(2.31), or, at least, any division by zero is avoided. The quaternion parameters are employed in this investigation within the numerical propagation of the spacecraft attitude dynamics.

Euler Angles

Elements of the direction cosine matrix or quaternion vector do not typically offer an immediate interpretation for the corresponding physical orientation of the vehicle. Alternative to those representations, Euler angles are usually employed to assist in the visualization of the physical configuration. Several Euler angles space and body sequences are presented in [82]; among such, the 3-2-1 body, 3-2-3 body, 3-1-3 body sequences are employed in this analysis to relate a generic initial $\hat{a}$-frame and a final $\hat{a}'$-frame. For the selected Euler angles sequences, the direction cosine matrix is obtained from

$$\underset{\hat{a}'\cdot\hat{a}}{A}{}_{321} = \begin{bmatrix} c_1c_2 & s_1c_2 & -s_2 \\ -c_3s_1 + s_3c_1s_2 & c_3c_1 + s_3s_1s_2 & s_3c_2 \\ s_3s_1 + c_3c_1s_2 & -s_3c_1 + c_3s_1s_2 & c_3c_2 \end{bmatrix} , \tag{2.32}$$

$$\underset{\hat{a}'\cdot\hat{a}}{A}{}_{323} = \begin{bmatrix} -s_3s_1 + c_3c_1c_2 & s_3c_1 + c_3s_1c_2 & -c_3s_2 \\ -c_3s_1 - s_3c_1c_2 & c_3c_1 - s_3s_1c_2 & s_3s_2 \\ c_1s_2 & s_1s_2 & c_2 \end{bmatrix} , \tag{2.33}$$

$$\underset{\hat{a}'\cdot\hat{a}}{A}{}_{313} = \begin{bmatrix} c_3 s_1 - s_3 s_1 c_2 & c_3 s_1 + s_3 c_1 c_2 & s_3 s_2 \\ -s_3 c_1 - c_3 s_1 c_2 & -s_3 s_1 + c_3 c_1 c_2 & c_3 s_2 \\ s_1 s_2 & -c_1 s_2 & c_2 \end{bmatrix} , \quad (2.34)$$

where c_i denotes the cosine function for the i-th angle within the sequence, and, similarly, s_i is a short form for the sine function calculated on the i-th angle within the sequence. Euler angles are used in this investigation to supply a visualization for the attitude configuration evolution that enables a more straightforward interpretation for the spacecraft physical motion.

Spacecraft orientation relative to inertial and rotating frame

A spacecraft attitude can be deduced by predicting the orientation of a body fixed frame $(\hat{\boldsymbol{b}}_1, \hat{\boldsymbol{b}}_2, \hat{\boldsymbol{b}}_3)$, also referred as $\hat{b}$-frame, with respect to a given observer. Several frames may provide a reference to describe a spacecraft orientation, and may be determined within a specific mission application. In this work, an inertial frame corresponding to the unit vectors $(\hat{\boldsymbol{X}}, \hat{\boldsymbol{Y}}, \hat{\boldsymbol{Z}})$, and the CR3BP rotating frame, which is constructed upon the unitary tern $(\hat{\boldsymbol{x}}, \hat{\boldsymbol{y}}, \hat{\boldsymbol{z}})$, are the principal references adopted. The inertial and rotating frame are also labelled $\hat{\imath}$-frame and $\hat{r}$-frame, respectively. At the initial time, the $\hat{\imath}$-frame and $\hat{r}$-frame are aligned. The quaternion vector ${}^{i}\boldsymbol{q}^{b}$ renders the orientation of the $\hat{b}$-frame in the $\hat{\imath}$-frame, and the corresponding DCM is

$$\underset{\hat{b}\cdot\hat{\imath}}{A} = \begin{bmatrix} q_1^2 - q_2^2 - q_3^2 + q_4^2 & 2(q_1 q_2 + q_3 q_4) & 2(q_1 q_3 - q_2 q_4) \\ 2(q_1 q_2 - q_3 q_4) & -q_1^2 + q_2^2 - q_3^2 + q_4^2 & 2(q_2 q_3 + q_1 q_4) \\ 2(q_1 q_3 + q_2 q_4) & 2(q_2 q_3 - q_1 q_4) & -q_1^2 - q_2^2 + q_3^2 + q_4^2 \end{bmatrix} , \quad (2.35)$$

where q_i are the components of ${}^{i}\boldsymbol{q}^{b}$. Known a vehicle attitude configuration with respect to the inertial frame as DCM, $\underset{\hat{b}\cdot\hat{\imath}}{A}$, it is also possible to express the DCM that describes the spacecraft orientation in the CR3BP rotating frame, i.e.,

$$\underset{\hat{b}\cdot\hat{r}}{A} = \underset{\hat{b}\cdot\hat{\imath}}{A}\,\underset{\hat{\imath}\cdot\hat{r}}{A} \quad ,$$

where

$$\underset{\hat{i}\cdot\hat{r}}{A} = \begin{bmatrix} \cos(t) & -\sin(t) & 0 \\ \sin(t) & \cos(t) & 0 \\ 0 & 0 & 1 \end{bmatrix} \tag{2.36}$$

is the rotation matrix from the $\hat{r}$-frame to the $\hat{i}$-frame. The quaternion vector that renders the spacecraft attitude in the rotating frame, ${}^{r}\boldsymbol{q}^{b}$, may be computed from the DCM, $\underset{\hat{b}\cdot\hat{r}}{A}$, using Eq. (2.30)-(2.31). Alternatively, the rule for successive rotations may be applied directly within the quaternion formalism, which yields the relationship

$${}^{i}\boldsymbol{q}^{b} = \begin{bmatrix} \cos(t/2) & -\sin(t/2) & 0 & 0 \\ \sin(t/2) & \cos(t/2) & 0 & 0 \\ 0 & 0 & \cos(t/2) & \sin(t/2) \\ 0 & 0 & -\sin(t/2) & \cos(t/2) \end{bmatrix} {}^{r}\boldsymbol{q}^{b} \quad . \tag{2.37}$$

In the following discussion, the quaternion representation ${}^{i}\boldsymbol{q}^{b}$ is employed within the formulation and propagation of the equations of motion, whereas ${}^{r}\boldsymbol{q}^{b}$ may facilitate the identification and visualization of orbit-attitude periodic solutions, consistently with the reference observer that is typically adopted within the classical CR3BP.

2.3.2 Kinematics Differential Equations

Consider two frames, e.g., $(\hat{\boldsymbol{a}}_1, \hat{\boldsymbol{a}}_2, \hat{\boldsymbol{a}}_3)$ and $(\hat{\boldsymbol{a}}'_1, \hat{\boldsymbol{a}}'_2, \hat{\boldsymbol{a}}'_3)$, that are moving relative to each other. In particular, the angular velocity for the final $\hat{a}'$-frame, relative to the initial $\hat{a}$-frame is known, and equal to

$$\underset{\hat{a}'}{{}^{a}\boldsymbol{\omega}^{a'}} = {}^{a}\omega_1^{a'}\hat{\boldsymbol{a}}'_1 + {}^{a}\omega_2^{a'}\hat{\boldsymbol{a}}'_2 + {}^{a}\omega_3^{a'}\hat{\boldsymbol{a}}'_3 \quad .$$

The relative motion between the two set of unit vectors, naturally, causes a time variation of the kinematics variables. For the quaternion vector ${}^{a}\boldsymbol{q}^{a'}$, the time rate of change in its elements can be expressed as a function of the angular velocity ${}^{a}\underset{\hat{a}'}{\boldsymbol{\omega}}{}^{a'}$, as

$$\begin{cases} 2\dot{q}_1 &= {}^{a}\omega_3^{a'} q_2 - {}^{a}\omega_2^{a'} q_3 + {}^{a}\omega_1^{a'} q_4 \\ 2\dot{q}_2 &= -{}^{a}\omega_3^{a'} q_1 + {}^{a}\omega_1^{a'} q_3 + {}^{a}\omega_2^{a'} q_4 \\ 2\dot{q}_3 &= {}^{a}\omega_2^{a'} q_1 - {}^{a}\omega_1^{a'} q_2 + {}^{a}\omega_3^{a'} q_4 \\ 2\dot{q}_4 &= -{}^{a}\omega_1^{a'} q_1 - {}^{a}\omega_2^{a'} q_2 - {}^{a}\omega_3^{a'} q_3 \quad . \end{cases} \tag{2.38}$$

Details for the derivation of Eq. (2.38) are presented in [82]. The set of equations in Eq. (2.38) may be numerically propagated to predict the orientation time profile for the $\hat{a}'$-frame with respect to the $\hat{a}$-frame in terms of quaternion parameters.

2.3.3 Dynamics Differential Equations

The basic differential equations to capture the rotational dynamics for a rigid body are straightforwardly derived from the application of the Newton's second law in its angular momentum form. Introduce a set of unit vectors $(\hat{\boldsymbol{b}}_1, \hat{\boldsymbol{b}}_2, \hat{\boldsymbol{b}}_3)$ that is fixed in the body center of mass, and aligned with the principal inertia axes, also called $\hat{b}$-frame. Let ${}^{i}\underset{\hat{b}}{\boldsymbol{\omega}}{}^{b} = \omega_1\hat{\boldsymbol{b}}_1 + \omega_2\hat{\boldsymbol{b}}_2 + \omega_3\hat{\boldsymbol{b}}_3$ be the angular velocity relative to an inertial frame and written in body axes. Then, the angular momentum law that predicts the rotational dynamics about the body center of mass simplifies to the following equations [83],

$$\begin{cases} I_1\dot{\omega}_1 &= -(I_3 - I_2)\omega_2\omega_3 + M_1 \\ I_2\dot{\omega}_2 &= -(I_1 - I_3)\omega_1\omega_3 + M_2 \\ I_3\dot{\omega}_3 &= -(I_2 - I_1)\omega_1\omega_2 + M_3 \quad , \end{cases} \tag{2.39}$$

where I_i denotes the principal inertial moment corresponding to the body axis $\hat{\boldsymbol{b}}_i$, and $\boldsymbol{M}^B = M_1\hat{\boldsymbol{b}}_1 + M_2\hat{\boldsymbol{b}}_2 + M_3\hat{\boldsymbol{b}}_3$ is the resultant external moment applied to the body center of mass, B, as written in the $\hat{b}$-frame. An analytical solution for Eqs. (2.39) may exist for a particular system configuration, such as in a torque-free scenario [82]; otherwise, when a generic time-varying moment is applied, Eqs. (2.39) are numerically solved, for example, using a variable-step and variable-order predictor-corrector integration scheme.

2.3.4 Gravity Torque on a Rigid Body Exerted by a Particle

Variation of the gravitational field in the three-dimensional space, often referred as gravity gradient, yields a variation of the local gravity force through a finite mass distribution, that may produce a net torque about the body center of mass. For a rigid body, the net gravity gradient moment about its center of mass, due to the gravitational attraction of the primary P_i, is expressed as

$$\boldsymbol{M}_i^B = -\boldsymbol{R}_i \times \boldsymbol{F}_i \quad , \tag{2.40}$$

where $\boldsymbol{R}_i$ is the position vector from the attracting body P_i to the spacecraft center of mass, B, illustrated in Figure 2.6, and $\boldsymbol{F}_i$ is the gravity force for P_i, which is defined in Eq. (2.11). Similarly to the simplification for the gravity force, a series expansion may be introduced for the gravity gradient moment, i.e.,

$$\boldsymbol{M}_i^B = \frac{3Gm_i}{R_i^3} \hat{\boldsymbol{R}}_i \times I \cdot \hat{\boldsymbol{R}}_i + \frac{Gm_i m}{R_i} \sum_{j=3}^{\infty} \boldsymbol{m}^{(j)} \quad , \tag{2.41}$$

one that is particularly useful for a body that is small compared to its distance from the primary, R_i. In fact, the terms of the summation, $\boldsymbol{m}^{(j)}$, are proportional to increasing powers of $(|\boldsymbol{p}-\boldsymbol{R}_i|/\boldsymbol{R}_i)^j$ larger than the second order, and may be negligible when $(|\boldsymbol{p} - \boldsymbol{R}_i|/\boldsymbol{R}_i) << 1$. After some algebra [82], the typical approximation of the gravity gradient torque for a small spacecraft about the body center of mass, B, appears as

$$\boldsymbol{M}_i^B \approx \frac{3Gm}{R_i^3} \left[(I_3 - I_2) c_2 c_3 \hat{\boldsymbol{b}}_1 + (I_1 - I_3) c_1 c_3 \hat{\boldsymbol{b}}_2 + (I_2 - I_1) c_1 c_2 \hat{\boldsymbol{b}}_3 \right] \quad , \tag{2.42}$$

where $I_j \triangleq \hat{\boldsymbol{b}}_j \cdot I \cdot \hat{\boldsymbol{b}}_j$ are the principal inertia moments in body axes, and $c_j \triangleq \hat{\boldsymbol{R}}_i \cdot \hat{\boldsymbol{b}}_j$ are the projections of the radial vector from the primary P_i to the body center of mass, B, in the body frame. When more attracting particles exist within the system, as for the

CR3BP, the total moment on the rigid body center of mass is simply the summation of each individual contribution, that is computed using Eq. (2.42). In this investigation, the gravity gradient torque exerted by any primary is the only environment action included within the attitude dynamics model, unless otherwise specified. External control moments may be applied in addition to the gravity gradient.

2.4 Coupled Orbit-Attitude Dynamics

In the work presented in this document, translational and rotational dynamics for a rigid space vehicle within the CR3BP, illustrated in Figure 2.8, are encapsulated in a set of differential equations similar to

$$\begin{cases} \dot{\boldsymbol{x}}_{\text{orb}} & = \boldsymbol{f}_x(\boldsymbol{x}_{\text{orb}}, {}^i\boldsymbol{q}^b, {}^i\boldsymbol{\omega}^b, t) \\ {}^i\dot{\boldsymbol{q}}^b & = \boldsymbol{f}_q(\boldsymbol{x}_{\text{orb}}, {}^i\boldsymbol{q}^b, {}^i\boldsymbol{\omega}^b, t) \\ {}^i\dot{\boldsymbol{\omega}}^b & = \boldsymbol{f}_\omega(\boldsymbol{x}_{\text{orb}}, {}^i\boldsymbol{q}^b, {}^i\boldsymbol{\omega}^b, t) \quad . \end{cases} \tag{2.43}$$

The orbital state vector, $\boldsymbol{x}_{\text{orb}} = \begin{bmatrix} x & y & z & v_x & v_y & v_z \end{bmatrix}^T$, comprises the spacecraft center of mass position and velocity relative to the rotating frame, consistently with the classical definition within the CR3BP. The vehicle orientation is represented by the quaternion vector ${}^i\boldsymbol{q}^b = \begin{bmatrix} q_1 & q_2 & q_3 & q_4 \end{bmatrix}^T$, that supplies the alignment within an inertial frame, denoted by i, for a set of body axes, denoted by b, that are fixed in the spacecraft principal directions of inertia. The time rate of change for the vehicle attitude configuration is reflected in the body angular velocity with respect to the inertial frame, as written in the $\hat{b}$-frame ${}^i\underset{\hat{b}}{\boldsymbol{\omega}}{}^b = {}^i\boldsymbol{\omega}^b = \begin{bmatrix} \omega_1 & \omega_2 & \omega_3 \end{bmatrix}^T$. The orbit-attitude dynamical system as formulated in Eq. (2.43) is generally non-autonomous. Most important, as evident in Eq. (2.43), a variation of the orbital state variables induces a variation for the attitude state variables, and vice-versa. Two specific frameworks for the generic coupled orbit-attitude dynamics in Eq. (2.43) are developed in the following sections, one to capture underlying dynamical structures in the form of orbit-attitude periodic motions, and another for application to solar sailing.

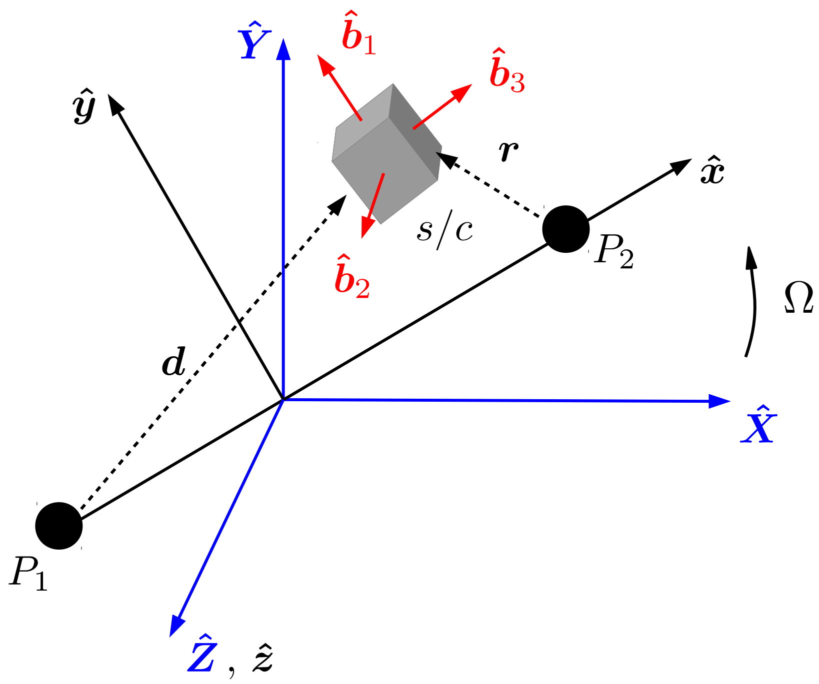

Figure 2.8. Frame representations in coupled orbit-attitude CR3BP. The blue vectors indicate the inertial $\hat{\imath}$-frame, the black vector indicate the CR3BP rotating $\hat{r}$-frame, the red vectors indicate the body $\hat{b}$-frame.

2.4.1 Simplified Coupled Model

To first explore the orbit-attitude dynamics within the CR3BP, a simplified version for a general coupled framework is employed. In particular, the influence of the orbital motion on the attitude dynamics is solely included, but not the inverse interaction. In this model, the time evolution of the orbital state variables is no longer a function of the attitude state variables, as expressed by the following system of vectorial equations

$$\begin{cases} \dot{\boldsymbol{x}}_{\text{orb}} &= \boldsymbol{f}_x(\boldsymbol{x}_{\text{orb}}) \\ {}^i\dot{\boldsymbol{q}}^b &= \boldsymbol{f}_q({}^i\boldsymbol{q}^b, {}^i\boldsymbol{\omega}^b) \\ {}^i\dot{\boldsymbol{\omega}}^b &= \boldsymbol{f}_\omega(\boldsymbol{x}_{\text{orb}}, {}^i\boldsymbol{q}^b, {}^i\boldsymbol{\omega}^b, t) \quad . \end{cases} \tag{2.44}$$

The vectorial differential system in Eq. (2.44) is referred as Simplified Coupled Model (SCM). The equations of motion for the SCM are numerically integrated to predict the orbit-attitude history of a space vehicle.

To reproduce the orbital dynamics of the spacecraft within the SCM, the gravity force is modelled neglecting the finite extension of the vehicle. Accordingly, the orbital behaviour of the vehicle is equivalent to the response of a point-mass located at the body center of mass. Perturbations that are equally significant when compared to the actual mass distribution, such as the solar radiation pressure, are also neglected in the SCM. The resulting orbital dynamics is the familiar Circular Restricted Three-Body Problem (CR3BP), which is presented in Eq (2.3):

$$\boldsymbol{f}_x(\boldsymbol{x}_{\text{orb}}) = \boldsymbol{f}_{\text{CR3BP}} = \begin{bmatrix} v_x \\ v_y \\ v_z \\ x + 2v_y - \dfrac{(1-\mu)(x+\mu)}{d^3} - \dfrac{\mu(x-1+\mu)}{r^3} \\ y - 2v_x - \dfrac{(1-\mu)y}{d^3} - \dfrac{\mu y}{r^3} - \dfrac{(1-\mu)z}{d^3} - \dfrac{\mu z}{r^3} \end{bmatrix}, \qquad (2.45)$$

where x, y, z are the position coordinates expressed in terms of the rotating frame; v_x, v_y, v_z are the velocity components of the spacecraft observed from the rotating frame and expressed in terms of rotating components. The distances from P_1 and P_2 are respectively denoted by $d = \sqrt{(x+\mu)^2 + y^2 + z^2}$, and $r = \sqrt{(x-1+\mu)^2 + y^2 + z^2}$. Recall that, particular solutions of Eq. (2.45) include equilibrium points, periodic orbits and quasi-periodic trajectories [78].

The orientation of the spacecraft is represented through a body reference frame ($\hat{\boldsymbol{b}}_{\mathbf{1}}$, $\hat{\boldsymbol{b}}_{\mathbf{2}}$, $\hat{\boldsymbol{b}}_{\mathbf{3}}$), with an origin fixed in the spacecraft center of mass, and aligned with spacecraft principal axes of inertia. The instantaneous orientation of the body frame (which is the orientation of the rigid vehicle) relative to the inertial frame is defined using the quaternion vector ${}^i\boldsymbol{q}^b = [q_1\ q_2\ q_3\ q_4]^T$; one of the components of ${}^i\boldsymbol{q}^b$, e.g., q_4, is implicitly defined by the constraint Eq. (2.28) with a sign ambiguity. Practically, the sign ambiguity is solved by assigning initial conditions for $[q_1\ q_2\ q_3]^T$ as well as q_4. Then, q_4 is solved via numerical integration of the equations of motion. The

4-dimensional quaternion vector is related to the body angular velocity ${}^i\boldsymbol{\omega}^b$ via the kinematics relationship,

$$\boldsymbol{f_q}({}^i\boldsymbol{q}^b, {}^i\boldsymbol{\omega}^b) = \frac{1}{2}\begin{bmatrix} \omega_3 q_2 - \omega_2 q_3 + \omega_1 q_4 \\ -\omega_3 q_1 + \omega_1 q_3 + \omega_2 q_4 \\ \omega_2 q_1 - \omega_1 q_2 + \omega_3 q_4 \\ -\omega_1 q_1 - \omega_2 q_2 - \omega_3 q_3 \end{bmatrix} . \tag{2.46}$$

Euler equations of motion in Eq. (2.39) reflect the rotational dynamics of the vehicle, incorporating the net gravity torque that is exerted by P_1 and P_2, and no other external moments. A second-order approximation is developed to express the gravitational moment as in Eq. (2.42). The resulting dynamical equations for the spacecraft attitude are written as follows:

$$\boldsymbol{f_\omega}(\boldsymbol{x}_{\text{orb}}, {}^i\boldsymbol{q}^b, {}^i\boldsymbol{\omega}^b, t) = \begin{bmatrix} \frac{I_3 - I_2}{I_1}\left(\frac{3\mu_1}{d^3} g_2 g_3 + \frac{3\mu_2}{r^3} h_2 h_3 - \omega_2\omega_3\right) \\ \frac{I_1 - I_3}{I_2}\left(\frac{3\mu_1}{d^3} g_1 g_3 + \frac{3\mu_2}{r^3} h_1 h_3 - \omega_1\omega_3\right) \\ \frac{I_2 - I_1}{I_3}\left(\frac{3\mu_1}{d^3} g_1 g_2 + \frac{3\mu_2}{r^3} h_1 h_2 - \omega_1\omega_2\right) \end{bmatrix} , \tag{2.47}$$

where ${}^i\boldsymbol{\omega}^b = [\omega_1 \; \omega_2 \; \omega_3]^T$ is the angular velocity vector of the body relative to the inertial frame and expressed using $(\hat{\boldsymbol{b}}_1, \hat{\boldsymbol{b}}_2, \hat{\boldsymbol{b}}_3)$ as the vectorial basis; I_1, I_2 and I_3 denote the principal central moments of inertia in the corresponding directions; μ_1 and μ_2 are the planetary constants of P_1 and P_2, which satisfy $\mu_1 = 1 - \mu$ and $\mu_2 = \mu$ in nondimensional units; h_i represent the projections of the spacecraft position unit vector relative to P_1 into the body frame, while g_i are the projections of the spacecraft position unit vector relative to P_2 into the body frame. Upon the introduction of direction cosine matrices, the projections g_i and h_i, which determine the gravitational moment in Eq. (2.47), are expressed as functions of the instantaneous position and orientation of the spacecraft, i.e.,

$$\begin{bmatrix} g_1 \\ g_2 \\ g_3 \end{bmatrix} = \underset{\hat{b}\cdot\hat{i}}{A}\,\underset{\hat{i}\cdot\hat{r}}{A}\,\frac{\boldsymbol{d}}{d} = \underset{\hat{b}\cdot\hat{i}}{A}\,\underset{\hat{i}\cdot\hat{r}}{A}\,\frac{1}{d}\begin{bmatrix} x + \mu \\ y \\ z \end{bmatrix} \tag{2.48}$$

and

$$\begin{bmatrix} h_1 \\ h_2 \\ h_3 \end{bmatrix} = \underset{\hat{b}\cdot\hat{\imath}}{A}\,\underset{\hat{\imath}\cdot\hat{r}}{A}\,\frac{\boldsymbol{r}}{r} = \underset{\hat{b}\cdot\hat{\imath}}{A}\,\underset{\hat{\imath}\cdot\hat{r}}{A}\,\frac{1}{r}\begin{bmatrix} x+\mu-1 \\ y \\ z \end{bmatrix} \quad . \tag{2.49}$$

Equations (2.45), (2.46) and (2.47) form the entire set of coupled equations of motion that is necessary to describe the orbit-attitude dynamics of a small rigid body within the context of the CR3BP. Given Eqs. (2.47) and (2.46), the attitude response is influenced by the orbital states, but no attitude terms are present in Eq. (2.45), so that, the classic structure of the CR3BP is preserved. Accordingly, this model may not be applicable to a spacecraft whose characteristic dimension is large compared to the distance from P_1 and P_2. External actions, other than gravity, may also introduce a dependency of the orbital path on the body orientation. However, the current model is easily modified to incorporate large spacecraft and external perturbations, and supplies a practical basis for the identification of fundamental, natural orbit-attitude behaviors that originate from the gravitational field.

2.4.2 Fully Coupled Model: Incorporating Solar Radiation Pressure

At interplanetary locations, such as the vicinity of the libration points, the Solar Radiation Pressure (SRP) may be one of the dominant environment factors to introduce a dynamical coupling between the spacecraft translational and rotational motion. Some technologies under development, e.g., solar sail architectures, aim to leverage such a coupling to control a vehicle trajectory. It is, therefore, significant to expand the SCM framework to incorporate SRP, and rewrite the equations of motion in the form

$$\begin{cases} \dot{\boldsymbol{x}}_{\text{orb}} &= \boldsymbol{f}_x(\boldsymbol{x}_{\text{orb}}, {}^i\boldsymbol{q}^b, t) \\ {}^i\dot{\boldsymbol{q}}^b &= \boldsymbol{f}_q({}^i\boldsymbol{q}^b, {}^i\boldsymbol{\omega}^b) \\ {}^i\dot{\boldsymbol{\omega}}^b &= \boldsymbol{f}_\omega(\boldsymbol{x}_{\text{orb}}, {}^i\boldsymbol{q}^b, {}^i\boldsymbol{\omega}^b, t) \quad ; \end{cases} \tag{2.50}$$

note that, the spacecraft orientation is, hereby, an explicit input for the vectorial function $\boldsymbol{f}_x$, in contrast with the SCM. The differential system in Eq. (2.50) is referred as Fully Coupled Model (FCM), since there exist a specific reciprocal influence between the orbit and attitude dynamics. In the present FCM, the net force on the vehicle center of mass that is produced by the SRP is solely applied. Any moment on the spacecraft that may originate from an interaction with the solar radiation, is neglected. Accordingly, the attitude dynamical equations stay identical to those in Eq. (2.44) for the SCM. The orbital vectorial equations are, however, updated as follow

$$\boldsymbol{f}_x(\boldsymbol{x}_{\text{orb}}, {}^i\boldsymbol{q}^b, t) = \boldsymbol{f}_{\text{FCM}} = \boldsymbol{f}_{\text{CR3BP}}(\boldsymbol{x}_{\text{orb}}) + \boldsymbol{a}_{ss}(\boldsymbol{x}_{\text{orb}}, {}^i\boldsymbol{q}^b, t) \quad , \tag{2.51}$$

where $\boldsymbol{a}_{ss}$ is the resultant, nondimensional, acceleration due to SRP that is applied to the body center of mass, and written in CR3BP rotating frame coordinates. The acceleration, $\boldsymbol{a}_{ss}$, may be derived from the SRP force model in Eq. (2.21) for a flat, perfectly specular surface, which is a classical abstraction for a solar sail architecture. The final expression for the acceleration $\boldsymbol{a}_{ss}$ may vary accordingly to the planetary system considered.

Sun-Planet system

Within a CR3BP model for a Sun-Planet combination, the acceleration $\boldsymbol{a}_{ss}$, in Eq. (2.51), that is generated by the SRP on a flat and perfectly reflective surface, reduces to

$$\boldsymbol{a}_{ss} = \underset{\hat{r}}{\boldsymbol{a}_{ss}} = \begin{bmatrix} a_{ss,x} \\ a_{ss,y} \\ a_{ss,z} \end{bmatrix} = \beta \left(\frac{1-\mu}{d_{\odot}^2} \right) (\hat{\boldsymbol{\ell}}_1 \cdot \underset{\hat{r}}{\hat{\boldsymbol{u}}})^2 \underset{\hat{r}}{\hat{\boldsymbol{u}}} \quad , \tag{2.52}$$

where β denotes the lightness parameter of the vehicle as defined in [84] (this quantity is originally introduced to describe the performances of an ideal solar sail); μ represents the CR3BP mass parameter for the corresponding Sun-Planet system; $d_{\odot}$ is the nondimensional distance from the Sun, $\hat{\boldsymbol{\ell}}_1$ is the incoming direction of the radiation and $\hat{\boldsymbol{u}}$ is the surface normal, both as written in the $\hat{r}$-frame. The surface normal may be more easily defined within the body fixed $\hat{b}$-frame and, then, transformed to a different vector basis using DCMs, straightforwardly,

$$\underset{\hat{r}}{\hat{\boldsymbol{u}}} = \underset{\hat{r}\cdot\hat{\imath}}{A}\,\underset{\hat{\imath}\cdot\hat{b}}{A}\,\underset{\hat{b}}{\hat{\boldsymbol{u}}} \quad . \tag{2.53}$$

For example, assume the sail normal to coincide with the $\hat{\boldsymbol{b}}_1$ body principal axis, i.e., $\underset{\hat{b}}{\hat{\boldsymbol{u}}} = [1\ 0\ 0]^T$. The DCM from the $\hat{\imath}$-frame to the $\hat{r}$-frame, $\underset{\hat{r}\cdot\hat{\imath}}{A}$, defined in Eq. (2.36), is only a function of the nondimensional time, t, and the DCM from the $\hat{b}$-frame to the $\hat{\imath}$-frame, $\underset{\hat{\imath}\cdot\hat{b}}{A}$, can be written in terms of the quaternion vector ${}^{i}\boldsymbol{q}^{b}$, similarly to Eq. (2.35). Accordingly, the final expression for the vector $\underset{\hat{r}}{\hat{\boldsymbol{u}}} = \boldsymbol{n}$ in the CR3BP rotating frame, is

$$\boldsymbol{n} = \begin{bmatrix} n_1 \\ n_2 \\ n_3 \end{bmatrix} = \begin{bmatrix} \cos(t)(q_1^2 - q_2^2 - q_3^2 + q_4^2) + 2\sin(t)(q_1q_2 + q_3q_4) \\ -\sin(t)(q_1^2 - q_2^2 - q_3^2 + q_4^2) + 2\cos(t)(q_1q_2 + q_3q_4) \\ 2(q_1q_3 - q_2q_4) \end{bmatrix} \quad , \tag{2.54}$$

and acceleration due to SRP results

$$\underset{\hat{r}}{\boldsymbol{a}}_{ss} = \beta\left(\frac{1-\mu}{d^4}\right)((x-\mu)n_1 + yn_2 + zn_3)^2 \begin{bmatrix} n_1 \\ n_2 \\ n_3 \end{bmatrix} = \beta\left(\frac{1-\mu}{d^4}\right)(\boldsymbol{d}\cdot\boldsymbol{n})^2\boldsymbol{n} \quad , \tag{2.55}$$

where is noted $d_{\odot} = d$, with d being the CR3BP distance from P_1, i.e., the Sun. The system of equations Eq. (2.50), that includes the definition for the acceleration $\underset{\hat{r}}{\boldsymbol{a}}_{ss}$ in Eq. (2.55), is employed in later chapters of this document as a model for the orbit-attitude dynamics of a solar sail travelling within the Sun-Earth system.

2.5 Planetary System Constants

To characterize a planetary system within the CR3BP, three quantities are fundamentally necessary: the mass parameter, μ, the distance between the primaries, L, and the system synodic period, $2\pi T$. Such quantities are summarized in Table 2.1 for the Earth-Moon and Sun-Earth systems, which represent the two environments considered within this investigation.

Table 2.1. Planetary system constants within the CR3BP.

Earth-Moon System	
L [km]	384400
T [days]	4.3421
μ	1.215e-2
Sun-Earth System	
L [km]	1.4960e+08
T [days]	58.1244
μ	3.003e-6

3. NUMERICAL TARGETING SCHEMES

The equations of motion for a rigid body immersed into a two-bodies gravitational field, and possibly including solar radiation pressure, do not possess a solution space that can be described in an analytical, closed-form. The trajectory and orientation evolution is, instead, numerically propagated. When a specific behavior, or a desired set of final conditions, is sought, numerical tools are required to manipulate the solution. In this investigation, a multiple shooting scheme, in combination with a multi-variable Newton-Raphson solver, is employed to construct orbit-attitude periodic solutions, and solar sail trajectories within a coupled orbit-attitude regime.

3.1 Linear Variational Equations

The numerical methods employed to generate an orbit-attitude periodic motion or a solar sail trajectory are based on the capability to predict motions nearby a reference solution. Such understanding is essential to estimate a series of incremental adjustments to the reference, that may converge on the desired translational and/or rotational history. Consider a generic system of nonlinear ordinary differential equations, written in vector form

$$\dot{\boldsymbol{x}} = \boldsymbol{f}(\boldsymbol{x}, t) \quad , \tag{3.1}$$

and a reference solution $\boldsymbol{x}^*(\boldsymbol{x}_0^*, t)$ that is generated by numerically propagating an initial state vector, $\boldsymbol{x}_0^*$, from the initial time t_0 to the final time t. To examine behaviors nearby the reference solution, perturb the initial conditions by a small amount $\delta\boldsymbol{x}_0$, such as

$$\boldsymbol{x}_0 = \boldsymbol{x}_0^* + \delta\boldsymbol{x}_0 \quad .$$

A linear estimate for the time evolution of the variation relative to the reference motion, i.e., $\delta\boldsymbol{x}(t) = \boldsymbol{x}(\boldsymbol{x}_0^* + \delta\boldsymbol{x}_0, t) - \boldsymbol{x}^*(\boldsymbol{x}_0^*, t)$, may be obtained as a solution for the following linear system of differential equations

$$\delta\dot{\boldsymbol{x}} \approx \left.\frac{d\boldsymbol{f}}{d\boldsymbol{x}}\right|_{\boldsymbol{x}^*(\boldsymbol{x}_0^*,t)} \delta\boldsymbol{x} = J(t)\delta\boldsymbol{x} \quad , \tag{3.2}$$

where $J(t) = \dfrac{d\boldsymbol{f}}{d\boldsymbol{x}}$ is the Jacobian matrix of the original nonlinear vectorial system in Eq. (3.1). The Jacobian matrix for the SCM and FCM equations of motion is fundamental for the implementation of the numerical correction algorithms adopted in this investigation.

3.1.1 Jacobian in the CR3BP

The Jacobian matrix for the differential equations in the classical CR3BP in Eq. (2.3), is produced by

$$J = \boldsymbol{f}_{x/x_{\mathrm{orb}}} \quad , \tag{3.3}$$

where

$$\boldsymbol{f}_{x/x_{\mathrm{orb}}} = \begin{bmatrix} 0 & 0 & 0 & 1 & 0 & 0 \\ 0 & 0 & 0 & 0 & 1 & 0 \\ 0 & 0 & 0 & 0 & 0 & 1 \\ U^*_{/xx} & U^*_{/xy} & U^*_{/xz} & 0 & 2 & 0 \\ U^*_{/yx} & U^*_{/yy} & U^*_{/yz} & -2 & 0 & 0 \\ U^*_{/zx} & U^*_{/zy} & U^*_{/zz} & 0 & 0 & 0 \end{bmatrix} \quad . \tag{3.4}$$

Recall U^* is the pseudo-potential function.

3.1.2 Jacobian in the Orbit-Attitude SCM

The Jacobian matrix for the SCM differential equations in Eq. (2.44), is produced by

$$J = \begin{bmatrix} \boldsymbol{f}_{x/x_{\text{orb}}} & \boldsymbol{f}_{x/q} & \boldsymbol{f}_{x/\omega} \\ \boldsymbol{f}_{q/x_{\text{orb}}} & \boldsymbol{f}_{q/q} & \boldsymbol{f}_{q/\omega} \\ \boldsymbol{f}_{\omega/x_{\text{orb}}} & \boldsymbol{f}_{\omega/q} & \boldsymbol{f}_{\omega/\omega} \end{bmatrix} \tag{3.5}$$

where $\boldsymbol{f}_{x/q} = \mathbf{0}$, $\boldsymbol{f}_{x/\omega} = \mathbf{0}$, and $\boldsymbol{f}_{q/x_{\text{orb}}} = \mathbf{0}$ are null. By definition of the SCM, the matrix $\boldsymbol{f}_{x/x_{\text{orb}}}$ coincides with the Jacobian for the classical CR3BP, and the remaining partial derivatives are

$$\boldsymbol{f}_{q/q} = \frac{1}{2} \begin{bmatrix} 0 & \omega_3 & -\omega_2 & \omega_1 \\ -\omega_3 & 0 & \omega_1 & \omega_2 \\ \omega_2 & -\omega_1 & 0 & \omega_3 \\ -\omega_1 & -\omega_2 & -\omega_3 & 0 \end{bmatrix} \quad , \tag{3.6}$$

$$\boldsymbol{f}_{q/\omega} = \frac{1}{2} \begin{bmatrix} q_4 & -q_3 & q_2 \\ q_3 & q_4 & -q_1 \\ -q_2 & q_1 & q_4 \\ -q_1 & -q_2 & -q_3 \end{bmatrix} \quad , \tag{3.7}$$

$$\boldsymbol{f}_{\omega/\omega} = \begin{bmatrix} 0 & \dfrac{I_2 - I_3}{I_1}\omega_3 & \dfrac{I_2 - I_3}{I_1}\omega_2 \\ \dfrac{I_3 - I_1}{I_2}\omega_3 & 0 & \dfrac{I_3 - I_1}{I_2}\omega_1 \\ \dfrac{I_1 - I_2}{I_3}\omega_2 & \dfrac{I_1 - I_2}{I_3}\omega_1 & 0 \end{bmatrix} \quad , \tag{3.8}$$

$$\boldsymbol{f}_{\omega/x_{\text{orb}}} = \begin{bmatrix} m_{1x} & m_{1y} & m_{1z} & 0 & 0 & 0 \\ m_{2x} & m_{2y} & m_{2z} & 0 & 0 & 0 \\ m_{3x} & m_{3y} & m_{3z} & 0 & 0 & 0 \end{bmatrix} \quad , \tag{3.9}$$

and

$$\boldsymbol{f}_{\omega/q} = \begin{bmatrix} m_{1q_1} & m_{1q_2} & m_{1q_3} & m_{1q_4} \\ m_{2q_1} & m_{2q_2} & m_{2q_3} & m_{2q_4} \\ m_{3q_1} & m_{3q_2} & m_{3q_3} & m_{3q_4} \end{bmatrix} \quad . \tag{3.10}$$

The matrix elements in Eq. (3.9) and Eq. (3.10) are computed accordingly to the following expressions:

$$m_{1x} = \frac{3\mu_1}{d^3}\frac{I_3 - I_2}{I_1}\left(\frac{-3(x+\mu)}{d^2}g_2g_3 + g_3g_{2/x} + g_2g_{3/x}\right) + \frac{3\mu_2}{r^3}\frac{I_3 - I_2}{I_1}\left(\frac{-3(x+\mu-1)}{r^2}h_2h_3 + h_3h_{2/x} + h_2h_{3/x}\right) \quad (3.11)$$

$$m_{1y} = \frac{3\mu_1}{d^3}\frac{I_3 - I_2}{I_1}\left(\frac{-3y}{d^2}g_2g_3 + g_3g_{2/y} + g_2g_{3/y}\right) + \frac{3\mu_2}{r^3}\frac{I_3 - I_2}{I_1}\left(\frac{-3y}{r^2}h_2h_3 + h_3h_{2/y} + h_2h_{3/y}\right) \quad (3.12)$$

$$m_{1y} = \frac{3\mu_1}{d^3}\frac{I_3 - I_2}{I_1}\left(\frac{-3z}{d^2}g_2g_3 + g_3g_{2/z} + g_2g_{3/z}\right) + \frac{3\mu_2}{r^3}\frac{I_3 - I_2}{I_1}\left(\frac{-3z}{r^2}h_2h_3 + h_3h_{2/z} + h_2h_{3/z}\right) \quad (3.13)$$

$$m_{2x} = \frac{3\mu_1}{d^3}\frac{I_1 - I_3}{I_2}\left(\frac{-3(x+\mu)}{d^2}g_1g_3 + g_3g_{1/x} + g_1g_{3/x}\right) + \frac{3\mu_2}{r^3}\frac{I_1 - I_3}{I_2}\left(\frac{-3(x+\mu-1)}{r^2}h_1h_3 + h_3h_{1/x} + h_1h_{3/x}\right) \quad (3.14)$$

$$m_{2y} = \frac{3\mu_1}{d^3}\frac{I_1 - I_3}{I_2}\left(\frac{-3y}{d^2}g_1g_3 + g_3g_{1/y} + g_1g_{3/y}\right) + \frac{3\mu_2}{r^3}\frac{I_1 - I_3}{I_2}\left(\frac{-3y}{r^2}h_1h_3 + h_3h_{1/y} + h_1h_{3/y}\right) \quad (3.15)$$

$$m_{2z} = \frac{3\mu_1}{d^3}\frac{I_1 - I_3}{I_2}\left(\frac{-3z}{d^2}g_1g_3 + g_3g_{1/z} + g_1g_{3/z}\right) + \frac{3\mu_2}{r^3}\frac{I_1 - I_3}{I_2}\left(\frac{-3z}{r^2}h_1h_3 + h_3h_{1/z} + h_1h_{3/z}\right) \quad (3.16)$$

$$m_{3x} = \frac{3\mu_1}{d^3}\frac{I_2 - I_1}{I_3}\left(\frac{-3(x+\mu)}{d^2}g_1g_2 + g_2g_{1/x} + g_1g_{2/x}\right) + \frac{3\mu_2}{r^3}\frac{I_2 - I_1}{I_3}\left(\frac{-3(x+\mu-1)}{r^2}h_1h_2 + h_2h_{1/x} + h_1h_{2/x}\right) \quad (3.17)$$

$$m_{3y} = \frac{3\mu_1}{d^3}\frac{I_2 - I_1}{I_3}\left(\frac{-3y}{d^2}g_1g_2 + g_2g_{1/y} + g_1g_{2/y}\right) + \frac{3\mu_2}{r^3}\frac{I_2 - I_1}{I_3}\left(\frac{-3y}{r^2}h_1h_2 + h_2h_{1/y} + h_1h_{2/y}\right) \quad (3.18)$$

$$m_{3z} = \frac{3\mu_1}{d^3}\frac{I_2 - I_1}{I_3}\left(\frac{-3z}{d^2}g_1g_2 + g_2g_{1/z} + g_1g_{2/z}\right) + \frac{3\mu_2}{r^3}\frac{I_2 - I_1}{I_3}\left(\frac{-3z}{r^2}h_1h_2 + h_2h_{1/z} + h_1h_{2/z}\right) \quad , \quad (3.19)$$

and

$$m_{1q_i} = \frac{3\mu_1}{d^3}\frac{I_3 - I_2}{I_1}\left(g_2g_{3/q_i} + g_3g_{2/q_i}\right) + \frac{3\mu_2}{r^3}\frac{I_3 - I_2}{I_1}\left(h_2h_{3/q_i} + h_3h_{2/q_i}\right) \quad (3.20)$$

$$m_{2q_i} = \frac{3\mu_1}{d^3}\frac{I_1 - I_3}{I_2}\left(g_1g_{3/q_i} + g_3g_{1/q_i}\right) + \frac{3\mu_2}{r^3}\frac{I_1 - I_3}{I_2}\left(h_1h_{3/q_i} + h_3h_{1/q_i}\right) \quad (3.21)$$

$$m_{3q_i} = \frac{3\mu_1}{d^3}\frac{I_2 - I_1}{I_3}\left(g_1g_{2/q_i} + g_2g_{1/q_i}\right) + \frac{3\mu_2}{r^3}\frac{I_2 - I_1}{I_3}\left(h_1h_{2/q_i} + h_2h_{1/q_i}\right) \quad (3.22)$$

In the definition of the Jacobian for the SCM there appear the derivatives for the terms g_i and h_i, specifically in Eq. (3.11)-(3.22). Recall, h_i represent the projections of the position vector relative to P_1 into the body frame, while g_i are the projections of the position vector relative to P_2 into the body frame. Their partial derivatives relative to the rotating frame coordinates are

$$\begin{bmatrix} g_{1/x} \\ g_{2/x} \\ g_{3/x} \end{bmatrix} = \underset{\hat{b}\cdot\hat{r}}{A}\,\frac{1}{d^3}\begin{bmatrix} d^2 - (x+\mu)^2 \\ -y(x+\mu) \\ -z(x+\mu) \end{bmatrix} \quad \begin{bmatrix} h_{1/x} \\ h_{2/x} \\ h_{3/x} \end{bmatrix} = \underset{\hat{b}\cdot\hat{r}}{A}\,\frac{1}{r^3}\begin{bmatrix} r^2 - (x+\mu-1)^2 \\ -y(x+\mu-1) \\ -z(x+\mu-1) \end{bmatrix} \quad , \quad (3.23)$$

$$\begin{bmatrix} g_{1/y} \\ g_{2/y} \\ g_{3/y} \end{bmatrix} = \underset{\hat{b}\cdot\hat{r}}{A}\,\frac{1}{d^3}\begin{bmatrix} -y(x+\mu) \\ d^2 - y^2 \\ -zy \end{bmatrix} \quad \begin{bmatrix} h_{1/y} \\ h_{2/y} \\ h_{3/y} \end{bmatrix} = \underset{\hat{b}\cdot\hat{r}}{A}\,\frac{1}{r^3}\begin{bmatrix} -y(x+\mu-1) \\ r^2 - y^2 \\ -zy \end{bmatrix} \quad , \quad (3.24)$$

$$\begin{bmatrix} g_{1/z} \\ g_{2/z} \\ g_{3/z} \end{bmatrix} = \underset{\hat{b}\cdot\hat{r}}{A}\,\frac{1}{d^3}\begin{bmatrix} -z(x+\mu) \\ -zy \\ d^2 - z^2 \end{bmatrix} \quad \begin{bmatrix} h_{1/z} \\ h_{2/z} \\ h_{3/z} \end{bmatrix} = \underset{\hat{b}\cdot\hat{r}}{A}\,\frac{1}{r^3}\begin{bmatrix} -z(x+\mu-1) \\ -zy \\ r^2 - z^2 \end{bmatrix} \quad . \quad (3.25)$$

The partial derivatives relative to quaternion vector elements are

$$\begin{bmatrix} g_{1/q_i} \\ g_{2/q_i} \\ g_{3/q_i} \end{bmatrix} = \frac{\partial \underset{\hat{b}\cdot\hat{i}}{A}}{\partial q_i} \underset{\hat{i}\cdot\hat{r}}{A} \frac{\boldsymbol{d}}{d} \qquad \begin{bmatrix} h_{1/q_i} \\ h_{2/q_i} \\ h_{3/q_i} \end{bmatrix} = \frac{\partial \underset{\hat{b}\cdot\hat{i}}{A}}{\partial q_i} \underset{\hat{i}\cdot\hat{r}}{A} \frac{\boldsymbol{r}}{r} \quad , \tag{3.26}$$

with

$$\frac{\partial \underset{\hat{b}\cdot\hat{i}}{A}}{\partial q_1} = 2 \begin{bmatrix} q_1 & q_2 & q_3 \\ q_2 & -q_1 & q_4 \\ q_3 & -q_4 & -q_1 \end{bmatrix} \quad \frac{\partial \underset{\hat{b}\cdot\hat{i}}{A}}{\partial q_2} = 2 \begin{bmatrix} -q_2 & q_1 & -q_4 \\ q_1 & q_2 & q_3 \\ q_4 & q_3 & -q_2 \end{bmatrix} \quad , \tag{3.27}$$

and

$$\frac{\partial \underset{\hat{b}\cdot\hat{i}}{A}}{\partial q_3} = 2 \begin{bmatrix} -q_3 & q_4 & q_1 \\ -q_4 & -q_3 & q_2 \\ q_1 & q_2 & q_3 \end{bmatrix} \quad \frac{\partial \underset{\hat{b}\cdot\hat{i}}{A}}{\partial q_2} = 2 \begin{bmatrix} q_4 & q_3 & -q_2 \\ -q_3 & q_4 & q_1 \\ q_2 & -q_1 & q_4 \end{bmatrix} \quad . \tag{3.28}$$

It is possible to analytically compute the Jacobian matrix in Eq. (3.5) using the expression provided in this section in combination with the knowledge of the orbit and attitude state variables at a specified time instant along the reference solution. If the reference solution is time-varying, the Jacobian matrix for the SCM also possesses time-varying coefficients.

3.1.3 Jacobian in the Orbit-Attitude FCM

The Jacobian matrix for the FCM under SRP is substantially equal to Eq. (3.5), including a modification of the partial for the orbital differential equations, represented by the vector function $\boldsymbol{f}_x$. In particular, variations for the acceleration, that are exerted by the SRP, are also accommodated within the Jacobian matrix, as

$$\boldsymbol{f}_{x/x_{\text{orb}}} = \begin{bmatrix} 0 & 0 & 0 & 1 & 0 & 0 \\ 0 & 0 & 0 & 0 & 1 & 0 \\ 0 & 0 & 0 & 0 & 0 & 1 \\ U^*_{/xx} + a_{ss,x/x} & U^*_{/xy} + a_{ss,x/y} & U^*_{/xz} + a_{ss,x/z} & 0 & 2 & 0 \\ U^*_{/yx} + a_{ss,y/x} & U^*_{/yy} + a_{ss,y/y} & U^*_{/yz} + a_{ss,y/z} & -2 & 0 & 0 \\ U^*_{/zx} + a_{ss,z/x} & U^*_{/zy} + a_{ss,z/y} & U^*_{/zz} + a_{ss,z/z} & 0 & 0 & 0 \end{bmatrix} \quad , \tag{3.29}$$

and

$$\boldsymbol{f}_{x/q} = \begin{bmatrix} \boldsymbol{a}_{ss/q_1} & \boldsymbol{a}_{ss/q_2} & \boldsymbol{a}_{ss/q_3} & \boldsymbol{a}_{ss/q_4} \end{bmatrix} \quad . \tag{3.30}$$

The SRP acceleration is not explicitly a function of the angular velocity vector, therefore $\boldsymbol{f}_{/\omega} = \boldsymbol{0}$. Assuming the spacecraft to travel within the Sun-Earth system, and the surface normal, $\underset{\hat{r}}{\boldsymbol{n}} = \boldsymbol{n}$, to be aligned with the $\hat{\boldsymbol{b}}_1$ body axis, then, the derivatives for the SRP acceleration relative to the orbit state variables, can be written as

$$\begin{aligned} \boldsymbol{a}_{ss/x} &= \beta(1-\mu)\left\{-4\frac{x+\mu}{d^6}(\boldsymbol{d}\cdot\boldsymbol{n})^2 + \frac{2}{d^4}(\boldsymbol{d}\cdot\boldsymbol{n})n_1\right\}\boldsymbol{n} \\ \boldsymbol{a}_{ss/y} &= \beta(1-\mu)\left\{-4\frac{y}{d^6}(\boldsymbol{d}\cdot\boldsymbol{n})^2 + \frac{2}{d^4}(\boldsymbol{d}\cdot\boldsymbol{n})n_2\right\}\boldsymbol{n} \\ \boldsymbol{a}_{ss/z} &= \beta(1-\mu)\left\{-4\frac{z}{d^6}(\boldsymbol{d}\cdot\boldsymbol{n})^2 + \frac{2}{d^4}(\boldsymbol{d}\cdot\boldsymbol{n})n_3\right\}\boldsymbol{n} \quad . \end{aligned} \tag{3.31}$$

Similarly, the derivatives for the SRP acceleration relative to quaternion vector elements, are

$$\boldsymbol{a}_{ss/q_i} = \beta\left(\frac{1-\mu}{d^4}\right)\left\{2(\boldsymbol{d}\cdot\boldsymbol{n})(\boldsymbol{d}\cdot\boldsymbol{n}_{/q_i})\boldsymbol{n} + (\boldsymbol{d}\cdot\boldsymbol{n})^2\boldsymbol{n}_{/q_i}\right\} \quad , \tag{3.32}$$

with

$$\boldsymbol{n}_{/q_1} = 2\underset{\hat{r}\cdot\hat{i}}{A}\begin{bmatrix} q_1 \\ q_2 \\ q_3 \end{bmatrix} \quad \boldsymbol{n}_{/q_2} = 2\underset{\hat{r}\cdot\hat{i}}{A}\begin{bmatrix} -q_2 \\ q_1 \\ -q_4 \end{bmatrix} \quad \boldsymbol{n}_{/q_3} = 2\underset{\hat{r}\cdot\hat{i}}{A}\begin{bmatrix} -q_3 \\ q_4 \\ q_1 \end{bmatrix} \quad \boldsymbol{n}_{/q_1} = 2\underset{\hat{r}\cdot\hat{i}}{A}\begin{bmatrix} q_4 \\ q_3 \\ -q_1 \end{bmatrix} \quad . \tag{3.33}$$

In general, corresponding to a system of nonlinear ordinary differential equations, it is also possible to numerically compute the Jacobian matrix. The effort in deriving an analytical expression of the Jacobian matrix, is justified by a reduction in computation cost for a numerical algorithm that utilizes such a matrix. The evaluation of analytical formulas, typically, demands fewer operations, than the estimation for the differential equations partials via finite differences, especially when a large set of equations and variables, such as for the targeting of a specific orbit-attitude behavior, is involved.

3.1.4 The State Transition Matrix

The Jacobian, $J(t)$, is an essential component to define the linear mapping between a variation of the initial state $\delta\boldsymbol{x}_0$, and the consequent variation of the final state $\delta\boldsymbol{x}(t)$, both relative to a reference solution. The mapping $\delta\boldsymbol{x}(t) = \Phi(t,0)\delta\boldsymbol{x}_0$ is described by the State Transition Matrix (STM), $\Phi(t,0)$, which is solution to the following set of differential equations

$$\begin{cases} \dfrac{d}{dt}\Phi(t,0) = J(t)\Phi(t,0) \\ \Phi(0,0) = \mathbb{I} \quad . \end{cases} \tag{3.34}$$

The differential system in Eq. (3.34) is propagated simultaneously to the equations of motion to produce the STM. Corresponding to the set of orbit-attitude equations of motion (SCM or FCM), the system that describes the translational and rotational behaviour of the spacecraft consists of 13 equations of motion, but only 12 equations are actually independent. The components of the quaternion vector are, in fact, related by Eq. (2.28), which implies that one of the kinematic relationships in Eq. (2.38) is unnecessary for the complete description of the system evolution. One of the quaternion vector components can be considered a function of the remaining components of the vector. Rather than substituting Eq. (2.28) into the equations of motion, it is more practical to maintain the whole set of equations and reduce only the Jacobian (and the STM, consequently) to a 12 by 12 matrix, which corresponds exclusively to the independent variables. Assume that q_4 is a function of q_1, q_2, q_3, such that

$$q_4^2(q_1,q_2,q_3) = 1 - q_1^2 - q_2^2 - q_3^2 \quad ;$$

the infinitesimal variation of q_4 is a function of the independent variations of the remaining quaternion elements, i.e.,

$$q_4\delta q_4 = -q_1\delta q_1 - q_2\delta q_2 - q_3\delta q_3 \quad . \tag{3.35}$$

The previous relationship between the infinitesimal variations yields

$$\frac{\partial q_4}{\partial q_i} = -\frac{q_i}{q_4} \qquad \text{for } i = 1,2,3 \tag{3.36}$$

which is eventually exploited to compute the partials of the Jacobian matrix relative to q_1, q_2, q_3

$$\frac{d\boldsymbol{f}}{dq_i}(q_1, q_2, q_3, q_4(q_1, q_2, q_3)) = \frac{\partial \boldsymbol{f}}{\partial q_i} + \frac{\partial \boldsymbol{f}}{\partial q_4}\frac{\partial q_4}{\partial q_i} \qquad \text{for } i = 1, 2, 3. \tag{3.37}$$

Since q_4 is not regarded as an independent variable, no partials of the equations of motion with respect to q_4 are necessary to construct the Jacobian matrix. The differential equation for $\dot{q}_4$ is then also excluded during the calculation of the Jacobian matrix. Incorporating one less variable and one less equation, the Jacobian is a 12 by 12 matrix. Including the trivial equations, there are 13+144 total differential equations to simulate the system response and access the linear differential relationship between the initial and final states, which is generally sufficient to identify and precisely compute specific solutions.

3.1.5 Observing Frame Transformation for the STM in the SCM

Orbit-attitude behaviors that are periodic in the CR3BP rotating frame are one of the main topic of this work. The state along a solution that is periodic, as observed in the rotating frame, does not necessarily preserve periodicity when described in terms of an inertial observer. This statement holds true for both the orbital and attitude variables. In the presence of resonances, the state variables may be periodic in both the rotating and inertial frames, but this type of motion is not generally the case. The monodromy matrix, i.e., the STM over one period, must reflect the correct choice of the observing frame, to supply accurate information about the periodic motion. Relative to the rotating frame, the spacecraft attitude is described by the quaternion vector ${}^r\boldsymbol{q}^b = [\tilde{q}_1 \;\; \tilde{q}_2 \;\; \tilde{q}_3 \;\; \tilde{q}_4]^T$; by the rule of successive rotations for the quaternion representation, ${}^{r}\boldsymbol{q}^{b}$ can be transformed into the vector ${}^{i}\boldsymbol{q}^{b}$ employed in Eq. (2.43), which describes the orientation of the body frame respect to the inertial frame

$$ {}^{i}\boldsymbol{q}^{b} = \begin{bmatrix} \cos(t/2) & -\sin(t/2) & 0 & 0 \\ \sin(t/2) & \cos(t/2) & 0 & 0 \\ 0 & 0 & \cos(t/2) & \sin(t/2) \\ 0 & 0 & -\sin(t/2) & \cos(t/2) \end{bmatrix} {}^{r}\boldsymbol{q}^{b} \quad , \tag{3.38} $$

where the quaternion representing the rotation from the inertial to the rotating frame is, in fact, ${}^{i}\boldsymbol{q}^{r} = [0\ 0\ \sin(t/2)\ \cos(t/2)]^{T}$. To seek periodic solutions relative to the rotating frame, a conversion of the STM to reflect the correct observer seems more practical than the direct substitution of Eq. (3.54) into the equations of motion and then a re-evaluation of the Jacobian. The STM in Eq. (3.34) linearly relates the variation of the initial states to the variation of the final states relative to the reference solution

$$ \begin{bmatrix} \delta\boldsymbol{x}_{\text{orb}}(t_f) \\ \delta^{i}\boldsymbol{q}_{R}^{b}(t_f) \\ \delta^{i}\boldsymbol{\omega}^{b}(t_f) \end{bmatrix} = \Phi(tf,0) \begin{bmatrix} \delta\boldsymbol{x}_{\text{orb}}(0) \\ \delta^{i}\boldsymbol{q}_{R}^{b}(0) \\ \delta^{i}\boldsymbol{\omega}^{b}(0) \end{bmatrix} = \begin{bmatrix} \Phi_{xx} & 0 & 0 \\ \Phi_{qx} & \Phi_{qq} & \Phi_{qw} \\ \Phi_{wx} & \Phi_{wq} & \Phi_{ww} \end{bmatrix} \begin{bmatrix} \delta\boldsymbol{x}_{\text{orb}}(0) \\ \delta^{i}\boldsymbol{q}_{R}^{b}(0) \\ \delta^{i}\boldsymbol{\omega}^{b}(0) \end{bmatrix} \quad , \tag{3.39} $$

where $\delta^{i}\boldsymbol{q}_{R}^{b}(t)$ denotes the independent variations at time t in the quaternion vector that describes the orientation of the body relative to the inertial frame. Using Eq. (3.38), the variation relative to the inertial frame can be related to the variation in the rotating frame as

$$ \delta\,{}^{i}\boldsymbol{q}_{R}^{b} = \begin{bmatrix} \delta q_1 \\ \delta q_2 \\ \delta q_3 \end{bmatrix} = \begin{bmatrix} \cos(t/2) & -\sin(t/2) & 0 & 0 \\ \sin(t/2) & \cos(t/2) & 0 & 0 \\ 0 & 0 & \cos(t/2) & \sin(t/2) \end{bmatrix} \begin{bmatrix} \delta\tilde{q}_1 \\ \delta\tilde{q}_2 \\ \delta\tilde{q}_3 \\ \delta\tilde{q}_4 \end{bmatrix} = T(t)\delta^{r}\boldsymbol{q}^{b} \quad . \tag{3.40} $$

Recall that the quaternion vector is comprised of four components, which are subjected to the constraint Eq. (2.28). Thus, only three components can actually describe independent variations. Assume Eq. (3.35) is employed to define $\delta\tilde{q}_4$ as function of the independent variations $\delta\tilde{q}_1$, $\delta\tilde{q}_2$, $\delta\tilde{q}_3$, such that $\delta^r\boldsymbol{q}_R^b(t) = [\delta\tilde{q}_1\,\delta\tilde{q}_2\,\delta\tilde{q}_3]^T$. Accordingly, it is convenient to rewrite Eq. (3.35) in a vector form to reduce the variation of the quaternion ${}^r\boldsymbol{q}^b$ to its independent components

$$\delta^r\boldsymbol{q}^b = \begin{bmatrix} \delta\tilde{q}_1 \\ \delta\tilde{q}_2 \\ \delta\tilde{q}_3 \\ \delta\tilde{q}_4 \end{bmatrix} = \begin{bmatrix} 1 & 0 & 0 \\ 0 & 1 & 0 \\ 0 & 0 & 1 \\ -\tilde{q}_1/\tilde{q}_4 & -\tilde{q}_2/\tilde{q}_4 & -\tilde{q}_1/q_3 \end{bmatrix} \begin{bmatrix} \delta\tilde{q}_1 \\ \delta\tilde{q}_2 \\ \delta\tilde{q}_3 \end{bmatrix} = V(\tilde{q}_1, \tilde{q}_2, \tilde{q}_3)\delta^r\boldsymbol{q}_R^b \quad . \tag{3.41}$$

Equations (3.40) and (3.41) combine to yield a linear time-varying relationship between the variations expressed in terms of the rotating and inertial frame, i.e.

$$\delta\,{}^i\boldsymbol{q}_R^b = T(t)V(\tilde{q}_1, \tilde{q}_2, \tilde{q}_3)\delta^r\boldsymbol{q}_R^b = T_R\delta^r\boldsymbol{q}_R^b \quad , \tag{3.42}$$

where T_R is equal to the identity matrix at the initial time, since the rotational frame is assumed to be initially aligned with the inertial frame. The variation of ${}^i\boldsymbol{q}^b$ at the final time t_f is computed from the variation at the initial time using Eq. (3.39); alternatively, $\delta^i\boldsymbol{q}^b(t_f)$ can also be calculated from Eq. (3.42), if the variation at final time is known relative to the rotating frame rather than the inertial frame. Equating the results from Eq. (3.42) and Eq. (3.39) at the final time t_f produces

$$\delta^i\boldsymbol{q}_R^b(t_f) = T_R(t_f)\delta^r\boldsymbol{q}_R^b(t_f) = \Phi_{qx}(t_f,0)\delta\boldsymbol{x}_{\text{orb}}(0) + \Phi_{qq}(t_f,0)\delta^i\boldsymbol{q}_R^b(0) + \Phi_{q\omega}(t_f,0)\delta\boldsymbol{\omega}(0) \tag{3.43}$$

which can be re-arranged to explicitly express the variation of the spacecraft orientation relative to the reference solution at the final time

$$\delta^r\boldsymbol{q}_R^b(t_f) = T_R(t_f)^{-1}\Phi_{qx}(t_f,0)\delta\boldsymbol{x}_{\text{orb}}(0) + T_R(t_f)^{-1}\Phi_{qq}(t_f,0)\delta^r\boldsymbol{q}_R^b(0) + T_R(t_f)^{-1}\Phi_{q\omega}(t_f,0)\delta\boldsymbol{\omega}(0) \quad , \tag{3.44}$$

where $\delta^i\boldsymbol{q}_R^b(0) = \delta^r\boldsymbol{q}_R^b(0)$. Leveraging Eq. (3.44), the STM can be transformed to reflect variations of the spacecraft attitude relative to the rotating frame

$$\begin{bmatrix} \delta\boldsymbol{x}_{\text{orb}}(t_f) \\ \delta^r\boldsymbol{q}_R^b(t_f) \\ \delta^i\boldsymbol{\omega}^b(t_f) \end{bmatrix} = \tilde{\Phi}(t_f,0) \begin{bmatrix} \delta\boldsymbol{x}_{\text{orb}}(0) \\ \delta^r\boldsymbol{q}_R^b(0) \\ \delta^i\boldsymbol{\omega}^b(0) \end{bmatrix} = \begin{bmatrix} \Phi_{xx} & 0 & 0 \\ T_R^{-1}\Phi_{qx} & T_R^{-1}\Phi_{qq} & T_R^{-1}\Phi_{qw} \\ \Phi_{wx} & \Phi_{wq} & \Phi_{ww} \end{bmatrix} \begin{bmatrix} \delta\boldsymbol{x}_{\text{orb}}(0) \\ \delta^r\boldsymbol{q}_R^b(0) \\ \delta^i\boldsymbol{\omega}^b(0) \end{bmatrix} \quad . \tag{3.45}$$

The STM $\tilde{\Phi}$ in Eq. (3.45) is the appropriate form to identify and correct solutions that are periodic in the orbital and attitude states relative to the rotating frame. The CR3BP $\hat{r}$-frame rotates at constant rate relative to the $\hat{\imath}$-frame, thus, the angular velocity of the spacecraft observed in the rotating frame differs by a constant offset from the angular velocity relative to the inertial observer. Because the offset is constant and it is not an explicit function of time, if a solution is periodic in the rotating frame, the angular velocity is periodic in both the rotating and inertial frames. Therefore, there is no necessity to further modify the STM in Eq. (3.45).

3.2 Multi-Variable Newton Method

In this investigation, the problem of computing specific orbit-attitude solutions is formulated as an extension of a simple root-finding problem. Given a vector of n free variables, $\boldsymbol{\xi}$, a desired solution is identified as the set $\boldsymbol{\xi}^*$ that satisfies an appropriate vector condition of m constraint equations

$$\boldsymbol{F}(\boldsymbol{\xi}^*) = \Big[F_1(\boldsymbol{\xi}^*),\ \ldots,\ F_m(\boldsymbol{\xi}^*)\Big]^T = \mathbf{0} \quad . \tag{3.46}$$

The free variables in $\boldsymbol{\xi}$ may include both orbital and attitude states along the path, as well as time variables. The multi-variable Newton-Raphson iterative scheme is a viable numerical approach to calculate the zeros for the vector constraint function in Eq. (3.46). First, the constraint function $\boldsymbol{F}$ is expanded about an initial guess $\boldsymbol{\xi}_0$ in a Taylor series to the first order

$$\boldsymbol{F}(\boldsymbol{\xi}) \cong \boldsymbol{F}(\boldsymbol{\xi}_0) + DF(\boldsymbol{\xi}_0)(\boldsymbol{\xi} - \boldsymbol{\xi}_0) \quad , \tag{3.47}$$

where DF is the Jacobian of the constraint function with respect to the design variables $\boldsymbol{\xi}$ (which is different from the Jacobian for a set of ordinary differential equations, as in Eq (3.1)). The linear expansion of $\boldsymbol{F}$ in Eq. (3.47) is set equal to zero and iteratively solved for $\boldsymbol{\xi}$. Given the current free variable vector $\boldsymbol{\xi}_k$, the algorithm computes an update of the free variables for the next iteration $\boldsymbol{\xi}_{k+1}$ that generally should yield

$|\boldsymbol{F}(\boldsymbol{\xi}_{k+1})| < |\boldsymbol{F}(\boldsymbol{\xi}_k)|$. If the above inequality is consistently true, an iteration $\boldsymbol{\xi}_{k+1}$ should emerge, such that $\boldsymbol{F}(\boldsymbol{\xi}_{k+1}) = \boldsymbol{F}(\boldsymbol{\xi}^*) = \mathbf{0}$, within a certain numerical tolerance. If $n = m$, DF is square and invertible for a well-formulated problem. Then, it is possible to compute an update for the free variables as

$$\boldsymbol{\xi}_{k+1} = \boldsymbol{\xi}_k + DF(\boldsymbol{\xi}_k)^{-1}\boldsymbol{F}(\boldsymbol{\xi}_k) \quad . \tag{3.48}$$

If there are more free variables than constraints equations, i.e., $n > m$, then the minimum norm solution is used to produce the update equation for the free variables

$$\boldsymbol{\xi}_{k+1} = \boldsymbol{\xi}_k + (DF^T(\boldsymbol{\xi}_k)DF(\boldsymbol{\xi}_k))^{-1}DF^T(\boldsymbol{\xi}_k)\boldsymbol{F}(\boldsymbol{\xi}_k) \quad . \tag{3.49}$$

Accordingly, Eq. (3.48) or Eq. (3.49) is recursively applied to update the free variables until the metric $|\boldsymbol{F}(\boldsymbol{\xi}_{k+1})|$ is below the desired tolerance.

3.2.1 General Multiple Shooting Formulation

The multi-variable Newton-Raphson method is utilized as a framework to assemble a multiple shooting algorithm. A solution to the set of Eq. (2.43) that describes the coupled orbit-attitude dynamics, is a trajectory in the state space. Within this section, the trajectory does not simply denote a curve in the configuration space (i.e., position states), but refers to a curve in the higher-dimensional space that includes the evolution of all the system states (both translational and rotational). Then, in a multiple shooting algorithm, this trajectory is discretized in N control points, termed "patch points", that sub-divide the curve in $N-1$ arcs, as appears in Figure 3.1(a). In the orbit-attitude coupled problem, each patch point is a 12-dimensional state $[\boldsymbol{x}_{\text{orb},j}\ ;^i\boldsymbol{q}_j^b\ ;^i\boldsymbol{\omega}_j^b]$ that includes position, velocity, orientation and rotation rate information for the spacecraft. The first and the last patch point corresponds to the initial and final conditions, respectively. The set of all patch point states along the trajectory, augmented by the time of flight T for a single arc, and constant along each arc, constitutes the free variables vector

$$\boldsymbol{\xi} = \left[\boldsymbol{x}_{\text{orb},1};\ {}^i\boldsymbol{q}_1^b;\ {}^i\boldsymbol{\omega}_1^b;\ \ldots\ ;\ \boldsymbol{x}_{\text{orb},N};\ {}^i\boldsymbol{q}_N^b;\ {}^i\boldsymbol{\omega}_N^b\ \mid T\right] \quad , \tag{3.50}$$

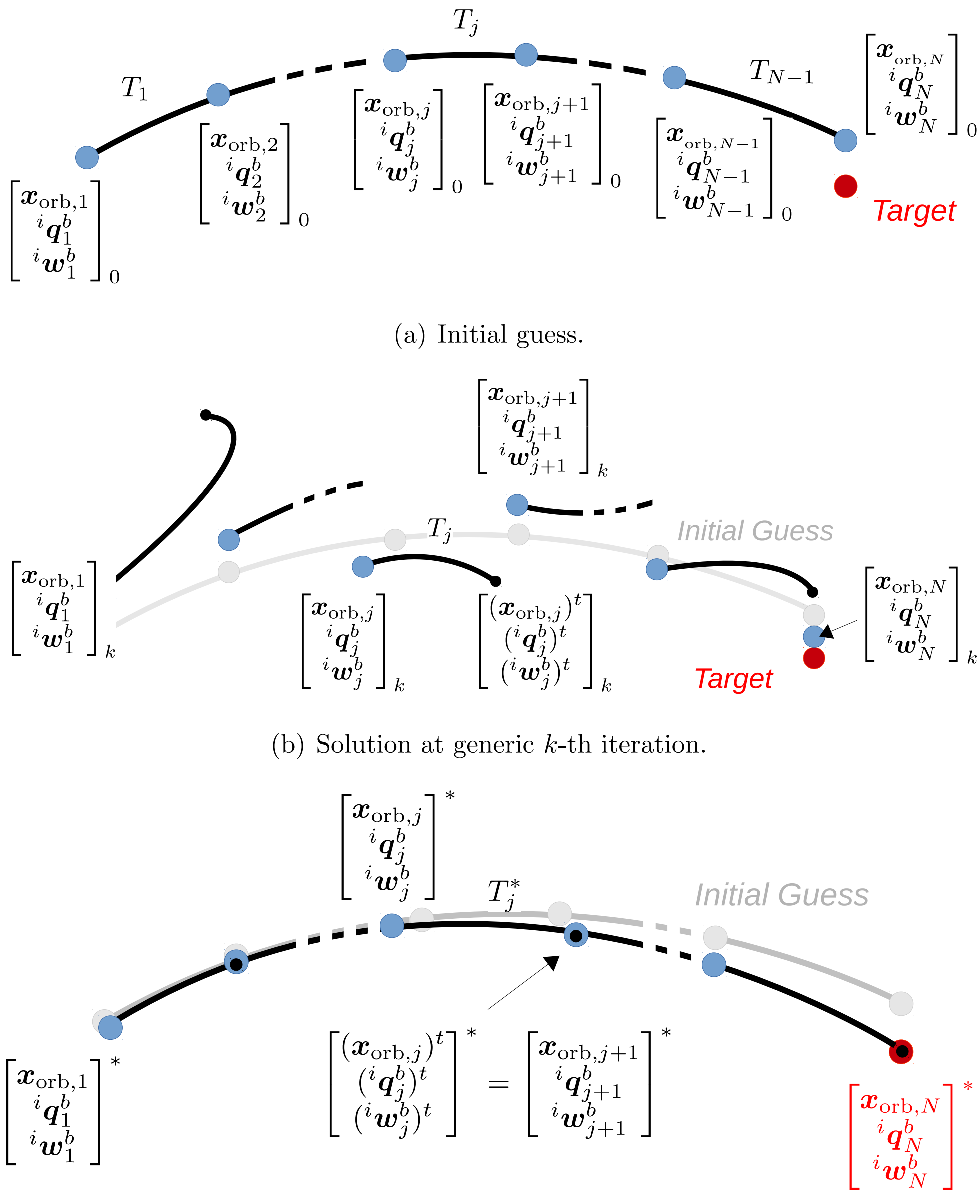

(a) Initial guess.

(b) Solution at generic k-th iteration.

(c) Converged continous solution.

Figure 3.1. Multiple shooting schematic.

which has dimension $n = 12N + 1$, given N 12-dimesional patch points corresponding to $(N-1)$ arcs. As T is assumed constant along each arc, the total time of flight for the solution is $(N-1)T$. The free variables in Eq. (3.50) are to be adjusted to satisfy the given set of constraints. A common implementation of multiple shooting, denoted parallel shooting, requires all the free variables in Eq. (3.50) to be simultaneously corrected to target the complete set of constraints along the path at each iteration.

The constraint vectorial function is then formulated as the next step. First, note that integrating the motion originating from each patch point, for the corresponding time of flight, does not necessarily yield a continuous path. The generic patch point $[\boldsymbol{x}_{\text{orb},j} \; ;^i \boldsymbol{q}_j^b \; ;^i \boldsymbol{\omega}_j^b]$ evolves on the time interval T to the final conditions $[(\boldsymbol{x}_{\text{orb},j})^t \; ; ({}^i\boldsymbol{q}_j^b)^t \; ; ({}^i\boldsymbol{\omega}_j^b)^t]$, consistent with the dynamical Eq. (2.43). On the arc j, the terminal states $[(\boldsymbol{x}_{\text{orb},j})^t \; ; ({}^i\boldsymbol{q}_j^b)^t \; ; ({}^i\boldsymbol{\omega}_j^b)^t]$ are typically different from the initial states $[\boldsymbol{x}_{\text{orb},j+1} \; ;^i \boldsymbol{q}_{j+1}^b \; ;^i \boldsymbol{\omega}_{j+1}^b]$ on the following arc $j+1$, as depicted in Figure 3.1(b). The trajectory may be, therefore, discontinuous at the patch points, unless a match exists: such that

$$[(\boldsymbol{x}_{\text{orb},j})^t \; ; ({}^i\boldsymbol{q}_j^b)^t \; ; ({}^i\boldsymbol{\omega}_j^b)^t] = [\boldsymbol{x}_{\text{orb},j+1} \; ;^i \boldsymbol{q}_{j+1}^b \; ;^i \boldsymbol{\omega}_{j+1}^b]$$

is explicitly enforced, as in Figure 3.1(c). Second, a number m_{add} of additional constraints, represented in the vector function $\boldsymbol{F}_{\text{add}}$, may be incorporated to render problem specific desired conditions, including periodicity or target states. The above considerations lead to one possible vectorial constraint function

$$\boldsymbol{F} = \left[\begin{array}{c} (\boldsymbol{x}_{\text{orb},1})^t - \boldsymbol{x}_{\text{orb},2} \\ ({}^i\boldsymbol{q}_1^b)^t -{}^i \boldsymbol{q}_2^b \\ ({}^i\boldsymbol{\omega}_1^b)^t -{}^i \boldsymbol{\omega}_2^b \\ \vdots \\ (\boldsymbol{x}_{\text{orb},N-1})^t - \boldsymbol{x}_{\text{orb},N} \\ ({}^i\boldsymbol{q}_{N-1}^b)^t -{}^i \boldsymbol{q}_N^b \\ ({}^i\boldsymbol{\omega}_{N-1}^b)^t -{}^i \boldsymbol{\omega}_N^b \\ \hline \\ \boldsymbol{F}_{\text{add}} \\ \end{array}\right] \begin{array}{c} \text{Continuity} \\ \text{for internal states} \\ \\ \\ \\ \text{Problem specific} \\ \text{constraints} \end{array} \quad ; \quad (3.51)$$

the result is a total of $m = 12(N-1) + m_{\text{add}}$ constraints equations, which may yield the desired orbit-attitude solution when satisfied.

In the Newton-Raphson scheme, the updates of the free variable vector are based on a linear prediction of the subsequent variations of the constraint function. As evident in the updates in Eqs. (3.48) and (3.49), the information on linear variations are encapsulated in the Jacobian of the constraint vector function. For the free variables and the constraints defined in Eqs. (3.50) and (3.51), respectively, the Jacobian can be written in the generic form

$$\boldsymbol{DF} = \frac{\partial \boldsymbol{F}}{\partial \boldsymbol{\xi}} = \begin{bmatrix} A_1 & -\mathbb{I} & & & & & B_1 \\ & \ddots & \ddots & & & & \vdots \\ & & A_j & -\mathbb{I} & & & B_j \\ & & & \ddots & \ddots & & \vdots \\ & & & & A_{N-1} & -\mathbb{I} & B_{N-1} \\ C_1 & \dots & & C_j & \dots & C_N & D \end{bmatrix} , \tag{3.52}$$

which is a $m \times n$ block-sparse matrix. The notation $\mathbb{I}$ indicates the identity matrix. The 12×12 blocks A_j on the diagonal denote the variations of the terminal states along each arc due to variations of the corresponding initial patch point states, such that

$$\begin{aligned} A_j &= \begin{bmatrix} \dfrac{\partial(\boldsymbol{x}_{\text{orb},j})^t}{\partial \boldsymbol{x}_{\text{orb},j}} & \dfrac{\partial(\boldsymbol{x}_{\text{orb},j})^t}{\partial {}^i\boldsymbol{q}_j^b} & \dfrac{\partial(\boldsymbol{x}_{\text{orb},j})^t}{\partial {}^i\boldsymbol{\omega}_j^b} \\ \dfrac{\partial({}^i\boldsymbol{q}_j^b)^t}{\partial \boldsymbol{x}_{\text{orb},j}} & \dfrac{\partial({}^i\boldsymbol{q}_j^b)^t}{\partial {}^i\boldsymbol{q}_j^b} & \dfrac{\partial({}^i\boldsymbol{q}_j^b)^t}{\partial {}^i\boldsymbol{\omega}_j^b} \\ \dfrac{\partial({}^i\boldsymbol{\omega}_j^b)^t}{\partial \boldsymbol{x}_{\text{orb},j}} & \dfrac{\partial({}^i\boldsymbol{\omega}_j^b)^t}{\partial {}^i\boldsymbol{q}_j^b} & \dfrac{\partial({}^i\boldsymbol{\omega}_j^b)^t}{\partial {}^i\boldsymbol{\omega}_j^b} \end{bmatrix} \\ &= \Phi(jT, (j-1)T) \quad \text{for} \quad j = 1 \ldots N-1 \end{aligned}$$

where $\Phi(jT, (j-1)T)$ is the 12×12 STM from the initial time $(j-1)T$ to the final time jT, as defined in Eq. (3.34). The 12×1 elements B_j in the last column represent the variations of the patch point states due to variation of the time of flight T along each arc, which can be expressed as a function of the time derivatives of the states and the STM as

$$B_j = \left[\frac{\partial(\boldsymbol{x}_{\text{orb},j})^t}{\partial T}; \frac{\partial({}^i\boldsymbol{q}_j^b)^t}{\partial T}; \frac{\partial({}^i\boldsymbol{\omega}_j^b)^t}{\partial T}\right]$$

$$= j\begin{bmatrix}(\dot{\boldsymbol{x}}_{\text{orb},j})^t \\ ({}^i\dot{\boldsymbol{q}}_j^b)^t \\ ({}^i\dot{\boldsymbol{\omega}}_j^b)^t\end{bmatrix} - (j-1)\Phi((j+1)T, jT)\begin{bmatrix}\dot{\boldsymbol{x}}_{\text{orb},j} \\ {}^i\dot{\boldsymbol{q}}_j^b \\ {}^i\dot{\boldsymbol{\omega}}_j^b\end{bmatrix} \quad .$$

In the last row of the DF matrix in Eq. (3.52), the $m_{\text{add}}\times 12$ blocks C_j, and the $m_{\text{add}}\times 1$ block D relate the variation of problem specific constraints to the corresponding variation of patch point state variables and time of flight, T, respectively.

3.2.2 Problem Specific Constraints

A multiple-shooting algorithm may assist the solution of several types of dynamical problems. Each type of application displays different problem specific constraints, in addition to the solution for internal continuity at the patch points. Constraints that describe periodicity of the orbit-attitude response, as well as the acquisition of a final desired state, are most relevant in this investigation.

Periodicity

Imposing a periodicity condition to govern the solution is simply adding a continuity relationship between the final and initial patch point. In this investigation, periodicity is defined for an observer fixed in the CR3BP rotating frame, and applied within the context of the SCM. Such conditions are reflected in the constraint formulation. The orbital states in the vector $\boldsymbol{x}_{\text{orb}}$ are already available in the rotating frame, whereas the orientation of the vehicle is expressed relative to the inertial frame. While enforcing periodicity, it is, therefore, necessary to transform the quaternion description ${}^{i}\boldsymbol{q}^{b}$ relative to the inertial frame to the vector ${}^{r}\boldsymbol{q}^{b}$, which describes the spacecraft attitude as observed in the rotating frame. The angular velocity ${}^{i}\boldsymbol{\omega}^{b}$ does not require a frame transformation: given the current assumptions, the $\hat{r}$-frame rotates at a constant rate relative to the inertial frame, thus, the angular velocity of the spacecraft observed in the rotating frame differs by a constant offset from the angular velocity relative to the inertial observer. Because the offset is constant and it is not an explicit function of time, if a solution is periodic in the rotating frame, the angular velocity is periodic in both the rotating and inertial frames. Thus, the periodicity constraint for the angular velocity is effectively expressed in either frame. In addition, the continuity between 5 of the initial and final translational states naturally extends to the remaining orbital component. Implicit continuity of the remaining orbital component is due to the existence of an integral of motion associated with the orbital dynamics within the SCM, i.e., the Jacobi constant. This constant is well known in the CR3BP and it is preserved in the adopted orbit-attitude SCM. A phasing constraint on any of the patch point states may also be introduced. For the periodicity of 5 arbitrary orbital states, 5 equations are introduced, 1 equation serves to phase an arbitrary state via an arbitrary patch point (e.g., $y_1 = 0$) and the 6 final equations enforce the periodicity of the attitude variables. The problem specific constraint vector that renders periodicity in the rotating frame for both the orbit and attitude state variables within the SCM, is

$$
\boldsymbol{F}_{\text{add}} = \begin{array}{c} \left[\begin{array}{c} x_N - x_1 \\ z_N - z_1 \\ v_{x_N} - v_{x_1} \\ v_{y_N} - v_{y_1} \\ v_{z_N} - v_{z_1} \\ \hline y_1 \\ \hline {}^r\boldsymbol{q}_N^b -{}^r \boldsymbol{q}_1^b \\ {}^i\boldsymbol{\omega}_N^b -{}^i \boldsymbol{\omega}_1^b \end{array}\right] \end{array}
\begin{array}{c} \\ \text{Orbit states} \\ \text{periodicity} \\ \\ \\ \hline \text{Phasing} \\ \hline \text{Attitude states} \\ \text{periodicity} \end{array}
\quad , \qquad (3.53)
$$

which becomes part of the overall constraint vector in Eq. (3.51), along with $12(N-1)$ equations that are required for continuity at the patch points; the only non-zero matrices, C_j, in Eq. (3.52), are explicitly written in the form

$$
C_1 = \begin{bmatrix} -1 & & & & \\ & -\mathbb{I}_{4\times4} & & & \\ 1 & & & & \\ & & -\dfrac{\partial^r \boldsymbol{q}_1^b}{\partial^i \boldsymbol{q}_1^b} & & \\ & & & & -\mathbb{I}_{3\times3} \end{bmatrix} , \quad C_N = \begin{bmatrix} 1 & & & & \\ & \mathbb{I}_{4\times4} & & & \\ 0 & & & & \\ & & \dfrac{\partial^r \boldsymbol{q}_N^b}{\partial^i \boldsymbol{q}_N^b} & & \\ & & & & \mathbb{I}_{3\times3} \end{bmatrix} .
$$

The variations of the periodicity and phasing constraints due to alterations of the time of flight along the arc, are included in the last 6×1 vector element

$$
D = \left[0_{6\times1};\ \frac{\partial^r \boldsymbol{q}_N^b}{\partial T};\ 0_{3\times1}\right] \quad ,
$$

which completes the construction of the $m \times n$ Jacobian matrix in Eq. (3.52).

Frame Transformation

In the constraint vector $\boldsymbol{F}_{\text{add}}$, from Eq. (3.53), the description of the attitude motion relative to the CR3BP rotating frame, i.e., ${}^{r}\boldsymbol{q}^{b}$, appears. Such a variable differs from the orientation relative to an inertial observer adopted as the reference in the equations of motion in Eq. (2.43). However, internal continuity of the solution is independent from the observing frame: a solution continuous relative to an inertial frame is simply continuous relative to any other ordinary frame as well. The same is not true for periodicity, which depends on the observer. Thus, in Eq. (3.51), the continuity constraints can be written by employing the same state variables, ${}^{i}\boldsymbol{q}^{b}$, that appear in the equations of motion in Eq. (2.43), but periodicity requires the use of ${}^{r}\boldsymbol{q}^{b}$, as it is defined – in this problem – relative to the CR3BP rotating frame. The two attitude kinematical representations ${}^{i}\boldsymbol{q}^{b}$ and ${}^{r}\boldsymbol{q}^{b}$, as expressed in terms of the quaternion formalism, are related by the rule of successive rotations, i.e.

$$
{}^{i}\boldsymbol{q}^{b} = \begin{bmatrix} \cos(t/2) & -\sin(t/2) & 0 & 0 \\ \sin(t/2) & \cos(t/2) & 0 & 0 \\ 0 & 0 & \cos(t/2) & \sin(t/2) \\ 0 & 0 & -\sin(t/2) & \cos(t/2) \end{bmatrix} {}^{r}\boldsymbol{q}^{b} \quad . \tag{3.54}
$$

The frame transformation is obviously reflected in the Jacobian matrix as well, specifically in the C_1, C_N and D blocks of Eq. (3.52). Assuming q_1, q_2, q_3 as independent variables, combining the rule for successive rotations in Eq. (3.54) with the constraint Eq. (2.28), yields the following partials

$$
\frac{\partial^{r}\boldsymbol{q}^{b}}{\partial^{i}\boldsymbol{q}^{b}}(t) = T_R(t) = \begin{bmatrix} \cos(t/2) & \sin(t/2) & 0 \\ -\sin(t/2) & \cos(t/2) & 0 \\ \sin(t/2)\dfrac{q_1}{q_4} & \sin(t/2)\dfrac{q_2}{q_4} & \cos(t/2)+\sin(t/2)\dfrac{q_3}{q_4} \end{bmatrix} \quad , \tag{3.55}
$$

with

$$\frac{\partial^r \boldsymbol{q}_N^b}{\partial^i \boldsymbol{q}_N^b} = T_R((N-1)T) \quad , \quad \frac{\partial^r \boldsymbol{q}_1^b}{\partial^i \boldsymbol{q}_1^b} = \mathbb{I}$$

as evaluated at the final time for Eq. (3.52). Recall that, q_1, q_2, q_3, q_4 are the elements of ${}^i\boldsymbol{q}^b$. The matrix $T_R(t)$ is also defined in Eq. (3.42). To conclude, the variation in orientation relative to the rotating frame at the final patch point, as a consequence of the variation in the arc time length, is

$$\frac{\partial^r \boldsymbol{q}_N^b}{\partial T} = (N-1)\frac{1}{2}\begin{bmatrix} -\sin(t/2) & \cos(t/2) & 0 & 0 \\ -\cos(t/2) & -\sin(t/2) & 0 & 0 \\ 0 & 0 & -\sin(t/2) & -\cos(t/2) \end{bmatrix}\begin{bmatrix} q_1 \\ q_2 \\ q_3 \\ q_4 \end{bmatrix} \quad , \tag{3.56}$$

where q_1, q_2, q_3, q_4 are again the components of ${}^i\boldsymbol{q}^b$.

Note on Axisymmetric Bodies

Axisymmetric bodies are extensively employed in this investigation. For an axisymmetric spacecraft subject solely to the gravity gradient, the body angular velocity about the axis of symmetry remains constant throughout the motion. Thus, including this state component at each patch point is superfluous, and introduces a redundant free variable. This redundant variable may produce an ill-conditioned formulation and convergence issues for the Newton-Raphson algorithm. A possible solution for the more specific application involving axisymmetric bodies, is the exclusion of the angular velocity component about the axis of symmetry from the patch point state vector, along with the introduction of a global spin rate (one that is constant throughout). Assuming $\hat{\boldsymbol{b}}_3$ as the axis of symmetry, the free variable vector is modified to

$$\boldsymbol{\xi} = \left[\boldsymbol{x}_{\text{orb},1};\ {}^i\boldsymbol{q}_1^b;\ {}^i\boldsymbol{\omega}_1^b;\ \ldots;\ \boldsymbol{x}_{\text{orb},N};\ {}^i\boldsymbol{q}_N^b;\ {}^i\boldsymbol{\omega}_N^b \,|\, T;\ \omega_3\right] \tag{3.57}$$

where ω_3 is the global spin rate and the angular velocity ${}^i\boldsymbol{\omega}_j^b$ only includes the two variable components

$$ {}^i\boldsymbol{\omega}_j^b = \Big[\omega_1;\ \omega_2\Big]_j \quad . $$

Identical considerations also apply to the continuity constraints, such that, only the following relationship,

$$ ({}^i\boldsymbol{\omega}_j^b)^t - {}^i\boldsymbol{\omega}_{j+1}^b = \left(\begin{bmatrix}\omega_1\\ \omega_2\end{bmatrix}_j\right)^t - \begin{bmatrix}\omega_1\\ \omega_2\end{bmatrix}_{j+1} = \mathbf{0} $$

is necessary to enforce continuity on the angular velocity vector between the terminal state on the j-th arc and the following segment. For an axisymmetric vehicle, the set of free variables is reduced to $n = 11N + 2$ and the set of elements in the constraint vector to $m = 11N$. The modification of the free variable vector is also reflected in the Jacobian matrix, which is then augmented by the column vector $\dfrac{d\boldsymbol{F}}{d\omega_3}$ to accommodate any variations in the constraint vector due to variations in the global spin rate about the axis of symmetry.

Final Target

Imposing a final target condition to govern the solution is simply adding constraint equations at the last patch-point. These constraint equations may be a nonlinear function of the final state variables; in it's simplest form, the constraint relationship is the difference between the actual final state variables and a desired set of state variables, that describes the arrival conditions. For example, consider targeting a desired final position and velocity, contained in the vector $\boldsymbol{x}_d$, that may reflect the insertion into a nominal orbit. Accordingly, the targeting problem may be formulated by augmenting the constraint vector in Eq. (3.51) with

$$ \boldsymbol{F}_{\text{add}} = \Big[\boldsymbol{x}_N - \boldsymbol{x}_d\Big] \quad , \tag{3.58} $$

which straightforwardly imposes the match between the final patch-point and the desired final configuration. Referring to a constraint vector that incorporates Eq.

(3.58), the matrix blocks C_j and D, that comprise the Jacobian in Eq. (3.52), are null, except for $C_N = \mathbb{I}$. More complex form for the targeting conditions at the final time are also possible, some that may include attitude state variables or a set of Keplerian parameters.

3.3 Continuation Schemes

In this investigation, the multiple shooting approach is employed to generate specific point solutions, ones that are possibly periodic in both the orbit and attitude states, or ones that satisfy a set of requirements at the final time. To offer a deeper insight into the solution space in certain dynamical regions, or supply a larger pool of design options, it is convenient to expand the solution range to nearby motions that continuously evolve from the initial point design. Such a group of solutions is also termed a family. There exist many techniques to produce a family of solutions; among the different algorithms, single-parameter continuation and pseudo-arclength continuation schemes are well-established in astrodynamics within the CR3BP.

3.3.1 Single-Parameter Continuation

A single-parameter continuation scheme leverages small adjustments for a selected parameter that is associated with the current solution, in combination with application of a differential correction algorithm. Specifically, a solution is converged to match a certain value for the selected parameter. Next, the parameter is varied by a small amount and the correction process is re-applied to target its updated value, and generate a slightly different response. The previously converged solution serves as an initial guess for the differential correction process at the current step. This straightforward sequence of parameter update and differential correction is iterated to produce a family of topologically related solutions. Energy, time-of-flight, state variables are practical quantities that may perform as continuation parameter. The step size and the selected parameter may vary during the continuation process.

Single-parameter continuation schemes are typically easy to implement and useful in a variety of applications.

3.3.2 Pseudo-Arclength Continuation

After a converged solution is available, solutions in the same family can be generated using a pseudo-arclength continuation procedure [41]. Essentially, the design variables are modified in the direction tangent to their exact nonlinear variation along the family. The tangential direction is computed as the null space of the Jacobian matrix DF for the last converged solution $\boldsymbol{\xi}^*$,

$$\kappa = \mathcal{N}(DF(\boldsymbol{\xi}^*)) \quad . \tag{3.59}$$

Next, an equation is appended to the constraint vector to impose a step of size ds in the tangent direction

$$\boldsymbol{G} = \begin{bmatrix} \boldsymbol{F} \\ (\boldsymbol{\xi} - \boldsymbol{\xi}^*)^T \kappa - ds \end{bmatrix} \quad , \tag{3.60}$$

such that the derivation of the augmented constraint vector yields a square augmented Jacobian matrix

$$DG = \begin{bmatrix} DF \\ \kappa^T \end{bmatrix} \quad .$$

Finally, a unique solution for the next member of the family is generated via the simple iterative update equation

$$\boldsymbol{\xi}_{i+1} = \boldsymbol{\xi}_i + DG(\boldsymbol{\xi}_i)^{-1}\boldsymbol{G}(\boldsymbol{\xi}_i).$$

Distinct from the single-parameter continuation, implementation of the pseudo-arclength continuation scheme does not depend upon previous knowledge of the family evolution from one member to the next; additionally, the pseudo-arclength approach is reasonably robust and generally prevents the continuation process from jumping to a different family of solutions.

4. BOUNDED LIBRATIONS: IDENTIFICATION OF ORBIT-ATTITUDE PERIODIC SOLUTIONS VIA FLOQUET THEORY

4.1 Overview

Orbit-attitude periodic solutions are a viable way to construct bounded attitude librations for a spacecraft travelling along a periodic orbit in the CR3BP. An orbit-attitude periodic response is attained when both the rotational and translational states periodically repeat as observed from the rotating frame. The desired degree of precision on the state variables periodicity is usually achieved through a Newton-Raphson method, which may be implemented as a targeting algorithm. When a Newton-Raphson method is applied to a highly nonlinear dynamics, such as the orbit-attitude coupled model within the CR3BP, a good initial guess for the periodic solution is crucial for the success of the correcting scheme. In this investigation, three approaches are suggested to retrieve orbit-attitude solutions that lay nearby a periodic motion:

- Floquet theory;
- Poinceré mapping;
- grid search;

The above mentioned approaches should be regarded as general guidelines, since the success of each method cannot be guaranteed a priori. Also, they are not exclusive to one another, as two or more techniques may, in fact, be combined to obtain a viable initial guess. The first approach is based on Floquet theory. The Floquet theory is able to predict, in terms of a linear approximation, the stability of a periodic solution;

then, moving across a family of periodic solutions, a change of the stability structure may indicate the existence of a new nearby periodic motion. The point where distinct dynamical behaviours share a common stability structure is denoted as a bifurcation.

Generally, the linear stability structure is defined by the eigenvalues λ_i of the monodromy matrix. Linear stable modes for the reference periodic solution are associated with eigenvalues for the monodromy matrix λ_i, real or complex, that possess a modulus value lower than 1; linear unstable modes correspond to $|\lambda_i| > 1$, while marginally linear stable modes to $|\lambda_i| = 1$. In the linear approximation, a periodic reference solution is stable (or marginally stable) if the inequality $|\lambda_i| \leq 1$ holds true for all the eigenvalues, whereas, it is unstable if any of the eigenvalues possess a modulus greater than one, i.e. $|\lambda_i| > 1$ for at least one eigenvalue. When the stability structure of the periodic reference solution changes, one pair of eigenvalues passes through the threshold $|\lambda_i| = 1$. If the threshold $|\lambda_i| = 1$ is visualized as a unitary circle on the complex plane, and if the crossing occurs on the real axis at $\lambda_i = 1$, the change of stability is labelled a tangent bifurcation and may indicate the existence of a new periodic solution in the vicinity of the reference with a similar period. When the stability change along the family occurs on the real axis at $\lambda_i = -1$, the dynamics may bifurcate to a new periodic solution with twice the period of the reference, denoted a period-doubling bifurcation. Other type of bifurcations, such as a Krein collision, are possible, but tangent and period-doubling are the only bifurcations considered in this investigation.

The utilization of Floquet theory requires a priori knowledge of a reference family of periodic solutions; the stability analysis developed by Floquet is, in fact, based on the assumption of periodic motion. However, solutions simultaneously periodic in the orbital and attitude responses, as viewed in the rotating frame, are not currently available in the CR3BP. Then, to start the procedure, one possible approach is the assumption of an elementary or intuitive scenario as an initial periodic reference; ultimately, the procedure can be reiterated as more complex solutions are produced. The approach based on Floquet theory is particularly useful to construct a network of periodic solutions that aid the understanding of the dynamical structure in the orbit-attitude coupled problem.

4.2 Definition of an Elementary Orbit-Attitude Periodic Motions on a Planar Orbit

When reference orbit-attitude periodic solutions are not available to initiate the procedure, elementary periodic motions may serve as a reference. Solutions that are expected a priori to be periodic in the rotating frame can be constructed. As reference orbital paths, several families of periodic orbits are already accessible in the CR3BP [30, 80]. In the SCP, such reference orbital states stay periodic regardless of the attitude behavior of the vehicle. Planar reference trajectories are first considered. Next, the spacecraft configuration and the initial conditions are selected to generate a simple rotational response that periodically repeats at each revolution along the reference periodic orbit.

An axisymmetric mass distribution facilitates the identification of a periodic attitude solution along the reference trajectories and it is a common configuration for space vehicles. There is, therefore, significant interest in commencing the search for orbit-attitude periodic behaviors from axisymmetric spacecraft. The vehicle is assumed to be axisymmetric about the $\hat{\boldsymbol{b}}_{\mathbf{3}}$ axis, such that $I_t = I_1 = I_2$ is the transversal moment of inertia and $I_a = I_3$ is the axial moment of inertia. Accordingly, the spacecraft topology is uniquely described by the inertia ratio

$$k = \begin{cases} \dfrac{I_a - I_t}{I_a} & \text{for} \quad I_a \geq I_t \\ \\ \dfrac{I_t - I_a}{I_t} & \text{for} \quad I_t > I_a \end{cases} \tag{4.1}$$

which varies in the interval $[0, 0.5]$ for a disk-like mass distribution with $I_a \geq I_t$, and within $[0.5, 1]$ for a rod-like mass distribution with $I_t > I_a$. If the spacecraft is axisymmetric and $I_1 = I_2$, the angular velocity about the axis of symmetry $\hat{\boldsymbol{b}}_{\mathbf{3}}$ is constant at all time, since $\dot{\omega}_3 = 0$ from Eq. (2.47). Then, assume that the orbit is planar and

$\hat{\boldsymbol{b}}_3$ is initially orthogonal to the orbiting plane $z = 0$, such that $q_1(0) = q_2(0) = 0$; also consider $\omega_1(0) = \omega_2(0) = 0$. Substituting $q_1 = q_2 = 0$ and $\omega_1 = \omega_2 = 0$ into Eq. (2.47) at the initial time yields the result that $\dot{\omega}_1$ and $\dot{\omega}_2$ are also equal to zero at any time, if the reference orbit is planar, i.e. $z = 0$. Under these conditions, the angular velocity vector is constant throughout the motion and spinning the spacecraft about $\hat{\boldsymbol{b}}_3$ at a rate Ω equal to the rate of the rotating frame produces a periodic solution. In fact, since the angular velocity vector is equal to ${}^I\boldsymbol{\omega}^b = [0\,0\,\Omega]^T$, and remains constant, the spin axis remains perpendicular to the orbiting plane and the vehicle maintains a rotation rate equal to the rate of the rotating frame relative to the inertial frame. Accordingly, for an observer fixed in the rotating frame the spacecraft never changes its initial orientation, regardless of the x, y location, which is trivially a periodic solution as the vehicle moves along the reference periodic path.

For example, consider examining an elementary periodic orbit-attitude reference solution in the Earth-Moon system for a disk-like vehicle. The solution is constructed assuming L_1 Lyapunov orbits as reference for the orbital motion. Members of this family, as viewed in the rotating frame, are displayed in Figure 4.1(a). The reference attitude motion is constructed consistently with $\hat{\boldsymbol{b}}_3$, the axis of symmetry, orthogonal to the orbital plane and ${}^I\boldsymbol{\omega}^b = [0\,0\,\Omega]^T$. In Figure 4.1(b) a series spacecraft orientations at representative instants of time along a L_1 Lyapunov reference trajectory are portrayed, both as observed in the rotating frame. Evident in the figure, the initial orientation of the vehicle is maintained throughout the orbit for a rotating frame observer. That is regardless of the specific L_1 Lyapunov orbit being selected. In addition, other types of planar trajectory, including L_2 Lyapunov orbit and DRO, may be selected as reference path. The spacecraft is displayed with a disk-like geometry, but the same solution holds even if the vehicle were rod-like shaped; the only assumption, is the body being axisymmetric with the axis of symmetry perpendicular to the orbital plane. The combination of one of the Lyapunov orbits in Figure 4.1(a) and the attitude behavior described by Figure 4.1(b) yields an elementary orbit-attidue periodic solution.

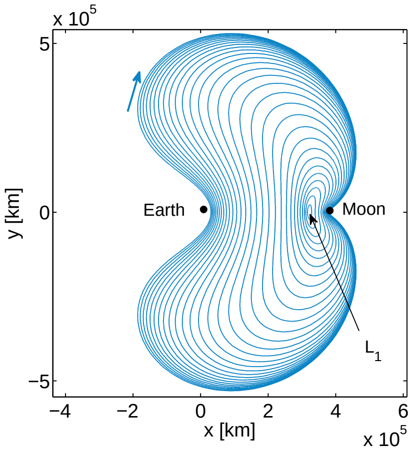

(a) L_1 Lyapunov family of periodic orbits in the Earth-Moon rotating frame.

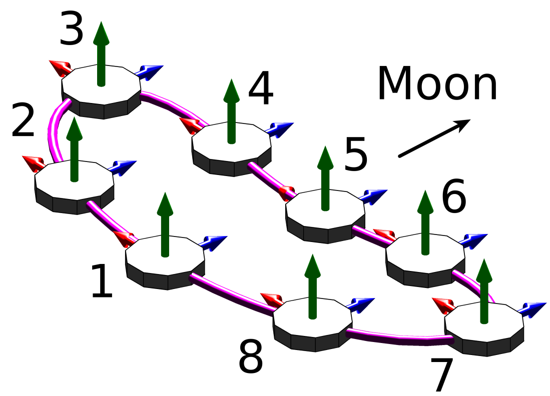

(b) Representation in the rotating frame of the elementary orbit-attitude solution that is assumed as reference. The colored axes denote the body frame, which remains aligned with the rotating frame at all the time.

Figure 4.1. Orbital and attitude reference periodic motion.

4.2.1 Linear Modes for the Reference Solution

The orbit-attitude reference solution is comprised of a well-known periodic trajectory, and periodic, possibly "elementary", attitude response along that path. Consistent with Floquet theory, the solutions nearby a periodic reference are linearly approximated by the modes of the STM over one period, i.e., the monodromy matrix. Let $\tilde{\Phi}(P, 0)$ be the 12x12 monodromy matrix that has been transformed to fully reflect a rotating frame observer, as detailed in Eq. (3.45). Associated to $\tilde{\Phi}(P, 0)$, there are 6 modes that incorporate both orbital and attitude states. The eigenvalues corresponding to these orbit-attitude coupled modes are equal to those of the isolated periodic orbit in the CR3BP. The remaining 6 modes include solely attitude state variables. The existence of purely rotational modes for the reference periodic solution is directly linked to the current model formulation, where variations of the attitude response do not involve alteration of the spacecraft trajectory[1]. For brevity, these purely rotational modes are simply denoted as attitude modes and the corresponding eigenvalues as attitude eigenvalues. However, the attitude eigenvalues for the coupled problem are different from the eigenvalues associated to an isolated attitude motion. This decomposition in coupled and attitude modes is possible because the monodromy matrix is a lower triangular block matrix, as discussed in [31].

4.3 Stability of the Attitude Modes for the Elementary Motions and Bifurcations to Non-Trivial Solutions

To begin with, the orbit-attitude reference solution is comprised of a well-known periodic trajectory, and an elementary periodic attitude regime along that trajectory. From orbit to orbit in the same family, the qualitative elementary rotational motion remains unaltered, but its intrinsic stability characteristic and nearby dynamics may be changing significantly. Varying the reference orbit across the members of a given family, possible bifurcations of the elementary attitude response to various complex periodic solutions may become evident. Recall that, one possible type of bifurcation is identified as a local mutation of the linear stability properties of the reference solution, which is tied to the eigenvalues of the monodromy matrix. Specifically, in the SCP, the monodromy matrix is block triangular and it is possible to univocally identify the attitude eigenvalues as the eigenvalues for the lower diagonal block of the STM in Eq. (3.45),

$$\tilde{\Phi}_{att} = \begin{bmatrix} \tilde{\Phi}_{qq} & \tilde{\Phi}_{q\omega} \\ \tilde{\Phi}_{\omega q} & \tilde{\Phi}_{\omega\omega} \end{bmatrix} \quad .$$

Then, monitoring the real component of the eigenvalues for $\tilde{\Phi}_{att}$ allows to capture points of possible bifurcation of the rotational regime. Consider a configuration identical to Figure 4.1, which includes an axisymmetric spacecraft orbiting L_1 Lyapunov trajectories in the Earth-Moon system. For a disk-like vehicle with inertia ratio

[1]The contrary, however, is not true. The attitude response changes if the orbital path is modified.

$k = 0.4$, Figure 4.2 displays a representative evolution of the real component in the non-trivial eigenvalues of $\tilde{\Phi}_{att}$, as the reference orbit, which is represented by the corresponding orbital period on the x-axis, shifts across the L_1 Lyapunov family. A single curve above 1 or below -1 indicates an eigenvalue with modulus certainly greater than 1, such that the reference attitude solution is unstable. When all the curves lie within the range [-1 1], the rotational motion may be marginally stable in terms of linear approximation (a more definitive assessment for the linear stability is achieved evaluating the modulus of the eigenvalues, not merely the real part)[2]. Two curves simultaneously crossing the line at 1, as depicted in Figure 4.2, may signal a tangent bifurcation, while a crossing through the line at -1, also indicated in Figure 4.2, may point to a period-doubling bifurcation. Two curves merging within the interval [-1,1] may reflect complex conjugate pairs of eigenvalues that collide along the unitary circle, i.e., a Krein collision.

The stability evolution depicted by Figure 4.2 is obtained by variation of the reference orbit across the given family while maintaining fixed the inertia ratio of the vehicle. The analysis is potentially replicable for any value of inertia ratio and for both disk- and rod-like geometries. However, to simplify the visualization of the stability information corresponding to the elementary periodic solution, a stability index, s, is defined. This quantity is set equal to $s = \frac{1}{2}\left(\lambda_{max} + \frac{1}{\lambda_{max}}\right)$, where $\lambda_{max} = \max|\lambda_i|$ denotes the magnitude of the dominant eigenvalue. A stability index with absolute magnitude equal to one identifies marginally stable behaviour, which corresponds to a family of quasi-periodic motion in the vicinity of the reference solution. Conversely, a stability index greater than one reflects unstable behavior in vicinity of the reference: a larger stability index is associated with a faster departure from the reference. The stability index enables a compact representation for the stability structure mutations due to variations of the reference orbit as well as the inertia ratio. Considering again

[2]This claim also assumes that the reference orbit is either stable or artificially fixed. Since the attitude response is naturally coupled to the orbital regime, if the reference orbit is unstable, such as L_1 Lyapunov orbits, the instability propagates to the attitude variables, regardless the eigenvalues from the matrix $\tilde{\Phi}_{att}$.

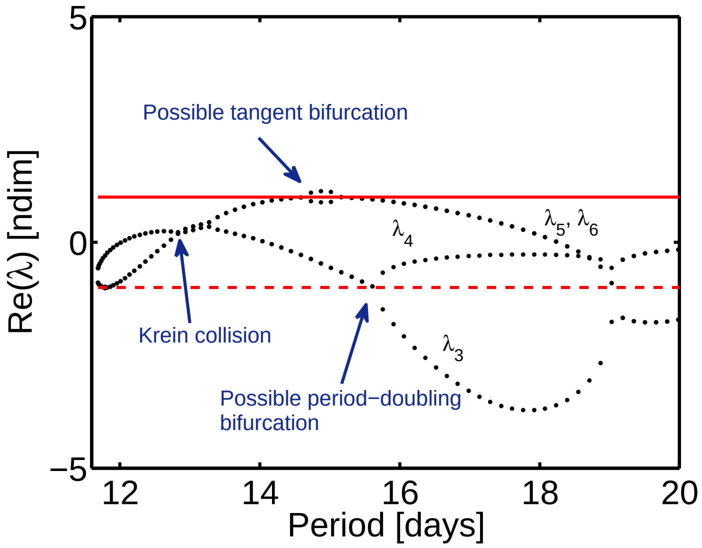

Figure 4.2. Dynamical bifurcation diagram of the reference solution for an axysimmetric disk-like spacecraft with inertia ratio $k = 0.4$ along the L_1 Lyapunov family in the Earth-Moon system.

a disk-like vehicle in L_1 Lyapunov orbits, Figure 4.3(a) represents the stability index as a function of the inertia ratio k, on the horizontal axis, and the reference orbit, denoted by its period on the vertical axis. Referring to that diagram, regions that corresponds to a stability index $s = 1$ (within a 10^{-5} tolerance) are shaded in white; in those regions, the linear analysis of the nominal motion predicts marginally stability. The colors indicate the approximate magnitude value of the stability index: blue is for values slightly above 1 and red is for values larger or equal to some maximum cap. To facilitate visualization, the color scale range does not span from 1 to the maximum stability index associated to the nominal motion; the color scale range is instead capped to an arbitrary value: stability index equal or greater to the capping value are plotted in red. From the figure, the challenge to identify specific orbit-attitude solutions in the CR3BP dynamical regime is evident. The high sensitivity of the stability to system parameters is apparent. A first set of candidate bifurcations for possible periodic solutions exist across the Lyapunov family as well as the inertia ratio range when the stability structure switches from marginally stable (i.e., $s = 1$, white regions in Figures 4.3(a)) to unstable (i.e., $s > 1$, colored regions in Figure 4.3(a)). Note that this form of representation only captures a global change of the nominal motion stability. The stability change of a single mode that does not affect the overall stability of the reference does not emerge in this type of chart. Nonetheless, also each single mode stability switch may indicate a bifurcation, regardless the global stability of the reference has changed or not. To monitor single mode components, a diagram such as in Figure 4.2 is more effective.

The elementary reference motion is studied for disk-like and rod-like configurations. Stability charts are generated for L_1 Lyapunov orbits, L_2 Lyapunov orbits and distant retrograde orbits as reference trajectory and appear in Figure 4.3, 4.4 and 4.5, respectively. Recall that the nominal solution is an axisymmetric spacecraft orbiting a planar reference orbit while the axis of symmetry remains orthogonal to the orbital plane; then, based on Figures 4.3-4.5, the following considerations about the stability of the nominal motion can be made:

- disk-like geometries displays a large variability of the stability structure, that corresponds to many possible bifurcations to non-trivial solutions - both for k or orbit variation;

- rod-like geometries are generally unstable and no bifurcations are evident in the stability index representation.

- In L_1/L_2 Lyapunov orbits, stable configurations of the nominal motion are more frequent on smaller orbits, while the instability of the reference solution becomes more predominant as the orbit grows and passes closer to the primaries.

- In L_1/L_2 Lyapunov orbits, larger orbit as well as inertia ratio yields faster divergence for rod-like vehicles, which is rendered by an higher stability index.

- In DRO, the nominal motion for disk-like vehicles is generally stable for small value of k, regardless the orbit size. However, for k approximately greater than 0.3, larger DRO are more suitable for a stable nominal motion.

- In DRO, the inertia ratio seems the driving factor for the nominal motion stability properties, given a rod-like vehicle. A larger inertia ratio corresponds to a faster diverging condition. No surprisingly, an inertia ratio tending to zero (i.e., equal inertias in all principal directions) corresponds to a slower diverging condition.

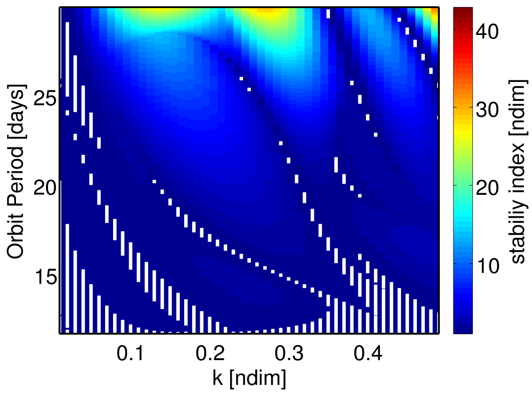

(a) Disk-like geometry.

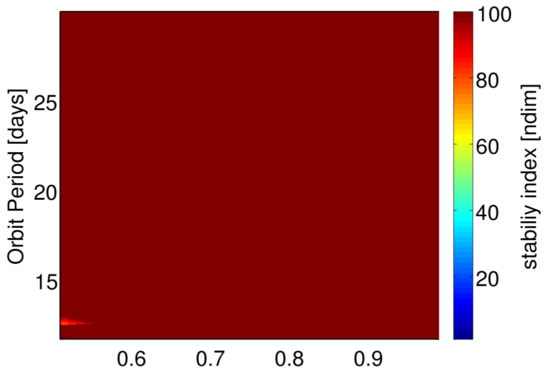

(b) Rod-like geometry.

Figure 4.3. Axisymetric spacecraft on L_1 Lyapunov orbits: stability index as function of the reference orbit (indicated by its orbital period) and the vehicle inertia ratio k. Regions where the stability index equals one (within a 10^{-5} tolerance) are shaded in white. Color scale is different in each subfigure.

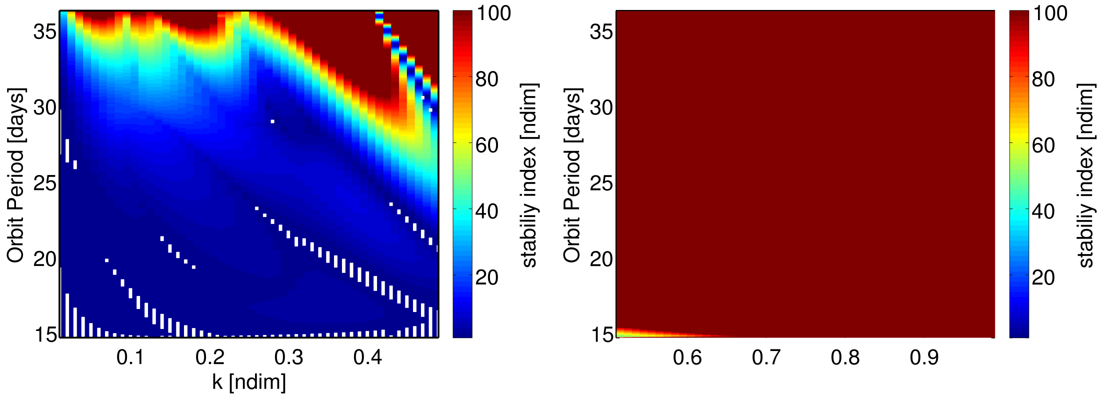

(a) Disk-like geometry. (b) Rod-like geometry.

Figure 4.4. Axisymetric spacecraft on L_2 Lyapunov orbits: stability index as function of the reference orbit (indicated by its orbital period) and the vehicle inertia ratio k. Regions where the stability index equals one (within a 10^{-5} tolerance) are shaded in white. Color scale is different in each subfigure.

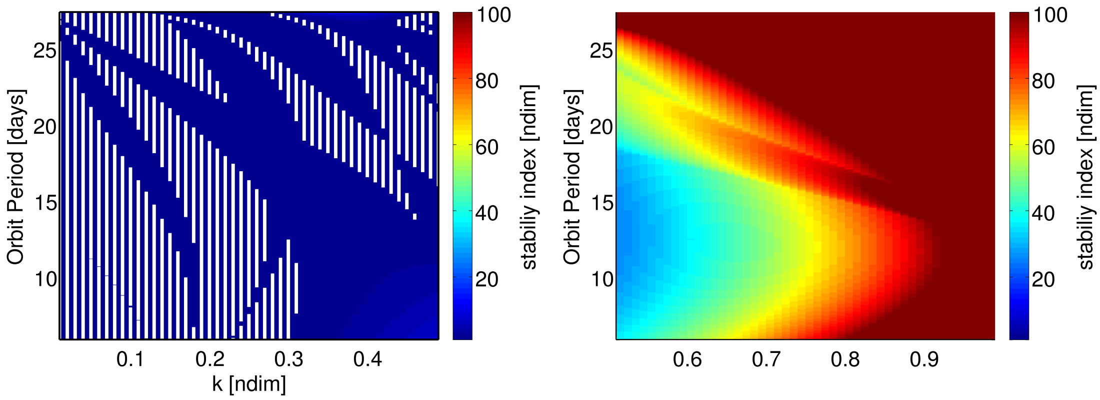

(a) Disk-like geometry. (b) Rod-like geometry.

Figure 4.5. Axisymetric spacecraft on DRO orbits: stability index as function of the reference orbit (indicated by its orbital period) and the vehicle inertia ratio k. Regions where the stability index equals one (within a 10^{-5} tolerance) are shaded in white. Color scale is different in each subfigure.

4.4 Orbit-Attitude Families of Periodic Solutions Emanating from the Bifurcations of an Elementary Motion

The stability index representation, the one portrayed in Figures 4.3-4.5, is compact, and allows for a quick, overall assessment of the possible periodic motions nearby a reference. The presence of several variations of the global stability structure for certain reference configurations can be interpreted as an higher degree of probability to find bifurcations to novel periodic motions. Global stability refers to the overall classification of the reference solution as marginally stable or unstable, ignoring the particular classification of each single eigenvalue. However, bifurcations may exist when any eigenvalue goes through the stability boundary, regardless of whether the global stability of the reference is affected. It is, then, possible that some bifurcating solutions do not appear in the stability index chart. The stability index chart are constructed by variation of the inertia ratio and reference orbit for the nominal solution. For a detailed analysis of the possible bifurcations, fix one of those two parameters, and observe the evolution of the eigenvalues as the remaining parameter is varied. For example, take a disk-like spacecraft on L_1 Lyapunov orbits and fix $k = 0.4$ while varying the reference trajectory: that corresponds to examining the eigenvalues profile for the vertical band boxed in Figure 4.6(a). Similarly to Figure 4.2, the eigenvalues evolution is displayed in term of the real component in Figure 4.6(b). The trivial unitary pair of eigenvalue, which is associated to the periodicity of the reference motion, is omitted. The remaining 4 eigenvalues can be grouped into 2 reciprocal pairs. Referring to Figure 4.6(b), intervals that correspond to stability index $s > 1$ (unstable reference) are shaded in blue; intervals that correspond to $s = 1$ remain in white (marginally stable reference). There is an obvious correspondence between the sequence of blue-white intervals in Figure 4.6(b), which mark some of the bifurcations in the eigenvalues evolution, and the sequence of unstable-marginally stable intervals for the reference motion indicated by a red box in Figure 4.6(a). Recall that, in Figure 4.6(a), marginally stable interval are shaded in white, whereas unstable intervals are colored by the value of the corresponding stability index. Possible bifurcations are associated to the crossing to the stability boundary for a pair of eigenvalues. The crossing is granted when the stability index for the reference solution shift from $s = 1$ to $s > 1$, or vice-versa. Additional crossings of the unitary circle, and the corresponding opportunity to bifurcate, are also possible within the blue regions in Figure 4.6(b), for example, the collision located near a period $P \approx 19$ days. A reference solution with 1 or 2 pairs of unstable eigenvalues is, in both cases, globally unstable; nonetheless, the variation of the number of unstable pairs requires the passage through the stability boundary and, there, it may exist a nearby novel periodic motion. It is worth noticing, that numerical challenges may occur in the classification of the eigenvalues pair. In fact, the numerical errors occurring in the eigenvalues computation may have caused the pair to surpass the tolerance that defines the stability frontier. If it is not possible to increase numerical accuracy, refining the discretization of reference orbits may help to identify whether the eigenvalue evolution nearby that interval is consistent with a dynamical feature or computational errors.

Consider a candidate bifurcation of the nominal motion: at that point, there is at least a pair of reciprocal attitude eigenvalues for $\tilde{\Phi}(P, 0)$ that is going through the stability frontier $|\lambda_i| = 1$; at the crossing, a linear approximation of the initial conditions for a periodic attitude motion different from the reference is given by

$$\begin{bmatrix} {}^I\dot{\boldsymbol{q}}^b(0) \\ {}^I\dot{\boldsymbol{\omega}}^b(0) \end{bmatrix}_{guess} = \begin{bmatrix} {}^I\dot{\boldsymbol{q}}^b(0) \\ {}^I\dot{\boldsymbol{\omega}}^b(0) \end{bmatrix}_{reference} + \epsilon \boldsymbol{V} \tag{4.2}$$

where ϵ is an appropriate scaling factor and $\boldsymbol{V}$ is a linear composition of the real and imaginary part for the eigenvectors associated to the stability crossing eigenvalues. At the stability boundary crossing, an initial guess for a novel periodic motion is obtained from Eq. (4.2). The guess is, subsequently, corrected for periodicity and continued to a family. If the correction and continuation algorithms are successful, then it is clear that the stability structure mutation is also associated to a bifurcation of the dynamical behavior. Select, for instance, the crossing near period $P = 14.60$ days in

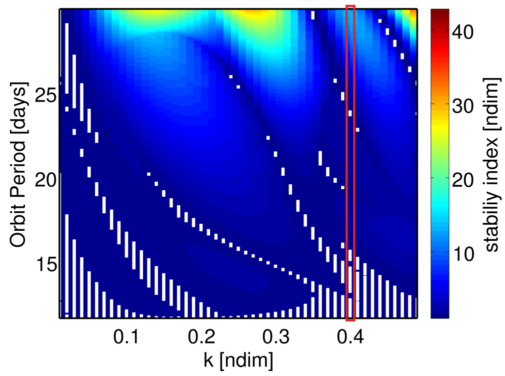

(a) Zoomed view about $k = 0.4$ of the stability index chart in Figure 4.3(a).

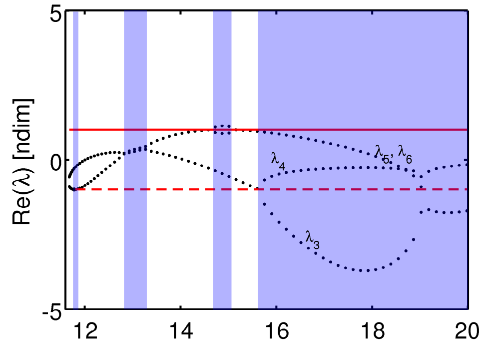

(b) Dynamical bifurcation diagram: evolution of the real component of the eigenvalues along the family of nominal motions for $k = 0.4$.

Figure 4.6. Comparison of the eigenvalues structure evolution and the stability index representation for axisymmetric spacecraft in nominal motion.

Figure 4.2. At that point, a pair of the attitude eigenvalues is converging to $\lambda = 1$, which indicates a change of stability for that mode. Such condition may indicate, but does not guarantee, a nearby non-trivial periodic motion. To assess the existence of a different periodic behavior, Eq. (4.2) is employed to guess the initial conditions for such motion. Recall that, in the current SCP model, the orbit is not affected by the rotational dynamics of the rigid body. Therefore, the attitude reference solution may initially bifurcate without altering the reference orbit. Equation (4.2) only predict initial conditions for the attitude set of variables, whereas the initial conditions for the orbit are not modified. Nonetheless, alteration of the reference orbit may be required to continue the family of novel attitude solutions. Figure 4.7 displays the result of the correction and continuation process of the initial guess for the stability boundary crossing located near period $P = 14.60$ in Figure 4.2. Figure 4.7 depicts the attitude motion relative to the rotating frame in terms of quaternions ${}^r\boldsymbol{q}^b$. Closed curves indicate that the motion is periodic as observed from the rotating reference frame. The curves emanate from a fixed point, red in Figure 4.7, which indicates a

constant attitude relative to the rotating frame; that is the original reference attitude configuration. Thus, the new family of solutions originates from the fixed point and demonstrates that the selected crossing in Figure 4.2 is an actual dynamical bifurcation.

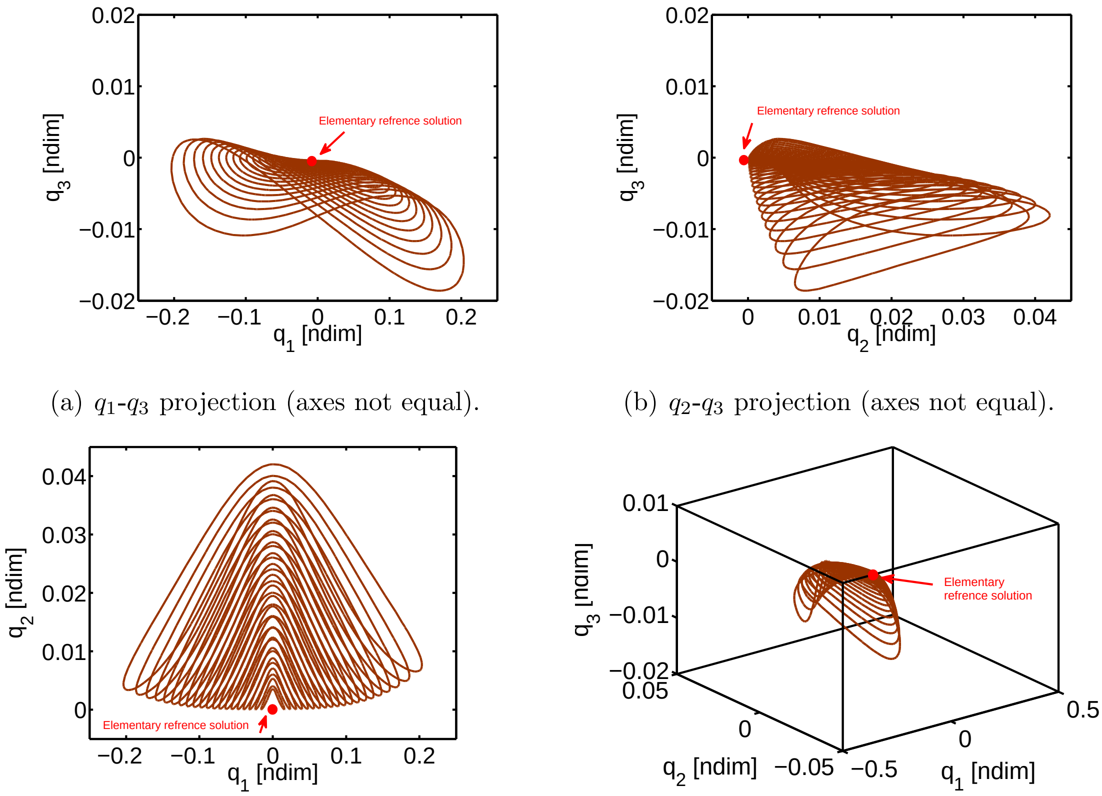

(a) q_1-q_3 projection (axes not equal). (b) q_2-q_3 projection (axes not equal).

(c) q_1-q_2 projection (axes equal). (d) 3D perspective (axes not equal).

Figure 4.7. Projection of the family of non-trivial orbit-attitude solution (*in dark red*) in the quaternion subspace. The quaternion subspace describes the orientation history of the vehicle relative to the rotating frame. The family emanates from an elementary reference solution (*in light red*).

Continuing the example for a disk-like satellite with inertia characteristics such that $k = 0.4$, one that is moving along L_1 Lyapunov trajectories in the Earth-Moon system, Figure 4.8 portrays the preliminary analysis of the attitude eigenvalue structures of the reference coupled motion as the reference orbit is varied along the family.

Some of the identified changes in the stability of the attitude modes are marked in Figure 4.8 by indicating the period of the corresponding Lyapunov reference path. At the known bifurcation point, an initial guess for a novel periodic motion is obtained from Eq. (4.2). The guess is, subsequently, corrected for periodicity and continued to construct a family as described in the previous section. Some representative novel families of attitude periodic solutions are represented in Figure 4.8 as they appear in the quaternion ${}^r\boldsymbol{q}^b$ subspace. For example, the bifurcating orbit at period $P = 15.15$ days yields a family as seen in Figure 4.8(b), that is displayed in the quaternion ${}^r\boldsymbol{q}^b$ subspace, similarly to Figure 4.7(c).

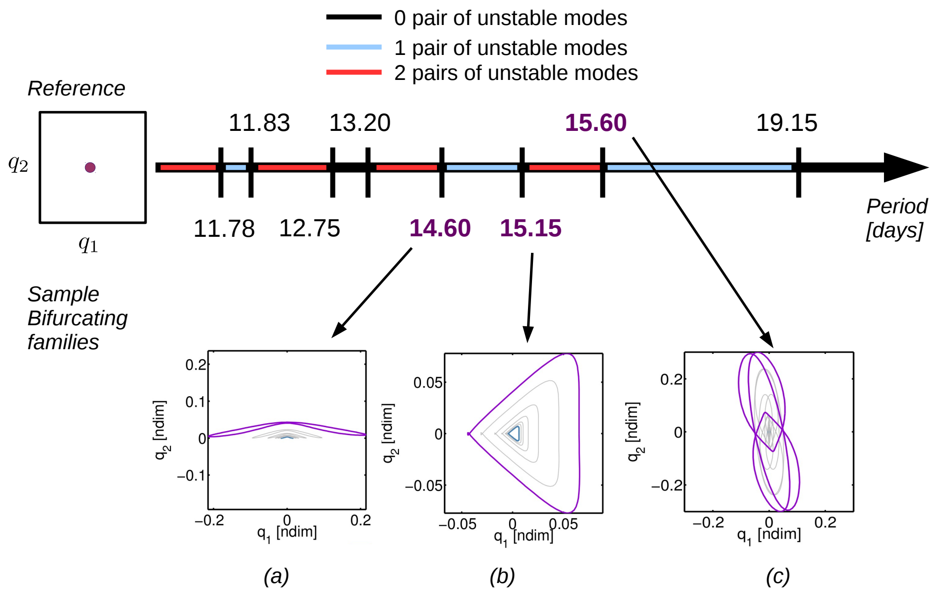

Figure 4.8. Dynamical bifurcation diagram along the family of reference elementary motions for $k = 0.4$ and L_1 Lyapunov orbits in the Earth-Moon system.

4.5 Analysis of Orbit-Attitude Families of Periodic Solutions on L_1 Lyapunov Orbits

In this section, a representative analysis of orbit-attitude families of periodic solutions is considered for a disk-like spacecraft with inertia ratio $k = 0.4$ that orbits

L_1 Lyapunov orbits in the Earth-Moon system. The selected configuration serves as a reference to introduce some general characteristics for orbit-attitude solutions. A similar analysis may be extended to any solution that is generated within the orbit-attitude coupled model.

4.5.1 Quaternion Representation and Physical Motion

Different kinematics variables may be adopted to describe the orientation of a rigid body. In this investigation, the attitude dynamics are numerically propagated using the quaternion representation. Additionally, in the numerical integration of the equations of motion, the vehicle attitude is defined relative to the inertial frame, which is described by the quaternion vector ${}^{I}\boldsymbol{q}^{b}$. However, orbit-attitude periodic solutions are sought for an observer fixed in the CR3BP rotating frame. That description requires transforming the orientation kinematic variable from ${}^{I}\boldsymbol{q}^{b}$ to ${}^{r}\boldsymbol{q}^{b}$. A response that is periodic in the rotating frame corresponds to a periodic profile in ${}^{r}\boldsymbol{q}^{b}$, but does not necessarily appears periodical in ${}^{I}\boldsymbol{q}^{b}$. As summarized in Figure 4.8, different bifurcations of the nominal attitude motion exist along the L_1 family of Lyapunov orbits in the Earth-Moon system. From those bifurcations emanate different sets of attitude periodic solutions that combine with particular reference periodic trajectories and form families of orbit-attitude periodic solutions. A sample for the computed families projects in the quaternion ${}^{r}\boldsymbol{q}^{b}$ subspace as in Figure 4.9. For clarity, only the components q_1 and q_2 are represented, which are most representative of the rotational profile for these particular solutions. The curves are, nonetheless, three-dimensional in general (or four-dimensional, if the dependent quaternion component, q_4, is included), as variations in the remaining measure number, q_3, also exist. In Figure 4.9, each family is denoted by the period of the Lyapunov orbit associated to the bifurcation of the attitude dynamics for the nominal motion. Such period corresponds to the orbital period of the smallest computed member of the family (described by a blue curve in Figure 4.9). The smallest member is the first converged solution corresponding to the initial guess from Eq.(4.2). As the family of orbit-attitude periodic solutions is continued, the period of the reference path may vary significantly and part from the period at the bifurcation. For certain families, such as Figure 4.9(e), the curves representing each attitude solution may rotate as the family grows. That is an artefact of the continuation process and corresponds to a shift of the initial point along the baseline trajectory. Incorporating phasing constrains into the continuation process may be employed to cancel the rotation of the curves along the family.

The quaternion vector representation is especially convenient to handle numerical computations, but its physical interpretation is not immediate. Recognizing the q_1, q_2, and q_3 as the components of the Euler axis, may aid to the understanding of the motion. The q_1-q_2 diagram in Figure 4.9 is, in fact, the trace of the Euler axis on the x-y plane. For the type of solutions in Figure 4.9, the trace in the q_1-q_2 plane seems to directly relate to the pointing of the axis of symmetry. In Figure 4.10, the gray sphere represents all the possible pointing directions in the CR3BP rotating frame; each red curve correspond to the trace of the axis of symmetry for a particular solution in the family, as viewed by a rotating observer; then, a point along the red curve is an instantaneous pointing direction of the spacecraft axis of symmetry for a given solution. The resemblance of Figure 4.10(a) to Figure 4.9(c), and Figure 4.10(b) to 4.9(e), is obvious. The same correspondence holds for all the families in Figure 4.9.

The observation of the axis of symmetry trace suggests that, the selected attitude solutions are a combination of nutation librations and precession relative to the x-axis of the rotating frame; both the nutation and precession are synchronized with the orbital period. Consider a body-two 3-2-3 Euler angle sequence, that describes the orientation of the body relative to the rotating frame. For the current configuration, the angles of the 3-2-3 sequence identifies precession-nutation-spin, respectively. First consider the family in Figure 4.9(c), that is represented by the nutation and precession profiles in Figure 4.11. The orientation history consistently originates from a $0°$ precession and a small nutation angle in the direction opposite to the orbital motion. Essentially, the $\hat{\boldsymbol{b}}_{\boldsymbol{3}}$ axis initially lies in a plane perpendicular to the y-axis of the

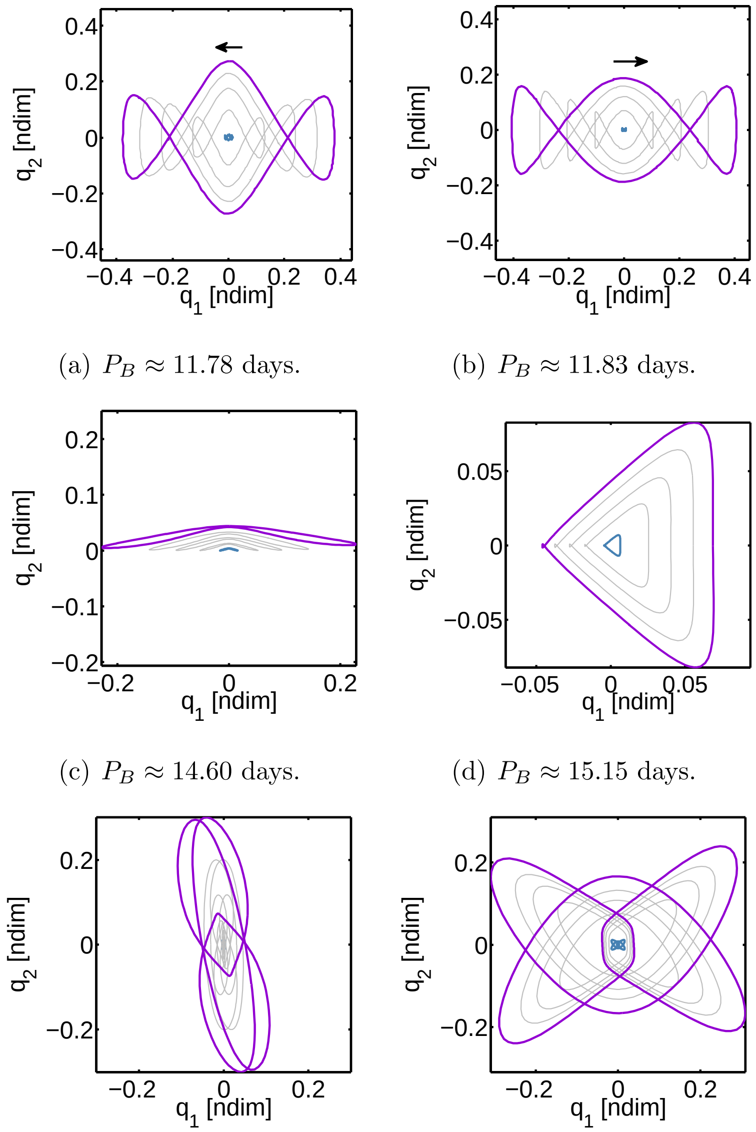

(a) $P_B \approx 11.78$ days.

(b) $P_B \approx 11.83$ days.

(c) $P_B \approx 14.60$ days.

(d) $P_B \approx 15.15$ days.

(e) $P_B \approx 15.60$ days.

(f) $P_B \approx 19.15$ days.

Figure 4.9. Sample families of orbit-attitude periodic solutions emanating from an elementary nominal solution for an axisymmetric disk-like vehicle ($k = 0.4$) orbiting a L_1 Lyapunov orbit in the Earth-Moon system. The attitude component of the solutions is represented into the q_1-q_2 subspace.

rotating frame, inclined toward $x > 0$. During the first half revolution along the L_1 Lyapunov orbit, the axis of symmetry precesses 90°, pointing opposite to the initial direction at the next crossing of the x-axis. During the remaining orbital path, the

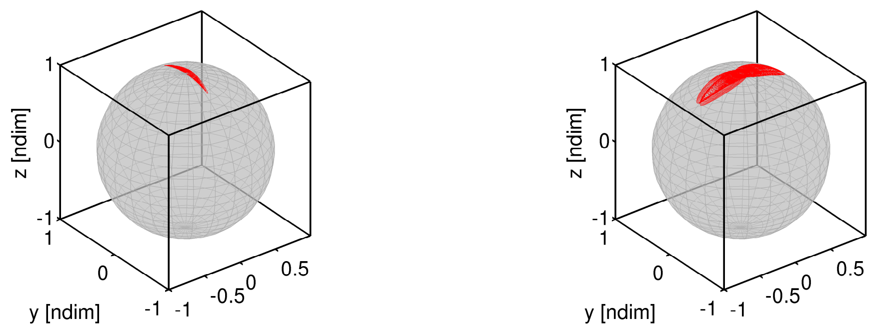

(a) $P_B = 14.60$ days.

(b) $P_B = 15.60$ days.

Figure 4.10. Evolution of the pointing direction of the spacecraft described by the trace of the symmetry axis in the rotating frame. Each curve corresponds to a different non-trivial orbit-attitude periodic solution.

nutation profile symmetrically replicates the first half revolution, while the precession anti-symmetrically follows the previous evolution. After a complete L_1 Lyapunov orbit, the vehicle returns to its initial orientation relative to the rotating frame in the CR3BP. Note that the original reference solution is described by a constantly null nutation that is marked in Figure 4.11(a). When the nutation is zero, precession is not defined; however, for convenience, a constant precession of 0° is marked in Figure 4.11(b) to describe a constant orientation of the spacecraft in the rotating frame.

Referring to Figure 4.8, all the bifurcating periodic motions corresponds to different periodic profiles for nutation of the body symmetry axis, that would be nominally orthogonal to the orbital plane. The nutation librations are the most significant component of the motion for those solutions. Large values of the precession angle, which appears in Figure 4.11(b), do not necessarily indicate large variations of the spacecraft orientation, especially if they are associated to small nutation angles. Precession principally describes the angular location of the plane containing the axis of symmetry relative to a reference direction. The families in Figure 4.9 correspond to the nutation profiles in Figure 4.12. Observing the currently available range of families, the maximum angular separation between the spacecraft axis of symmetry and the

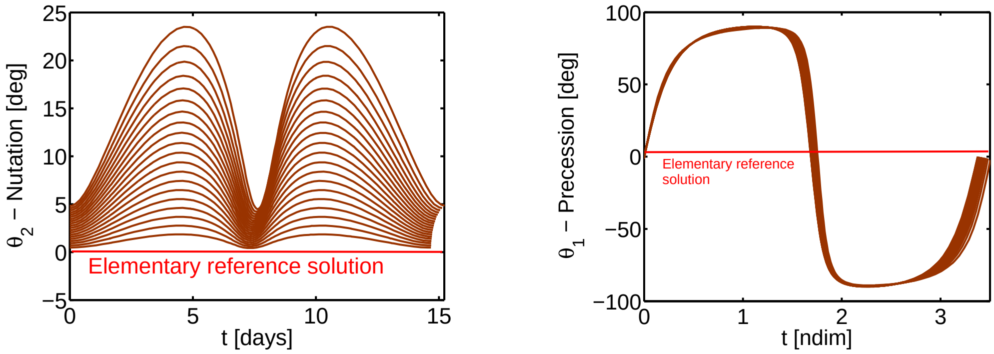

(a) Nutation angle.

(b) Precession angle.

Figure 4.11. Orientation history for the family of non-trivial orbit-attitude periodic solution (in blue) compared to the elementary reference motion (in red).

orbit normal is ≈ 50 deg. In general, all the available families of solutions have a finite amplitude oscillation, as opposite to an infinitesimal amplitude that is associated the initial guess. Further explorations are, however, warranted to investigate the difficulties encountered in the continuation process to larger values for the nutation angle, that may be associated with more numerically complex dynamics.

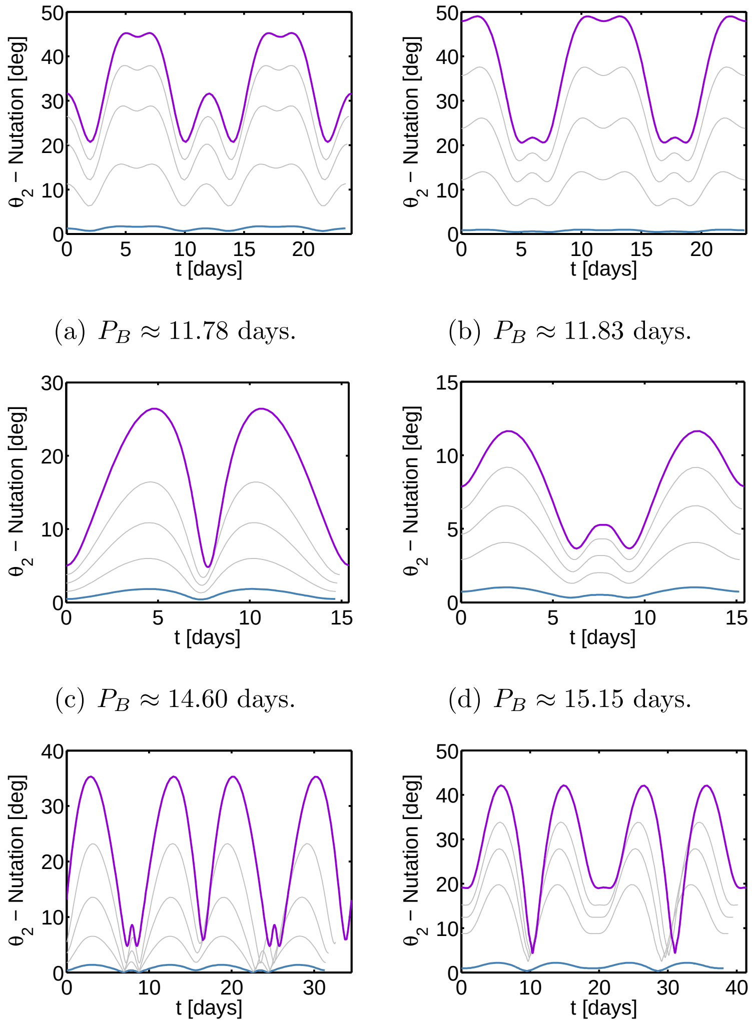

(a) $P_B \approx 11.78$ days. (b) $P_B \approx 11.83$ days.

(c) $P_B \approx 14.60$ days. (d) $P_B \approx 15.15$ days.

(e) $P_B \approx 15.60$ days. (f) $P_B \approx 19.15$ days.

Figure 4.12. Nutation history for sample families of orbit-attitude periodic solutions emanating from an elementary nominal solution for an axisymmetric disk-like vehicle ($k = 0.4$) orbiting a L_1 Lyapunov orbit in the Earth-Moon system.

4.5.2 Coupled Orbit-Attitude Nature of the Continuation Process

In a model that incorporates the gravity gradient torque, the attitude evolution is affected by the spacecraft location relative to the gravitational attractors. In such scenario, rotational periodic motions are only possible if the position configuration of the spacecraft relative to the primary bodies is also periodic, and the period is commensurate to the period of the attitude profile. The integer ratio between the period of the attitude motion and the period of the orbit yields an orbit-attitude periodic solution. The definition of the orbit-attitude elementary reference solution aids to the identification of orbits hosting complex periodic attitude behaviors. Those orbits corresponds to bifurcation of the attitude component of the elementary solution. Associated to a bifurcation orbit there exist a non-trivial periodic rotational response, along with the elementary motion. The non-trivial bifurcating solution has period equal, as well as multiple, of the reference orbit. For example, referring to Figure 4.8, the bifurcations at period $P_B \approx 11.78$ days and $P_B \approx 11.83$ days correspond to a period-doubling of the attitude solution: the spacecraft completes two orbits before the repetition of the rotational response.

As evident in Figure 4.8, there are several bifurcation points for the reference attitude motion along the reference family of periodic orbits. As the attitude motion is continued from the bifurcation, the reference orbit also need adjustment. Generally, the continuation process varies the period of the attitude motion. Accordingly, the orbit has to be corrected to match the period of the attitude response. Different solutions possess different periods, hence, they can not possibly share the same reference periodic orbit, which would be characterized by a unique orbital period. The adoption of an orbit-attitude corrections algorithm is, therefore, warranted to seek rotational periodic behaviors for vehicles on periodic orbits, even if the orbital path is known a priori and does not depend on the spacecraft orientation. A periodic attitude motion and a periodic orbital path that possess commensurate periods naturally yield an orbit-attitude periodic solution. Figure 4.13 depicts the variation of the reference orbit as the attitude solutions are continued from the bifurcation at $P_B \approx 14.60$, which corresponds to the light red orbit in the figure. Figure 4.14 displays the range of adjustments to the reference periodic orbit that are necessary to continue some of the families of orbit-attitude solutions at the bifurcations marked in Figure 4.8.

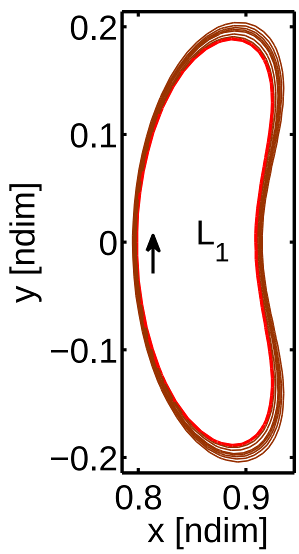

Figure 4.13. Adjustment of the initial L_1 Lyapunov periodic orbit at $P_B \approx 14.60$ days (*in light red*) to continue the family of non-trivial orbit-attitude solutions.

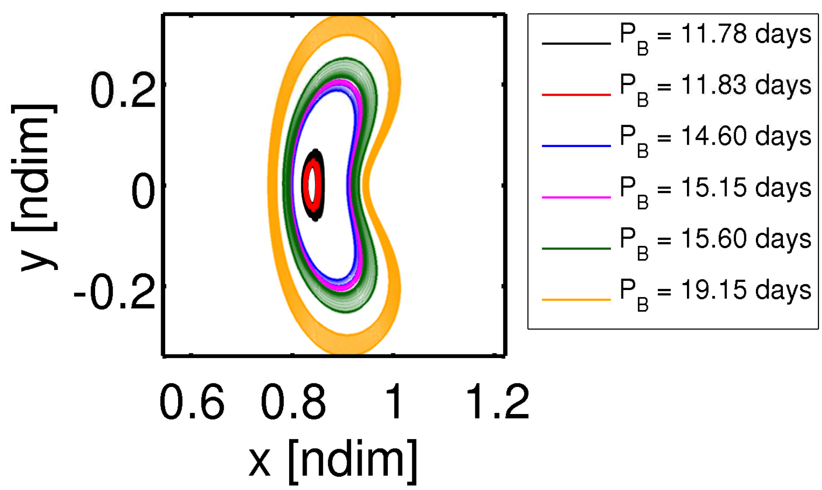

Figure 4.14. Ranges of L_1 Lyapunov orbits in the Earth-Moon system associated with the families of orbit-attitude periodic solution for an axisymmetric disk-like spacecraft ($k = 0.4$).

4.5.3 Stability for the Attitude Modes for Non-Trivial Solutions

Similarly to the analysis of the elementary reference motion, the exploration of the stability properties for the non-trivial set of orbit-attitude periodic solutions aids to the understanding of dynamics in vicinity of the nominal motion. Such analysis produces a valuable estimation for the effects of small perturbations on the nominal solution. In this section, only the stability of the attitude components of the motion is discussed. The stability properties of the orbital motion are well-known within the CR3BP. Consequences of the reference path stability on the attitude dynamics are not considered in the present discussion. Adopt the transformed STM, $\tilde{\Phi}(T, 0)$, over one period, to fully reflect a CR3BP rotating frame observer. Then, the stability index is computed, one that is associated to the 6 attitude eigenvalues.

Consider the representative orbit-attitude families of periodic solutions for a disk-like spacecraft ($k = 0.4$) on L_1 Lyapunov orbits in the Earth-Moon system, that correspond to the bifurcations in Figure 4.8. For the computed range, this set of families is associated to a stability index no greater than 40 (refer to Table 4.1-4.6 in the next section). Given a small perturbation to the reference, a small stability index is indicative of potentially slow diverging behavior from the nominal motion. Quite interesting, the family of orbit-attitude solutions that bifurcates at $P = 14.60$ days (see Figure 4.8) is marginally stable in the attitude response, i.e. $s = 1$, throughout the members currently computed. A simple way to display the consequences of different stability characteristics is to observe the motion over a long term numerical propagation. Select a solution from the orbit-attitude periodic family that bifurcates at $P = 14.60$ days (see Figure 4.9(c)) and a solution from the family bifurcating at $P = 15.60$ days (see Figure 4.9(e)). The former is associated with a stability index value $s = 1$ for the attitude modes, whereas the latter corresponds to stability index value slightly larger than 1. For both solutions, artificially fix the nominal orbit and integrate the attitude response for 500 periods. Observe the nutation history in Figure 4.15. As is evident, the nutation angle for a slowly diverging reference remains bounded for a considerable amount of time (about 250 revolutions), but eventually diverges under the perturbations introduced by the numerical errors. Conversely, the marginally stable reference solutions seems immune to such small perturbations and remains bounded on the entire time window of observations.

Both responses are consistent with the attitude eigenvalues structures in Figure 4.16. The family bifurcating at $P = 15.60$ days possesses an eigenvalue that is outside of the stability boundary, as visible in Figure 4.16(b). An unstable mode associated with an eigenvalue greater than one, eventually drives the amplitude of the nutation libration to diverge; however, a considerable time window may be required to observe the response diverging, in particular, when the eigenvalue magnitude is small (which is reflected in a large time constant for the diverging mode). The eigenvalues evolution in Figure 4.16(a) corresponds to the family bifurcating at $P = 14.60$ days. That description is consistent with a marginally stable reference, as all the non-trivial eigenvalues are within the stability boundary. In Figure 4.15, the corresponding nutation angle remains bounded for the whole propagation. Slowly diverging or marginally stable rotational motion may be an useful attitude configuration for various space infrastructures, such as manned habitats in proximity of the Moon.

This example is simple and straightforward, but, further investigation is warranted to fully characterize the stability of both solutions. An underlying assumption of this analysis is that the reference orbit is either stable or artificially fixed. Since the attitude response is naturally coupled to the orbital regime, if the reference orbit is unstable, such as L_1 Lyapunov orbits, the instability propagates to the attitude variables, regardless the attitude eigenvalues. Thus, given the coupling of the attitude and orbit motion, mutual influence on the stability properties should also be considered. Nonetheless, it is reasonable to assume station keeping of the reference orbit, so that, the stability analysis of the attitude motion alone is a good initial estimate for the stability of the rotational behavior in the coupled dynamics.

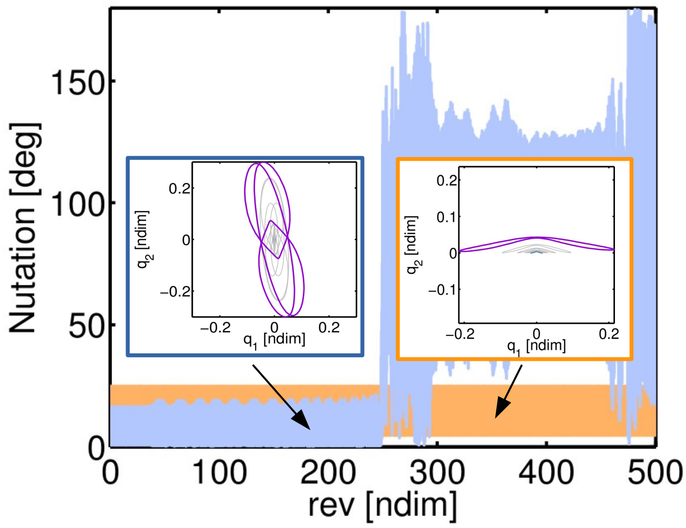

Figure 4.15. Comparison of a slow diverging (in light blue) and a marginally stable (in orange) nutation response for an orbit-attitude periodic solution on L_1 Lyapunov orbits in the Earth-Moon system for an axisymmetric disk-like spacecraft ($k = 0.4$).

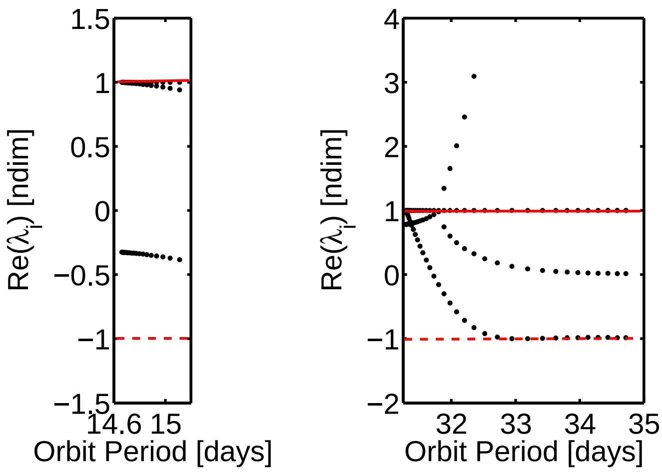

(a) $P_B = 14.00$ days. (b) $P_B = 14.00$ days.

Figure 4.16. Comparison of the eiganvalues structure (represented as real component) for a slow diverging (left) and a marginally stable (right) nutation response for an orbit-attitude periodic solution on L_1 Lyapunov orbits in the Earth-Moon system for an axisymmetric disk-like spacecraft ($k = 0.4$).

4.6 Initial Conditions for Representative Orbit-Attitude Families of Periodic Solutions on L_1 Lyapunov Orbits

In this section, the initial conditions, and other useful information, for the representative solutions depicted in Figures 4.9 and 4.12 are collected in Tables from 4.1 to 4.6. Consistently to Figures 4.9 and 4.12, each set of solutions is identified by the bifurcating period of the elementary nominal motion. In the tables, the L_1 Lyapunov orbit is identified by the coordinate of the x-crossing on the left of the L_1 Lagrangian point in the Earth-Moon system; that uniquely identifies the Lyapunov orbit and, hence, the orbital component of the motion. The initial orientation is given as the components of the quaternion vector ${}^i\boldsymbol{q}^b(0) ={}^r \boldsymbol{q}^b(0)$, which assumes the rotating frame to be aligned to the inertia frame at $t = 0$. The body angular velocity relative to the inertial frame completes the set of initial conditions that is necessary to fully reproduce the coupled orbit-attitude periodic solutions, once the period of the motion is known. Note that, the period of the coupled response may be multiple of the period of the reference orbit. In addition, the direct numerical integration of the initial conditions supplied in Tables from 4.1 to 4.6 for one full period may not yield an exact periodic motion; truncation errors to fit the values into tables and intrinsic finite numerical precision of the propagation are the cause. The application of a correction scheme to target periodicity to an higher degree of precision is warranted, even if the initial conditions for such motion are given.

Table 4.1. Initial conditions for a non-trivial orbit-attitude family of solutions bifurcating at $P_B \approx 11.78$ days. The solutions assume an axisymmetric spacecraft with inertia ratio $k = 0.4$ in the Earth-Moon system.

$\boldsymbol{x}$ [ndim]	$\boldsymbol{q_1}$ [ndim]	$\boldsymbol{q_2}$ [ndim]	$\boldsymbol{q_3}$ [ndim]	$\boldsymbol{\omega_1}$ [ndim]	$\boldsymbol{\omega_2}$ [ndim]	$\boldsymbol{\omega_3}$ [days]	$\boldsymbol{P}$ [ndim]	$\boldsymbol{s}$ [ndim]
0.827	0.000	0.011	0.000	-0.043	0.000	1.000	23.570	1.000e+00
0.827	0.001	0.098	0.009	-0.391	0.007	0.977	23.615	1.000e+00
0.825	0.001	0.176	0.008	-0.710	0.012	0.919	23.735	1.002e+00
0.823	0.002	0.229	0.007	-0.920	0.014	0.852	23.889	1.065e+00
0.821	0.002	0.273	0.007	-1.075	0.015	0.779	24.081	1.172e+00

Table 4.2. Initial conditions for a non-trivial orbit-attitude family of solutions bifurcating at $P_B \approx 11.83$ days. The solutions assume an axisymmetric spacecraft with inertia ratio $k = 0.4$ in the Earth-Moon system.

$\boldsymbol{x}$ [ndim]	$\boldsymbol{q_1}$ [ndim]	$\boldsymbol{q_2}$ [ndim]	$\boldsymbol{q_3}$ [ndim]	$\boldsymbol{\omega_1}$ [ndim]	$\boldsymbol{\omega_2}$ [ndim]	$\boldsymbol{\omega_3}$ [days]	$\boldsymbol{P}$ [ndim]	$\boldsymbol{s}$ [ndim]
0.827	0.007	-0.000	0.001	0.000	0.046	1.000	23.607	1.000e+00
0.826	-0.097	0.044	0.406	0.001	0.658	0.985	23.623	1.001e+00
0.826	-0.188	0.084	0.397	0.001	1.171	0.947	23.653	1.000e+00
0.825	-0.280	0.123	0.383	0.001	1.602	0.885	23.689	1.008e+00
0.824	-0.373	0.161	0.362	0.000	1.980	0.798	23.742	1.071e+00

Table 4.3. Initial conditions for a non-trivial orbit-attitude family of solutions bifurcating at $P_B \approx 14.60$ days. The solutions assume an axisymmetric spacecraft with inertia ratio $k = 0.4$ in the Earth-Moon system.

$\boldsymbol{x}$ [ndim]	$\boldsymbol{q_1}$ [ndim]	$\boldsymbol{q_2}$ [ndim]	$\boldsymbol{q_3}$ [ndim]	$\boldsymbol{\omega_1}$ [ndim]	$\boldsymbol{\omega_2}$ [ndim]	$\boldsymbol{\omega_3}$ [days]	$\boldsymbol{P}$ [ndim]	$\boldsymbol{s}$ [ndim]
0.799	-0.004	0.000	0.993	-0.050	0.000	1.000	14.661	1.000e+00
0.798	0.000	0.013	-0.001	-0.162	0.000	0.997	14.690	1.000e+00
0.798	0.000	0.023	-0.002	-0.292	-0.001	0.990	14.765	1.000e+00
0.797	0.000	0.033	-0.003	-0.435	-0.003	0.977	14.911	1.000e+00
0.794	-0.001	0.044	-0.009	-0.668	-0.016	0.940	15.389	1.000e+00

Table 4.4. Initial conditions for a non-trivial orbit-attitude family of solutions bifurcating at $P_B \approx 15.15$ days. The solutions assume an axisymmetric spacecraft with inertia ratio $k = 0.4$ in the Earth-Moon system.

$\boldsymbol{x}$ [ndim]	$\boldsymbol{q_1}$ [ndim]	$\boldsymbol{q_2}$ [ndim]	$\boldsymbol{q_3}$ [ndim]	$\boldsymbol{\omega_1}$ [ndim]	$\boldsymbol{\omega_2}$ [ndim]	$\boldsymbol{\omega_3}$ [days]	$\boldsymbol{P}$ [ndim]	$\boldsymbol{s}$ [ndim]
0.795	0.006	0.000	0.000	0.000	0.049	1.000	15.152	1.000e+00
0.795	0.025	0.000	-0.001	0.000	0.198	0.997	15.182	1.000e+00
0.795	0.040	0.000	-0.002	-0.001	0.318	0.992	15.233	1.000e+00
0.794	0.055	0.000	-0.003	-0.003	0.443	0.985	15.316	1.000e+00
0.794	0.069	0.001	-0.004	-0.007	0.559	0.976	15.427	1.000e+00

Table 4.5. Initial conditions for a non-trivial orbit-attitude family of solutions bifurcating at $P_B \approx 15.60$ days. The solutions assume an axisymmetric spacecraft with inertia ratio $k = 0.4$ in the Earth-Moon system.

$\boldsymbol{x}$ [ndim]	$\boldsymbol{q_1}$ [ndim]	$\boldsymbol{q_2}$ [ndim]	$\boldsymbol{q_3}$ [ndim]	$\boldsymbol{\omega_1}$ [ndim]	$\boldsymbol{\omega_2}$ [ndim]	$\boldsymbol{\omega_3}$ [days]	$\boldsymbol{P}$ [ndim]	$\boldsymbol{s}$ [ndim]
0.792	-0.003	0.000	-0.001	0.000	0.049	1.000	31.296	1.000e+00
0.792	-0.014	-0.007	-0.450	0.003	-0.235	0.999	31.392	1.000e+00
0.791	-0.026	-0.015	-0.470	0.019	-0.486	0.995	31.728	1.000e+00
0.788	-0.036	-0.027	-0.519	0.084	-0.825	0.987	32.614	2.455e+00
0.781	-0.029	-0.041	-0.531	0.463	-1.149	0.973	34.513	2.867e+01

Table 4.6. Initial conditions for a non-trivial orbit-attitude family of solutions bifurcating at $P_B \approx 19.15$ days. The solutions assume an axisymmetric spacecraft with inertia ratio $k = 0.4$ in the Earth-Moon system.

$\boldsymbol{x}$ [ndim]	$\boldsymbol{q_1}$ [ndim]	$\boldsymbol{q_2}$ [ndim]	$\boldsymbol{q_3}$ [ndim]	$\boldsymbol{\omega_1}$ [ndim]	$\boldsymbol{\omega_2}$ [ndim]	$\boldsymbol{\omega_3}$ [days]	$\boldsymbol{P}$ [ndim]	$\boldsymbol{s}$ [ndim]
0.767	0.000	-0.008	-0.001	-0.031	0.000	1.000	38.085	1.663e+00
0.764	0.002	-0.076	-0.025	-0.270	-0.014	1.000	38.782	9.019e+00
0.761	0.004	-0.108	-0.038	-0.367	-0.028	0.997	39.488	1.588e+01
0.758	0.006	-0.132	-0.046	-0.431	-0.041	0.993	40.176	2.335e+01
0.753	0.010	-0.166	-0.055	-0.510	-0.058	0.981	41.375	3.706e+01

5. BOUNDED LIBRATIONS: IDENTIFICATION OF ORBIT-ATTITUDE PERIODIC SOLUTIONS BY POINCARÉ MAPPING

5.1 Overview

Accurate initial guesses for orbit-attitude periodic solutions may also be identified through Poincaré mapping. Poincaré maps are an useful tool to capture dynamical structures of a n dimensional system $\dot{\boldsymbol{x}} = \boldsymbol{f}(\boldsymbol{x})$, such as periodic solutions, via a discrete and lower dimensional representation of the dynamical flow.

The Poincaré mapping approach to the identification of periodic motion can be summarized in the following steps:

1. Define a $n-1$ dimensional surface of section that is transversal to the dynamical flow;
2. Define a grid of initial conditions on the surface of section;
3. Propagate the initial conditions for several returns to the surface of section;
4. Record and display the returns to the surface of section;
5. Identify ordered features that correspond to periodic solutions.

The surface of section can be defined by any combination of the system states as well as by the time variable. The requirement of transversality implies that the initial conditions on the surface of section generate a flow that again intersects the surface, as schematically represented in Figure 5.1. Accordingly, the trajectories are followed from one intersection with the surface to the next, which generate the Poincaré map, i.e., a mapping of the surface of section to itself.

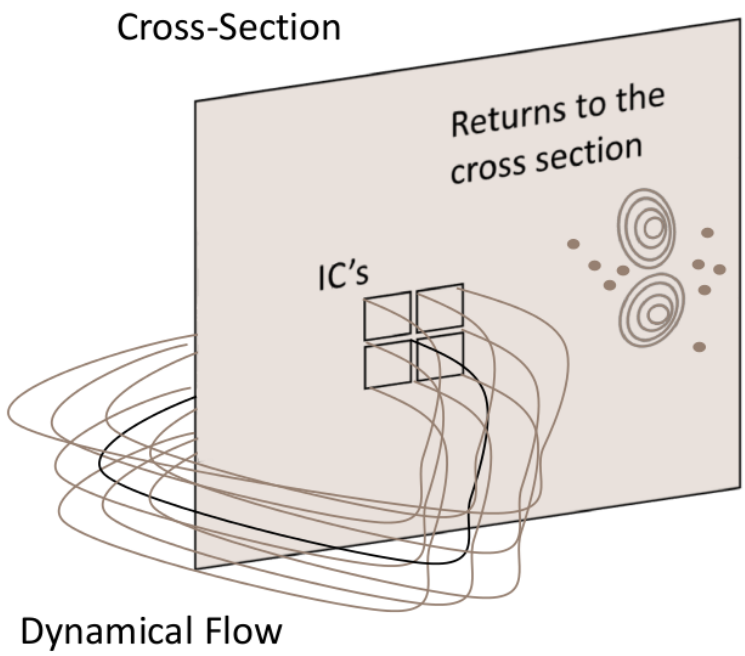

Figure 5.1. Schematics of the Poincaré map.

Intersections of a trajectory with the surface of section can be represented in terms of the state variables at the crossing. When two variables are selected, each return to the map is represented by a dot in a planar space. A two-dimensional portrait may be not a complete description of the system state, but may be sufficient to capture dynamical structures of interest. In particular, considering a two-dimensional representation, the returns associated to bounded and quasi-periodic solutions align along a closed curve on the map. Closed curves are generally not isolated, but they aggregate in islands, as displayed in Figure 5.2. An island renders the bounded motions within the neighborhood of a marginally stable periodic solution, that exists at the center of the island. On the contrary, chaotic trajectories intersect the surface of section in an seemingly random fashion, and consequently, the crossings tend to fill the entire space on the map. The regions of the map that do not display any recognizable pattern are also referred as chaotic sea. Structures related to other type of behaviors, such as manifold trajectories, may also be recognized on a map. On a properly defined surface of section, ordered patterns aid, in fact, the identification of initial conditions that correspond to periodic solutions.

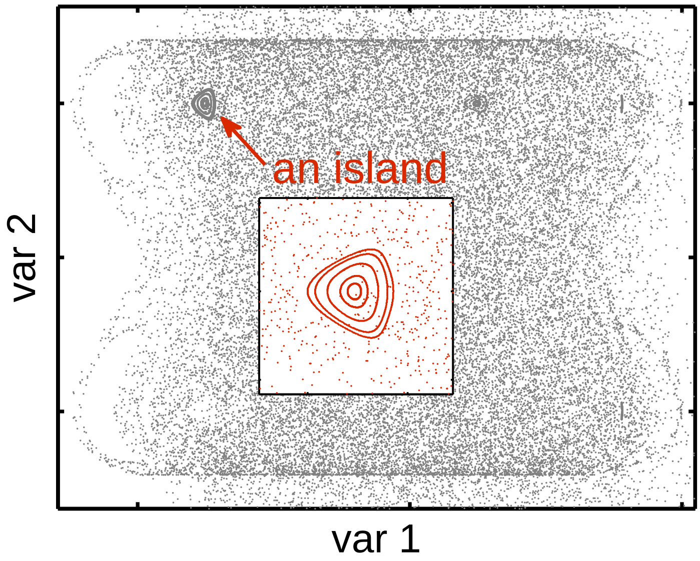

Figure 5.2. Poincaré map where ordered patterns of returns are visible.

Poincaré maps are particularly convenient to characterize the dynamical structure, and possibly identify desired solutions, for a fixed configuration of the system parameters and a specific set of initial conditions. System parameters may include the spacecraft characteristics or known integrals of motion, e.g., the total mechanical energy. The set of initial conditions contains the definition of the surface of section. In some applications, such as the preliminary stages of a mission design, however, it may be necessary to explore the impact of system parameters or analyse different set of initial conditions. Capturing the evolution of the dynamical structure for a large number of possible configurations via Poincaré mapping requires generating several maps. Accordingly, the inspection of each resulting portrait may easily become tedious and turn into a cumbersome process. An algorithm to automatically identify island structures that are present on the map is, therefore, warranted to facilitate the exploration of a large set of simulations for different initial settings.

5.2 Automatic Statistical Identification of Ordered Patterns

An algorithm for the automatic detection of island, and possibly other, patterns on a Poincaré map is proposed. The algorithm is constructed upon some empirical observations for the returns spatial frequency distribution on the surface of section, and the definition of statistical indexes that may signal the existence of an island.

Island regions and chaotic regions on the map possess different crossing variables frequency distribution on the surface of section. Define a surface of section and select two generic variables to represent the intersections of a generic trajectory with the surface of section on a two-dimensional space. Propagate the trajectory for several returns to the map and display the crossings on the two-dimensional space. Each variable that defines the two-dimensional space, appears in a range that is discretized into intervals. Then, the occurrence of returns in each interval is measured to construct a frequency distribution. If the trajectory is chaotic, the returns to the surface of section seem to disperse stochastically on the two-dimensional portrait, as displayed in Figure 5.3(a). The corresponding frequency distribution is apparent in Figure 5.3(b) for the first variable, and in Figure 5.3(c) for the second variable. If the trajectory is bounded, the returns align along a closed curve in the two-dimensional description of the map, as displayed in Figure 5.4(a). The corresponding frequency distribution is evident in Figure 5.4(b) for the first variable, and in Figure 5.4(c) for the second variable. To quantify the difference between the distributions in Figures 5.3 and 5.4 two testing strategies are next proposed.

The first testing strategy is built by comparing the observed frequency distribution with an equivalent Gaussian profile. This comparison may provide an heuristic determination for the level of disorder in the occurrence of the returns. If the intersections of the trajectory with the surface of section were a perfectly random phenomena, the

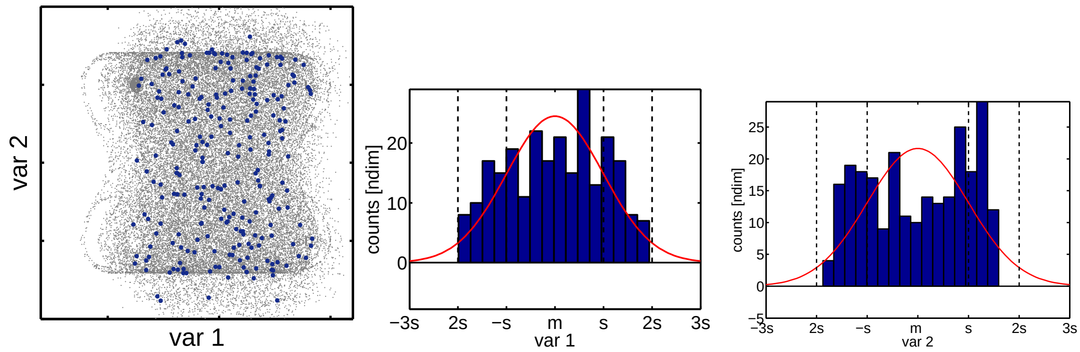

(a) Surface of section. (b) Occurence of returns along the horizontal axis of the surface of section. (c) Occurence of returns along the vertical axis of the surface of section.

Figure 5.3. Spatial frequency distribution for the returns to the surface of section for a chaotic pattern.

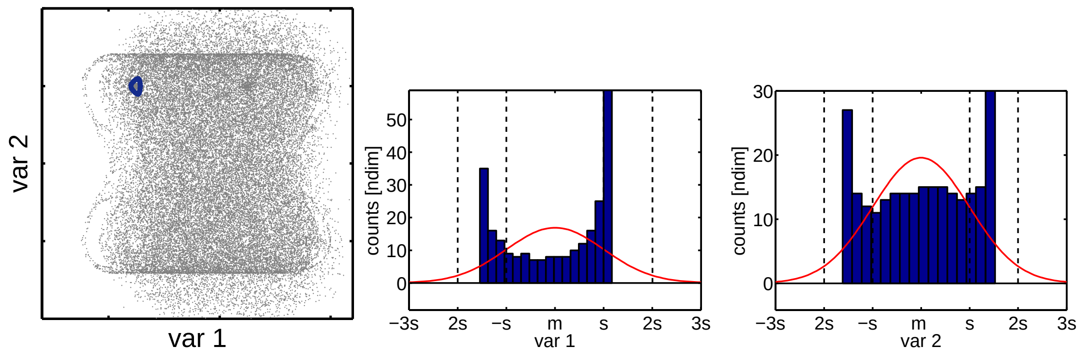

(a) Surface of section. (b) Occurence of returns along the horizontal axis of the surface of section. (c) Occurence of returns along the vertical axis of the surface of section.

Figure 5.4. Spatial frequency distribution for the returns to the surface of section for an island pattern.

occurrence of points on the two-dimensional space describing the map may be described by a Gaussian distribution for each variable that defines the observed space. Accordingly, the definition of the testing criteria assumes that, the more an observed frequency distribution for a given variable differs from an equivalent Gaussian bell, the more likely a trajectory corresponds to a dynamical structure on the map. For such comparison, an equivalent Gaussian curve is generated, one that possesses the same mean and standard deviation as the corresponding observed distribution. The Chi-Square Goodness of Fit Test (CSGFT) is employed to quantify the resemblance of two frequency distributions. The CSGFT statistic is the variable Chi-Square, χ^2, calculated as

$$\chi^2 = \sum_{i=1}^{n} \frac{(O_i - E_i)^2}{E_i} \quad , \tag{5.1}$$

where O_i is the observed frequency count in the interval ith and E_i is the expected frequency count in the interval ith. The total number of intervals is denoted by n. In this analysis, the expected count of occurrences in each interval is calculated assuming an equivalent Gaussian distribution. In general, if the value for χ^2 obtained from Eq. (5.1) is greater than a given threshold, the hypothesis that the observed distribution is similar to the expected random distribution (also known as the null hypothesis) is rejected. The critical value for χ^2 is estimated assuming a chi-square distribution with significance level, α, and $(k - c)$ degrees of freedom, where k is the number of non-empty intervals and c is the number of parameters that describe the expected distribution, plus one. The significance level, α, describes the probability of being wrong in assuming the existence of a relationship between the observed and expected distributions. Consider a seemingly random series of returns, such the one depicted in Figure 5.3(a). For the series marked in that figure, apply the CSGFT to each of the two variables describing the map. The observed distribution for the first variable, in Figure 5.3(b), and the observed distribution for the second variable, in Figure 5.3(c), correspond to a value $\chi^2 = 40.34$ and $\chi^2 = 111.39$, respectively. Also apply the CSGFT to a series of returns that outlines an island structure on the map, such as in Figure 5.4(a). In result, the observed distributions, which are again compared to a Gaussian-like outcome, produce $\chi^2 = 505.06$ for the first variable (Figure 5.4(b)) and $\chi^2 = 174.52$ for the second variable (Figure 5.4(c)). All the distributions in Figure 5.3 and 5.3 have been discretized in $k = 16$ non-empty intervals. As the expected distribution is Gaussian and is described by two degrees of freedom (e.g., mean and standard deviation), $c = 3$. Then the critical value for the CSGFT is

$\chi^2_{crit}(k-c,\alpha) = 85.52$, for a significance level $\alpha \rightarrow 0$ (precisely $\alpha = 10^{-12}$). In this example, the CSGFT metrics appears to better capture ordered behavior on the first variable, where $\chi^2 > \chi^2_{crit}$ for the sample series of returns on the island and $\chi^2 < \chi^2_{crit}$ for the sample series of returns in the chaotic sea. The CSGFT metrics highly depends on the definition of the map variables, the number of returns and the number of intervals in the frequency distribution. It is also possible that, returns patterns seemingly chaotic do not form a precisely Gaussian distribution and surpass the critical threshold, when tested with the CSGFT method. Returning to the example, the CSGFT statistic is, in fact, less effective with respect to the second variable, where $\chi^2 > \chi^2_{crit}$ for both the sample series, those corresponding to an island and to the chaotic see. It is generally observed, however, that the CSGFT provide the highest χ^2 values on close curves, ones that form an island structure. To facilitate the clear identification of islands, the critical threshold may be increased by a margin factor. In our analysis, a value for χ^2 that is significantly larger than the critical threshold describes a frequency distribution notably different from a Gaussian bell, and may indicate the formation of an island on the map.

The second test is based on the detection of occurrences picks at the side of the frequency distribution. An example of this type of distribution is displayed in Figure 5.3(b) and Figure 5.3(c). The frequency distribution associated to certain island structures appears to flatten around the average, and rapidly increase at the edges of its finite support. The identification of such picks is, again, constructed by comparison with the Gaussian distribution. The underlying idea is to measure the excess of occurrences in intervals at the sides of the distribution support, relative to the random probability of events in such intervals. A distance of 1 sigma from the average is arbitrarily selected to define the sides of the distribution support. Then, the number of occurrences in the intervals above 1 sigma, O_σ, is divided by the expected count in the same intervals, E_σ, if the distribution were Gaussian, such that

$$\mathcal{A}_\sigma = \frac{O_\sigma}{E_\sigma} \quad . \tag{5.2}$$

Large values for $\mathcal{A}_\sigma$ describes events accumulating at the side of the distribution support, and may indicate the presence of a closed curve on the map. The contrary is not true. Small values for $\mathcal{A}_\sigma$ do not necessarily exclude the existence of an island. For certain configurations, in fact, the picks may occur below 1 sigma and, therefore, stand undetected by the current definition of the $\mathcal{A}_\sigma$ metrics. Also, similarly to the CSGFT statistic, the $\mathcal{A}_\sigma$ parameter does not supply a criteria for a precisely accurate detection of islands, but only enables a measurement for the degree of possibility that the observed series of returns lies along a defined structure on the map. A greater ratio $\mathcal{A}_\sigma$ may indicate the presence of a large number of events on the side of the distribution support, and simply reinforce the likelihood of corresponding to an island type of behavior.

The metrics χ^2 and $\mathcal{A}_\sigma$ are incorporated into an algorithm for the automatic detection of island, and possibly other, structures on a Poincaré map. The scope of the algorithm is to provide an estimate for the likelihood of island structures that may exist on a given Poincaré map. The precise identification of each single structure or the accurate count of islands on the map is beyond the purpose of such algorithm. The algorithm for the automatic detection of island curves is outlined by the following steps:

1. From the grid of initial conditions that define the Poincaré map, propagate a single trajectory;
2. For each variable that describes the surface of section, generate the frequency distribution of the crossings;
3. Compute the metrics χ_2 and $\mathcal{A}_\sigma$ for each of the frequency distributions from the previous step;
4. Define a threshold for each metrics. Above the chosen threshold, a single metrics predicts the existence of an island. Define this event as a successful test;
5. Define a minimum number of successful tests;

6. If the actual number of successful tests is greater than the minimum defined at the previous steps, flag the trajectory;

7. Move to the next propagation and repeat.

The outcome of this procedure is a number of flags that marks any trajectory possibly associated to different island structures on the Poincaré map. Such algorithm is combined with the generation of several Poincaré maps for different system configurations. Following the recognition of maps with a desired number of flags, selected configurations can be inspected manually, or via strategies that enable a more definitive analysis of the dynamical patterns. The algorithm is a practical and straightforward implementation of a strategy for the preliminary automatic examination of a large number of maps, however it does not guarantee to successfully flag each trajectory that is genuinely associated to an island. The accuracy for the proposed procedure may be easily improved by incorporating additional testing metrics for the definition of a frequency distribution that corresponds to an ordered pattern, such as an island structure.

The general framework for the automatic inspection of Poincaré maps via statistical metrics is applied to the identification of attitude periodic solutions along periodic orbits in the CR3BP. Such framework facilitates the analysis of several Poincaré maps corresponding to different spacecraft topologies and reference orbits. Configurations that more likely enable marginally stable dynamical behaviors, consistent with the map definition, are automatically detected.

5.3 Poincaré Mapping Campaign for Orbit-Attitude Periodic Planar Motions

Considering both rod-like and disk-like geometries for a wide range of possible mass distributions, that travel along planar periodic orbits in the CR3BP, several Poincaré maps are generated and analysed to identify periodic attitude behaviors. For simplicity, the rotational dynamics are also planar.

For a given combination of spacecraft mass distribution and reference orbit, a Poincaré map is produced as follows. Consider an axisymmetric vehicle moving along a planar periodic orbit in the Earth-Moon system. L_1 Lyapunov, L_2 Lyapunov and DRO orbits are employed as nominal trajectory. Assume the spacecraft initiates its motion from the x-axis: on the crossing closest to Earth for L_1 Lyapunov and DRO type of motions, on crossing farthest from the Moon for L_2 Lyapunov orbits. At the initial time, two orientations of the vehicle are considered: for a rod-like spacecraft, the axis of symmetry $\hat{\boldsymbol{b}}_{\mathbf{3}}$ is aligned with the x-axis of the CR3BP rotating frame, if the vehicle is rod-like; for a disk-like spacecraft, the axis of symmetry $\hat{\boldsymbol{b}}_{\mathbf{3}}$ is instead aligned with the y-axis of the CR3BP rotating frame. An initial angular velocity component for the vehicle is introduced in the z-axis direction. The angular velocity remains orthogonal to the orbital plane throughout the motion; accordingly, the axis of symmetry of the vehicle moves in the xy-plane. The xz-plane constitutes the surface of section transverse to the dynamical flow in configuration space. Without altering the spacecraft geometry or the reference periodic orbit, assume that the initial angular velocity magnitude is varied within the range $[-4, 4]$ nondimensional units with a step size of 0.1 nondimensional units, which forms a grid of initial conditions. Then, for each value assigned to the angular velocity, the initial conditions are propagated for 500 revolutions of the periodic orbit, which is artificially maintained. The attitude states are recorded at every crossing of the xz-plane in the positive y direction. Monitor the orientation of the vehicle relative to the CR3BP frame via the quaternion vector ${}^{r}\boldsymbol{q}^{b}$, as well as its body angular velocity ${}^{i}\boldsymbol{\omega}^{b}$. Create a two-dimensional visualization of the map using one component of ${}^{r}\boldsymbol{q}^{b}$, say q_2, and the angular velocity component orthogonal to the orbital plane, i.e., ω_2, for each set of initial conditions and each return to the surface of section. Since the nominal motion is planar in both its translational and rotational components, a two-dimensional portrait ideally contains all the necessary information to represent the attitude state on the map. Utilizing this general definition of Poincaré section, maps are generated for a large number of inertia characteristics and reference orbit combinations.

The inspection of an extensive sample of system configurations is enabled via an automatic detection of island patterns, as is introduced in the previous section. For the simulation campaign, the spacecraft inertia ratio, k, is varied within the interval [0.5 1] for rod-like geometries, and [0 0.5] for disk-like vehicles, with a step size equals to 0.01. Consistently, a total of 100 configurations are employed to describe the possible mass distribution for the spacecraft. The set of periodic orbits examined includes 140 L_1 Lyapunov trajectories within the period range of [11.68 29.95] days, 90 L_2 Lyapunov orbits within the period range of [14.64 36.2] days, and 150 members in the DRO family within the period range of [5.87 27.37] days. The selected periodic orbits are not necessarily equispaced within the period range. The total size of the sample of periodic motions is 380 reference trajectories. Combining such sample of orbits with the total number of selected inertia ratios, the simulation campaign produces 38000 surface of sections, that require examination. Leveraging the automatic statistical algorithm for the identification of island structures, each map is analysed. The inspection employs the frequency distribution for the variables q_2 and ω_2, which describe the surface of section as a two-dimensional plane. The distributions are calculated over the first 250 returns on the map. Reducing the number of returns facilitate the identification of structures that may be perturbed by the accumulation of numerical errors, or that may be associated to slowly diverging periodic behaviors. Recall that, ordered patterns in each returns series are detected by statistical indexes, χ^2 and $\mathcal{A}_\sigma$ precisely. Presently, if the CSGFT metrics are greater than 1.5 times the critical value, χ^2_{crit} (calculated for a significance level $\alpha = 10^{-12}$), the CSGFT test associates the distribution to a structure within the map. Similarly, when the statistics denoted by $\mathcal{A}_\sigma$ is larger than 3, the distribution is related to a pattern that would be visible on the surface of section. The thresholds are determined by the analysis of the statistical metrics for a small sample of representative maps. Describing the Poincaré map with two variables and incorporating two statistics, 4 tests are applied to each propagation to determine the existence of ordered structures, such as an island of bounded motion. When two over four tests are successful, regardless of the type of metrics, then, the propagation is flagged to indicate the possible existence of an ordered pattern. The procedure to flag a sequence of crossings may be elaborated to weight differently each test, accordingly to the metrics used or the variable examined. The minimum number of successful tests to flag may also be increased to reflect an higher level of certainty. As a result, the number of propagations that are likely to correspond with island structures is calculated for each map.

The outcome for the automatic statistical inspection of several Poincaré maps, which include L_1, L_2 Lyapunov, and DRO as reference orbit and an axisymmetric vehicle as reference geometry, is summarized visually in Figures 5.5-5.10. In those figures, the horizontal axis describes the reference mass distribution via the inertia ratio, k; the vertical axis reflects the period of the reference orbit. For each combination of mass distribution and reference orbit a Poincaré map is generated and automatically analysed. Consequently, different Poincaré maps correspond to different locations on the diagram, that are colored by the number of solutions potentially reflecting island structures. Yellow denotes a large number of propagations that may correspond to islands or other ordered structures, whereas dark green denotes none or few propagations that satisfy the algorithm criteria for preliminary pattern detection. To initially assess the degree of accuracy offered by the algorithm predictions, representative Poincaré maps complement the color-coded diagram in each figure. On the single Poincaré map, the series of returns that the algorithm flags as probable dynamical structure, are marked in red. Ideally, there should exist an effective correspondence between the color on the diagram (i.e., the prediction) and the actual topology of the map. For example, such correspondence is well defined in Figures 5.5 - 5.7: maps that corresponds to yellow regions in the diagram, actually display an highly ordered topology (e.g., upper-left inset in Figure 5.7); maps that correspond to the darkest green areas in the diagram, are entirely chaotic (e.g., upper-right inset in Figure 5.6); intermediate shades on the color scale describe maps with fewer islands emerging from chaotic series of returns, to the extend that even significantly isolated structures may be identified (e.g., lower-center inset in Figure 5.7). Limited prediction accuracy, however, may also occur, especially in presence of fast diverging behaviors. For example, a rod-like spacecraft along Lyapunov periodic orbit for the given set of initial conditions tend to degenerate in a fast rotating motion for a large variety of system parameter configurations. In this scenario, the statistical analysis is less precise. For example, certain maps associated to the scatter regions in Figures 5.8 and 5.9, such as the upper-right inset in Figure 5.8 may contain seemingly chaotic patterns that are, nonetheless, identified as ordered motions by the statistical analysis of the crossings. Dynamics that are, in fact, associated to a rapidly accelerating profile for the vehicle rotations, generate distributions of returns different from a Guassian bell (i.e., the reference distribution implemented in the algorithm), but yet that do not correspond to any significant structure on the surface of section. Alternative definition of the Poincaré map, one that is most suitable to fast accelerating solutions, may aid to improve the accuracy of the identification process. Additionally, there may also exist slow diverging periodic solutions that initially form patters on the map, and later degenerate into chaos. As in the upper-left inset in Figure 5.10, such type of behaviors may be included in those captured by the automatic procedure. Finally, note that the identification algorithm only provides an approximate prediction of the structures existing on the surface of section, but, does not guarantee the recognition of all actual patterns (e.g., upper-left inset of Figure 5.6). Figures 5.5 - 5.10 provide a concise representation of the informations for over 30000 Poincaré maps and preliminarily substantiate the efficacy of an automatic scheme for islands detection.

The simulation campaign demonstrates a viable procedure for the quick identification of candidate periodic solutions through the recognition of map patterns for several configurations of the system, including a variation of the mass distribution and reference orbit.

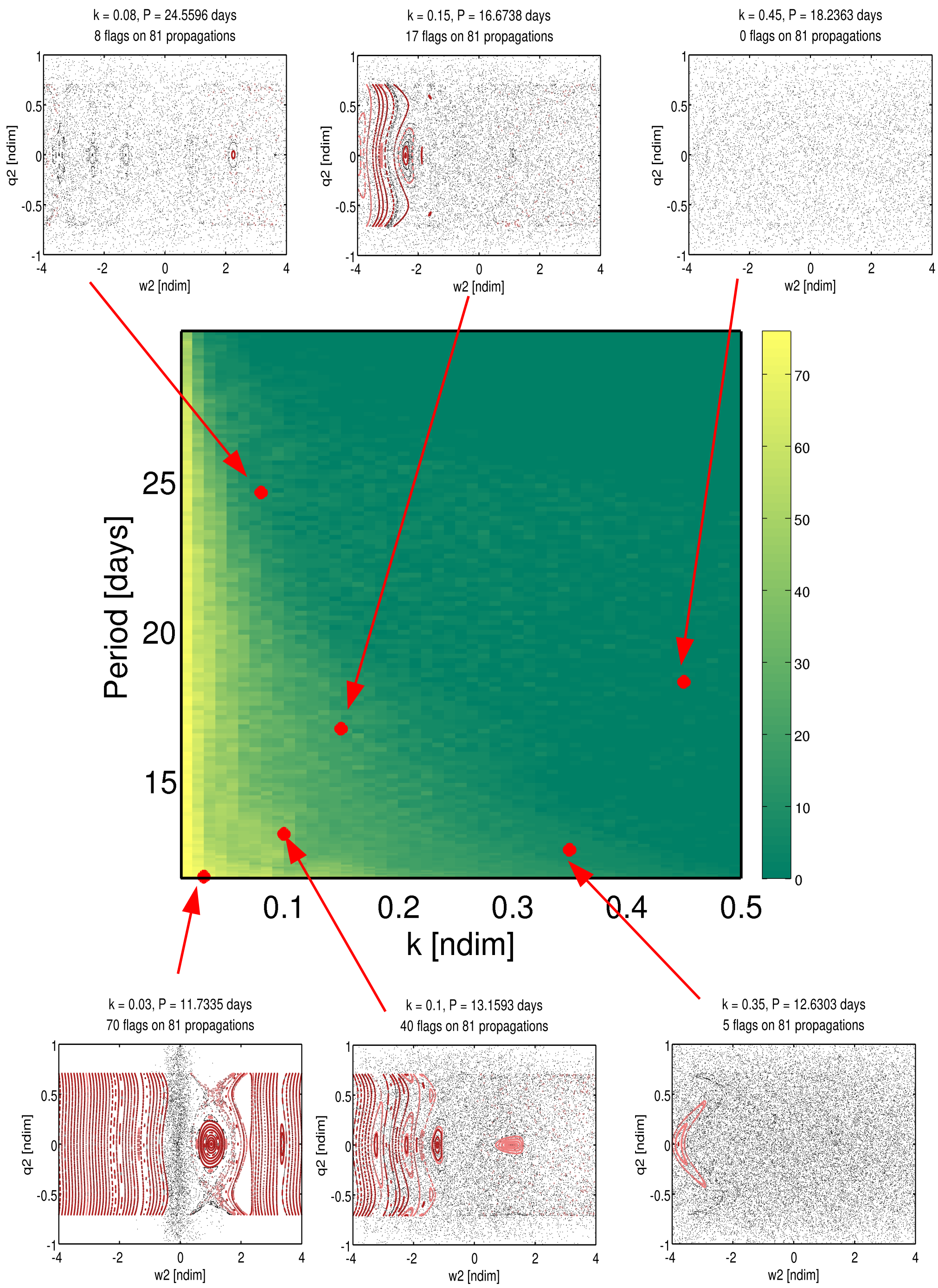

Figure 5.5. Automatic statistical summary of several Poincaré maps for different disk-like satellites (identified by the inertia ratio, k) along different Earth-Moon L_1 Lyapunov orbits (identified by the orbital period, P). The color scale represents the number of propagations possibly associated to ordered structures on a single Poincaré map.

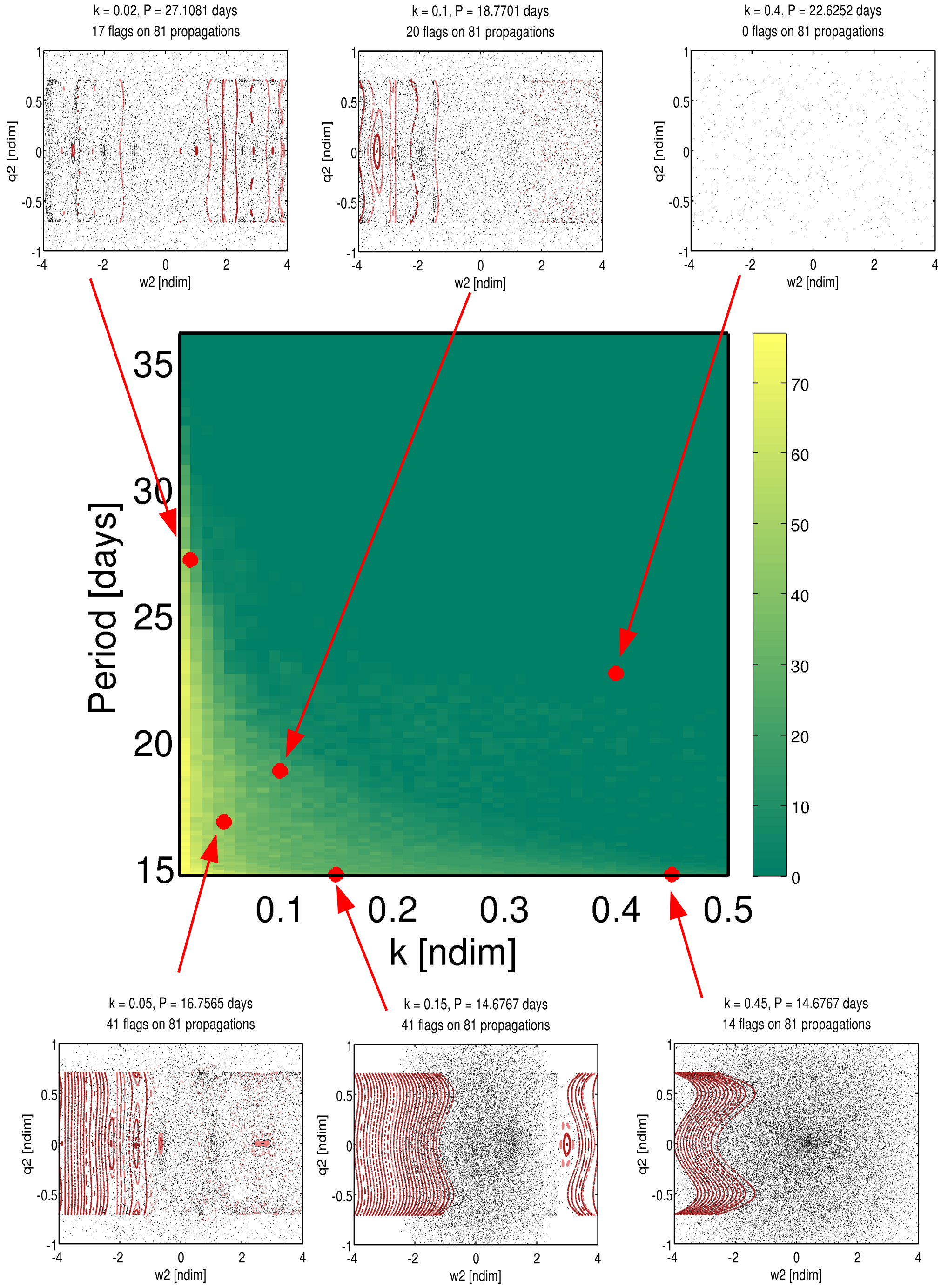

Figure 5.6. Automatic statistical summary of several Poincaré maps for different disk-like satellites (identified by the inertia ratio, k) along different Earth-Moon L_2 Lyapunov orbits (identified by the orbital period, P). The color scale represents the number of propagations possibly associated to ordered structures on a single Poincaré map.

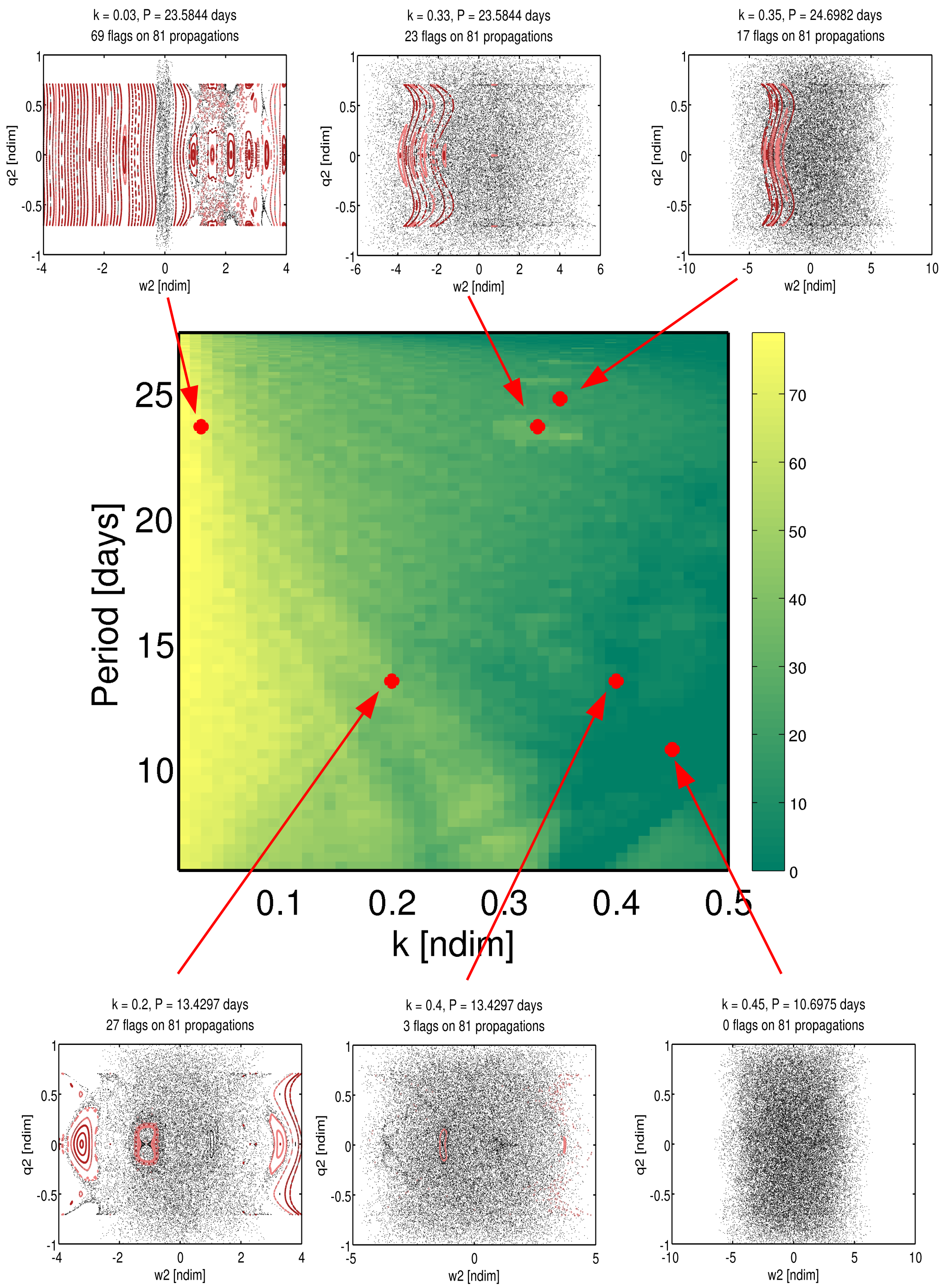

Figure 5.7. Automatic statistical summary of several Poincaré maps for different disk-like satellites (identified by the inertia ratio, k) along different Earth-Moon distant retrograde orbits (identified by the orbital period, P). The color scale represents the number of propagations possibly associated to ordered structures on a single Poincaré map.

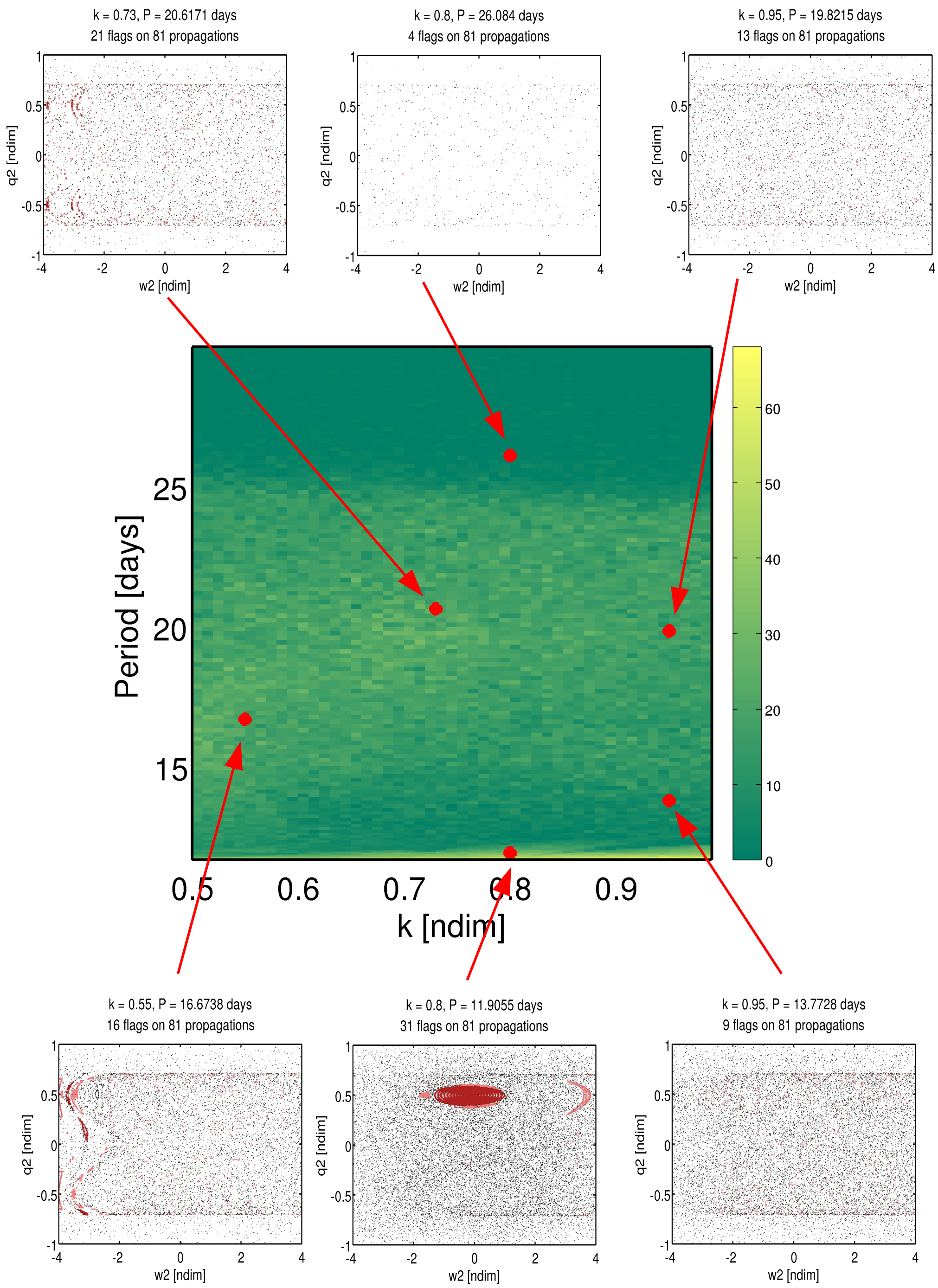

Figure 5.8. Automatic statistical summary of several Poincaré maps for different rod-like satellites (identified by the inertia ratio, k) along different Earth-Moon L_1 Lyapunov orbits (identified by the orbital period, P). The color scale represents the number of propagations possibly associated to ordered structures on a single Poincaré map.

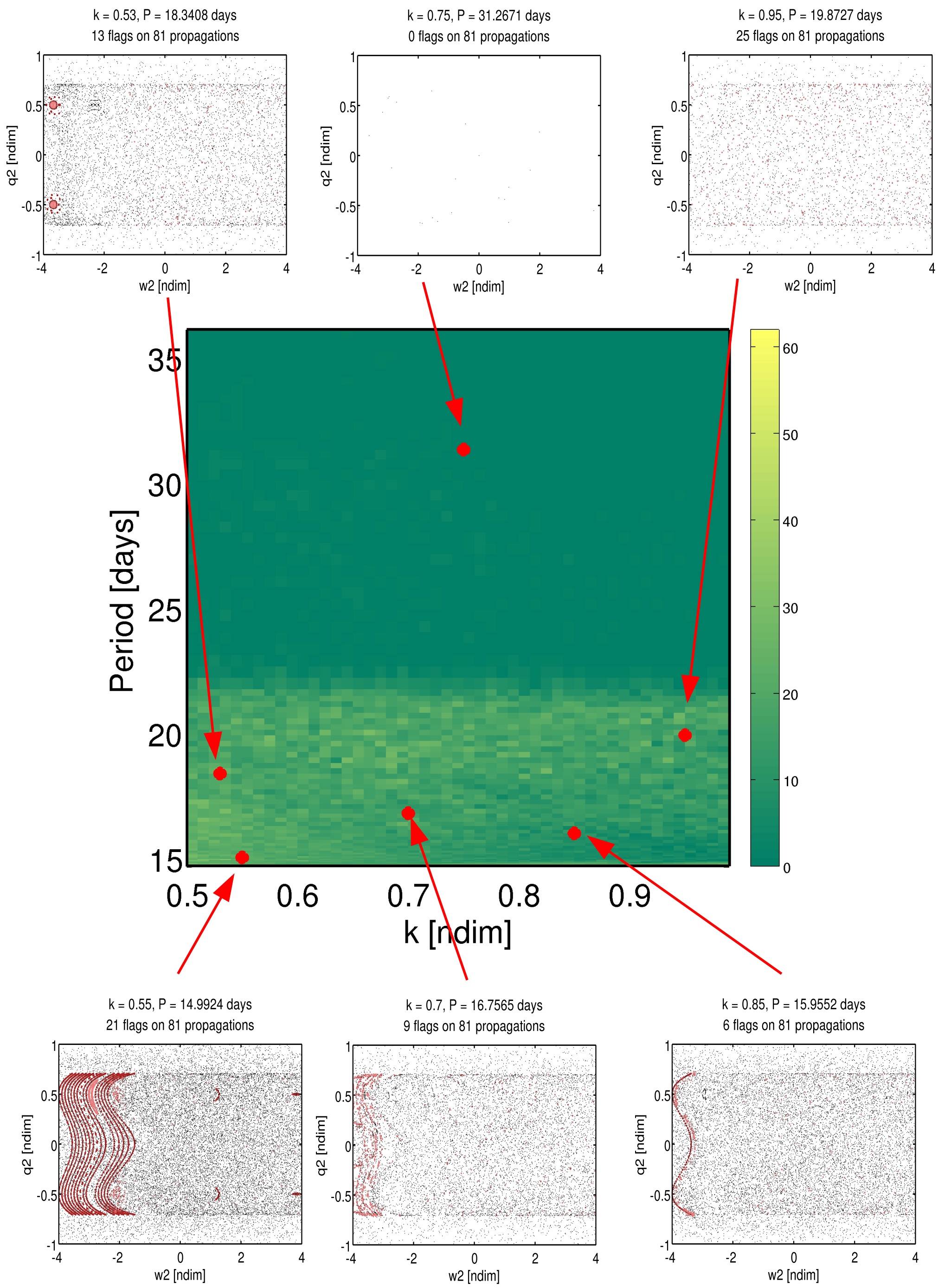

Figure 5.9. Automatic statistical summary of several Poincaré maps for different rod-like satellites (identified by the inertia ratio, k) along different Earth-Moon L_2 Lyapunov orbits (identified by the orbital period, P). The color scale represents the number of propagations possibly associated to ordered structures on a single Poincaré map.

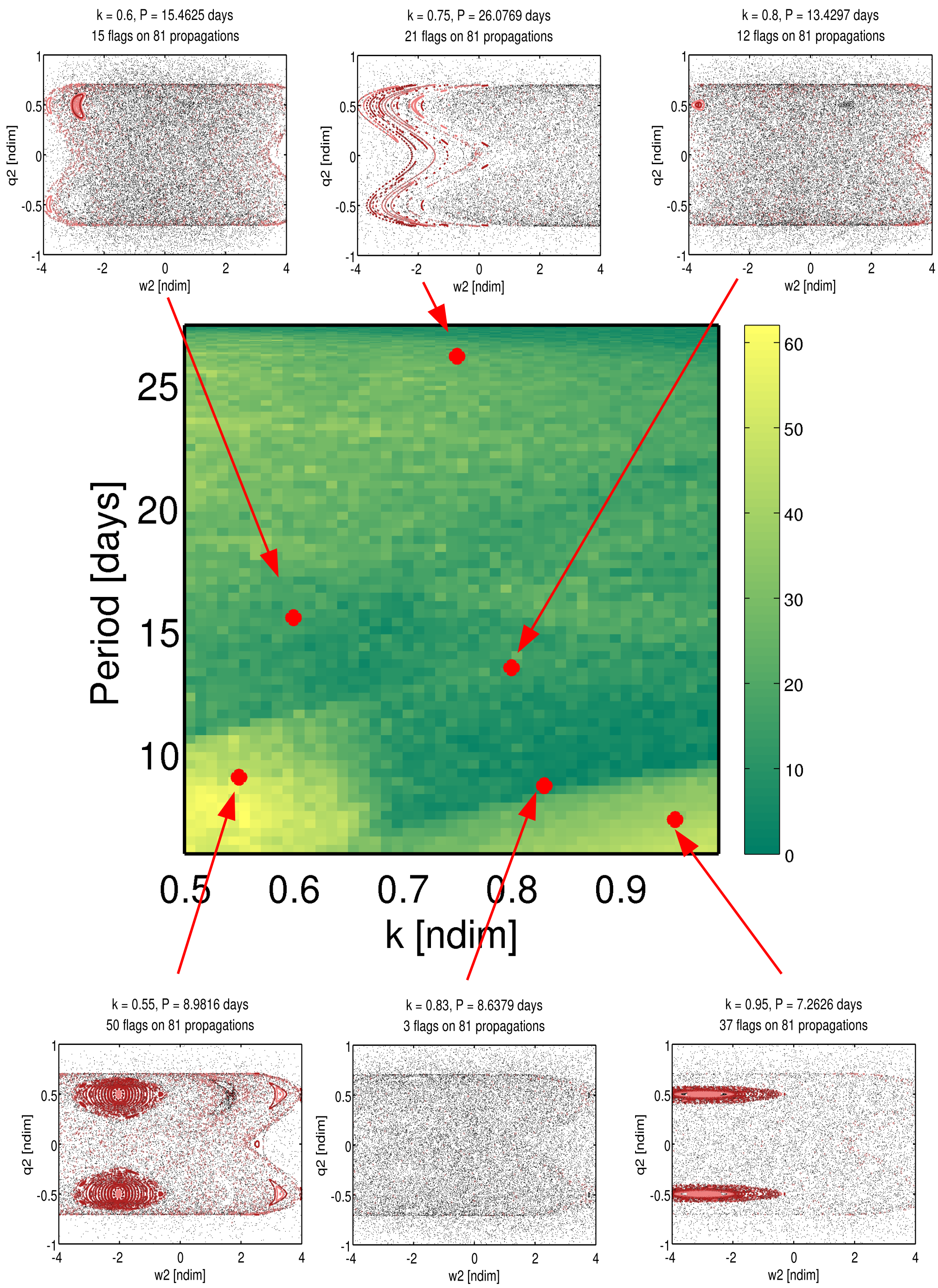

Figure 5.10. Automatic statistical summary of several Poincaré maps for different rod-like satellites (identified by the inertia ratio, k) along different Earth-Moon distant retrograde orbits (identified by the orbital period, P). The color scale represents the number of propagations possibly associated to ordered structures on a single Poincaré map.

5.4 Representative Orbit-Attitude Families of Periodic Planar Solutions

To conclude the identification process of orbit-attitude periodic solutions, the combination of an approximate attitude periodic motion identified by visible structures on a Poincaré map, and a reference periodic trajectory produces a guess for an orbit-attitude periodic solution that is corrected via a multiple shooting algorithm.

Select three representative scenarios: a rod-like vehicle moving on L_1 Lyapunov orbit, a disk-like spacecraft travelling along L_2 Lyapunov orbit, and a rod-like body in distant retrograde orbit motion. Considering these selected configurations, Figures 5.8, 5.6, 5.10 display regions in term of inertia ratio, k, and orbital period, P, that are potentially associated to the existence of ordered structures on the surface of section, for the current definition of the Poincaré map. Thus, select a combination of inertia ratio and orbital period that corresponds to the detection of some distinguishable patterns by the automatic statistical identification algorithm, and compute the corresponding Poincaré map. For example, select the combination $k = 0.8$ and $P = 11.91$ days for a rod-like spacecraft and L_1 Lyaponov orbit, matching with the Poincaré map depicted in the lower-central inset of Figure 5.8. A magnified view of the chosen island structure is portrayed in Figure 5.11(a), for clarity. As indicated by the red arrow in Figure 5.11(a), a guess for the initial angular velocity, one that yields an approximately periodic attitude response along the associated periodic orbit, is taken from the center of an island. For the current framework, the initial orientation for the spacecraft is implicitly determined by the definition of the Poincaré map, as discussed in the previous section. Finally, the predicted initial conditions are corrected into an precisely periodic motion via a targeting algorithm. Consistently to the adopted definition for the Poincaré map, the rotational motion is planar and it is described by the out-of-plane component of the body angular velocity relative to the inertial frame, that is displayed in Figure 5.11(b) as time evolution for one orbit revolution. The angular velocity profile, after the correction, is, in fact, periodic over one period of the L_1 Lyaponov orbit.

Representative periodic solutions are also computed for the remaining disk/L_2 Lyapunov and rod/DRO scenarios. The combination $k = 0.05$ and $P = 16.65$ days is selected for a disk-like spacecraft and L_2 Lyaponov orbit, which corresponds to the Poincaré map depicted in the lower-left inset of Figure 5.6. Several patterns are evident and successfully detected on the surface of section for this configuration, among them, the two-islands chain that is portrayed in Figure 5.12(a) is chosen for further examination. The two centers of the chain reflect a period-double solution: the rotation of the spacecraft is periodic over two revolution of the reference orbit. This map is also representative of a fairly large L_2 orbit, one that is outside of any approximately linear regime. The red arrow in Figure 5.12(a) marks, again, the guess for the initial angular velocity, that is next corrected to produce a periodic motion. Figure 5.12(b) displays the converged solution as angular velocity time history. It is immediate to observe that, the initial angular velocity repeats precisely after 2 periods of the reference orbit, as expected. Similarly, the pair $k = 0.8$ and $P = 13.42$ days is selected for a rod-like body and a distant retrograde orbit. The corresponding Poincaré map is visible in the upper-right inset of Figure 5.10, whereas a zoomed view for the island of interest (one that is detected by the automatic identification algorithm) is presented in Figure 5.13(a). In Figure 5.13(a), the red arrow points to an angular velocity, $\omega_2 \approx -3.75$, that is used as initial guess to compute the periodic attitude solution (see Figure 5.13(b) for the final angular velocity time profile along the orbit).

The selected orbit-attitude periodic solutions do not exist isolated but they are part of a larger dimensional dynamical structure, i.e., a family. Families of periodic solutions are in general not directly apparent on a surface of section, but they can be constructed via numerical continuation of a single solution that, in fact, emerges on the map. Nearby to each of the identified orbit-attitude periodic solution there exist a similar periodic motion. Using a continuation process, e.g., natural parameter or pseudo-arc length, it is possible to sequentially step the motion through nearby periodic solutions. Accordingly, a continuous group of attitude periodic responses is obtained, such as in Figure 5.14(b) for a rod-like spacecraft and L_1 Lyapunov orbit, in Figure 5.15(b) for a disk-like spacecraft and L_2 Lyapunov orbit, and in Figure 5.16(b) for a rod-like spacecraft and distant retrograde orbit. In those figures, the blue curve marks the first member of the family, which is computed leveraging the initial guess from the map, whereas the purple curve denotes the last member currently available within the family. Note that, the purple member is not representative for the dynamical termination of the family; it may be possible to expand the families beyond the displayed range. In the current implementation of the continuation process, the periodic orbit is also adjusted at each step. Each profile of angular velocity in Figures 5.14(b), 5.15(b), and 5.16(b), matches a distinct orbit, which is represented within Figures 5.14(a), 5.15(a), and 5.16(a), respectively. The identified orbit-attitude periodic solutions exist for a relevant portion of the corresponding orbit family, and potentially indicate a valuable and flexible set of design options for incorporating periodic attitude behaviors into mission design for CR3BP orbits.

As revealed by a few representative examples, periodic solutions for the orbit-attitude dynamics are conveniently identified using Poincaré map for different configurations of the systems, that reflect various reference periodic orbits and spacecraft mass distributions. Poincaré mapping is a framework that can be easily extended to a variety of scenarios relevant for the orbit-attitude dynamics, others than the initial demonstrations presented.

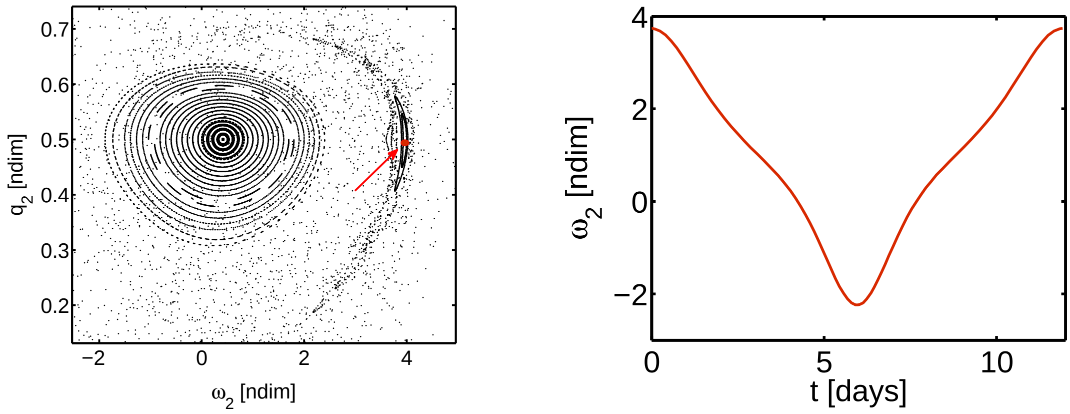

(a) Surface of section. Red arrow indicates initial guess for the periodic solution.

(b) Converged solution, profile for the body angular velocity relative to an inertial frame.

Figure 5.11. Representative attitude periodic response identified via Poincaré mapping for a L_1 Lyapunov orbit with period $P \approx 11.91$ days and rod-like spacecraft with inertia ratio $k = 0.8$.

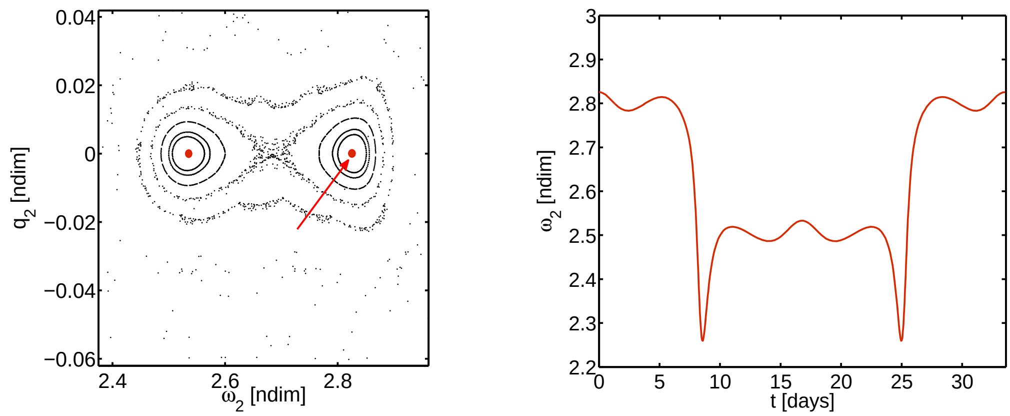

(a) Surface of section. Red arrow indicates initial guess for the periodic solution.

(b) Converged solution, profile for the body angular velocity relative to an inertial frame.

Figure 5.12. Representative attitude periodic response identified via Poincaré mapping for a L_2 Lyapunov orbit with period $P \approx 16.65$ days and disk-like spacecraft with inertia ratio $k = 0.05$.

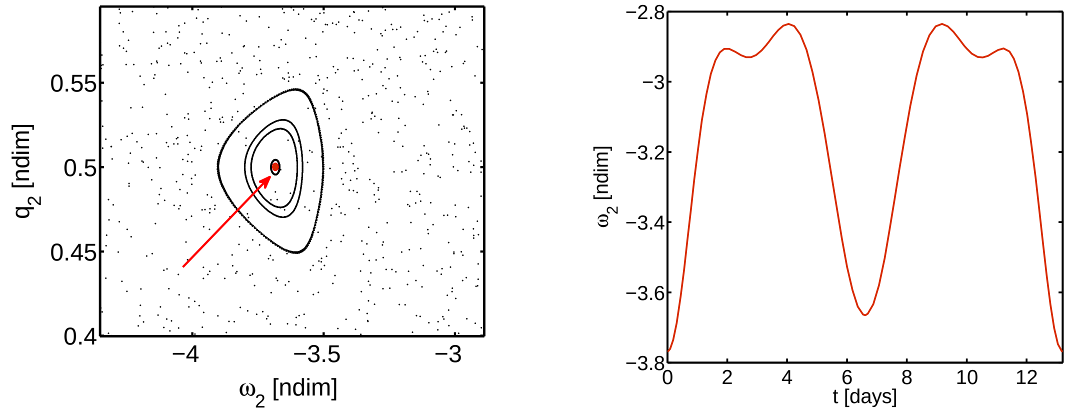

(a) Surface of section. Red arrow indicates initial guess for the periodic solution.

(b) Converged solution, profile for the body angular velocity relative to an inertial frame.

Figure 5.13. Representative attitude periodic response identified via Poincaré mapping for a distant retrograde orbit with period $P \approx 13.42$ days and rod-like spacecraft with inertia ratio $k = 0.8$.

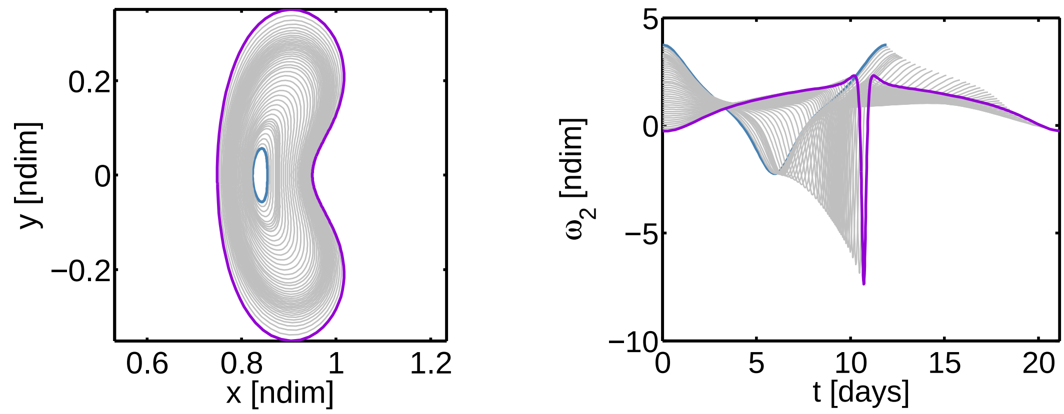

(a) Orbital components of the motion.

(b) Attitude components of the motion, in terms of the body angular velocity relative to an inertial frame.

Figure 5.14. Family of orbit-attitude periodic solutions identified via Poincaré mapping for a rod-like spacecraft with inertia ratio $k = 0.8$, travelling along $L1$ Lyapunov orbit.

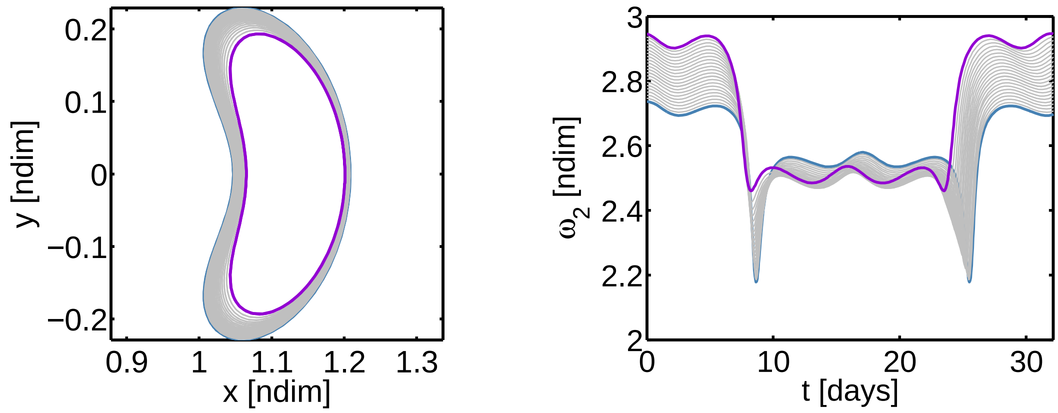

(a) Orbital components of the motion.

(b) Attitude components of the motion, in terms of the body angular velocity relative to an inertial frame.

Figure 5.15. Family of orbit-attitude periodic solutions identified via Poincaré mapping for a disk-like spacecraft with inertia ratio $k = 0.05$, travelling along $L2$ Lyapunov orbit.

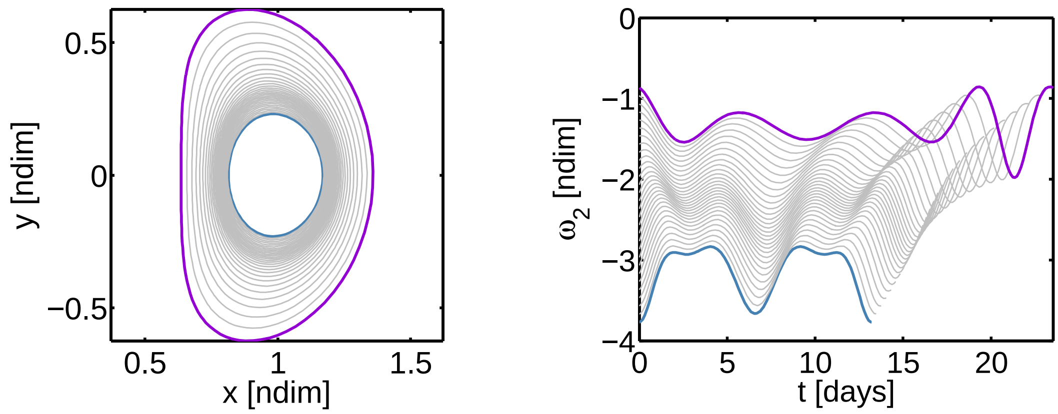

(a) Orbital components of the motion.

(b) Attitude components of the motion, in terms of the body angular velocity relative to an inertial frame.

Figure 5.16. Family of orbit-attitude periodic solutions identified via Poincaré mapping for a rod-like spacecraft with inertia ratio $k = 0.8$, travelling along distant retrograde orbit.

5.4.1 An Example of an Elementary Orbit-Attitude Stable Solutions on a Distant Retrograde Orbit

Distant retrograde orbits have been recently proposed for important mission applications in the Earth-Moon system, such as crewed orbiting infrastructures and redirected natural bodies. One of the presented representative solutions corresponds to a marginally stable rotational motion for a rod-like spacecraft that travels along a distant retrograde orbit. Adding a marginally stable periodic attitude profile to a marginally stable DRO of the same period generates a fully marginally stable orbit-attitude coupled solution. Such solution is particularly valuable to obtain a configuration that is likely to remain naturally bounded relative to the reference path, not only for the orbital motion but also for its orientation evolution. It is, therefore, beneficial to further examine the family of solution portrayed in Figure 5.16.

The linear stability of distant retrograde orbits in the Earth-Moon CR3BP is well-know. Excluding nonlinear and resonance effects, a DRO trajectory is marginally stable for any orbital period lower than approximatively 27 days [85]. Accordingly, all the orbits displayed in Figure 5.16(a) are marginally stable. To investigate the stability properties for the selected attitude periodic motion, one that is associated to such orbits, the eigenvalues corresponding to the attitude modes are plotted in Figure 5.17, as they evolve throughout the available portion of the family. The attitude motion along a fixed reference orbit is marginally stable when the corresponding eigenvalues reside on the unitary circle. According to Figure 5.17(a), such criteria is satisfied for the most part of the family, which indicates a large majority of marginally stable attitude solutions for a fixed reference orbit.

The corrected solutions in Figure 5.16 are essentially a periodic pitch motion of the axis of symmetry of the vehicle relative to the CR3BP x-axis. A schematic of this behavior appears in Figure 5.18(a). Referring to location (A) in the figure, the symmetry axis is initially aligned with the x-axis; then, the spacecraft completes a 180 degree rotation about the vector normal to the orbital plane during the first

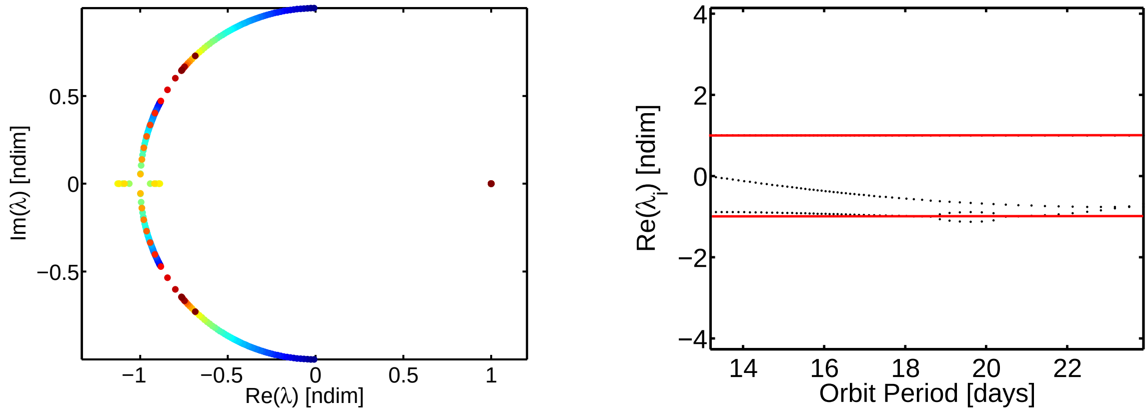

(a) Attitude eigenvalues in the complex plane. Colors from blue to red describes an increasing orbital period.

(b) Real component of the attitude eigenvalues as function of the orbital period.

Figure 5.17. Stability structure for a selected orbit-attitude family of solutions for a rod-like spacecraft with inertia ratio $k = 0.8$, travelling along distant retrograde orbit.

quarter of orbit (location (B) in Figure 5.18(a)). After a half orbit, i.e., location (C), the body has rotated 360 degrees, such that the axis of symmetry is again aligned with the x-axis. This type of behavior repeats over another half orbit and the orientation history of the vehicle is periodic, as visible in Figure 5.18(a). The angular velocity is also repeated at the return to the initial configuration. Relative to the radial direction toward the Moon, the minimum and maximum axis of inertia of the vehicle alternates in a periodic fashion. That also corresponds to a monotonically decreasing precession angle, as plotted in Figure 5.18(b). Quite interestingly, for the given DRO and inertia ratio, this behavior reflects a marginally stable configuration in the CR3BP, as evidenced by the existence of an island of quasi-periodic motion surrounding this solution on the Poincaré map. Figure 5.19 portrays the continuation of the initial angular velocity throughout a portion of the DRO family. The complete set of initial conditions for representative members of the family are given in Table 5.1. In the table, the distant retrograde orbit is identified by the coordinate of the x-crossing on the left of the Moon; that uniquely identifies the DRO trajectory

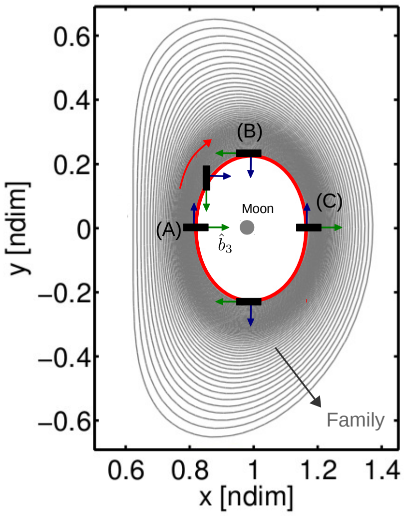

(a) Schematic of the attitude profile. In red a DRO with period $P = 13.22$ days. In gray, DROs that can be associated with the same qualitative behavior.

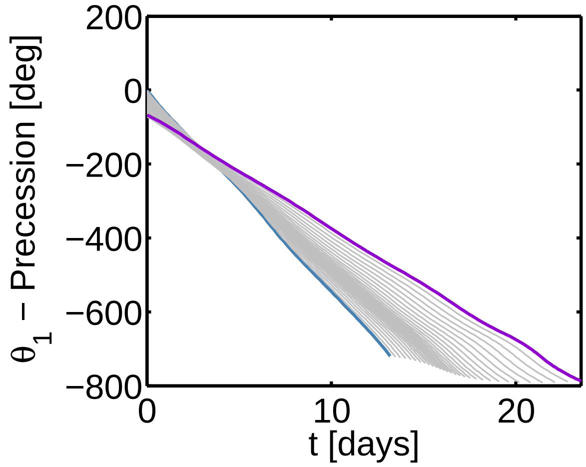

(b) Precession angle profile.

Figure 5.18. Marginally stable orbit-attitude family of solutions for a rod-like spacecraft with inertia ratio $k = 0.8$, travelling along distant retrograde orbit.

and, hence, the orbital components of the motion. The initial orientation is given as the components of the quaternion vector ${}^{i}\boldsymbol{q}^{b}(0) ={}^{r} \boldsymbol{q}^{b}(0)$, which assume the rotating frame to be aligned to the inertia frame at $t = 0$. The body angular velocity relative to the inertial frame completes the set of initial conditions that is necessary to fully reproduce the coupled orbit-attitude periodic solutions, knowing the period of the motion. Note that, because of truncation errors, a correction algorithm may be necessary to reproduced precisely periodic solutions given the initial states in Table 5.1. The attitude periodic solution is first identified along a DRO close to a 2:1 resonance with the Moon period, however, as Figure 5.19 reveals, such type of rotational motion is possible for a considerably large range along the DRO family, also including orbital periods that are not commensurate to the Moon revolution time. The attitude profile remains qualitatively unchanged as the orbit size and period increase. The marginally stability properties are retained along most of the family as well.

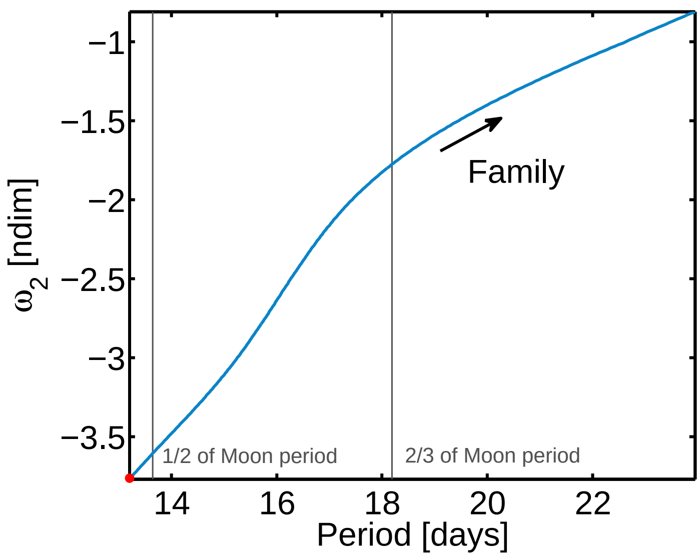

Figure 5.19. Initial angular velocity for different DROs. Red dot marks DRO with period $P = 13.22$ days.

The behavior that emerges from Figure 5.18(a) is simple and may be interpreted as an elementary torque-free motion. To further examine the origin of such dynamics and isolate any distinct driving factor, the attitude moments model is simplified at different levels. First, some reference solutions are generated in the current force model via initial angular velocity values, ω_2, that correspond to Figure 5.19. The resulting number of spacecraft rotations along one revolution of the orbit is plotted as reference black dashed lines in Figure 5.20. Figure 5.20(a) reflects the motion along a small DRO, Figure 5.20(b) along a large DRO. Next, the same initial conditions are propagated in a torque-free environment (blue curve in Figure 5.20). As the original initial values for the angular velocity are generally not commensurate to the DROs orbital period, the torque-free solutions are not exactly periodic. Corresponding to the dynamics denoted by the blue lines in Figure 5.20, the vehicle, in fact, does not complete an integer number of rotations in one revolution of the orbit. Finally, the gravity gradient torques exerted by the Earth and by the Moon are re-introduced, separately. As displayed in Figure 5.20(a), the action of the Moon alone seems sufficient to replicate a nearly periodic behavior along a small DRO. Along a large DRO, however, the moment due to the gravity gradient from the Moon appears negligible, and a nearly periodic solution is obtained by incorporating the Earth action only (see Figure 5.20(b)). In conclusion, although the resulting dynamics are linked to an intuitive application of a torque-free solution, relevant modifications of the initial angular velocity for each DRO trajectory are necessary to establish periodicity when the free motion is coupled to the CR3BP gravitational field. Such modifications may be required to compensate significant fluctuations of the angular velocity along the DRO, ones that are consequent to the gravity gradient exerted by the primaries; the rotation rate, ω_2, is, in fact, constant in an equivalent torque-free environment, and, therefore, different from the profile that is observed for a gravity gradient driven motion. Adjustments necessary to transition the torque-free motion to the CR3BP may be identified using Poincaré mapping and a differential correction algorithm. Eventually, within the CR3BP gravitational field, the relevance of the Earth or Moon contribution to this orbit-attitude family of periodic solutions is related to the size of the DRO.

Considering marginally stable distant retrograde orbits, Poincaré maps are especially useful to identify rotational profiles that are also characterized –within the adopted dynamical model– by nearby bounded motions. The presented orbit-attitude marginally stable solutions appear a simple rotating motion; nonetheless, the initial conditions to identify such precisely periodic solutions in an orbit-attitude CR3BP are not necessarily trivial. Poincaré maps, that aid the identification of this elementary marginally stable response, may also be applied to seek more complex attitude dynamics. In this investigation, the stability of orbit-attitude reference solutions is explored in the CR3BP framework; further stability analysis in higher fidelity models is warranted for practical mission implementations.

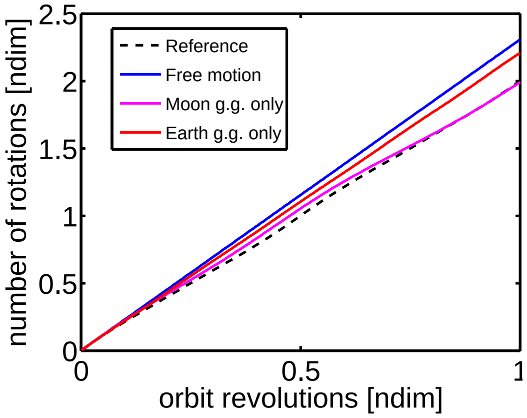

(a) Small DRO, $P \approx 13$ days.

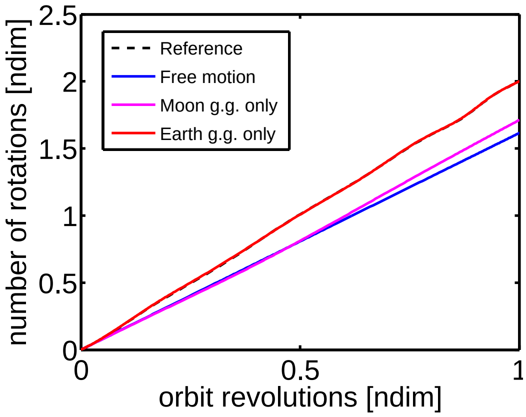

(b) Large DRO, $P \approx 22$ days.

Figure 5.20. Comparison of different force models for elementary orbit-attitude periodic solutions along DRO orbits.

Table 5.1. Initial conditions for an orbit-attitude family of solutions along distant retrograde orbits. The solutions assume an axisymmetric rod-like spacecraft with inertia ratio $k = 0.8$ in the Earth-Moon system.

$\boldsymbol{x}$ [ndim]	$\boldsymbol{q_1}$ [ndim]	$\boldsymbol{q_2}$ [ndim]	$\boldsymbol{q_3}$ [ndim]	$\boldsymbol{\omega_1}$ [ndim]	$\boldsymbol{\omega_2}$ [ndim]	$\boldsymbol{\omega_3}$ [days]	$\boldsymbol{P}$ [ndim]	$\boldsymbol{s}$ [ndim]
0.814	0.500	0.500	0.500	0.000	-3.768	0.000	13.201	1.000e+00
0.808	-0.503	0.497	0.497	0.000	-3.571	0.000	13.749	1.000e+00
0.801	-0.529	0.469	0.469	0.000	-3.387	0.000	14.313	1.000e+00
0.795	-0.550	0.444	0.444	0.001	-3.227	0.000	14.849	1.000e+00
0.789	-0.566	0.423	0.424	0.003	-3.097	0.000	15.324	1.000e+00
0.784	-0.579	0.407	0.407	0.005	-2.990	0.000	15.742	1.000e+00
0.779	-0.589	0.392	0.393	0.007	-2.897	0.000	16.134	1.000e+00
0.773	-0.599	0.376	0.378	0.009	-2.808	0.000	16.534	1.000e+00
0.768	-0.610	0.358	0.360	0.010	-2.715	0.000	16.982	1.000e+00
0.760	-0.624	0.333	0.336	0.012	-2.611	0.000	17.524	1.000e+00
0.750	-0.642	0.297	0.301	0.013	-2.491	0.000	18.217	1.000e+00
0.736	-0.663	0.247	0.250	0.012	-2.358	0.000	19.098	1.005e+00
0.718	-0.684	0.177	0.180	0.009	-2.221	0.000	20.182	1.004e+00
0.693	-0.701	0.090	0.091	0.003	-2.096	0.000	21.446	1.000e+00
0.658	-0.707	-0.013	-0.015	-0.007	-2.006	0.000	22.831	1.000e+00

6. BOUNDED LIBRATIONS: IDENTIFICATION OF ORBIT-ATTITUDE PERIODIC SOLUTIONS BY GRID SEARCH

6.1 Overview

For certain applications, the systematic variation of some mission parameters within a specified range may also prove useful to the identification of orbit-attitude periodic solutions. In the context of this work, a systematic exploration of the parameter space is referred as a grid search. During the implementation of a grid search, the motion is integrated for each combination of the selected parameters; next, quantities representative of the solution boundedness (e.g. a maximum values for selected Euler angles) are recorded for each propagation. In general, the initial attitude conditions are fixed and remain constant throughout the campaign of simulations. Eventually, the quantities selected to describe the dynamical behavior are plotted against the grid of configuration combinations; in the resulting map, regions in term of the selected parameters, emerge in connection to bounded responses on the sample integration time. This approach is mostly beneficial for the identification of periodic solutions as function of some mission variables for a given initial attitude configuration.

To demonstrate the application of grid search maps for the exploration of bounded dynamics, a representative scenario is constructed using L_1 and L_2 orbits. These families display a quasi-linear orbital response in the proximity of the equilibrium point; however, far from the equilibrium or libration point, the trajectories evolve under the effects of the fully nonlinear dynamics. Considering these orbits, that are well-understood in terms of orbital dynamics, a grid search approach is implemented as a way to deliver a global portrait of the rotational motions, without limiting the dynamical region of interest or considering specific point solutions. Bounded responses are sought via a grid of configurations that describes variation of the reference orbit and the spacecraft geometry.

Initially, the reference orbit and the spacecraft model are defined. The orbit is selected among the members of the L_1 or L_2 family, some of which are displayed in Figure 6.1. The L_1 family spans an amplitude A_y (maximum displacement in the y direction over the single orbit) from 12694 km to 332644 km, while the L_2 family extends from 11889 km to 181648 km in the A_y direction. Alternatively, the L_1 family covers a range in orbital period from 11.77 days to 31.72 days; the L_2 family of orbits ranges from 14.69 days to 26.49 days. The spacecraft model is represented by three

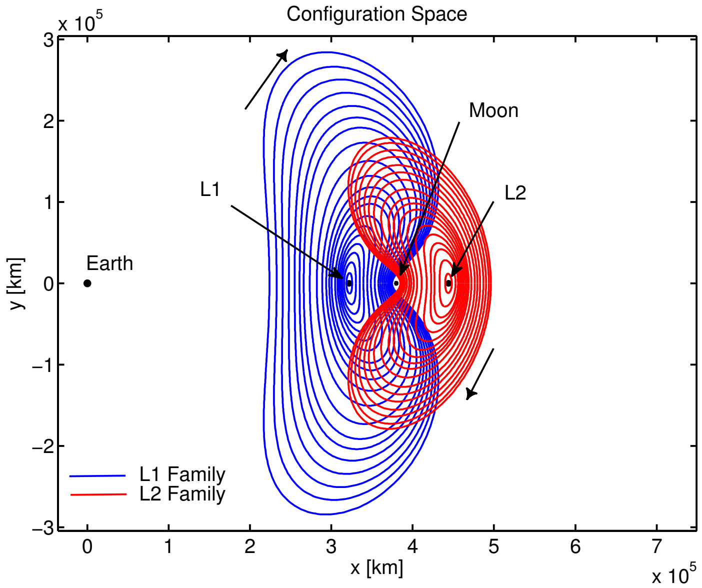

Figure 6.1. Lyapunov families about the equilibrium point L_1 and L_2.

inertia moments in the principal body directions, written as

$$k_1 = \frac{I_3 - I_2}{I_1} \tag{6.1}$$

$$k_2 = \frac{I_1 - I_3}{I_2} \tag{6.2}$$

$$k_3 = \frac{I_2 - I_1}{I_3} \quad , \tag{6.3}$$

where I_1, I_2, I_3 are the moments of inertia in the body $\hat{\boldsymbol{b}}_1$, $\hat{\boldsymbol{b}}_2$, and $\hat{\boldsymbol{b}}_3$ directions, respectively. By definition, any inertia ratio k_i cannot be greater than 1 or smaller than -1. The inertia ratios, k_i, control the rotational dynamics regardless of the body shape, and the outcome is independent of the actual physical geometry of the spacecraft. However, to facilitate visualizing the physical implications of k_i, the spacecraft is assumed, without limiting the results, to be a rectangular plate lying in the orbital plane of the primaries. The plate possesses a uniform distribution of mass and the $\hat{b}$-frame is attached to the center of mass of the structure. The sides of the rectangle are aligned with the coordinates axes of the $\hat{b}$-frame. Thus, the $\hat{b}$-frame also represents the principal inertia axes. Given this configuration, $k_3 = 1$ represents a rod aligned along $\hat{\boldsymbol{b}}_{\mathbf{1}}$ (the $\hat{\boldsymbol{b}}_{\mathbf{2}}$ dimension disappears), $k_3 = -1$ represents a rod aligned along $\hat{\boldsymbol{b}}_{\mathbf{2}}$ (the $\hat{\boldsymbol{b}}_{\mathbf{1}}$ dimension disappears) and $k_3 = 0$ denotes a square plate. Varying the value of k_3 from 0 to 1, or -1, continuously stretches the initial square to a rectangle and eventually to a rod.

Next, the initial conditions and the grid search map are specified. The spacecraft is located on the line through P_1 and P_2 (x-axis of rotating frame) at the initial time. For both L_1 and L_2 Lyapunov orbits, the vehicle starts on the left side of the equilibrium point, while the $\hat{b}$-frame is aligned with the CR3BP rotating frame. At $t = 0$, the body also appears to possess no initial angular velocity when observed in the rotating frame. Such initial conditions yield planar dynamics, as the displacements and the rotations of the vehicle will only occur in the orbital plane of the attracting bodies. In such a case, assuming the $\hat{b}$-frame to be aligned with the body principal directions, only the inertia ratio k_3 defined in eq. (6.3) (rather than the entire inertia tensor) is required to describe the rigid body distribution of mass. Maintaining fixed the initial conditions, different simulations are completed by varying the reference orbit along the members of the family and by testing different spacecraft topologies via the variation of k_3 within the range $[-1, 1]$. In a set of infinite many combinations, this specific set of initial conditions is preferred because the principal axis of minimum inertia (for $k_3 > 0$) is initially aligned with Earth-Moon line, which would represent a stable configuration if the spacecraft were to be artificially maintained along the same line. An increment of the initial pitch angle (defined as the angle between the

$\hat{\boldsymbol{b}}_1$ and the x positive direction of the rotating frame), currently $\phi(t{=}0) = 0$ deg, would more likely trigger a diverging response. Similarly, as the spacecraft moves along the orbit, the vehicles crosses the lunar neighborhood, which appears as a more sensitive dynamical environment. Maintaining fixed the initial states, a large number of simulations are completed by varying the body shape (k_3) and the reference Lyapunov orbit. Since each Lyapunov orbit is uniquely represented by its amplitude in the y direction of the rotating frame (A_y), the results are represented in terms of a A_y versus k_3 map. In this context, a grid search map essentially is a visual display of regions where the orientation remains aligned with respect to the CR3BP rotating frame and, in contrast, regions where the orientation is changing relative to such a frame. Specifically, in planar dynamics, the pitch angle ϕ is the only angle necessary to describe the spacecraft attitude. Thus, the attitude maps reflect the time history for ϕ over one or more revolutions. On the map, the maximum pitch angle in the orientation history is reported by colors coding; a cut-off might be applied for a maximum value over an arbitrary threshold. For brevity, the grid search approach is first presented on this simple representative scenario, nonetheless, other, possibly more complex, configurations may also be explored via systematic analysis of the system parameters. For example, the application of a grid search approach to a more complex scenario is demonstrated later in this chapter, aiding the identification of orbit-attitude periodic solutions for a spacecraft travelling along three-dimensional halo orbits and involving the mapping of rotations about three different axes.

6.2 Regions of Bounded Motion in Grid Search Maps for L_1 Lyapunov Orbits

Among the two Lyapunov families considered, the first map to be produced explores the planar Lyapunov orbits about L_1. Figure 6.2 represents the global response in ϕ, over one revolution, for each Lyapunov reference orbit.

Considering the map in Figure 6.2, areas in terms of orbit amplitude, A_y, and inertia ratio, k_3 are colored differently. Darker coloured regions correspond to conditions of motion where the body frame stays closely aligned with the rotating frame of the CR3BP, over one revolution. The darkest color corresponds to a rotation relative to the initial conditions of 0 deg ($\phi = 0$ deg for all the simulation time). However, a vehicle with fixed orientation relative to the $\hat{r}$-frame is rotating about 13 deg/day in the Earth-Moon system relative to an inertial observer, such as the $\hat{\imath}$-frame. For instance, over a Lyapunov orbit with period of 11 days, a spacecraft which maintains a fixed orientation in the $\hat{r}$-frame, actually undergoes a rotation of 143 deg per revolution as observed from the $\hat{\imath}$-frame. Therefore, dark areas predict a bounded response in the attitude as observed relative to the CR3BP rotating frame. Conversely, lighter areas are regions where the spacecraft orientation, in terms of pitch angle, is changing significantly relative to the CR3BP rotating frame. The lightest color on the map highlights angles greater than 90 deg relative to the initial orientation over one revolution. The color-code, therefore, is employed to rapidly identify regions, in terms of the grid search parameters, that result into bounded behaviors, accordingly to the map definition.

From the map in Figure 6.2, three clear regions of bounded responses over one orbit period appear; the expression "stable" is employed for a bounded response in the pitch angle ϕ as measured relative to the $\hat{r}$-frame. Thus, a first "stable" zone is the vertical band centered around $k_3 = 0$. For $k_3 = 0$ the spacecraft is a perfect square and the gravitational torque (at the second order approximation) is zero, supporting the "stability" of this region. A second region of bounded motions is the dark band near $A_y = 0$ km and $k_3 > 0$ (the bottom-right part of the plot); this region corresponds to the dynamical region investigated by Wong, Patil and Misra in [12], who examine quasi-linear orbits as a reference path. On a quasi-linear Lyapunov orbit, the oscillations of the pitch angle have limited amplitude as long as the minor inertia axis is initially aligned with the line through the primaries; in the given kinematic framework, that orientation corresponds to a positive k_3 value. Figure 6.3 shows a

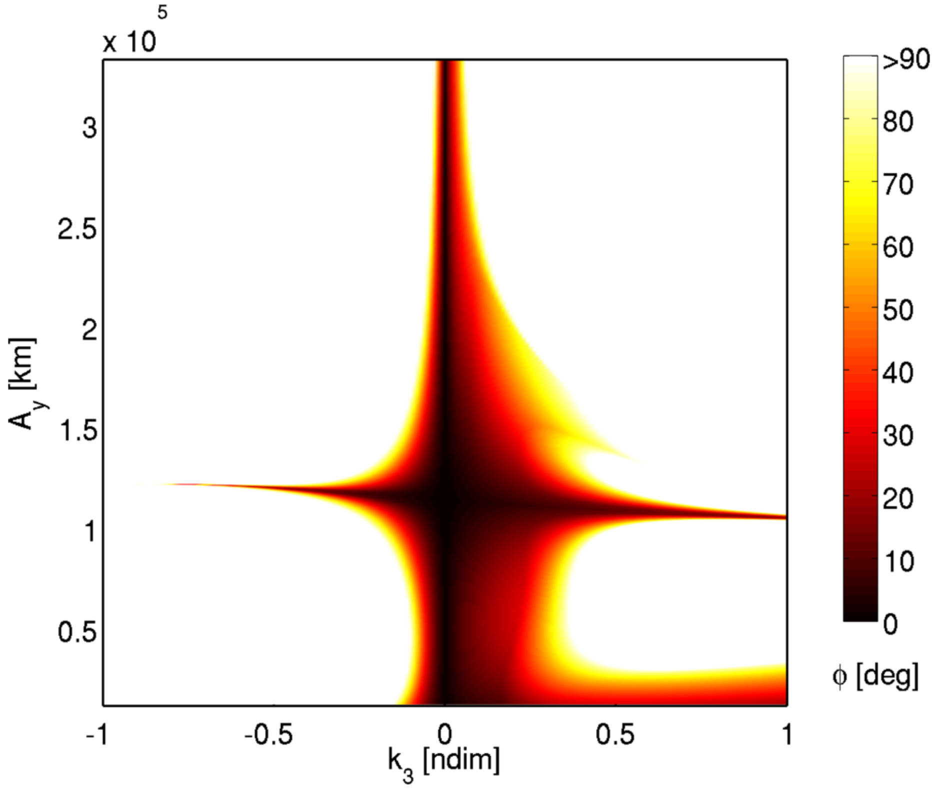

Figure 6.2. Maximum response in ϕ (precession relative to the x-axis of the rotating frame) across the L_1 Lyapunov family (Earth-Moon System) over one revolution for different inertia ratios.

sample of quasi-linear Lyapunov orbits and the correspondent pitch angle solution. For the sake of completeness, a resonant condition in k_3 does exist in this motion regime [12]. Nonetheless, the amplitude of the oscillations grows quite slowly, such that the increment is not noticeable over one-period in a map and this particular region appears as "stable". As first observed by Knutson in [17], a completely opposite behavior arises when nonlinearities in the orbital motion are incorporated, i.e., when the orbital amplitude increases. This behavior corresponds to the lightest area on the right side of the map, that denotes an attitude history diverging from the initial orientation. As discussed by Guzzetti et al. [15, 16], the transition between the two regimes can be triggered as function of the orbit size as well as the body topology, but no specific characterization of the transition was previously provided. Moreover, it was postulated in [15, 16] that it was not possible to naturally maintain the initial alignment of the body frame relative to the rotating frame over large Lyapunov orbits for elongated structures. The map confirms the existence of such a transition and also better characterizes the phenomena. A clear picture of the dynamics was not necessarily apparent when only considering specific test cases, as accomplished in the previous investigations.

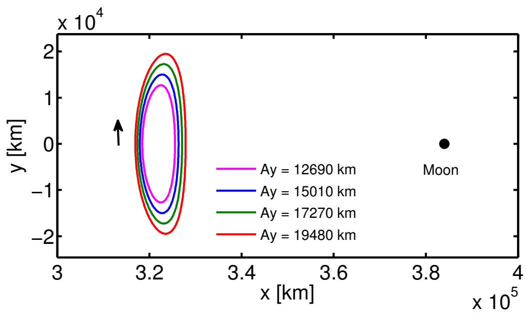

(a) Set of small L_1 planar Lyapunov orbits (Earth-Moon system).

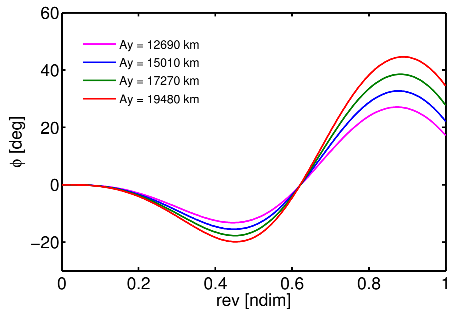

(b) Precession angle response.

Figure 6.3. Orbital and attitude response in the quasi-linear region ($k_3 = 0.6$) over one revolution. Courtesy of Knutson [20].

New information also emerges from the map in Figure 6.2. First, the shift from one regime to the other appears smooth. The smoothness of the transition suggests that small uncertainties in the investigated parameters do not lead to a drastic and sudden change in the attitude behavior. Second, quite unexpectedly, a third dark slightly diagonal band of small librations emerges from the map for a narrow set of Lyapunov orbits (near amplitudes $A_y \approx 1.1 \times 10^6$ km). Even in certain large reference orbits, spacecraft with specified inertia ratios, which lie on the dark line, remain relatively stable in orientation with respect to the CR3BP rotating frame. As visible on the map (light areas), the pitch response for elongated bodies ($|k_3| > 0.3$) along large Lyapunov orbits is generally unstable; however, the dark regions offer bounded solutions in a truly-nonlinear orbital dynamics model for a fairly wide range of k_3 values. Moreover, negative as well as positive values of k_3 are included; this observation implies that the spacecraft could be stretched in both the coordinate directions relative to the $\hat{b}$-frame and small rotations might still exist. Beyond the horizontal dark band, the spacecraft always rotates more than 90 deg from the initial condition, if it possesses a geometry sufficiently extended in the $\hat{\boldsymbol{b}}_{\mathbf{2}}$ direction, which is the direction initially orthogonal to the line through P_1-P_2. Different space structures, such as deep space gateway facilities or astronomical observatories [86], are proposed for flight in the vicinity of the Lagrangian points. The mass distribution of such architectures is unlikely axisymmetrical in the orbiting plan, yielding an inertia ratio k_3 certainly not zero. Such space structures or long-term facilities or habitats would be likely similar to those already flying near Earth, such as the International Space Station ($k_3 \approx 0.2$, [87]) or the Hubble Space Telescope ($k_3 \approx 0.6^*$).

The orbits involved in the horizontal "stable" zone about $A_y \approx 1.1\times10^6$ km (visible in the map in Figure 6.2) are depicted in Figure 6.4(a): they span an amplitude range A_y from 101108 km to 114621 km, one that corresponds to an interval from 17.57 days to 19.04 days in terms of orbital period. It is worth noting that this span of orbital periods is located in the neighbourhood of the 2/3 resonant ratio of the lunar period; a p/q resonant ratio implies that the spacecraft accomplishes q revolutions along the reference orbit (in the $\hat{r}$-frame) in the same time interval that the Moon requires to complete p orbits about the Earth (in the $\hat{i}$-frame). In such a resonance, the Earth, the Moon and the spacecraft return to the same inertial configuration after p lunar periods. Also, across this region an inversion of the direction of pitch rotation occurs after the close approach to the Moon at 0.5 revolutions. Consider the example from Figure 6.4(b) (which corresponds to $k_3 = 0.6$); a vehicle transiting along the smaller orbit in this amplitude region eventually rotates counter-clockwise (as observed in the rotating frame) after departing the x-axis at the crossing closest to the Moon. Conversely, the ultimate direction of rotation is clockwise, when the spacecraft is moving in the larger orbit in Figure 6.4(b). Between these opposite behaviours, the

[1]http://www.pha.jhu.edu/groups/hst10x, last visited May 2014

pitch dynamics seem to transition smoothly from one limit to the other, generating the set of bounded responses that characterize this zone. Also, the nature of the "stable" response in this region is highly nonlinear and significantly differs from what it is observed in the quasi-linear zone (as seen in Figure 6.3).

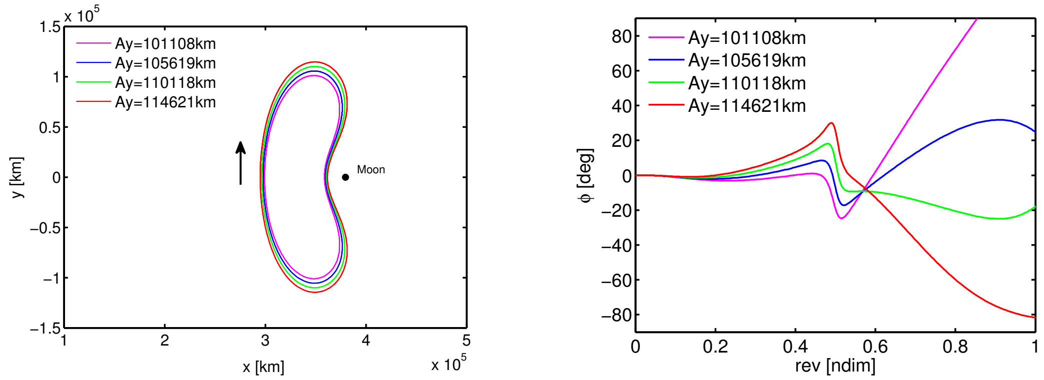

(a) Set of large L_1 planar Lyapunov orbits (Earth-Moon System).

(b) Precession angle response.

Figure 6.4. Orbital and attitude response in the dark horizontal band region ($k_3 = 0.6$) over one revolution. Courtesy of Knutson [20].

6.3 Additional Grid Search Maps for L_1 Lyapunov and L_2 Lyapunov Orbits

Thus far, regions of bounded motions emerge on the grid search map for the natural attitude dynamics across the L_1 family after one revolution along each orbit. Regions of bounded motion may, however, also exist for different observation windows or reference orbits.

For example, while the focus is maintained on the L_1 planar Lyapunov family, the observation time is increased to 2 revolutions. No correction to the orbit or attitude is applied over the 2 revs. As a result, the attitude map in Figure 6.5 emerges. Compared to the previous plot in Figure 6.2, an overall reduction of the dark "stable" areas is perceived; specifically, the central horizontal band is disappearing and the bottom-right region is squeezed by an inflating unstable light zone. The vanishing of the horizontal band is more pronounced on the left side of the map, which corresponds to $k_3 < 0$; such that this region is now nearby completely (besides a minimal trace of the horizontal band) dominated by unbounded responses. Additionally, the transition to unbounded librations along the edge of the central vertical band becomes sharper. Given the current framework for the analysis, a structure mainly elongated in the $\hat{b}_2$ direction necessarily undergoes a natural rotation greater than 90 deg over a longer period. Conversely, spacecraft whose major extension is identified by $\hat{\boldsymbol{b}}_{\mathbf{1}}$ (i.e., $k_3 >$ 0) still preserve some bounded solutions. However, it is noted that the bottom-right region, related to the pitch responses addressed by Wong, Patil and Misra [12], significantly reduces in size and alters in outline. The linear behaviour in Wong et al. [12] predicts an oscillatory response with limited amplitude, unless k_3 equals a critical value that triggers a resonance between the orbital frequency and the attitude librations. In a fully nonlinear regime, these predicted solutions hold true up to a certain amplitude of the quasi-linear orbits, as visible in Figure 6.2. Increasing the integration time reduces the maximum orbit amplitude that guarantees a rotation less that 90 deg over the observation interval. In addition, the region in the vicinity of the linear resonant k_3 value (i.e., $k_3 \simeq 0.36$ in the Earth-Moon system) appears more unstable than observed over the time window of one revolution, as deducible from the light bulge that penetrates in the bottom-right dark area of Figure 6.5, such that the latter zone almost splits in two regions.

Not only the integration time but the orbital reference corresponding to the map can also be changed. Thus, the same procedure and the same structure of the initial conditions yields similar depictions for the L_2 family. In this case, the family spans an amplitude range in A_y from 11889 km to 181648 km, which corresponds to a set of orbital periods from 14.69 days to 26.49 days. The resulting attitude map appears in Figure 6.6 for one revolution. Under the set of initial conditions investigated, there is no clear evidence of a central "stable" horizontal band in the

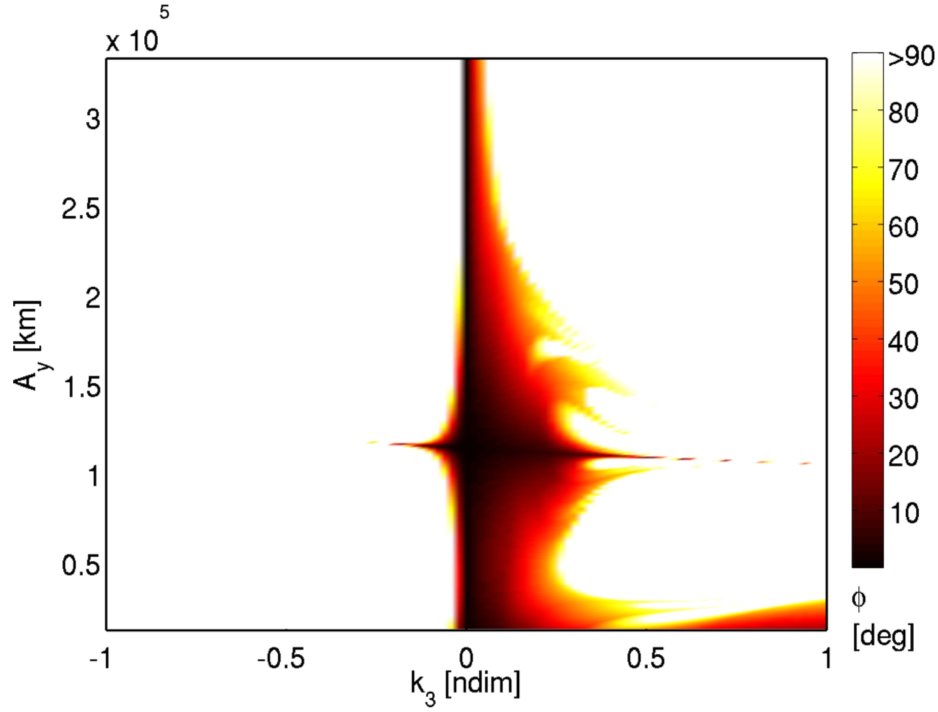

Figure 6.5. Maximum response in ϕ (precession relative to the x-axis of the rotating frame) across the L_1 Lyapunov family (Earth-Moon System) over two revolutions for different inertia ratios.

L_2 family; a more predictable portrait comes to light. This map is characterized only by the central vertical band associated with a value $k_3 = 0$ and the bottom-right region, corresponding to the quasi-linear behavior; however, the latter area covers a larger extension than its counterpart in the L_1 map. Both the attractors P_1 and P_2 are located on the same side relative to the orbit, thus, the dynamical behavior more closely resembles a single attractor regime. Additionally, extending the integration to 2 revolutions, new features emerge, as displayed in Figure 6.7. Over the longer period, the bottom-right area associated with the quasi-linear motion contracts, but a small double-spike-like region remains for larger A_y amplitudes. The overall double-spike-like region extends approximately from $A_y = 26800$ km to $A_y = 43800$ km, which locates this zone in the neighbourhood of the first bifurcation of the L_2 Lyapunov family (at $Ay \simeq 34140$ km). A similar outcome is also observed in the L_1 Lyapunov family; a double-spike-like region can be located within A_y = 28900 km and A_y = 18900 km on the map of Figure 6.5.

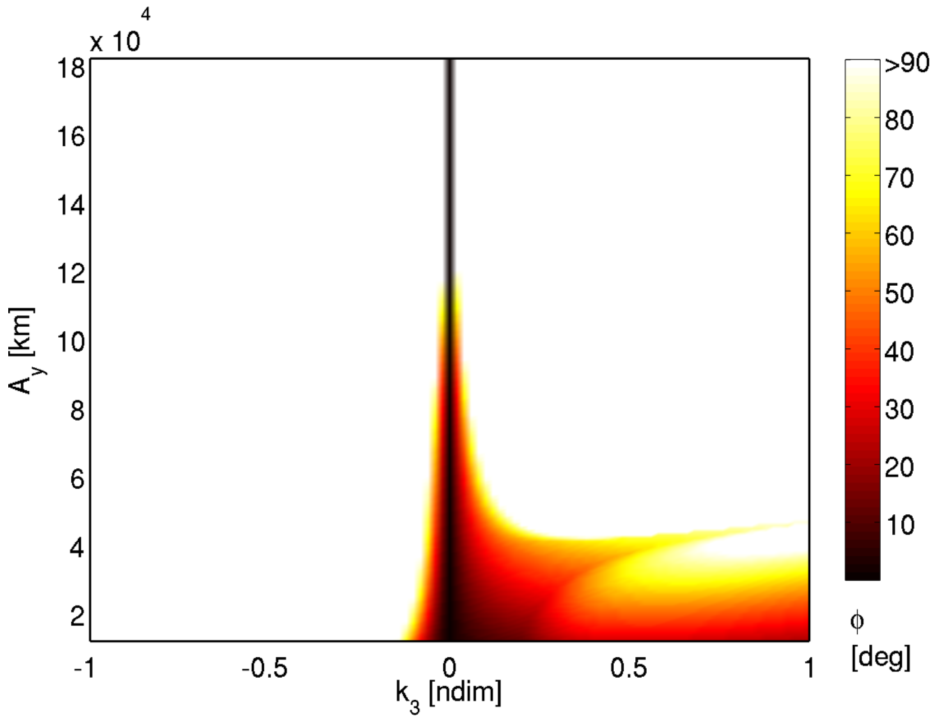

Figure 6.6. Maximum response in ϕ (precession relative to the x-axis of the rotating frame) across the L_2 Lyapunov family (Earth-Moon System) over one revolution for different inertia ratios.

Grid search algorithms are a straightforward approach that may be employed to investigate bounded solutions for a wide panorama of applications, including motions altered by perturbations to the reference orbit [19] or to the initial orientation of the vehicle [20], as well as spinning satellite dynamics [19].

6.4 A Relationship between a Region of Bounded Motion and Orbit-Attitude Periodic Solutions for L_1 Lyapunov Orbits

To deepen the insight into the dynamical behavior associated to regions of bounded response, that may emerge on a grid search map, further explorations are conducted.

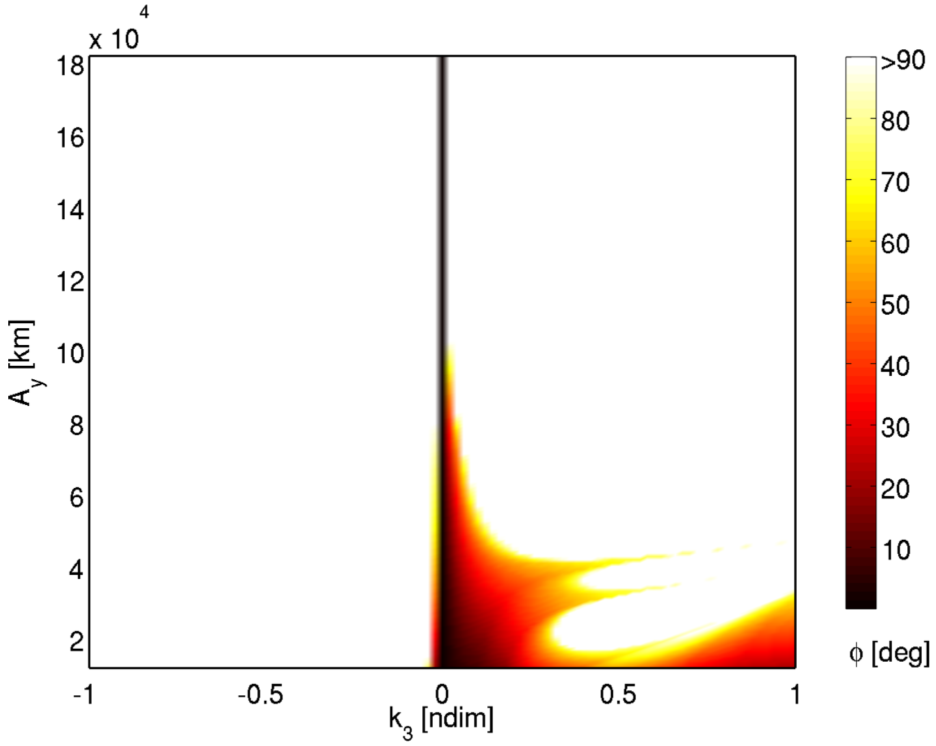

Figure 6.7. Maximum response in ϕ (precession relative to the x-axis of the rotating frame) across the L_2 Lyapunov family (Earth-Moon System) over two revolutions for different inertia ratios.

Accordingly, the analysis is initiated considering L_1 Lyapunov orbits, and a grid search map that is consistent with Figure 6.2. Observing that figure, the horizontal dark band on the map, one that reflects small librations relative to the rotating frame over one revolution of the nominal path, is investigated.

Regions of bounded motions in a grid search map, reflect a transition of the attitude dynamics that is may be linked to a transition of the orbital regime. The eigenvalue analysis along the family describes some of the mutations for the orbital dynamics nearby a reference orbit, ones that may correspond to the appearance of "stable" regions on the grid search map. Considering the L_1 Lyapunov family, for each member of this family of periodic orbits, it is possible to compute the monodromy matrix and the associated eigenvalues. Given the symplecticity of the monodromy matrix, the eigenvalues occur in reciprocal pairs: one real pair is associated with the existence of planar manifolds, one unitary pair is associated with the periodic nature of the orbit and the existence of a family, and one pair corresponds to the out-of-plane dynamics. For planar Lyapunov orbits, the latter pair determines the changes of the eigenstructure throughout the family. Such mutations are usually investigated because they correspond to orbital bifurcations, but the attitude behaviour may also relate to the eigenstructure. As apparent in Figure 6.8, the orbits forming the "stable" horizontal band in the attitude map displayed in Figure 6.2 corresponds to the vicinity of the second of the Lyapunov family bifurcations. Specifically, the system mutates from hyperbolic to non-hyperbolic as the considered pair of eigenvalues shifts from the real axis to the unitary circle in the Argand-Gauss diagram. It is noted that, also, the quasi-linear "stable" region (terminating roughly at $A_y \approx 27890$ km) encompasses one earlier bifurcation along the family (i.e., the first one at $A_y \approx 21640$ km). Generally speaking, bifurcations indicate zones where the system is subject to a change of the dynamical regime, thus, it is reasonable that this transition may be reflected in both the orbital and attitude motions. Additional investigations are, however, necessary to completely understand this mechanism.

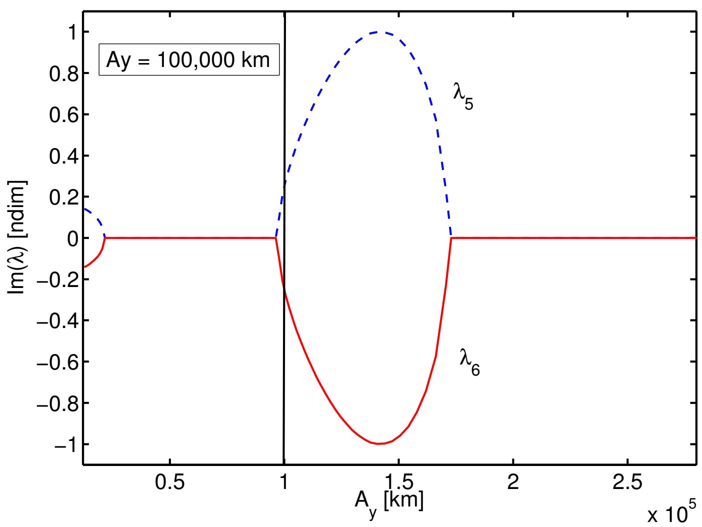

Figure 6.8. Out-of-plane eigenvalues of the L_1 planar Lyapunov family.

Selecting solutions within the horizontal "stable" band in Figure 6.2 for examination, the pitch angle time profile may be compared with known families of orbit-attitude periodic solution. Among the available orbit-attitude periodic motions, some of the curves within the family in Figure 6.9, most resemble the dynamics rendered by the horizontal "stable" region. The family in Figure 6.9 is generated for a satellite with inertia ratio $k_3 = 0.8$ that travels along L_1 Lyapunov orbit. Additionally, the pitch angle is zero at the crossings of the x-axis of the CR3BP rotating frame, which is consistent with the initial condition for the grid search map. Observing the pitch angle time response in Figure 6.9(a), a resemblance of the red curves to the solutions in Figure 6.4(b) is noted. Although Figure 6.4 and Figure 6.9(a) actually display the pitch dynamics for a different mass distribution, $k_3 = 0.6$ and $k_3 = 0.8$, respectively, the existing similarities indicate a possible link between a subset of orbit-attitude periodic solutions and the materialization of "stable" regions on a grid search map. A correspondence is also revealed in the angular velocity at the crossing of the x-axis of the rotating frame in the positive y direction. By definition, such angular velocity is initially equal to one for motions associated with the grid search map; interestingly, moving across the periodic members of orbit-attitude family computed for $k_3 = 0.8$, some solutions also display an angular velocity proximate to one at the positive x-axis crossing. As depicted in Figure 6.9(b), a unitary angular velocity at the crossing is encountered along a L_1 Lyapunov orbit with period $P \approx 18$ days. A L_1 Lyapunov orbit with period $P \approx 18$ days possesses an amplitude $A_y \approx 1.1 \times 10^6$ km, which matches the location for the horizontal "stable" region in Figure 6.2. Orbit-attitude periodic solutions nearby a period $P \approx 18$ days mostly resemble the pitch profile that is associated with the horizontal "stable" region (red curves in Figure 6.9(a)). Additionally, these solutions are consistent with the definition of the grid search and consistently position within the horizontal dark band on the map.

There is strong indication that the dynamics within one of the "stable" region on the L_1 Lyapunov grid search map is, in fact, representative of the dynamical neighborhood for a set of orbit-attitude periodic solutions throughout a range of spacecraft

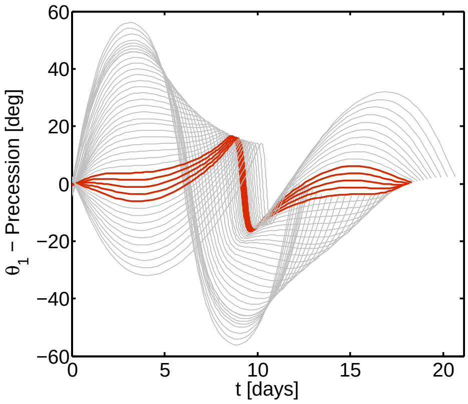

(a) Pitch angle history. The solutions that most resemble the dynamics in the grid search map horizontal "stable" region are colored in red.

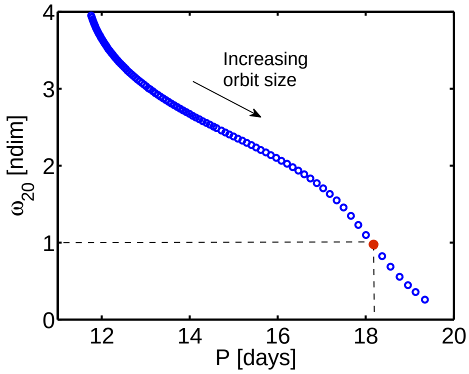

(b) Angular velocity at the positive crossing of the x-axis for different solutions within the family.

Figure 6.9. Family of orbit-attitude periodic solutions for a spacecraft with $k_3 = 0.8$ along L_1 Lyapunov orbit.

mass distributions. To verify such hypothesis, a set of solutions is computed and overlaid on the grid search map. First, take an initial periodic solution, e.g., for $k_3 = 0.8$, that locates within the "stable" region of interest, and thet is consistent with the grid search definition. Then, step onto a nearby motion by a small modification of the mass distribution, and re-converge the solution to be precisely periodic via, for instance, differential correction. By reiterating this process, which is a simple implementation of a continuation algorithm, a family of orbit-attitude solutions across different spacecraft mass configurations, represented by k_3, is obtained. The time evolution for the pitch angle for representative members of this family is portrayed in Figure 6.10(a). During the continuation process the reference orbit, as well as the angular velocity at the positive crossing of the x-axis, are free to vary; the orientation of the vehicle at the crossing is however constrained to be consistent with the grid search map. Figure 6.10(b) displays that, the angular velocity at the crossing of the x-axis of the CR3BP rotating frame (in positive y direction) only necessitates minimal adjustments during the continuation of the solution and closely align with the definition of the grid search. The family of orbit-attitude behviors obtained for different values of k_3 can, therefore, be overlaid to the grid search map by plotting the orbit amplitude, A_y, for representative members, as in Figure 6.11. The family of orbit-attitude periodic responses that is initiated at $k_3 = 0.8$ (indicated by the arrow in Figure 6.11) and continued for different inertia ratios, well aligns with the horizontal "stable" band that emerges in the map at $A_y \approx 1.1 \times 10^6$ km, for the interval of solutions computed. Thus, the horizontal region of bounded response at $A_y \approx 1.1 \times 10^6$ km appears to be a reflection of a set of orbit-attitude periodic motions throughout different spacecraft mass configurations.

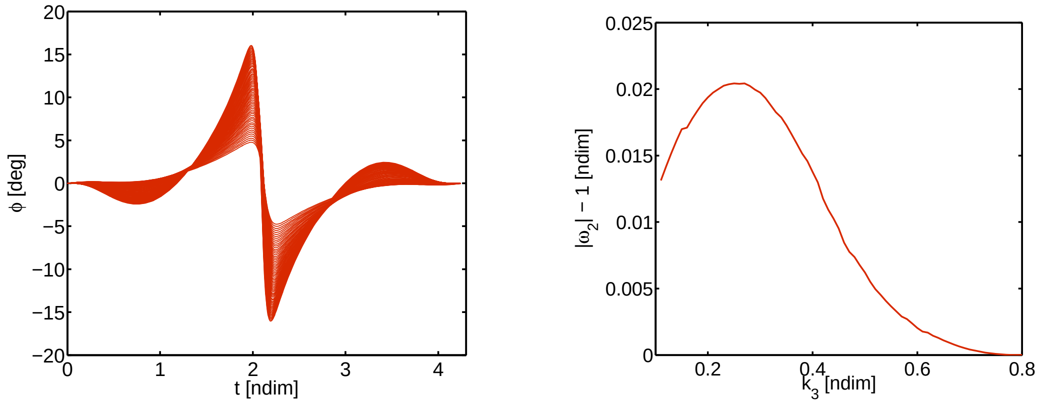

(a) Pitch angle.

(b) Out-of-plane angular velocity at the crossing of the x-axis for the rotating frame.

Figure 6.10. Continuation for different values for k_3.

The grid search approach is initially applied to the identification of system parameters that produce bounded solutions for some fixed initial conditions. Exploring the orbit-attitude dynamics along L_1 Lyapunov orbit, bounded responses emerge on the grid search map for non-intuitive regions in terms of orbit amplitude and inertia ratio. The further analysis for one of those regions, reveals that, the appearance of

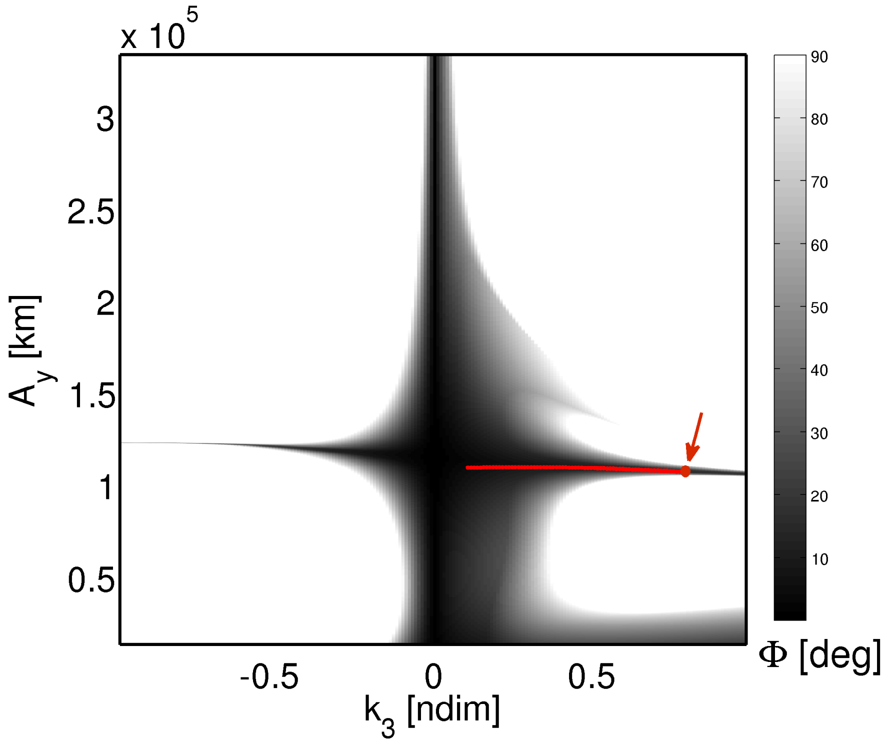

Figure 6.11. Comparison of the horizontal "stable" region with a family of orbit-attitude periodic solutions.

bounded motions on the grid search map may be directly related to the existence nearby of an orbit-attitude family of periodic solutions.

6.5 Application to Three-Dimensional Reference L_1 Halo Orbits

A grid search approach may also be employed in more complex scenarios, e.g., the dynamics along a three-dimensional reference orbit, to identify a set of bounded solutions that is possibly linked to orbit-attitude periodic behaviors.

Suppose to seek a precise initial guess for an orbit-attitude periodic solution using L_1 northern halo orbits in the Earth-Moon system as reference. Accordingly to the analysis presented by Wong et al. [12], bounded, oscillatory solutions are easily identified by selecting small linear halo orbits as reference path. Later results from Knutson [18], display, however, that the motion may be, in general, less oscillatory and less predictable when larger halo trajectory and nonlinear dynamics are considered. Within a highly sensitive nonlinear regime, the capability to identify bounded, possibly periodic solutions, is valuable. A grid search strategy is implemented to recover such solutions. Take a spacecraft that is initially located at the intersection of a halo orbit with the xz-plane as defined in the CR3BP rotating frame. Only consider the intersection where the velocity relative to the CR3BP rotating frame is directed toward the positive y-axis. The initial orientation of the vehicle is such that the body axes are aligned with the axes of the rotating frame, and there exist a null angular velocity relative to an observer fixed in the CR3BP rotating frame. Next, the motion is propagated for one period of the reference orbit, considering different combinations of halo orbit and spacecraft mass distribution. Three parameters generally define the vehicle inertia properties, i.e. k_1, k_2, and k_3 defined in equations (6.1)-(6.3); however, in this discussion, only the inertia ratio k_1 is varied, with a range $[-1, 1]$. A body fixed 3-2-1 (θ, φ, ψ) Euler angle sequence is utilized to describe the spacecraft orientation relative to the CR3BP rotating frame. In particular, the maximum values of these three angles are recorded for each integration and plotted on separate grid search maps, as in Figure 6.12. The resulting representation is functional to the identification of a pair of northern halo orbit, denoted by the orbit amplitude in the z direction, A_z, and inertia ratio, k_1, that enables the vehicle to maintain the alignment of the body axes with the CR3BP rotating frame over one revolution of the reference path. Recall that, the Euler angles are zero at the initial time, which is consistent with the body and rotating axes aligned in the same directions. Observing Figure 6.12, darker areas indicate regions where the specific Euler angle is small (black denoting a zero degree angle), whereas lightest colored areas reflect an angle that exceed an upper threshold of 180 deg. Darker regions that systematically emerge on all of the Euler angle maps, correlate to a configuration in terms of reference orbit and inertia ratio where, for the pre-determined set of initial conditions, the body frame stays closely aligned with the CR3BP rotating frame, for one revolution of the reference trajectory. Maps, similar to those displayed in Figure 6.12, are also presented by Knutson [20].

One of the areas where the spacecraft attitude changes negligibly with respect to the CR3BP rotating observer is marked by an arrow on the map for each angle in Figures 6.12(a)-6.12(c). As discussed in the previous section, a zone of bounded oscillations may reflect the existence of a nearby orbit-attitude periodic solution. In fact, selecting an initial guess within the darker region, as indicated by the arrow in Figures 6.12(a)-6.12(c), an orbit-attitude family of periodic behaviors is identified. The starting periodic solution is computed for a reference northern halo orbit with amplitude $A_z \approx 70550$ km and a spacecraft with inertia ratio $k_1 = 0.428$: a pair that lies within the bounded oscillatory zone. The map in Figure 6.12 applies, in general, to an asymmetric vehicle, but, for simplicity, the orbit-attitude solution is first constructed for a disk-like spacecraft. Then, by stepping onto nearby periodic responses via a continuation process, a family of periodic orbit-attitude solutions along three-dimensional halo orbits is also produced, as displayed in Figure 6.13. Each attitude periodic motion in Figure 6.13 corresponds to a different reference path, which is portrayed in Figure 6.14. Observing Figure 6.14, the family of orbit-attitude periodic solutions exist over a large range of halo orbits. Assuming that the spacecraft is initially located along the halo orbit at the crossing of the xz-plane in the positive y direction of the CR3BP frame, initial conditions that produce an approximately periodic motion are given in Table 6.1. Truncation errors for the values in this table, may be adjusted with a differential corrector to target a precisely periodic orbit-attitude solution. In Table 6.1, the reference orbit is identified by the orbital period and the x coordinate of the intersection to the xz-plane in the CR3BP rotating frame.

It is generally challenging to identify ordered and predictable behavior in complex dynamical scenarios, such as the coupled orbit-attitude motion along three-dimensional halo orbits. In this context, a grid search map for bounded motions is an effective strategy to identify an initial guess for fundamental coupled periodic solutions, that are, later, precisely computed via differential correction and a continuation process.

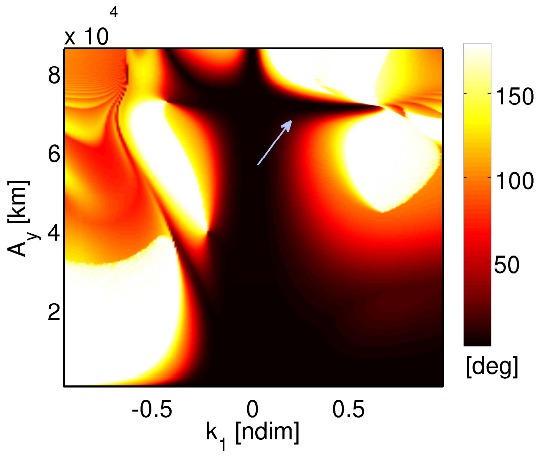

(a) θ angle.

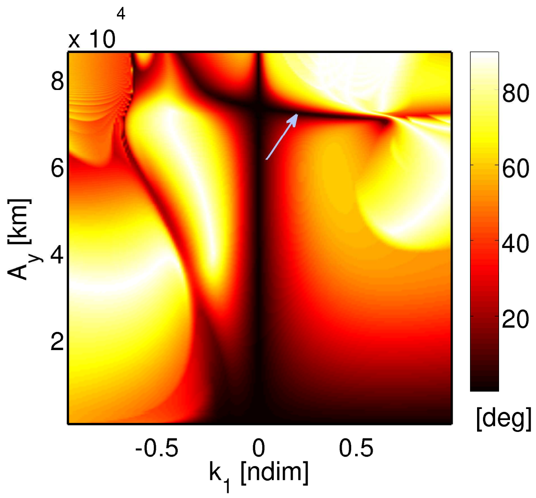

(b) φ angle.

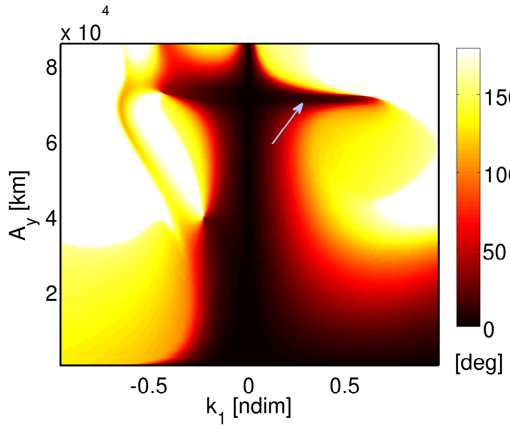

(c) ψ angle.

Figure 6.12. Maximum spacecraft orientation change relative to the CR3BP rotating frame in terms of a body fixed 3-2-1 Euler angles (θ, φ, ψ), across the L_1 northern halo family (Earth-Moon System) over one revolution for different inertia ratios.

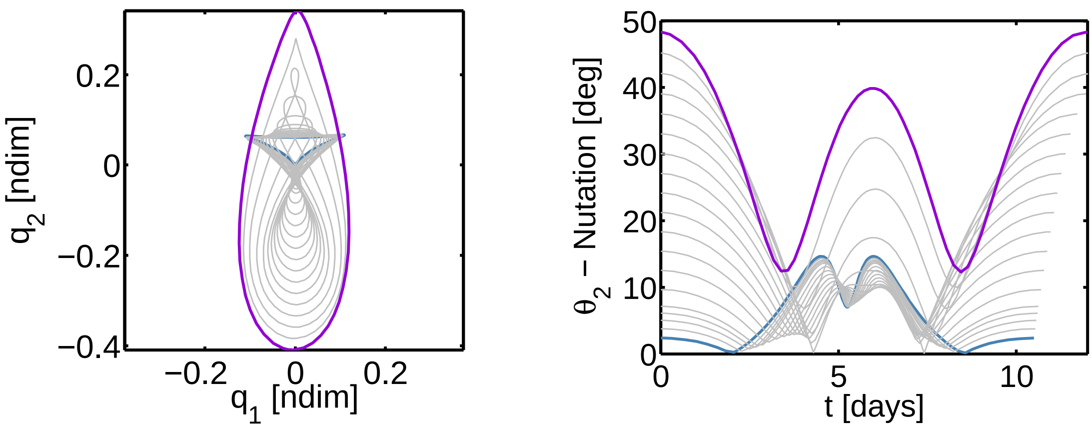

(a) Quaternion subspace. (b) Quaternion subspace.

Figure 6.13. Family of orbit-attitude periodic solutions along L_1 northern halo reference trajectories for a disk-like satellite with $k_1 = 0.428$. Blue denotes the starting solution, purple, the last solution currently computed.

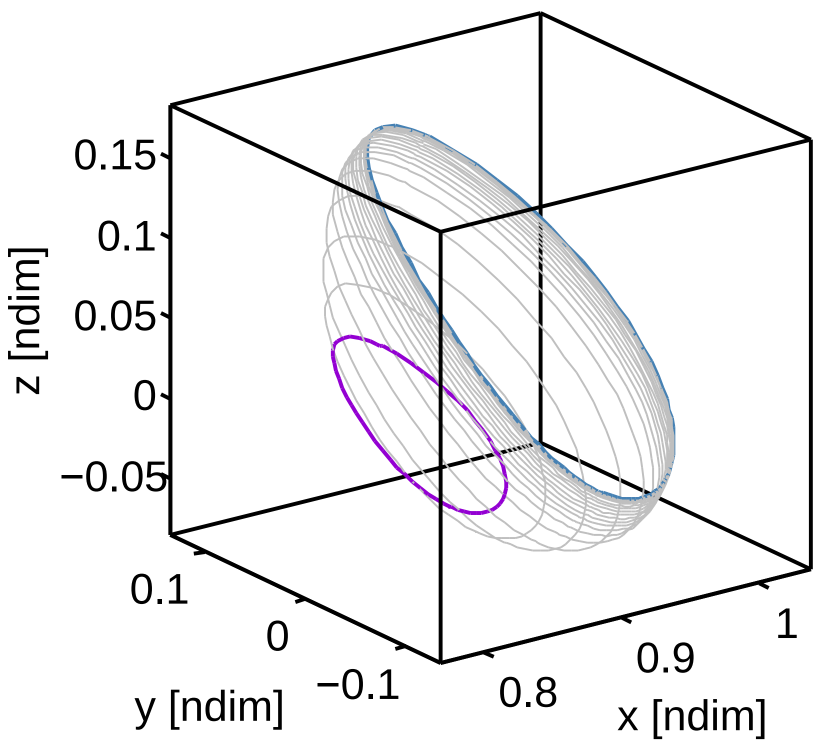

Figure 6.14. Successive adjustments to the northern halo reference trajectories during the continuation process. Blue denotes the starting orbit, purple, the last solution currently computed.

Table 6.1. Initial conditions for an orbit-attitude family of solutions along northern halo orbits. The solutions assume an axisymmetric disk-like spacecraft with inertia ratio $k_1 = 0.428$ in the Earth-Moon system.

$\boldsymbol{x}$ [ndim]	$\boldsymbol{q_1}$ [ndim]	$\boldsymbol{q_2}$ [ndim]	$\boldsymbol{q_3}$ [ndim]	$\boldsymbol{\omega_1}$ [ndim]	$\boldsymbol{\omega_2}$ [ndim]	$\boldsymbol{\omega_3}$ [days]	$\boldsymbol{P}$ [ndim]	$\boldsymbol{s}$ [ndim]
0.859	0.000	-0.021	-0.010	-0.018	0.000	0.983	10.501	4.879e+00
0.858	0.001	-0.033	-0.020	-0.006	0.000	0.983	10.537	4.753e+00
0.858	0.001	-0.044	-0.030	0.005	0.000	0.982	10.570	4.639e+00
0.857	0.002	-0.053	-0.040	0.014	0.001	0.981	10.599	4.538e+00
0.857	0.003	-0.062	-0.040	0.023	0.002	0.980	10.627	4.439e+00
0.856	0.001	-0.084	-0.009	0.044	0.001	0.978	10.698	4.196e+00
0.855	0.001	-0.109	-0.009	0.069	0.001	0.976	10.783	3.913e+00
0.853	0.001	-0.134	-0.009	0.094	0.002	0.973	10.871	3.627e+00
0.852	0.001	-0.159	-0.009	0.118	0.002	0.970	10.964	3.345e+00
0.850	0.002	-0.184	-0.009	0.143	0.003	0.967	11.060	3.070e+00
0.849	0.002	-0.209	-0.009	0.167	0.003	0.963	11.161	2.809e+00
0.847	0.002	-0.234	-0.009	0.191	0.004	0.960	11.269	2.572e+00
0.846	0.003	-0.259	-0.009	0.214	0.004	0.957	11.386	2.372e+00
0.844	0.276	-0.066	0.928	0.234	0.005	0.955	11.528	2.236e+00
0.840	0.302	-0.065	0.926	0.247	0.005	0.957	11.725	2.207e+00
0.836	0.328	-0.062	0.923	0.244	0.004	0.968	11.963	2.179e+00
0.831	0.354	-0.063	0.918	0.236	0.001	0.986	12.095	1.661e+00
0.827	0.377	-0.072	0.909	0.240	-0.003	1.004	12.084	1.428e+00
0.824	0.400	-0.085	0.898	0.261	-0.008	1.019	12.004	1.689e+00

7. SOLAR SAILING: MANEUVERING STRATEGIES

7.1 Overview

The development of a coupled orbit-attitude dynamics framework for mission design in the CR3BP may also incorporate artificial devices that necessarily link the spacecraft orbital and attitude motions. Through the application of such means, the attitude configuration may be potentially employed in a control scheme to direct the orbital motion of the spacecraft. The ability to steer the orbital motion may be, then, leveraged to maintain the vehicle nearby a given reference orbit. Presently, solar sails are likely the most promising, as well as the most advanced, among the orbit-attitude coupling devices.

Many studies have already demonstrated that, a sailcraft trajectory may be effectively controlled by reorienting a sail structure. However, few investigations have directly incorporated the attitude dynamics of the solar sail into the initial mission design process. The attitude history is usually imposed afterwards, as it results from the solution for the trajectory design problem. This approach has some limitations, in general: fast turning rates may result, ones that exceed feasible limit; the control authority required from the attitude control devices may be impractical to implement; the sail orientation that is computed by the path control algorithm may clash with some payload pointing constraints, or other similar mission requirements. Currently, some of the principal challenges for the implementation of a solar sail mission reside, in fact, in constraints on the sail attitude dynamics [88]. Thus, including an orbit-attitude model into the early stages of the design process may aid to mitigate such difficulties. Once the attitude dynamics are also considered, incorporating certain pointing or turn rate constraints into the trajectory design process may become more effective.

Different control strategies that utilize the vehicle orientation as an instrument to guide the orbital path are developed, while, envisioning their particular application to solar sailing. A well-known approach to this problem, denoted as Turn and Hold (TnH), assumes that, the spacecraft attitude is artificially fixed along different segments of the path. The orbit is, then, controlled by introducing a finite series of vehicle re-orientations at the locations where the various trajectory arcs connect. In a TnH approach, the pointing direction of the spacecraft may be hold constant relative to an arbitrary reference, including the solar rays direction or an inertial observer. The attitude dynamics, however, is not directly considered during the construction of the controlled trajectory. As the orientation of the spacecraft is artificially fixed within a TnH design, active control of the body rotations is necessary to follow the nominal orbital path, when the natural attitude dynamics are incorporated. Instantaneous re-orientations of the vehicle, that emerge in a TnH solution, also require additional transformation into feasible attitude maneuvers. A possible modification of the TnH strategy, is the inclusion of a spacecraft attitude dynamics model along the trajectory, while maintaining the capability to instantaneously change the vehicle orientation at certain locations. A control strategy that seeks a direct solution for the coupled orbit-attitude dynamics is a further option. To this end, the attitude dynamics are fully incorporated into the model and the orientation of the spacecraft necessary to execute a certain orbital path is obtained by the application of external control moments, which become the design variables. Then, if a solution exists, it is continuous in both the orbital and attitude state variables, and instantaneous body rotations are no longer necessary. Similarly, an additional step to derive the control moments from the spacecraft orientation history is not required, as the moments are already available for this type of coupled orbit-attitude control scheme. The orbit-attitude design approach may be supplementarily elaborated with the inclusion of a dynamical model for the devices that generate the control torque. Accordingly, the actuator inputs may be employed as design variables to converge the trajectory, instead a the generic expression for the control torque. Note that, adding complexity to the dynamics may negatively impact on the capacity to numerically compute a solution.

In conclusion, starting from a TnH approach, further modifications are proposed to incorporate the coupled orbit-attitude dynamics into the design of trajectories that are guided via the spacecraft orientation, with specific application to solar sailing.

7.2 STM with Input Function

When a control action is incorporated, e.g., one that is employed to guide a solar sail towards a desired destination, the differential equations describing the dynamics for the controlled system, may be generally formulated as

$$\dot{\boldsymbol{x}} = \boldsymbol{f}(\boldsymbol{x}, t) + \boldsymbol{g}(\boldsymbol{x}, \boldsymbol{y}, t) \quad , \tag{7.1}$$

where the first term reflects the natural evolution of the motion (equivalent to the original model, without including the control input) as a function of the state variables and time only, $\boldsymbol{f}(\boldsymbol{x}, t)$; the second term, is the contribution of the control action, represented by a vector $\boldsymbol{y}$, which may also be a function of the state variables and time, $\boldsymbol{g}(\boldsymbol{x}, \boldsymbol{y}, t)$. The control vector may be, in general, evolve with time, consistently with a set of ordinary differential equations,

$$\dot{\boldsymbol{y}} = \boldsymbol{h}(\boldsymbol{x}, \boldsymbol{y}, t) \quad . \tag{7.2}$$

The linear variational equations, for both the state and control variables, can be written as

$$\boldsymbol{\delta}\dot{\boldsymbol{x}} = \left.\frac{\partial \boldsymbol{f}}{\partial \boldsymbol{x}}\right|_{\boldsymbol{x}_0(t)} \boldsymbol{\delta x} + \left.\frac{\partial \boldsymbol{g}}{\partial \boldsymbol{x}}\right|_{\boldsymbol{x}_0(t),\, \boldsymbol{y}_0(t)} \boldsymbol{\delta x} + \left.\frac{\partial \boldsymbol{g}}{\partial \boldsymbol{y}}\right|_{\boldsymbol{x}_0(t),\, \boldsymbol{y}_0(t)} \boldsymbol{\delta y} \tag{7.3}$$

$$\boldsymbol{\delta}\dot{\boldsymbol{y}} = \left.\frac{\partial \boldsymbol{h}}{\partial \boldsymbol{x}}\right|_{\boldsymbol{x}_0(t),\, \boldsymbol{y}_0(t)} \boldsymbol{\delta x} + \left.\frac{\partial \boldsymbol{h}}{\partial \boldsymbol{y}}\right|_{\boldsymbol{x}_0(t),\, \boldsymbol{y}_0(t)} \boldsymbol{\delta y} \quad , \tag{7.4}$$

or equivalently, in matrix form

$$\begin{bmatrix} \boldsymbol{\delta}\dot{\boldsymbol{x}} \\ \boldsymbol{\delta}\dot{\boldsymbol{y}} \end{bmatrix} = \begin{bmatrix} A_{xx}(t) & B_{xy}(t) \\ A_{yx}(t) & B_{yy}(t) \end{bmatrix} \begin{bmatrix} \boldsymbol{\delta x} \\ \boldsymbol{\delta y} \end{bmatrix} \quad , \tag{7.5}$$

via the definition of

$$A_{xx}(t) = A_{fx} + A_{yx} = \left.\frac{\partial \boldsymbol{f}}{\partial \boldsymbol{x}}\right|_{\boldsymbol{x}_0(t)} + \left.\frac{\partial \boldsymbol{g}}{\partial \boldsymbol{x}}\right|_{\boldsymbol{x}_0(t),\, \boldsymbol{y}_0(t)} \quad , \tag{7.6}$$

and

$$B_{xy}(t) = \left.\frac{\partial \boldsymbol{g}}{\partial \boldsymbol{y}}\right|_{\boldsymbol{x}_0(t),\, \boldsymbol{y}_0(t)} \quad . \tag{7.7}$$

The sub-matrices A_{yx}, and B_{yy} similarly represent the partials of $\boldsymbol{h}(\boldsymbol{x}, \boldsymbol{y}, t)$ relative to the state and control variables, respectively. The partials appearing in Eq.s (7.3) and (7.4), are typically not constant, as they are evaluated along a time varying reference solution, $\boldsymbol{x}_0(t)$ and $\boldsymbol{y}_0(t)$. Corresponding to the system of linear variational equations (7.3) and (7.4), there exist a state transition matrix,

$$\Phi = \begin{bmatrix} \Phi_{xx} & \Psi_{xy} \\ \Phi_{yx} & \Psi_{yy} \end{bmatrix} \quad ,$$

one that is solution of the following differential equations

$$\frac{d}{dt}\begin{bmatrix} \Phi_{xx} & \Psi_{xy} \\ \Phi_{yx} & \Psi_{yy} \end{bmatrix} = \begin{bmatrix} A_{xx}(t) & B_{xy}(t) \\ A_{yx}(t) & B_{yy}(t) \end{bmatrix} \begin{bmatrix} \Phi_{xx} & \Psi_{xy} \\ \Phi_{yx} & \Psi_{yy} \end{bmatrix} \quad , \tag{7.8}$$

given $\Phi(t = 0) = \mathbb{I}$ at the initial time. For a system with n_x state variables and n_y control variables, the blocks A_{xx}, and Φ_{xx} are $n_x \times n_x$ matrices; the blocks B_{xy}, and Φ_{xy} are $n_x \times n_y$ matrices; the blocks A_{yx}, and Φ_{yx} are $n_y \times n_x$; the blocks A_{yy}, and Φ_{yy} are $n_y \times n_y$ matrices.

The state transition matrix for a system that includes a control action is preparatory, in this discussion, to the development of strategies to direct the path of a solar sail, or a similar device.

7.3 Turn and Hold Guidance

A Turn and Hold (TnH) strategy is typically based on the formulation of the control input as a function of the solar sail pointing direction, $\boldsymbol{g} = \boldsymbol{g}(\boldsymbol{x}, \hat{\boldsymbol{u}}, t)$. The pointing direction, $\hat{\boldsymbol{u}}(t)$, is expressed relative to an arbitrarily selected reference frame (e.g., the sun-light direction or some inertial axis), and may be coinciding with the solar sail normal, for a perfectly flat surface. The Turn and Hold model is often applied to the classical CR3BP, without directly incorporating the attitude motion, by replacing the generic vectorial function that describes the natural dynamics in Eq. (7.1), $\boldsymbol{f}(\boldsymbol{x}, t)$, with the set of ordinary differential equations in Eq. (2.45). If the representation of the CR3BP in Eq. (2.45) is selected, the input function $\boldsymbol{g}(\boldsymbol{x}, \hat{\boldsymbol{u}}, t)$ represents the acceleration of the solar sail in nondimensional units, and expressed in the rotating frame. The solution of the control problem, to target some specific intermediate or final state, is the vehicle pointing direction, $\hat{\boldsymbol{u}}(t)$, which is normally a function of time. For a TnH algorithm, the pointing history, $\hat{\boldsymbol{u}}(t)$, is assumed as a discrete series of constant orientations, $\hat{\boldsymbol{u}}_j$, that guide the sail along the desired path. Specifically, divide the controlled path in $N-1$ sub-arcs. Each arc is identified by its initial state $\boldsymbol{x}_j$ at time t_j, and it's propagated for a fixed time $T = t_{j+1} - t_j$ to a final state, $(\boldsymbol{x}_j)^t$. Assume that, along every jth-arc, the alignment of the sail is constant relative to a reference direction (inertial or relative). A trajectory leading a sail to a desired final state, $\boldsymbol{x}_d$, is computed as the zero of a constraint function,

$$\boldsymbol{F} = \begin{bmatrix} (\boldsymbol{x}_j)^t - \boldsymbol{x}_{j+1} \\ \text{———} \\ \boldsymbol{x}_N - \boldsymbol{x}_d \\ \text{———} \\ \hat{\boldsymbol{u}}_j \cdot \hat{\boldsymbol{u}}_j - 1 \\ \text{———} \\ \cos(\alpha_{max}) - \hat{\boldsymbol{\ell}}_{1,j} \cdot \hat{\boldsymbol{u}}_j + \eta^2_{\alpha,j} \end{bmatrix} \begin{array}{c} \text{Internal continuity, j = 1,..,N-1} \\ \text{———} \\ \text{Final Target} \\ \text{———} \\ \text{Normalization, j=1,..,N-1} \\ \text{———} \\ \text{Maximum incidence angle, j=1,..,N-1} \end{array} , \quad (7.9)$$

where, the first set of vectorial constraints describes the continuity between the final state along the jth-arc and the initial conditions on the next; the second set of constraints, enforces the final target states. When the pointing of the solar sail is represented by an unit vector, an additional set of constraint equations is necessary to guarantee the unitary norm of $\hat{\boldsymbol{u}}_j$ along each arc, as reflected in the third set of equations in Eq. (7.9). Finally, in some applications, it may be required to maintain the orientation of the sail within a maximum incident angle, α_{max}, relative to the Sun-light direction. When a maximum angle is not specified, it is good practice to select $\alpha_{max} = 90$ deg, so that the reflective area of the sail is always facing the Sun. The fourth set of equations in Eq. (7.9) is adopted to include the maximum incidence inequality constraint, where $\hat{\boldsymbol{u}}_j$ is, in fact, the solar sail normal, $\hat{\boldsymbol{\ell}}_{1,j}$ denotes the direction of the Sun-light, and $\eta_{\alpha,j}$ is a slack variable. Note that, in the formulation in Eq. (7.9), a maximum incident angle is only imposed at the beginning of each arc, thus, does not apply throughout the entire solution. The solution to Eq. (7.9) is obtained iteratively by updating the vector of the free variables,

$$\boldsymbol{\xi} = \begin{bmatrix} \boldsymbol{x}_2 \\ \vdots \\ \boldsymbol{x}_N \\ \hat{\boldsymbol{u}}_1 \\ \vdots \\ \hat{\boldsymbol{u}}_{N-1} \\ \eta_{\alpha,1} \\ \vdots \\ \eta_{\alpha,N-1} \end{bmatrix}, \tag{7.10}$$

via a Newton-Raphson method. The implementation of such algorithm requires the construction of the Jacobian matrix for the constraint vectorial function in Eq. (7.9), relative to the free variables in Eq. (7.10), which can be written as

$$DF = \frac{\partial \boldsymbol{F}}{\partial \boldsymbol{\xi}} = \begin{bmatrix} DF_{xx,n(N-1)\times n(N-1)} & DF_{xu,n(N-1)\times m(N-1)} & 0_{n(N-1)\times N-1} \\ 0_{N-1\times n(N-1)} & DF_{uu,N-1\times m(N-1)} & 0_{N-1\times N-1} \\ 0_{N-1\times n(N-1)} & DF_{\eta u,N-1\times m(N-1)} & DF_{\eta\eta,N-1\times N-1} \end{bmatrix}, \tag{7.11}$$

where the dimensions of each sub-matrix are given as a function of the number of state variables, n, the number of control inputs, m, and the number of arcs, $N-1$. The specific expression for the blocks appearing in Eq. (7.11) is

$$DF_{xx} = \begin{bmatrix} -\mathbb{I} & & & & \\ \Phi_{xx}(t_2,t_3) & -\mathbb{I} & & & \\ & & \ddots & & \\ & & & \Phi_{xx}(t_{N-1},t_N) & -\mathbb{I} \\ & & & & \mathbb{I} \end{bmatrix} \tag{7.12}$$

$$DF_{xu} = \begin{bmatrix} \Psi_{xu}(t_1,t_2) & & \\ & \ddots & \\ & & \Psi_{xu}(t_{N-1},t_N) \\ & 0_{n\times m(N-1)} & \end{bmatrix} \tag{7.13}$$

$$DF_{uu} = \begin{bmatrix} 2\hat{\boldsymbol{u}}_1^T & & \\ & \ddots & \\ & & 2\hat{\boldsymbol{u}}_{N-1}^T \end{bmatrix} \tag{7.14}$$

$$DF_{\eta u} = \begin{bmatrix} -\hat{\boldsymbol{\ell}}_{1,1}^T & & \\ & \ddots & \\ & & -\hat{\boldsymbol{\ell}}_{1,N-1}^T \end{bmatrix} \tag{7.15}$$

$$DF_{\eta\eta} = \begin{bmatrix} 2\eta_{\alpha,1} & & \\ & \ddots & \\ & & 2\eta_{\alpha,N-1} \end{bmatrix} , \tag{7.16}$$

with $\mathbb{I}$ being the identity matrix with proper dimension, and utilizing the definition of the STM block components as in Eq. (7.8) (recall, $\boldsymbol{y} = \hat{\boldsymbol{u}}$ for this application).

A solution presenting a solar sail pointing that is constant relative to a certain reference, is computationally convenient, and may be practical for a large number of application. However, the motion within the TnH model is independent of the attitude dynamics. The orientation history is afterwards reconstructed by imposing the control sequence of pointing directions onto the attitude dynamics. A time varying control action for the spacecraft rotations is generally necessary to follow a trajectory that adopts a TnH guidance.

7.3.1 Turn and Hold Guidance with Constant Pointing relative to the Sun-light Direction in a Sun-Planet System

The pointing direction for the solar sail may be expressed relative to different reference frames. Details for the TnH formulation are supplied assuming that the spacecraft orientation is described by a sail normal unit vector, which is expressed in a frame fixed relatively to the Sun-light direction.

$$\underset{\hat{\ell}}{\hat{\boldsymbol{u}}} = u_1\hat{\boldsymbol{\ell}}_{\mathbf{1}} + u_2\hat{\boldsymbol{\ell}}_{\mathbf{2}} + u_3\hat{\boldsymbol{\ell}}_{\mathbf{3}} \quad , \tag{7.17}$$

where the unit vectors for the Sun-light frame are defined relative to the Sun-Planet CR3BP rotating frame, ($\hat{\boldsymbol{x}}$,$\hat{\boldsymbol{y}}$,$\hat{\boldsymbol{z}}$), as

$$\hat{\boldsymbol{\ell}}_{\mathbf{1}} = \frac{\boldsymbol{d}}{d} \quad , \quad \hat{\boldsymbol{\ell}}_{\mathbf{2}} = \frac{\hat{\boldsymbol{z}} \times \hat{\boldsymbol{\ell}}_{\mathbf{1}}}{|\hat{\boldsymbol{z}} \times \hat{\boldsymbol{\ell}}_{\mathbf{1}}|} \quad , \quad \hat{\boldsymbol{\ell}}_{\mathbf{3}} = \hat{\boldsymbol{\ell}}_{\mathbf{1}} \times \hat{\boldsymbol{\ell}}_{\mathbf{2}} \quad , \tag{7.18}$$

with $\hat{\boldsymbol{\ell}}_{\mathbf{1}}$ denoting the solar radiation direction and $\boldsymbol{d}$ is vector position of the spacecraft relative to the Sun. The measure numbers, u_1, u_2 and u_3, in Eq. (7.17) essentially designate the control variables for each arc of the trajectory. Express the Sun-light direction as function of the instantaneous coordinates of the vehicle in the rotating frame,

$$\hat{\boldsymbol{\ell}}_{\mathbf{1}} = \hat{\boldsymbol{\ell}}_{\mathbf{1}}(x, y, z) = \frac{(x+\mu)}{d}\hat{\boldsymbol{x}} + \frac{y}{d}\hat{\boldsymbol{y}} + \frac{z}{d}\hat{\boldsymbol{z}} \quad , \tag{7.19}$$

and define the input function as the nondimensional acceleration induced by the solar radiation pressure for a flat ideal sail (generally described in Eq. (2.21)),

$$\boldsymbol{g}(\boldsymbol{x}, \hat{\boldsymbol{u}}, t) = \underset{\hat{r}}{\boldsymbol{a}_{ss}} = \beta\left(\frac{1-\mu}{d^2}\right)u_1^2\begin{bmatrix} n_1 \\ n_2 \\ n_3 \end{bmatrix} \quad , \tag{7.20}$$

with

$$n_1 = u_1 \frac{x+\mu}{d} - u_2 \frac{y}{\sqrt{(x+\mu)^2+y^2}} - u_3 \frac{z(x+\mu)}{d\sqrt{(x+\mu)^2+y^2}} \tag{7.21}$$

$$n_2 = u_1 \frac{y}{d} + u_2 \frac{x+\mu}{\sqrt{(x+\mu)^2+y^2}} - u_3 \frac{zy}{d\sqrt{(x+\mu)^2+y^2}} \tag{7.22}$$

$$n_3 = u_1 \frac{z}{d} + u_3 \frac{\sqrt{(x+\mu)^2+y^2}}{d} \quad . \tag{7.23}$$

The derivatives of the control function with respect to the position state variables are

$$g_{x/x} = \beta u_1^2(1-\mu)\left[\frac{-2(x+\mu)}{d^4}n_1 + \frac{1}{d^2}\left(u_1 f_{1/x}(x+\mu,y,z)\right.\right.$$
$$\left.\left.-u_2 f_{2/x}(y,x+\mu) - u_3 f_{4/x}(x+\mu,y,z)\right)\right]$$
$$g_{x/y} = \beta u_1^2(1-\mu)\left[\frac{-2y}{d^4}n_1 + \frac{1}{d^2}\left(u_1 f_{1/y}(x+\mu,y,z)\right.\right.$$
$$\left.\left.-u_2 f_{2/y}(y,x+\mu) - u_3 f_{4/y}(x+\mu,y,z)\right)\right]$$
$$g_{x/z} = \beta u_1^2(1-\mu)\left[\frac{-2z}{d^4}n_1 + \frac{1}{d^2}\left(u_1 f_{1/z}(x+\mu,y,z)\right.\right.$$
$$\left.\left.-u_2 f_{2/z}(y,x+\mu) - u_3 f_{4/z}(x+\mu,y,z)\right)\right]$$
$$g_{y/x} = \beta u_1^2(1-\mu)\left[\frac{-2(x+\mu)}{d^4}n_2 + \frac{1}{d^2}\left(u_1 f_{1/x}(y,x+\mu,z)\right.\right.$$
$$\left.\left.-u_2 f_{2/x}(x+\mu,y) - u_3 f_{4/x}(y,x+\mu,z)\right)\right]$$
$$g_{y/y} = \beta u_1^2(1-\mu)\left[\frac{-2y}{d^4}n_2 + \frac{1}{d^2}\left(u_1 f_{1/y}(y,x+\mu,z)\right.\right.$$
$$\left.\left.-u_2 f_{2/y}(x+\mu,y) - u_3 f_{4/y}(y,x+\mu,z)\right)\right]$$
$$g_{y/z} = \beta u_1^2(1-\mu)\left[\frac{-2z}{d^4}n_2 + \frac{1}{d^2}\left(u_1 f_{1/z}(y,x+\mu,z)\right.\right.$$
$$\left.\left.-u_2 f_{2/y}(x+\mu,z) - u_3 f_{4/z}(y,x+\mu,z)\right)\right]$$
$$g_{z/x} = \beta u_1^2(1-\mu)\left[\frac{-2(x+\mu)}{d^4}n_3 + \frac{1}{d^2}\left(u_1 f_{1/x}(z,x+\mu,y)\right.\right.$$
$$\left.\left.-u_3 f_{3/x}(x+\mu,y,z)\right)\right]$$
$$g_{z/y} = \beta u_1^2(1-\mu)\left[\frac{-2y}{d^4}n_3 + \frac{1}{d^2}\left(u_1 f_{1/y}(z,x+\mu,y)\right.\right.$$
$$\left.\left.-u_3 f_{3/y}(x+\mu,y,z)\right)\right]$$
$$g_{z/z} = \beta u_1^2(1-\mu)\left[\frac{-2z}{d^4}n_3 + \frac{1}{d^2}\left(u_1 f_{1/z}(z,x+\mu,y)\right.\right.$$
$$\left.\left.-u_3 f_{3/z}(x+\mu,y,z)\right)\right] \quad ,$$

with

$$
\begin{aligned}
f_1(a,b,c) &= \frac{a}{\sqrt{a^2+b^2+c^2}} \\
f_{1/a} &= \frac{1}{\sqrt{a^2+b^2+c^2}} - \frac{a^2}{(a^2+b^2+c^2)^{\frac{3}{2}}} \\
f_{1/b} &= -\frac{ab}{(a^2+b^2+c^2)^{\frac{3}{2}}} \\
f_{1/c} &= -\frac{ac}{(a^2+b^2+c^2)^{\frac{3}{2}}} \\
f_2(a,b,c) &= \frac{a}{\sqrt{a^2+b^2}} \\
f_{2/a} &= \frac{1}{\sqrt{a^2+b^2}} - \frac{a^2}{(a^2+b^2)^{\frac{3}{2}}} \\
f_{2/b} &= -\frac{ab}{(a^2+b^2)^{\frac{3}{2}}} \\
f_{2/c} &= 0 \\
f_3(a,b,c) &= \frac{\sqrt{a^2+b^2}}{\sqrt{a^2+b^2+c^2}} \\
f_{3/a} &= \frac{a(a^2+b^2)^{-\frac{1}{2}}}{\sqrt{a^2+b^2+c^2}} - \frac{a\sqrt{a^2+b^2}}{(a^2+b^2+c^2)^{\frac{3}{2}}} \\
f_{3/b} &= \frac{b(a^2+b^2)^{-\frac{1}{2}}}{\sqrt{a^2+b^2+c^2}} - \frac{b\sqrt{a^2+b^2}}{(a^2+b^2+c^2)^{\frac{3}{2}}} \\
f_{3/c} &= -\frac{c\sqrt{a^2+b^2}}{(a^2+b^2+c^2)^{\frac{3}{2}}}
\end{aligned}
$$

$$
\begin{aligned}
f_4(a,b,c) &= \frac{ac}{\sqrt{a^2+b^2+c^2}\sqrt{a^2+b^2}} \\
f_{3/a} &= \frac{c}{\sqrt{a^2+b^2+c^2}\sqrt{a^2+b^2}} - \frac{ca^2}{(a^2+b^2+c^2)^{\frac{3}{2}}\sqrt{a^2+b^2}} - \frac{ca^2}{(a^2+b^2)^{\frac{3}{2}}\sqrt{a^2+b^2+c^2}} \\
f_{3/b} &= -\frac{cab}{(a^2+b^2+c^2)^{\frac{3}{2}}\sqrt{a^2+b^2}} - \frac{cab}{(a^2+b^2)^{\frac{3}{2}}\sqrt{a^2+b^2+c^2}} \\
f_{3/c} &= \frac{a}{\sqrt{a^2+b^2+c^2}\sqrt{a^2+b^2}} - \frac{ac^2}{(a^2+b^2+c^2)^{\frac{3}{2}}\sqrt{a^2+b^2}} \quad .
\end{aligned}
$$

The derivatives of the control function relative to the control variables are written as

$$
\begin{aligned}
g_{x/u_1} &= \beta\frac{1-\mu}{d^2}\left[2u_1n_1 + u_1^2\frac{x+\mu}{d}\right]\\
g_{x/u_2} &= \beta\frac{1-\mu}{d^2}\left[-u_1^2\frac{y}{\sqrt{x^2+y^2}}\right]\\
g_{x/u_3} &= \beta\frac{1-\mu}{d^2}\left[-u_1^2\frac{z(x+\mu)}{d\sqrt{x^2+y^2}}\right]\\
g_{y/u_1} &= \beta\frac{1-\mu}{d^2}\left[2u_1n_2 + u_1^2\frac{y}{d}\right]\\
g_{y/u_2} &= \beta\frac{1-\mu}{d^2}\left[+u_1^2\frac{x+\mu}{\sqrt{x^2+y^2}}\right]\\
g_{y/u_3} &= \beta\frac{1-\mu}{d^2}\left[-u_1^2\frac{zy}{d\sqrt{x^2+y^2}}\right]\\
g_{z/u_1} &= \beta\frac{1-\mu}{d^2}\left[2u_1n_3 + u_1^2\frac{z}{d}\right]\\
g_{z/u_2} &= 0\\
g_{z/u_3} &= \beta\frac{1-\mu}{d^2}\left[+u_1^2\frac{\sqrt{x^2+y^2}}{d}\right]
\end{aligned}
$$

The partials of the control function are preliminary to the construction of the B_{xy} block for the STM, accordingly to Eq. (7.8), that is generally employed within the Jacobian matrix in Eq. (7.11). The definition for the A_{xx} sub-matrix is known from the classical CR3BP. The blocks A_{yx} and B_{yy} are null, because of the assumption for a constant pointing direction along each arc (i.e., $\dot{\hat{\boldsymbol{u}}} = 0$).

7.4 Incorporating the Attitude Dynamics into the Turn and Hold Guidance

Within a classical Turn and Hold (TnH) strategy, some assumptions are posed on the pointing direction of the sailcraft. Specifically, a direction representative of the sail orientation is fixed in a given observing frame. Introducing the attitude dynamics into a TnH approach to control the path for a solar sail, is equivalent to link the vehicle pointing to the attitude states that describe the actual, instantaneous orientation of the vehicle. For example, the pointing direction can be written as a function of the quaternion vector, i.e., $\hat{\boldsymbol{u}} = \hat{\boldsymbol{u}}(\boldsymbol{q}(t), t)$. Consequently, the control input variable, $\boldsymbol{y}$, in Eq. (7.1) may be expressed in term of the rotational state variables for the spacecraft, as

$$\boldsymbol{y} = \begin{bmatrix} {}^{i}\boldsymbol{q}^{b} \\ {}^{i}\boldsymbol{\omega}^{b} \end{bmatrix} \quad , \tag{7.24}$$

and it is in general a time-varying function, $\boldsymbol{y} = \boldsymbol{y}(t)$. The variation for the control variable over time is governed by a set of ordinary differential equations that fully reflects the spacecraft attitude dynamics. In fact,

$$\begin{cases} \dot{\boldsymbol{y}} = \boldsymbol{h}(\boldsymbol{x}, \boldsymbol{y}, t) = \begin{bmatrix} \boldsymbol{f}_{q}(\boldsymbol{y}) \\ \boldsymbol{f}_{\omega}(\boldsymbol{y}) \end{bmatrix} \\ \boldsymbol{y}(t = t_0) = \boldsymbol{y}_0 = \begin{bmatrix} {}^{i}\boldsymbol{q}_0^{b} \\ {}^{i}\boldsymbol{\omega}_0^{b} \end{bmatrix} \end{cases} \tag{7.25}$$

where $\boldsymbol{f}_{q}$ and $\boldsymbol{f}_{\omega}$ define the attitude equations of motion from Eq. (2.46) and Eq. (2.47), respectively, and $\boldsymbol{y}_0$ denotes the spacecraft orientation and angular velocity at the initial time. The differential equations describing the control variables dynamics, Eq. (7.25), are integrated along with the evolution of the orbital state variables, that is expressed in Eq. (7.1). Specifically, the natural component of the motion, $\boldsymbol{f}(\boldsymbol{x}, t)$, evolves accordingly to the orbital model only, for example the CR3BP, such that

$$\boldsymbol{f}(\boldsymbol{x}, t) = \boldsymbol{f}_{\mathrm{CR3BP}}(\boldsymbol{x}) \quad ,$$

where $\boldsymbol{f}_{\mathrm{CR3BP}}(\boldsymbol{x})$ is defined in Eq. (2.45); the control input is the solar sail acceleration expressed consistently with the description of the natural dynamics.

A multiple shooting algorithm may be implemented to determine the vehicle orientation time history that direct the sailcraft along a desired path. Discretize the trajectory in $N-1$ sub-arcs. Every jth arc is generated by propagating, for a fixed time $T_j = t_{j+1} - t_j$, a given initial orbital state vector $\boldsymbol{x}_j = \boldsymbol{x}(t_j)$, and a starting value for the control variable vector, $\boldsymbol{y}_j = \boldsymbol{y}(t_j)$ (which corresponds to an initial orientation and angular velocity for the solar sail). The vectors $\boldsymbol{x}_j$ and $\boldsymbol{y}_j$ are iteratively updated, until a continuous trajectory, $\boldsymbol{x}(t)$, and some desired final or intermediate conditions are both obtained, within a selected tolerance. Note that, the orientation history associated to $\boldsymbol{y}_j$, is not necessarily continuous along the final trajectory. Discontinuities in the control variable $\boldsymbol{y}(t)$ profile locate at time t_j, and fundamentally correspond to an instantaneous reorientation of the solar sail. For practical implementation, it may be more convenient to express the initial orientation of the spacecraft via an unit vector, $\hat{\boldsymbol{u}}_j$, that defines the pointing direction of the solar sail. For each segment of the path, then, the initial control input is expressed as a function of the pointing direction $\hat{\boldsymbol{u}}_j$, as

$$\boldsymbol{y}_j = \begin{bmatrix} {}^i\boldsymbol{q}^b(\hat{\boldsymbol{u}}_j) \\ 0 \end{bmatrix} \quad ,$$

where, for simplicity, the initial angular velocity is null, i.e., ${}^i\boldsymbol{\omega}_0^b = 0$. The starting angular velocity may be modified or included into the correction process, without altering the general framework for the solution. The multiple shooting problem is formulated to update the pointing direction $\hat{\boldsymbol{u}}_j$, instead of directly modifying the vector $\boldsymbol{y}_j$, as defined in Eq. (7.24). Upon the substitution of the vector $\hat{\boldsymbol{u}}_j$ to the vector $\boldsymbol{y}_j$ as the free variable, the targeting problem may be expressed as in Eq.s (7.9), (7.10), and (7.11), which reflect a typical formulation for the TnH strategy. As the attitude dynamics is now introduced, it is, however, necessary to evaluate the dependence of the pointing direction on the control input variable $\boldsymbol{y}$, during the construction of the Jacobian in Eq. (7.11). Specifically, the original sub-matrix DF_{xu} becomes

$$DF_{xu} = \begin{bmatrix} \Psi_{xy}(t_1, t_2)\dfrac{d\boldsymbol{y}_1}{d\hat{\boldsymbol{u}}_1} & & \\ & \ddots & \\ & & \Psi_{xy}(t_{N-1}, t_N)\dfrac{d\boldsymbol{y}_{N-1}}{d\hat{\boldsymbol{u}}_{N-1}} \\ & 0_{n\times m(N-1)} & \end{bmatrix} \quad . \tag{7.26}$$

7.4.1 Reconstructing the Body Orientation from the Solar Sail Normal

During the implementation of a TnH correction algorithm that includes attitude dynamics, it may be computationally more efficient to update an initial pointing direction instead of the quaternion vector that defines the body orientation. To propagate the attitude motion and quantify the dependence of the targeted variables on the pointing direction is, however, necessary to define the body orientation for any given pointing direction, i.e., express ${}^i\boldsymbol{q}^b(\hat{\boldsymbol{u}})$.

The knowledge of a single direction is not sufficient to uniquely determine the body orientation. In fact, any rotation of the body around the known direction, is a attitude configuration. Therefore, the definition of the function ${}^i\boldsymbol{q}^b(\hat{\boldsymbol{u}})$ requires some assumptions. Suppose $\hat{\boldsymbol{u}}$ is written relatively to the Sun-light frame, precisely

$$\hat{\boldsymbol{u}} = \underset{\hat{\ell}}{\hat{\boldsymbol{u}}} = u_1\hat{\boldsymbol{\ell}}_1 + u_2\hat{\boldsymbol{\ell}}_2 + u_3\hat{\boldsymbol{\ell}}_3 \quad .$$

The Sun-light frame, $(\hat{\boldsymbol{\ell}}_1, \hat{\boldsymbol{\ell}}_2, \hat{\boldsymbol{\ell}}_3)$, is defined in Eq. (7.18). Given the pointing direction, $\underset{\hat{\ell}}{\hat{\boldsymbol{u}}}$, a possible option to re-construct the body frame is by

$$\begin{aligned} \underset{\hat{\ell}}{\hat{\boldsymbol{b}}_1} &= \underset{\hat{\ell}}{\hat{\boldsymbol{u}}} \\ \underset{\hat{\ell}}{\hat{\boldsymbol{b}}_2} &= \frac{\underset{\hat{\ell}}{\boldsymbol{v}} \times \underset{\hat{\ell}}{\hat{\boldsymbol{u}}}}{||\underset{\hat{\ell}}{\boldsymbol{v}} \times \underset{\hat{\ell}}{\hat{\boldsymbol{u}}}||} \quad , \\ \underset{\hat{\ell}}{\hat{\boldsymbol{b}}_3} &= \underset{\hat{\ell}}{\hat{\boldsymbol{b}}_1} \times \underset{\hat{\ell}}{\hat{\boldsymbol{b}}_2} \end{aligned} \tag{7.27}$$

where $\underset{\hat{\ell}}{\boldsymbol{v}}$ is an arbitrary vector such that $\underset{\hat{\ell}}{\boldsymbol{v}} \times \underset{\hat{\ell}}{\hat{\boldsymbol{u}}} \neq 0$. The vector $\underset{\hat{\ell}}{\boldsymbol{v}}$ substantially determines the rotation of the body frame about the direction $\underset{\hat{\ell}}{\hat{\boldsymbol{u}}}$. The body unit vectors relative to the Sun-light frame, in Eq. (7.27), are related to the body unit vectors expressed in the body frame, via a concatenation of successive rotations, written as

$$\begin{bmatrix} \underset{\hat{b}}{\hat{\boldsymbol{b}}_1} & \underset{\hat{b}}{\hat{\boldsymbol{b}}_2} & \underset{\hat{b}}{\hat{\boldsymbol{b}}_3} \end{bmatrix} = \underset{\hat{b}\cdot\hat{r}}{A}\ \underset{\hat{r}\cdot\hat{\ell}}{A} \begin{bmatrix} \underset{\hat{\ell}}{\hat{\boldsymbol{b}}_1} & \underset{\hat{\ell}}{\hat{\boldsymbol{b}}_2} & \underset{\hat{\ell}}{\hat{\boldsymbol{b}}_3} \end{bmatrix} \tag{7.28}$$

where

$$\underset{\hat{r}\cdot\hat{\ell}}{A} = \begin{bmatrix} \underset{\hat{r}}{\hat{\boldsymbol{\ell}}_1} & \underset{\hat{r}}{\hat{\boldsymbol{\ell}}_2} & \underset{\hat{r}}{\hat{\boldsymbol{\ell}}_3} \end{bmatrix}$$

is the rotation matrix between the Sun-light and the CR3BP rotating frame, and the matrix $\underset{\hat{b}\cdot\hat{r}}{A}$ describes the orientation of the body relative to the rotating frame, which is unknown in this equation. The body unit vectors expressed in the body frame are simply the identity matrix, thus, Eq. (7.28) simplifies to

$$\mathbb{I} = \underset{\hat{b}\cdot\hat{r}}{A}\,\underset{\hat{r}\cdot\hat{\ell}}{A}\,\underset{\hat{\ell}}{B}, \tag{7.29}$$

and it is solved for

$$\underset{\hat{b}\cdot\hat{r}}{A} = \underset{\hat{\ell}}{B^{-1}}\,\underset{\hat{r}\cdot\hat{\ell}}{A^T} \quad . \tag{7.30}$$

The knowledge of the rotation matrix $\underset{\hat{b}\cdot\hat{r}}{A}$ supplies the orientation of the spacecraft relative to rotating frame. Alternatively, the vehicle attitude may also be described relatively to an inertial frame, by $\underset{\hat{b}\cdot\hat{\imath}}{A} = \underset{\hat{b}\cdot\hat{r}}{A}\,\underset{\hat{r}\cdot\hat{\imath}}{A}$. Both the rotation matrices, $\underset{\hat{b}\cdot\hat{r}}{A}$ and $\underset{\hat{b}\cdot\hat{\imath}}{A}$, may be transformed to a corresponding quaternion representation using Eq.s (2.30), and (2.31).

7.4.2 Implicit Formulation of the Sail-On Constraint

To facilitate the convergence of the correction process to a series of sail orientations that guide the spacecraft along a desired path, the normal vector to the non-reflective surface of the sail always points within a 90 deg cone angle measured from the Sun-light direction, at the beginning of each control arc. This condition is also denoted as sail-on configuration. A sail-on constraint may be explicitly formulated by imposing a maximum incidence angle, as in Eq. (7.9).

Alternatively, a sail-on configuration at the jth control point, i.e., the starting point of the jth trajectory segment, may be obtained by implicitly defining one of the components for the pointing vector, during the correction process. First, define a unitary pointing vector in the Sun-light reference frame,

$$\underset{\hat{\ell}}{\hat{\boldsymbol{u}}} = u_1\hat{\boldsymbol{\ell}}_{\mathbf{1}} + u_2\hat{\boldsymbol{\ell}}_{\mathbf{2}} + u_3\hat{\boldsymbol{\ell}}_{\mathbf{3}} \quad , \tag{7.31}$$

and assume that the sail is facing the Sun for $u_1 > 0$. The component u_1 is, in fact, the component of the pointing vector along the solar ray direction, $\hat{\boldsymbol{\ell}}_{\mathbf{1}}$. Next, assemble the free variables vector as

$$\boldsymbol{\xi} = \begin{bmatrix} \boldsymbol{x}_2 \\ \vdots \\ \boldsymbol{x}_N \\ \boldsymbol{u}_1^R \\ \vdots \\ \boldsymbol{u}_{N-1}^R \\ \gamma_1 \\ \vdots \\ \gamma_{N-1} \end{bmatrix} , \tag{7.32}$$

where γ_i is a slack variable, and the vector $\boldsymbol{u}^R$ only includes the two components of the unit vector $\underset{\hat{\ell}}{\hat{\boldsymbol{u}}}$ that are orthogonal to the Sun-light direction, i.e.,

$$\boldsymbol{u}^R = \begin{bmatrix} u_2 \\ u_3 \end{bmatrix} .$$

Accordingly to the alternative definition of the free variables vector, the constraint vector is written as

$$\boldsymbol{F} = \begin{bmatrix} (\boldsymbol{x}_j)^t - \boldsymbol{x}_{j+1} \\ \overline{} \\ \boldsymbol{x}_N - \boldsymbol{x}_d \\ \overline{} \\ \sqrt{\boldsymbol{u}_j^R \cdot \boldsymbol{u}_j^R} - 1 + \gamma^2 \end{bmatrix} \begin{matrix} \text{Internal continuity, j = 1,..,N-1} \\ \overline{} \\ \text{Final Target} \\ \overline{} \\ \text{Norm less than one, j=1,..,N-1} \end{matrix} . \tag{7.33}$$

The relevant modification of the constraint vector is the equation $\sqrt{\boldsymbol{u}_j^R \cdot \boldsymbol{u}_j^R} - 1 + \gamma_j^2 = 0$, that, via a slack variable, γ_j^2, reflects the inequality $||\boldsymbol{u}_j^R|| < 1$. Eventually, the unitary norm for the pointing vector, as well as the sail-on configuration are implicitly defined by calculating the remaining component for the vector $\underset{\hat{\ell}}{\hat{\boldsymbol{u}}}$ as

$$u_1 = \sqrt{1 - u_2^2 - u_3^2} > 0 \tag{7.34}$$

An implicit computation of the component for the pointing direction that aligns with the solar rays, u_1, may be beneficial in certain applications to improve, or even enable, the convergence of the correction algorithm to a feasible solution.

7.5 Moment Hold Guidance

The TnH strategy supplies a solution to the sailing of a spacecraft that, even when the attitude dynamics are incorporated, necessitates, in general, instantaneous reorientation of the solar sail. Continuity of the attitude history throughout the controlled path may be a more successful piloting option for certain applications, as it may eliminate the utilization of fast solar sail pointing maneuvers. Additionally, a preliminary outline is immediately available for both the orbital path as well as the attitude profile. Without the derivation of the attitude history from the resulting TnH sequence, the number of steps in the design process is also reduced. When the attitude dynamics are included, it is possible to formulate a control problem to achieve continuity in both the translational and rotational state variables.

Considering to the control problem generally posed as in Eq. (7.1), first, introduce an orbit-attitude description of the natural dynamics for a solar sail, for example $\boldsymbol{f}(\boldsymbol{x}, t) = \boldsymbol{f}_{\text{FCM}}(\boldsymbol{x}, \boldsymbol{t})$, where $\boldsymbol{f}_{\text{FCM}}(\boldsymbol{x}, \boldsymbol{t})$ is defined in Eq. (2.44). The state variables, $\boldsymbol{x}$, are comprised of the orbital states, the quaternion vector (which describes the body orientation), and the body angular velocity, i.e.,

$$\boldsymbol{x} = \begin{bmatrix} \boldsymbol{x}_{\text{orb}} \\ {}^{i}\boldsymbol{q}^{b} \\ {}^{i}\boldsymbol{\omega}^{b} \end{bmatrix} \quad .$$

An external control moment may be applied to govern the rotation of the sail and, consequently, guide the spacecraft along a desired path. A moment action may replace instantaneous adjustments of the solar sail pointing as an instrument to control the orbital motion. Accordingly, the control input vectorial function is written as

$$\boldsymbol{g} = \boldsymbol{g}(\boldsymbol{M}) = \begin{bmatrix} 0_{6\times 1} \\ 0_{4\times 1} \\ \boldsymbol{M}_{3\times 1} \end{bmatrix} \quad ,$$

where $\boldsymbol{M}$ represents an external moment vector in body axes. In the same manner of the TnH strategy, the trajectory is divided in $N-1$ sub-arcs and a multiple shooting algorithm is implemented to achieve a feasible solution of the control problem. Continuity of the state variables, however, includes continuity of the attitude states at the conjunction of adjacent arcs as well, and corresponds to the following constraint vector,

$$\boldsymbol{F} = \begin{bmatrix} (\boldsymbol{x}_{\text{orb},j})^t - \boldsymbol{x}_{\text{orb},j+1} \\ ({}^i\boldsymbol{q}_j^b)^t - {}^i\boldsymbol{q}_{j+1}^b \\ ({}^i\boldsymbol{\omega}_j^b)^t - {}^i\boldsymbol{\omega}_{j+1}^b \\ \hline \\ \boldsymbol{x}_{\text{orb},N} - \boldsymbol{x}_{\text{orb},d} \end{bmatrix} \begin{array}{c} \\ \text{Internal continuity, j = 1,..,N-1} \\ \\ \hline \\ \text{Final Target} \end{array} \quad , \tag{7.35}$$

which also contains a desired final target condition for the orbital state variables. To solve for $\boldsymbol{F} = \boldsymbol{0}$, the state variables, both orbital and rotational, that identify every jth segment of the trajectory are updated, along with a control moment vector, $\boldsymbol{M}_j$, also different for each control segment. The control moment, $\boldsymbol{M}_j$, is, however, assumed constant along the corresponding arc. Consequently, this implementation of the control strategy is labelled Moment Hold guidance (MH). The free variables vector is

$$\boldsymbol{X} = \begin{bmatrix} \boldsymbol{x}_{\text{orb},2} \\ {}^{i}\boldsymbol{q}_2^b \\ {}^{i}\boldsymbol{\omega}_2^b \\ \vdots \\ \boldsymbol{x}_{\text{orb},N-1} \\ {}^{i}\boldsymbol{q}_{N-1}^b \\ {}^{i}\boldsymbol{\omega}_{N-1}^b \\ \boldsymbol{M}_1 \\ \vdots \\ \boldsymbol{M}_{N-1} \end{bmatrix} , \tag{7.36}$$

noting that, ${}^{i}\boldsymbol{q}_j^b$ only represents three independent components for the four dimensional quaternion vector. Resulting from the definition for the constraint function in Eq. (7.35), and the free variables vector in Eq. (7.36), the Jacobian matrix is

$$DF = \frac{\partial \boldsymbol{F}}{\partial \boldsymbol{X}} = \begin{bmatrix} DF_{xx,n(N-1)\times n(N-1)} & DF_{xM,n(N-1)\times m(N-1)} \end{bmatrix} , \tag{7.37}$$

where

$$DF_{xM} = \begin{bmatrix} \Psi_{xM}(t_1,t_2) & & \\ & \ddots & \\ & & \Psi_{xM}(t_{N-1},t_N) \\ & 0_{n\times m(N-1)} & \end{bmatrix} . \tag{7.38}$$

For the computation of the B_{xy} block for the STM, accordingly to Eq. (7.8), the partials of the control function, $\boldsymbol{g}$, are needed. Relative to the control variables, $\boldsymbol{M}$, the partials for the control function are

$$\frac{d\boldsymbol{g}}{d\boldsymbol{M}} = \begin{bmatrix} 0_{6\times 3} \\ 0_{4\times 3} \\ \mathbb{I} \end{bmatrix} , \tag{7.39}$$

where $\mathbb{I}$ is a 3×3 identity matrix. The partials with respect to the state variables are null, i.e., $\dfrac{d\boldsymbol{g}}{d\boldsymbol{x}} = \boldsymbol{0}$. The definition for the A_{xx} sub-matrix is known from the

FCM incorporating solar pressure. The blocks A_{yx} and B_{yy} are null, because of the assumption for constant moment along each arc (i.e., $\dot{\boldsymbol{M}} = \mathbf{0}$).

7.6 Angular Moment Hold Guidance

The application of reaction wheels to attitude control is well-established, therefore, it is worth to examine the possibility of their implementation within a coupled orbit-attitude control strategy. Note that, reaction wheels, may not always be a practical design solution for any solar sail configuration, especially when a significantly large structure, or a fast sail spin rate, is involved [73, 74].

When reaction wheels are added, they bring a contribution to the dynamics that may be expressed as an additional external moment. Assume the followings: 1) the reaction wheels maintain a constant spin relatively to the carrying vehicle; 2) the inertia of the rotors is included in the total inertia for the carrier; 3) the spinning direction of the reaction wheels is fixed. Thus, the moment exerted by the presence of the spinning components is

$$\boldsymbol{M} = -{}^{i}\boldsymbol{\omega}^{b} \times \boldsymbol{h}_r \quad ,$$

where ${}^{i}\boldsymbol{\omega}^{b}$ is the body angular velocity relative to the inertial frame, written as ${}^{i}\boldsymbol{\omega}^{b} = \omega_1 \hat{\boldsymbol{b}}_1 + \omega_2 \hat{\boldsymbol{b}}_2 + \omega_3 \hat{\boldsymbol{b}}_3$, and $\boldsymbol{h}_r$ is the total relative angular momentum for the reaction wheels, which is expressed in body axes as $\boldsymbol{h}_r = \underset{\hat{b}}{\boldsymbol{h}_r} = h_1 \hat{\boldsymbol{b}}_1 + h_2 \hat{\boldsymbol{b}}_2 + h_3 \hat{\boldsymbol{b}}_3$. The resulting control function is

$$\boldsymbol{g} = \boldsymbol{g}(\boldsymbol{x}, \boldsymbol{h_r}) = \begin{bmatrix} 0_{6\times 1} \\ 0_{4\times 1} \\ -\boldsymbol{\omega} \times \boldsymbol{h}_r \end{bmatrix} \quad .$$

Similar to the MH model, the control path is divided into different sub-arcs; the current strategy assumes the utilization of reaction wheels spinned at a constant rate during each segment. Consistently, the strategy is named Angular momentum Hold (AH). The wheel spin rates can vary from one arc to the other. The command input is, then, a sequence of control spin rates, rather than a sequence of moments or sail orientation configurations. The constraint function is identical to Eq. (7.35), while the free variables vector is simply modified to replace the control moment vectors, $\boldsymbol{M}_j$, with relative angular momentum vectors, $\boldsymbol{h}_{r,j}$, yielding

$$\boldsymbol{X} = \begin{bmatrix} \boldsymbol{x}_{\text{orb},2} \\ {}^i\boldsymbol{q}_2^b \\ {}^i\boldsymbol{\omega}_2^b \\ \vdots \\ \boldsymbol{x}_{\text{orb},N-1} \\ {}^i\boldsymbol{q}_{N-1}^b \\ {}^i\boldsymbol{\omega}_{N-1}^b \\ \boldsymbol{h}_{r,1} \\ \vdots \\ \boldsymbol{h}_{r,N-1} \end{bmatrix}, \tag{7.40}$$

For the computation of the B_{xy} block for the STM, accordingly to Eq. (7.8), the partials for the control function, $\boldsymbol{g}$, are necessary. Relative to the control variables, $\boldsymbol{h}_r$, the partials for the control function are

$$\frac{d\boldsymbol{g}}{d\boldsymbol{h}_r} = \begin{bmatrix} & 0_{6\times 3} & \\ & 0_{4\times 3} & \\ 0 & \omega_3 & -\omega_2 \\ -\omega_3 & 0 & \omega_1 \\ \omega_2 & -\omega_1 & 0 \end{bmatrix}, \tag{7.41}$$

whereas, the partial with respect to the state variables are written as

$$\frac{d\boldsymbol{g}}{d\boldsymbol{x}} = \begin{bmatrix} 0_{6\times 10} & & 0_{6\times 3} & \\ 0_{4\times 10} & & 0_{4\times 3} & \\ & 0 & -h_3 & h_2 \\ 0_{3\times 10} & h_3 & 0 & -h_1 \\ & -h_2 & h_1 & 0 \end{bmatrix} \tag{7.42}$$

The definition for the A_{xx} sub-matrix is known from the FCM incorporating solar pressure. The blocks A_{yx} and B_{yy} are null, because of the assumption for constant angular momentum along each arc (i.e., $\dot{\boldsymbol{h}}_{\boldsymbol{r}} = \mathbf{0}$).

8. SOLAR SAILING: APPLICATION TO A SIMPLE STATION KEEPING SCENARIO IN THE SUN-EARTH SYSTEM

Some spacecraft configurations, such as solar sails, offer the possibility to direct the orbital path by controlling the orientation of the vehicle. In this context, the attitude dynamics may be incorporated into the guidance law at different stages of the design process and levels of information. The Turn and Hold (TH) model is a classical approach to the determination of solar sails trajectories. The TH strategy is also predominantly focused on the orbital motion, which, next, defines the attitude profile. Guidance algorithms alternative to the TH approach, ones that simultaneously consider orbit and attitude dynamics, are tested on a simple, representative scenario. A solar sail may, for example, be employed to maintain the vicinity of a reference orbit, potentially reducing the consumption of propellant for station keeping. As a simplification for a station keeping operation, the guidance strategy attempts to mitigate an initial perturbation to the nominal orbit within one revolution, and target a final state along the reference.

Successfully counteracting the initial errors in position and velocity for a basic orbit correction maneuvering, is preliminary to studies for more realistic applications, and may aid the early identification of benefits and flaws for a new guidance scheme. For example, long-term strategies tend to target final conditions many revolutions downstream the orbit and, generally, offer more robust predictions. Even if long-term strategies are not currently examined, concatenation and a moving horizon are simple ways to effectively extend a short-term strategy to a longer time window. In a similar manner, an open-loop controller may be converted to a closed-loop guidance.

8.1 Reference Orbit and Targeting Conditions

An orbit, periodic relatively to the CR3BP rotating frame, is selected as a reference trajectory for a simple station keeping operation, to test the implementation of different guidance strategies for solar sailing. A reference path is identified in the Sun-Earth system, one that is periodic when a flat, perfectly reflective solar sail is included, and maintained orthogonal to the incoming flux of photons.

A halo orbit type of behavior is chosen within the Sun-Earth systems. A family of trajectories that resembles the halo dynamics within the unperturbed CR3BP, exists in the Sun-Earth system, also when an ideal flat solar sail is added. That motion is referred as modified halos. Despite the inclusion of the Solar Radiation Pressure (SRP), the perturbed CR3BP dynamical model for the Sun-Earth system is autonomous, under the current assumptions, which allows the existence for solutions that are linked to dynamical structures for the original problem. The Sun-Earth system is a representative environment for several current solar sail mission proposals, and halo orbits are, also, often adopted as an initial baseline for the terminal destination. It seems, therefore, reasonable to select this type of reference motion.

Modified halo orbits are a three-dimensional type of periodic trajectories (as observed in the rotating frame) that originate from the classical CR3BP, and are then modified to preserve periodicity under the solar radiation perturbation. Richardson develops a third-order approximation for a small halo orbit in the vicinity of the equilibrium collinear points [89]. As discussed by McInnes [61], the coefficients of the Richardson's approximation for halo orbits can be modified to include the solar sail force generated by a flat and perfectly reflective surface within the Sun-Earth system. The modified coefficients for the Richardson's formula are constructed upon the further assumption that the sail is constantly orthogonal to the Sun-light direction throughout its motion. The approximation available in McInnes' work [61] is successfully employed as an initial guess to generate a family of precisely periodic modified halo orbits near the L_1 equilibrium point, one that is depicted in Figure 8.1. Note that, the location for the equilibrium points is also artificially translated as a consequence for the solar radiation pressure [59]. Details on the construction of this family are also accessible in [61]. The modified trajectories in Figure 8.1 correspond to a sail with lightness parameter $\beta = 0.035$. Such a value is comparable to the performance for the solar sail concept recently proposed in the Sunjammer mission [72]. Families of modified halo orbits within the Sun-Earth system can be easily constructed for a wide range of sail lightness factors, including values corresponding to currently feasible design solutions, and members of different size can be selected as a reference to preliminary demonstrate the guidance schemes.

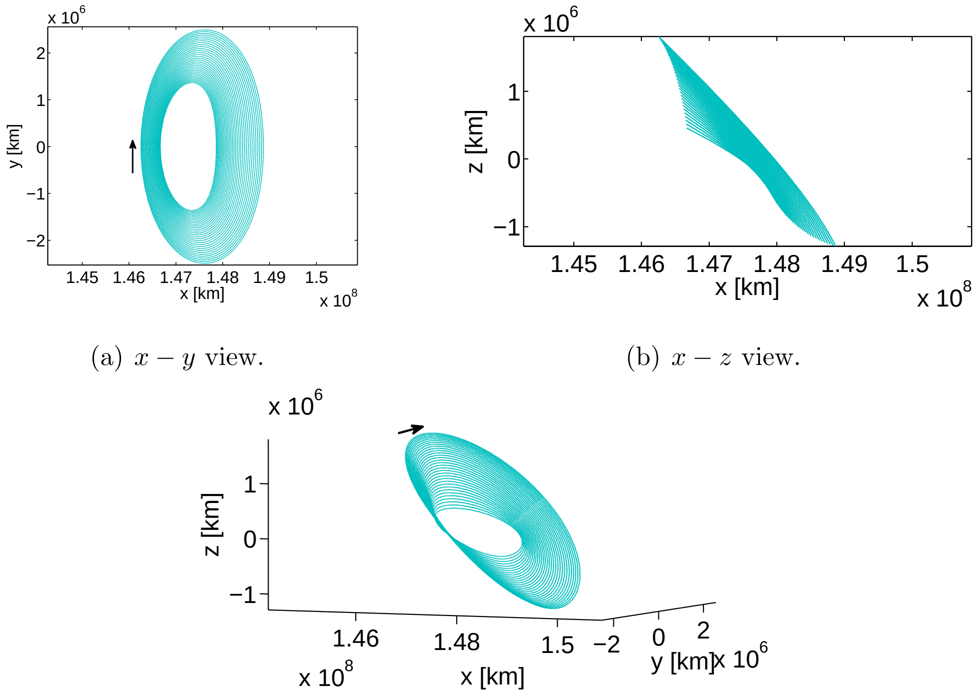

(c) Three-dimensional view.

Figure 8.1. Family of modified halo orbits near the L_1 libration point in the Sun-Earth system for $\beta = 0.035$.

In general, navigation and injection errors, or other unmodelled perturbations, cause the trajectory for a solar sail to diverge from the reference path, and their consequences may be further amplified by unstable manifolds in vicinity of the nominal trajectory. This phenomenon is quite common in dynamics associated with the CR3BP and it is also evident in a simple scenario. Consider a large and a small member of the L_1 modified halo family, which are displayed in Figure 8.2. The larger orbit has amplitude $A_z = 1.8 \times 10^7$ km and period $P = 269.41$ days; the smaller orbit has amplitude $A_z = 7.9 \times 10^5$ km and period $P = 268.90$ days. Identify the crossing of the orbit with the $x-z$ plane with positive y velocity relative to the rotating frame. For the trajectories in Figure 8.2, such a crossing corresponds to a positive z position component. At the selected crossing, introduce errors in the position and velocity

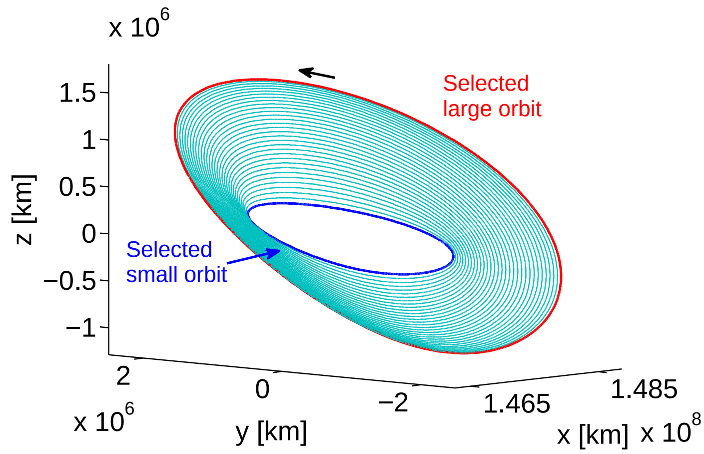

Figure 8.2. Selected modified L_1 halo orbits in the Sun-Earth system for $\beta = 0.035$.

vectors. These errors may be representative of injection errors or orbit determination uncertainties. An error of 5×10^{-4} nondimensional units (i.e., approximately 75000 km) is independently applied to each position component; an error of 1×10^{-4} nondimensional units (i.e., approximately 3 m/s) is individually applied to each velocity component. Such error levels are arbitrarily selected, and do not constitute a reference for the navigation of solar sails within the Sun-Earth system. They are, however, chosen conservatively, as better accuracy is most likely expected for an actual solar sail mission implementation. Consequent to the perturbation of the initial position and velocity vector, the motion departs from the nominal path as portrayed in Figure

8.3, for both large and small modified L_1 halo orbits. Observing Figure 8.3, a guidance algorithm is necessary to direct the spacecraft toward a final state sufficiently near the reference path. For this discussion, each guidance strategy is tested on its capability to target a final position and velocity equal to the unperturbed state at the crossing, within a given tolerance. The final time may be fixed or variable, but in general comparable to one revolution along the original orbit.

Modified halo orbits in vicinity of the Sun-Earth L_1 equilibrium point are selected as a representative environment to preliminary explore different guidance strategies for solar sails, ones that incorporates attitude dynamics. In fact, as demonstrated on a small and a large modified halo orbit, when position and velocity errors are added to the initial state, the motion quickly diverges from the nominal path, and supplies a simple test bed for a control scheme possibly useful in station keeping.

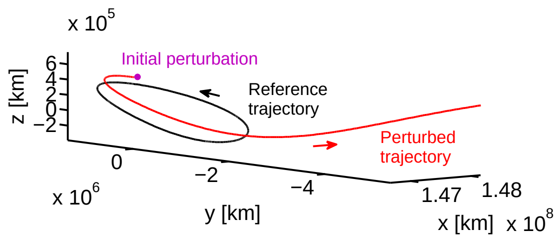

(a) Small orbit.

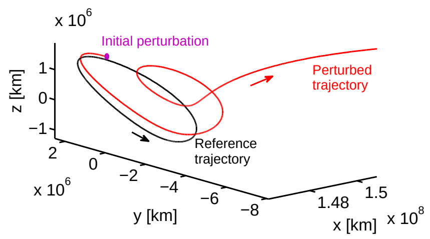

(b) Large orbit.

Figure 8.3. Trajectory departure due to position and velocity errors on the initial conditions.

8.2 Results for the Turn and Hold Guidance

To compensate an initial error in the position and velocity vector, a TnH guidance may be implemented to maintain the sailcraft in vicinity of its nominal path. The TnH scheme supplies a steering law based on the assumption that the sail pointing is fixed relative to a reference direction along the control arc, and an instantaneous reorientation of the vehicle is possible at the beginning of that arc.

8.2.1 Pointing Direction Fixed Relative to the Sun-Light Direction

The TnH guidance may be implemented fixing the orientation for a solar sail relatively to the Sun-light direction along each control segment. That is a common practice for TnH applications.

The objective for the TnH scheme, within a simple scenario, is to correct the paths in Figure 8.3, that correspond to perturbed trajectories departing from a small and a large modified L_1 halo within the Sun-Earth system. As described in the previous section, the TnH algorithm is formulated as a multiple shooting problem, which is solved via Newton-Raphson updates. The TnH approach is sufficiently robust, in general, to construct a viable solution starting from a poor initial guess, and using a small number of control segments. For example, the solutions in Figure 8.4, that reflects different size for the nominal orbit, are converged using 5 patch points or, equivalently, 4 control segments. Figure 8.4 demonstrates the efficacy of a TnH guidance applied to a simplification for a station keeping problem.

Corresponding to Figure 8.4, the control input for the TnH guidance is a sequence of orientation configurations that are defined with respect to the direction for the solar radiation. The pointing for the spacecraft may be described by the unit vector normal to the sail surface, $\hat{\boldsymbol{u}}$, as written in Eq. (7.17) relatively to the Sun-light frame. Nominally, the unit vector $\hat{\boldsymbol{u}}$ is aligned with the incoming direction of the photons flux, $\hat{\boldsymbol{\ell}}_1$; equivalently, the measure numbers for the unit vector $\hat{\boldsymbol{u}}$, written in the Sun-light frame, are $u_1 = 1$, $u_2 = 0$, and $u_3 = 0$ along the reference path. When a perturbation is added to the initial position and velocity, the TnH guidance computes adjustments to u_1, u_2, and u_3 to correct the trajectory, substantially reorienting the solar sail. For the selected reference orbits and error level, the control input sequence is displayed in Figure 8.5. A quick estimate for the cone angle between the sail normal and the Sun-light unit vector, $\hat{\boldsymbol{\ell}}_1$, is $\alpha = \arccos(u_1)$. Accordingly, a normal component $u_1 \approx 0.9985$ (such as for the first control segment in Figure 8.5(b)) corresponds to shifting the vehicle pointing of about 3.1 deg from the nominal direction. Small adjustments

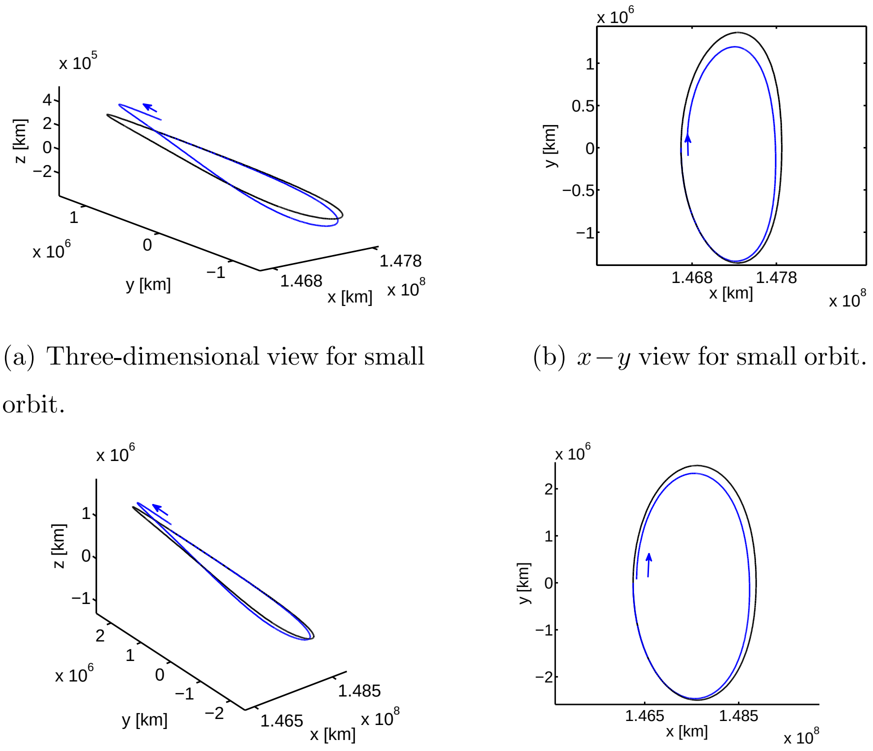

(a) Three-dimensional view for small orbit.

(b) $x - y$ view for small orbit.

(c) Three-dimensional view for large orbit.

(d) $x - y$ view for large orbit.

Figure 8.4. Trajectory for a TnH guidance applied to modified L_1 halo orbits in the Sun-Earth system for $\beta = 0.035$.

of the pointing direction relative to the Sun-light direction seem to be frequently observed during the implementation of TnH strategies [84]. A precise reconstruction of the entire spacecraft orientation also involves the components u_2 and u_3, as well as a definition for the initial spin angle of the body about the $\hat{\boldsymbol{u}}$ direction. Although the measure numbers u_1, u_2, and u_3 are constant along a control arc, as obvious in Figure 8.5, an inertial observer experiences a continuous rotation of the sail; such rotation is necessary to maintain a constant attitude relative to the Sun radiation direction (which is not inertially fixed). Consistently with the revolution of the Earth about the Sun, the solar sail rotation is equal 1 deg/day, in a very first approximation. This turn rate is not generally problematic, but a continuous time-varying control moment is required to follow the desired attitude configuration along each segment. On a 50 days control segment, such that may be employed along a modified L_1 halo orbit, a 50 deg rotation for the sailcraft relative to an inertial reference is, in fact, necessary. Additional reorientation maneuvers correspond to the discontinuities within the u_i profile. A variation of u_i reflects, in fact, a new attitude configuration. In Figure 8.5 each re-alignment for the sail, matching the gaps evident in the u_i history, is within a 5 deg cone from the previous pointing direction. Even for a maximum turn rate, that is limited by a solar sail structural characteristics (e.g., a turn rate of 0.02 deg/s is reported in [88]), a rotation of 5 deg seems obtainable within a short time interval. If such time interval is sufficiently short when compared to the length of the following control arc, then, the reorientation process may be reasonably represented by a point discontinuity within the overall orientation history. In conclusion, a TnH guidance that is associated with a control input similar to Figure 8.5, depends on the precise determination of the Sun-light direction, fast (as compared to the time scale for the selected dynamics) attitude maneuvers at the origin of the control segments, and maintenance of a solar sail alignment fixed in a reference frame.

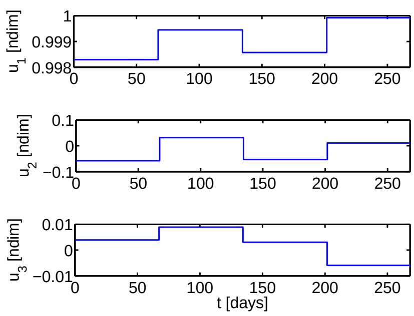

(a) Small orbit.

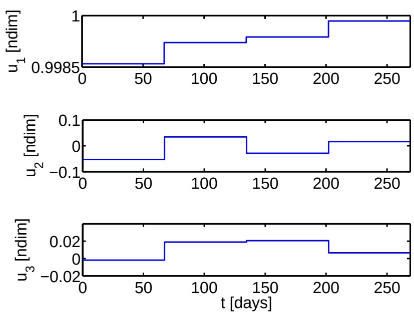

(b) Large orbit.

Figure 8.5. Control input sequence for a TnH guidance, with solar sail orientation fixed relatively to the Sun-light direction along each control segment.

The TnH strategy, implemented for a constant solar radiation incidence angle along each control arc, successfully counteracts the initial perturbation within the selected scenario.

8.2.2 Pointing Direction Fixed Relative to the Inertial Frame

The TnH guidance may also be implemented by fixing the solar sail orientation relatively to an inertial observer. This control scheme may be more practical for a larger range of mission applications.

Similar to the previous application, the objective for the TnH scheme, is to correct the paths in Figure 8.3, that correspond to a perturbed trajectory departing from a small and a large modified L_1 halo within the Sun-Earth system. The multiple shooting problem, is adjusted to accommodate a fixed pointing direction in the inertial frame. Solutions to the control problem still exist, with two examples of converged trajectory in Figure 8.6, but require, in general, a larger number of control segments. As a TnH guidance formulated in the Sun-light frame is numerically more robust, it may be employed to generate an initial guess for a TnH scheme written in the inertial frame. The control input is a sequence of attitude configurations that are

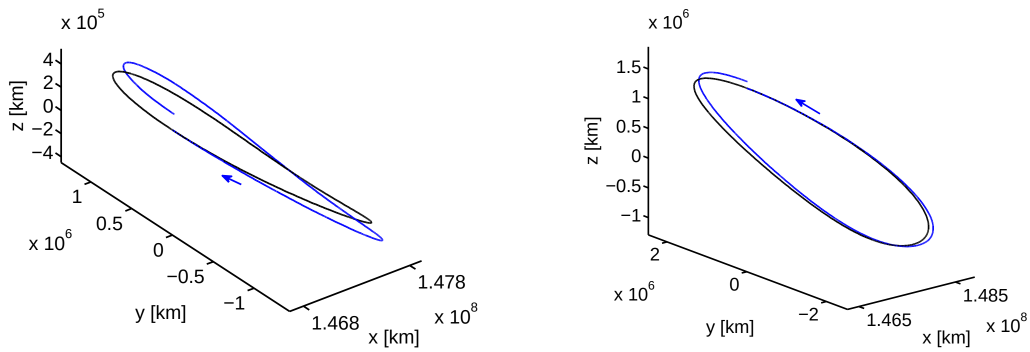

(a) Small orbit. (b) Large orbit.

Figure 8.6. Trajectory for a TnH guidance formulated in a inertial frame and applied to modified L_1 halo orbits in the Sun-Earth system for $\beta = 0.035$.

fixed in the inertial frame. Corresponding to the controlled trajectories in Figure 8.6, the components of the quaternion vector that are plotted in Figure 8.7 describe the inertial orientation of the spacecraft. As evident in this figure, the quaternion vector, which is represented by its components, remains unchanged along each control arc. That reflects an inertially fixed orientation for the vehicle. On the contrary, the gray curve is the initial guess for the control input generated with a TnH algorithm that is formulated in the Sun-light frame. Naturally, the TnH scheme written for the Sun-light frame does not produce a sequence of constant attitude configurations relative to an inertial reference. Equivalently, the spacecraft orientation may be displayed relative to the solar radiation direction by defining the sail normal unit vector, $\hat{\boldsymbol{u}}$, and its components in the Sun-light frame, as in Figure 8.8. Referring to the figure, the blue curves are the inertial pointing solution and the gray curves are again the initial guess. The blue curve for u_1 reveals that, to maintain a fixed inertial orientation, the sail normal forms an angle $\alpha = \arccos(u_1)$ with the indecent flux direction that may increase up to approximately 16 deg during a control arc, for the selected simulation. A longer arc corresponds to a larger drift for the pointing direction in the Sun-light reference, with a limiting incidence angle, α, equal to 90 deg, when the sail reflective surface becomes parallel to the solar rays, and hence, ineffective to direct the path. Additionally, at the connection of adjacent control arcs, correction manuevures that require a vehicle to realign its pointing direction are noted in the control profile in Figure 8.8, with a maximum reorientation of 20 deg.

The TnH strategy, implemented as a sequence of inertially fixed attitude configurations, successfully counteracts the initial perturbation within the selected scenario. An orientation fixed in an inertial frame is generally less complex to implement, and its acquisition may be facilitated by spinning the solar sail or introducing some internal rotating parts, that are commonly used for attitude control. It may, however, be a less efficient exploitation of the solar sail thrusting capabilities, as the angle relative to the direction of the incoming radiation flux varies along the control arc, and does not necessarily reflects an optimal configuration. Also, larger and more numerous

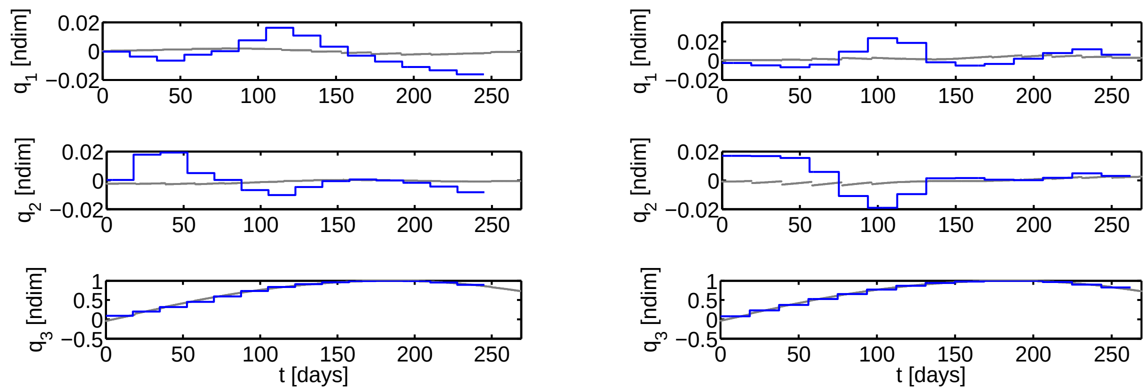

(a) Small orbit.

(b) Large orbit.

Figure 8.7. Control input sequence for an inertial TnH guidance, as experience by an inertial observer.

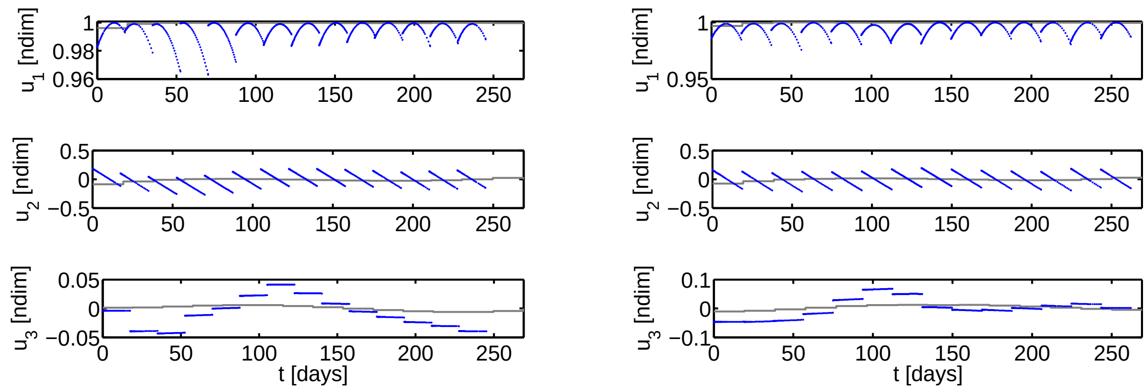

(a) Small orbit.

(b) Large orbit.

Figure 8.8. Control input sequence for an inertial TnH guidance, as experience by an observer fixed in the Sun-light frame.

reorientation maneuvers seem to be required along the path to target a desired final state, which may increase the complexity of the attitude control mission profile.

8.3 Results for the Turn and Hold Guidance with Attitude Dynamics

The series of attitude configurations that constitute a TnH control law are artificial. When the natural attitude dynamics are incorporated, the TnH guidance information cannot be directly leveraged to direct the sail motion, and therefore, the control scheme needs further elaborations.

If the TnH corrections are applied within the coupled orbit-attitude model, the sail most likely will depart, rather than approach, the reference orbit [20]. In Figure 8.9, a display for a representative outcome is presented. The back curve denotes the reference trajectory, the red curves are the arcs propagated from the control points within the coupled orbit-attitude dynamics. The sailcraft is modelled as an axisymmetric disk with inertia ratio $k = 0.4$. The motion in Figure 8.9 demonstrates that, allowing the natural orbit-attitude dynamics dominates the response, and jeopardize the decoupled TnH guidance.

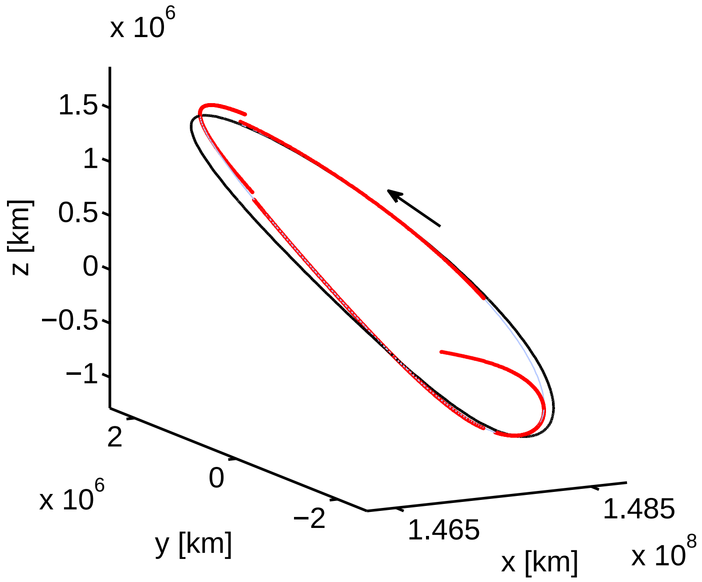

Figure 8.9. TnH corrections applied within the natural coupled orbit-attitude model nearby a modified, large L_1 halo orbit in the Sun-Earth system.

Two different approaches are, next, discussed to embrace the coupled orbit-attitude dynamics within the context of a TnH guidance.

8.3.1 Conversion for the TnH Guidance

The decoupled TnH guidance supplies a pointing history for the sail that steers the vehicle along a desired path. A control torque may be computed to impose the pointing direction within the coupled orbit-attitude model and, consequently, enable the spacecraft to follow a path set by the decouple TnH solution.

Information on the spacecraft orientation at any instant of time along a control segment, in the form of sail normal direction, $\hat{\boldsymbol{u}}$, may be converted to torque commands to obtain an equivalent response within the orbit-attitude dynamics. Outline of the conversion process follows:

1. Determine the body orientation in terms of the selected kinematics variables from the given sail normal direction. For example, transform the pointing vector $\hat{\boldsymbol{u}}(t)$ to the quaternion vector ${}^{i}\boldsymbol{q}^{b}(t)$ as described in Section 7.4.1.

2. Numerically estimate the time derivatives for the kinematics variables. Use, for example, a finite difference formula, such as

$$ {}^{i}\dot{\boldsymbol{q}}^{b}(t_i) = \frac{{}^{i}\boldsymbol{q}^{b}(t_{i+1}) - {}^{i}\boldsymbol{q}^{b}(t_i)}{t_{i+1} - t_i} \quad . $$

3. Derive the body angular velocity from the derivative of the kinematic variables. If employing a quaternion representation,

$$ {}^{i}\boldsymbol{\omega}^{b}(t) = 2E({}^{i}\boldsymbol{q}^{b})\,{}^{i}\dot{\boldsymbol{q}}^{b}(t) \quad , $$

where

$$ E({}^{i}\boldsymbol{q}^{b}) = \begin{bmatrix} q4 & q3 & -q2 & -q1 \\ -q3 & q4 & q1 & -q2 \\ q2 & -q1 & q4 & -q3 \end{bmatrix} \quad . $$

4. Numerically estimate the time derivative for the body angular velocity. Use, for example, a finite difference formula, such as
$$ {}^{i}\dot{\boldsymbol{\omega}}^{b}(t_i) = \frac{{}^{i}\boldsymbol{\omega}^{b}(t_{i+1}) -^{i} \boldsymbol{\omega}^{b}(t_i)}{t_{i+1} - t_i} \quad . $$

5. Compute the control moment vector,
$$ \boldsymbol{M} = I^{i}\dot{\boldsymbol{\omega}}^{\boldsymbol{b}} +^{i} \boldsymbol{\omega}^{b} \times I^{i}\boldsymbol{\omega}^{b} - \boldsymbol{M_e} \quad , $$
where $\boldsymbol{M_e}$ denotes the remaining known environment torques, and I is the principal inertia tensor. It is evident from the equation that, the resulting control action is a function of the desired spacecraft attitude dynamics, as well as the vehicle mass distribution and the external moments.

This process is potentially applicable to transition any decoupled TnH solution to a coupled orbit-attitude model. Considering, for example, the TnH driven path in Figure 8.4(c), convert the history for the pointing direction to a torque that would enable an equivalent response. The magnitude for the resulting torque, consistent with the selected TnH orbit and a disk-like spacecraft with inertia ratio $k = 0.4$, is plotted in Figure 8.10. Upon the application of the control moment correspondent with Figure 8.10 within the coupled orbit-attitude dynamics, the trajectory in Figure 8.11 is created, and appears to follow the original decoupled TnH baseline. Figure 8.11 compares directly to Figure 8.9, the latter representing the decoupled TnH guidance applied within the natural coupled dynamics (i.e., without adding a control moment). A realignment for the pointing direction is still included at the origin of each control arc, as reflected in the discontinues for moment curve in Figure 8.10. A gap that is encountered along the moment profile, indicates an instantaneous reorientation for the sailcraft. The attitude dynamics for such rotational maneuvers is not accurately modelled. These maneuvers are assumed fast relative to the time length of the subsequent control arc, so to be reasonably represented by point discontinuities.

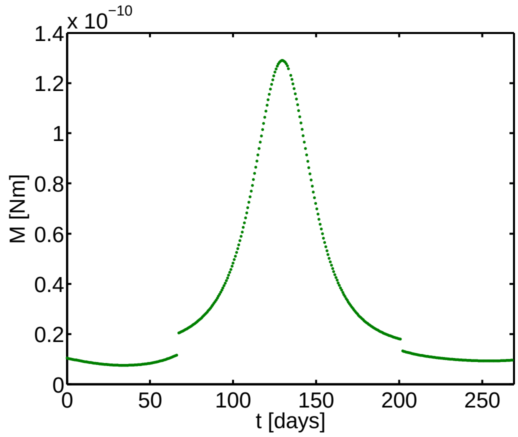

Figure 8.10. Magnitude for the torque vector producing an equivalent decoupled TnH guidance for a modified, large L_1 halo orbit in the Sun-Earth system.

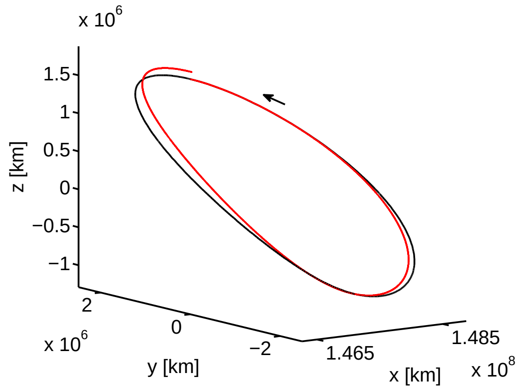

Figure 8.11. Trajectory equivalent to a decoupled TnH solution when incorporating a control torque in a coupled orbit-attitude dynamics nearby a modified, large L_1 halo orbit in the Sun-Earth system.

The application of a properly defined control torque, appears to effectively reproduce the trajectory engineered within the sole orbital dynamics model. The efficacy of a decoupled TnH control law transitioned to a coupled orbit-attitude model depends on the approximations introduced during the conversion process (e.g., the accuracy for the finite difference scheme), the knowledge for environmental disturbances, and the confidence in estimating the spacecraft characteristics. For simplicity, the transition from the decouple TnH guidance to a coupled orbit-attitude control scheme is presented via an open-loop solution for the control torque, however, a closed-loop control scheme may also be easily implemented.

8.3.2 TnH Guidance within a Coupled Orbit-Attitude Model

A strategy, alternative to the augmentation of a decoupled TnH guidance with a control torque, is the direct inclusion of the coupled orbit-attitude dynamics within the design process. This approach is described in Section 7.4.

Consider a solar sail that possesses a relevant angular momentum component along the direction normal to the reflective surface. Such angular momentum aligning with the sail normal, may be representative for a spinned solar sail or for internal fast-rotating parts. In this context, the natural attitude dynamics may be a dominant factor during the path control. Rather than adjusting afterwards the natural attitude dynamics with the addition of a time-varying control torque throughout each trajectory arc, design a sequence of orientations that already balances the natural rotational behavior, while steering the spacecraft along the desired path. Following an instantaneous and artificial modification of the pointing direction, the spacecraft rotates accordingly to the natural flow and does not, in general, maintain a fixed direction relative to any selected reference (as it does for the decoupled TnH guidance). Figure 8.12 presents the converged trajectories for a disk-like sail with inertia ratio $k = 0.5$ that is initially displaced, in terms of both potion and velocity, from the nominal orbit, and selecting two representative modified L_1 halo orbits as a reference. A sail angular momentum component equal to 10 nondimensional units along the sail normal direction is assumed. Initial guess may be provided by the solution for the decoupled TnH algorithm. Figure 8.13 portrays the attitude history as described by the quaternion vector relative to the inertial frame. That profile comprises both reorientation events, and subsequent natural evolution of the attitude configuration.

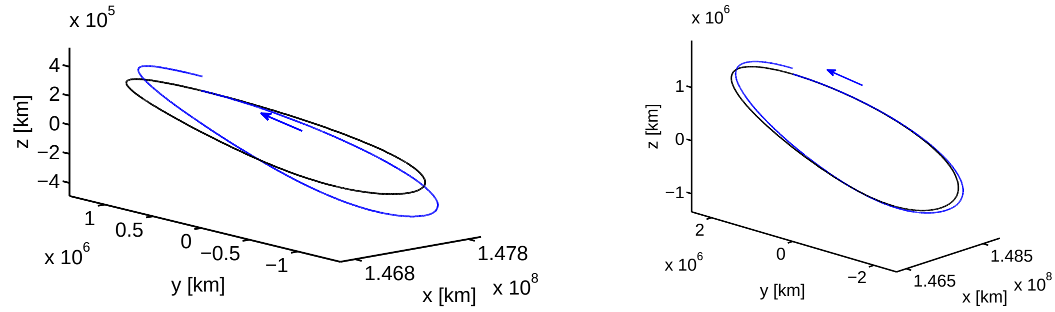

(a) Small orbit.

(b) Large orbit.

Figure 8.12. Trajectory for a coupled orbit-attitude TnH guidance applied to modified L_1 halo orbits in the Sun-Earth system for $\beta = 0.035$.

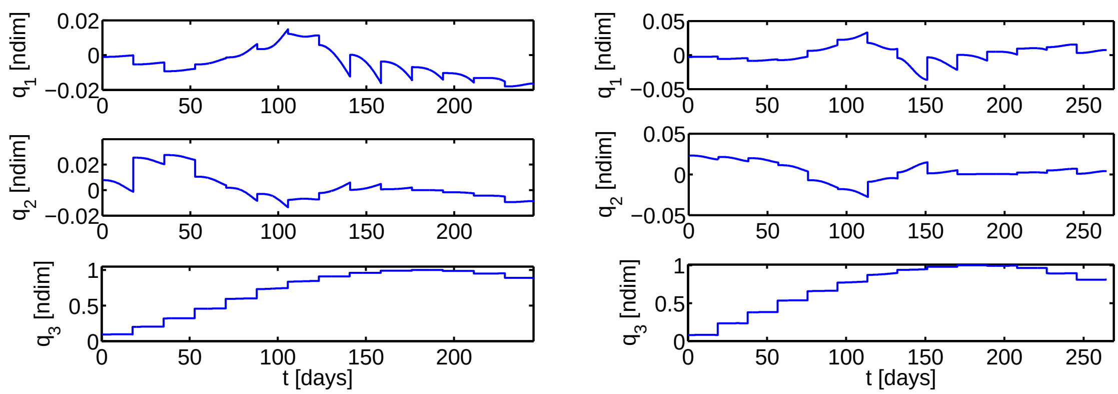

(a) Small orbit.

(b) Large orbit.

Figure 8.13. Inertial spacecraft orientation via the quaternion vector for a coupled orbit-attitude TnH guidance applied to modified L_1 halo orbits in the Sun-Earth system for $\beta = 0.035$.

Ideally (i.e., neglecting any perturbation to the selected dynamical model and uncertainties in the state variables), the trajectories in Figure 8.12 do not require any additional control action following a sail realignment. This example, that is generally presenting the case for a spinned solar sail, demonstrates the possibility to directly leverage the natural attitude dynamics information within the series of orientation configurations that guide the spacecraft along a desired path. This approach may be a good compromise between the numerical robustness of a decoupled TnH guidance and a simplification of the attitude control scheme, one that is possible via a more accurate coupled dynamics description at the early stages of the design process.

A sailing strategy, that is constructed expanding the idea of sail pointing reconfigurations to enable natural orbit-attitude dynamics along each control segment (idea original to the decoupled TnH guidance), is demonstrated feasible for the selected simple station keeping application.

8.4 Results for the Moment Hold Guidance

Within a coupled orbit-attitude model for the spacecraft dynamics, a guidance strategy may be constructed to directly employ attitude inputs, such as a constant control torque, and smoothly maneuver the solar sail. Point adjustments for the sail orientation may be eliminated with a proper torque profile. When torques that are constant along each control segment are employed, the guidance is named Moment Hold (MH).

As the dynamical model acquires more complexity and the number of state variables increases, the correction process becomes more sensitive, numerically. As a consequence, the identification for a desired solution critically depends on a more accurate initial guess. In particular, an initial estimate for the control input is needed, i.e., an estimate for the the control moment. A decoupled TnH solution is generally available and may be converted to an equivalent control torque profile, as in Figure 8.10. Information contained in a plot similar to Figure 8.10 may serve as a basis for the initial MH input. A time varying evolution for the control moment may, in fact, be converted to a sequence of constant torques by averaging on the control intervals, and, next used as an initial guess for the MH control input. A torque profile derived from the decoupled TnH guidance generally supplies a good initial guess for the MH strategy. Next, a first trajectory to counteract the initial errors and guide the spacecraft nearby the nominal orbit, is constructed for a centrobaric body. The gravity gradient moment is null when applied on a centrobaric moment. This type of the mass distribution may be not representative for a solar sail or a similar structure, however, it is a convenient initial baseline configuration. Even supplied with a guess from the decoupled TnH algorithm, the correction process may still be numerically too sensitive to converge for any arbitrary spacecraft inertia distribution. Note that, the resulting control moment to steer the sailcraft along the desired path is not null for a centrobaric vehicle, only the gravity gradient torque is. Once a solution is available for a centrobadic body, the correction process may be reiterated through small adjustments for the spacecraft mass distribution, until the desired inertial configuration is achieved. As an example, Figure 8.14 portraits the trajectory obtained via the application of constant control torques, which direct the solar sail to a final state on the reference modified L_1 halo orbit (in black). The corrected paths in Figure 8.14 are displayed for both a centrobaric body (light blue) and a disk-like spacecraft with inertia ratio $k = 0.5$ (dark blue). The corresponding control sequence is presented in Figure 8.15. The control moment vector, represented by its magnitude, remains constant along each arc of the trajectory, which may enable a simplification for the design of the attitude control system in certain applications. Within this specific example, the magnitude of the control torque is significantly small, and may be challenging to reproduce due to a limited precision for the actuating devices. A similar consideration also applies to the control moment resulting from a decoupled TnH approach (see Figure 8.10).

The update equation for the MH algorithm may be modified to facilitate the convergence for the correction process and avoid overshooting. Overshooting is particularly problematic when it affects the quaternion variables. An update that is too large may yield a quaternion component greater than one, hence, in violation of the unitary norm constraint. Then, the update equation revised as

$$\boldsymbol{\xi}_{j+i} = \boldsymbol{\xi}_j + (1 - \theta_j)\boldsymbol{\Delta\xi}_j \quad ,$$

where $\boldsymbol{\Delta\xi}_j$ is the update to the free-variables vector $\boldsymbol{\xi}_j$ at the jth iteration, and θ_j is a penalty factor that may vary at each iteration. For a penalty factor $\theta_j = 0$, the update equation resembles the original formulation. Any penalty value larger than 0

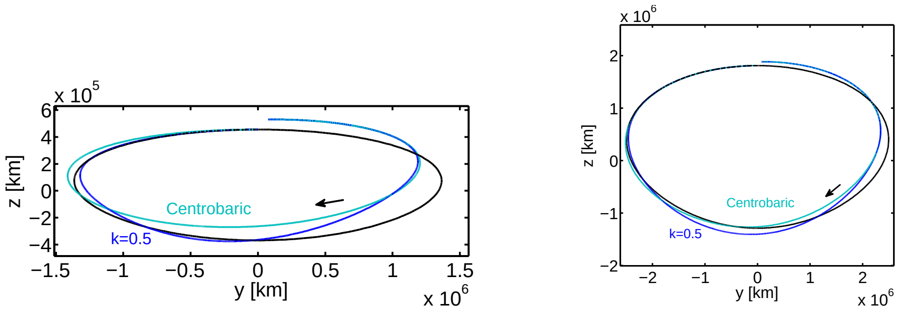

(a) Small orbit.   (b) Large orbit.

Figure 8.14. Trajectory for a MH guidance applied to modified L_1 halo orbits in the Sun-Earth system for $\beta = 0.035$.

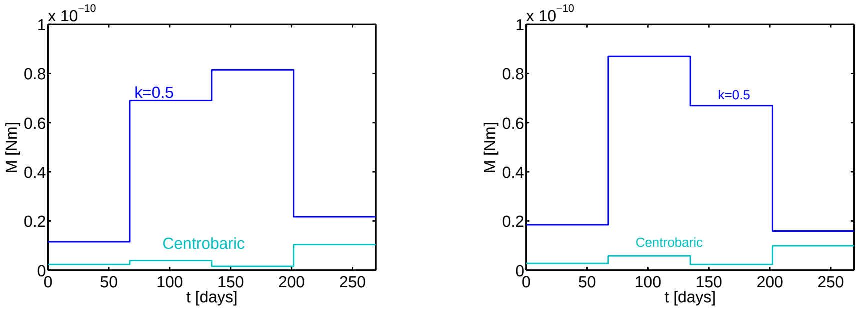

(a) Small orbit.   (b) Large orbit.

Figure 8.15. Control input for a MH guidance applied to modified L_1 halo orbits in the Sun-Earth system for $\beta = 0.035$.

describes a smaller step in the update direction defined by $\boldsymbol{\Delta\xi}$. In the limiting case, for a penalty factor $\theta_j = 1$, there is no adjustment to the current free-variables vector. For the selected examples, the penalty factor is initially set to $\theta_j = 0.75$. When the current iterate is sufficiently near to a viable solution, e.g., $||\boldsymbol{F}|| < 10^{-4}$, the penalty factor may be cancelled ($\theta_j = 0$), to reduce the convergence time. As demonstrated by successfully correcting the orbital path for a motion nearby modified L_1 halo orbits in the Sun-Earth system, a penalized update equation combined with a continuation process for the spacecraft inertia characteristics, effectively aids the construction of a MH guidance for an arbitrary vehicle configuration and reference orbit.

A solar sail is guided along a desired path, returning to a nominal orbit, via the application of control torques that are constant along each trajectory arc. That represents a preliminary demonstration for the possibility of simultaneously developing orbit and attitude control schemes. The numerical challenges associated with natural orbit-attitude dynamics may be worth examination, if they enable a simplification for the control system and lessen the control effort, for example by limiting the necessity of instantaneous reorientation maneuvers. Various instruments, e.g., reaction wheels, are available to produce a control torque along a trajectory arc. Limitations for the MH guidance may connect to the capability of such devices to generate a continuous and constant action along the path.

8.5 Results for the Angular Momentum Hold

Engineering the angular momentum vector is a well-established method to passively, or actively, control a vehicle rotational behavior. A coupled orbit-attitude dynamics may allow to extend the utilization of the angular momentum to steer the orbital path along a desired trajectory, as well. The angular momentum vector may be adjusted by spinning the entire vehicle or some internal components. In this discussion, as described in Section 7.6, the global angular momentum is controlled internally, via rotating parts (as reaction wheels) that modify a component for angular momentum vector relatively to the body frame, $\boldsymbol{h}_r$. Specifically, the relative momentum vector, $\boldsymbol{h}_r$, is hold constant along each control arc, hence, this strategy is denoted as Angular momentum Hold (AH).

Similarly to the MH guidance, the correction process for the AH algorithm requires an accurate initial guess. In particular, an initial estimate for the control input is needed, i.e., an estimate for the relative angular momentum, $\boldsymbol{h}_r$. To construct a viable guess, the decoupled TnH solution for the control problem, that is generally available, is first reconverged as a MH solution for a centrobaric spacecraft. Next, to produce a motion equivalent to the MH guidance, but employing solely reaction wheels that create a relative angular momentum vector, $\boldsymbol{h}_r$, the following differential equation is integrated simultaneously to the orbit-attitude dynamics along the MH trajectory

$$\dot{\boldsymbol{h}}_r = -\boldsymbol{M} - {}^{i}\boldsymbol{\omega}^{b} \times \boldsymbol{h}_r \quad ,$$

where $\boldsymbol{M}$ is the moment originally applied within the MH solution and all vectors are expressed in body axes. A sample time evolution for the relative angular momentum is plotted in Figure 8.16, assuming the MH solution in Figure 8.15 for a large modified L_1 halo orbit within the Sun-Earth system, including both a centrobaric and disk-like vehicle. The time varying history for the relative angular momentum vector, as in Figure 8.16, may be converted to a sequence of constant values by averaging on the control intervals, and employed as an initial guess for the AH control input. Relative angular momentum vectors derived from the MH guidance generally supplies a good initial guess for the AH strategy.

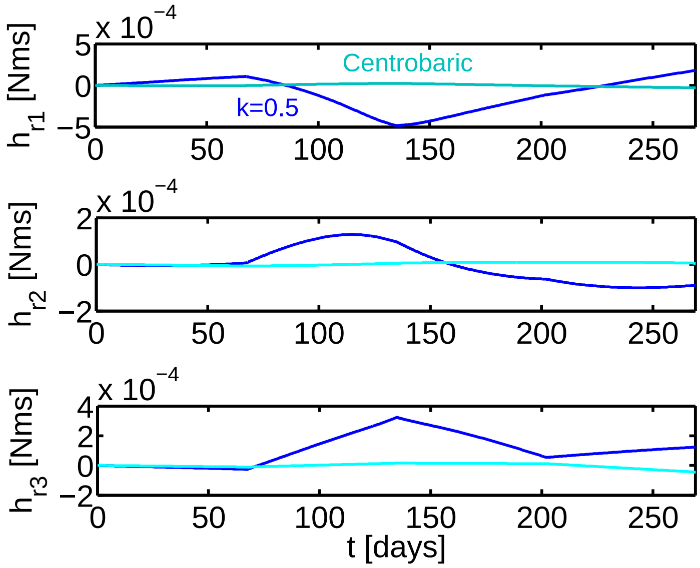

Figure 8.16. Relative angular momentum vector producing an equivalent MH guidance for a modified, large L_1 halo orbit in the Sun-Earth system.

An initial guess is typically not precisely continuous, nor does accurately meet the final conditions on the path. Then, iterative adjustments for the state variables at the patch points and for the relative angular momentum vector along each control arc follow. The correction process may be implemented as a multiple shooting algorithm. Similarly to the MH scheme, inclusion of a penalty factor into the update equation and continuation from a centrobaric solution may aid the construction for the desired motion. A time varying formulation may be considered, as well. Despite the improvements granted by those modifications, the AH algorithm still experiences critical, numerical challenges. The remaining principal cause of failure appears to be an overshoot for the quaternion variables, q_1, q_2, and q_3, that are updated during the correction process. Consider to represent the evolution for the selected independent quaternion components q_1, q_2, and q_3 along the trajectory as the radial distance from the origin, $\sqrt{q_1^2 + q_2^2 + q_3^2}$, plotted versus the elapsed time from the initial epoch, as depicted in Figure 8.17. The radial distance from the origin, $\sqrt{q_1^2 + q_2^2 + q_3^2}$, is never larger than 1, consistently with the unitary norm constraint equation that defines the complete quaternion vector. The unitary norm constraint is represented as an horizontal boundary in Figure 8.17. Observing that figure, the curve for the radius $\sqrt{q_1^2 + q_2^2 + q_3^2}$ may become tangent to the unitary boundary at some time instant along the trajectory. If a patch point is located nearby the tangency condition, there exist the possibility that, updating the quaternion variables q_1, q_2, and q_3 via a linear prediction, such as that employed within the Newton-Raphson method, violates the unitary norm constraint, and triggers the failure of correction process. Simply ignoring updates that trespass the unitary limit is not necessarily effective, as it introduces a discontinuity in the linear variations for the constraint vector relative to variations for the free-variables. Discontinuous variations are generally challenging within a correction process. Modifying the orientation of the vehicle at the initial epoch may enable to avoid tangency conditions along the trajectory. Recall that, for a given pointing direction, the sail orientation is undefined for rotations about the pointing axis and, for instance, arbitrarily determined by the vector $\boldsymbol{v}$ in Eq. (7.27).

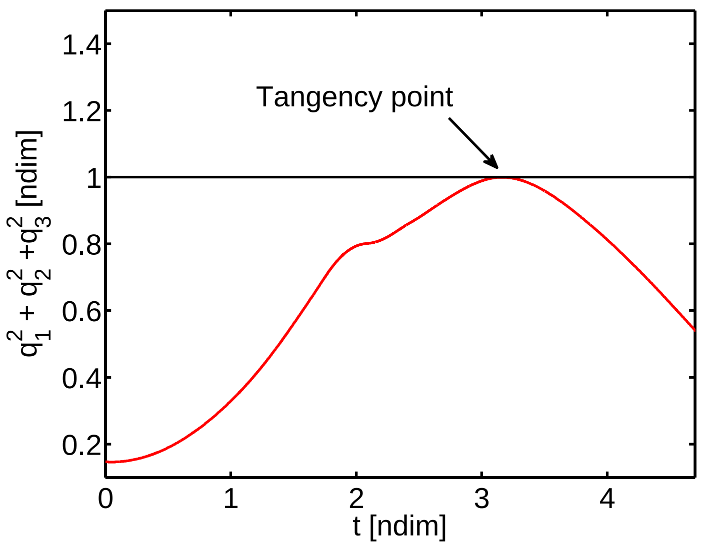

Figure 8.17. Evolution for quaternion vector components along the trajectory.

In certain applications, it is possible to select the vector $\boldsymbol{v}$ (i.e., the initial spin angle about the pointing direction) to elude the encounter of tangency conditions along the trajectory. Small updates, continuation procedures, and selective choice of the initial orientation effectively facilitate the convergence for the AH algorithm. Modification to the current AH implementation is, however, warranted to incorporate a more conclusive treatment for the tangency condition. A different representation for the spacecraft attitude during the correction process, one that is not bounded to a unitary constraint, may be considered.

As an example, the orbit-attitude motion nearby a modified, large L_1 halo orbit is considered. A converged solution for a disk-like solar sail with inertia ratio $k = 0.5$ is depicted in Figure 8.18. The application of a constant angular momentum vector along each arc guides the solar sail toward the precise final injection into the nominal orbit. The corresponding control history is displayed in Figure 8.19. A constant relative angular momentum is a simple control input, commonly implemented via reaction wheels. Internal rotors may, however, not represent a viable option for large, fast spinning solar sails. Regardless of the instrument that enables the control action, the AH guidance preliminary demonstrates the possibility to elaborate the coupled orbit-attitude design approach to include different forms for the control input, that were not possible within the decoupled TnH strategy.

In conclusion, the sailcraft is directed along the desired path implementing an AH guidance. The natural orbit-attitude dynamics are leveraged to further simplify the control input, along with assuming a specific class of actuators. As currently implemented, this strategy does not appear sufficiently robust, numerically, to extend its application within a large span of possible scenarios. An enhanced algorithm is warranted to strengthen the convergence performances for the AH guidance.

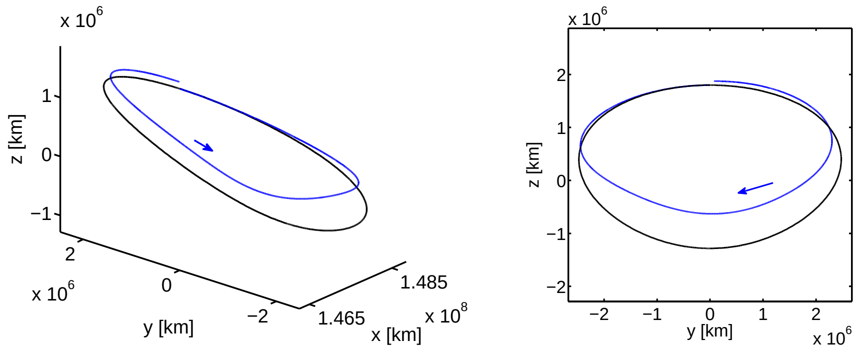

(a) Three-dimensional view. (b) $y - z$ view.

Figure 8.18. Trajectory for a AH guidance applied to modified, large L_1 halo orbits in the Sun-Earth system for $\beta = 0.035$.

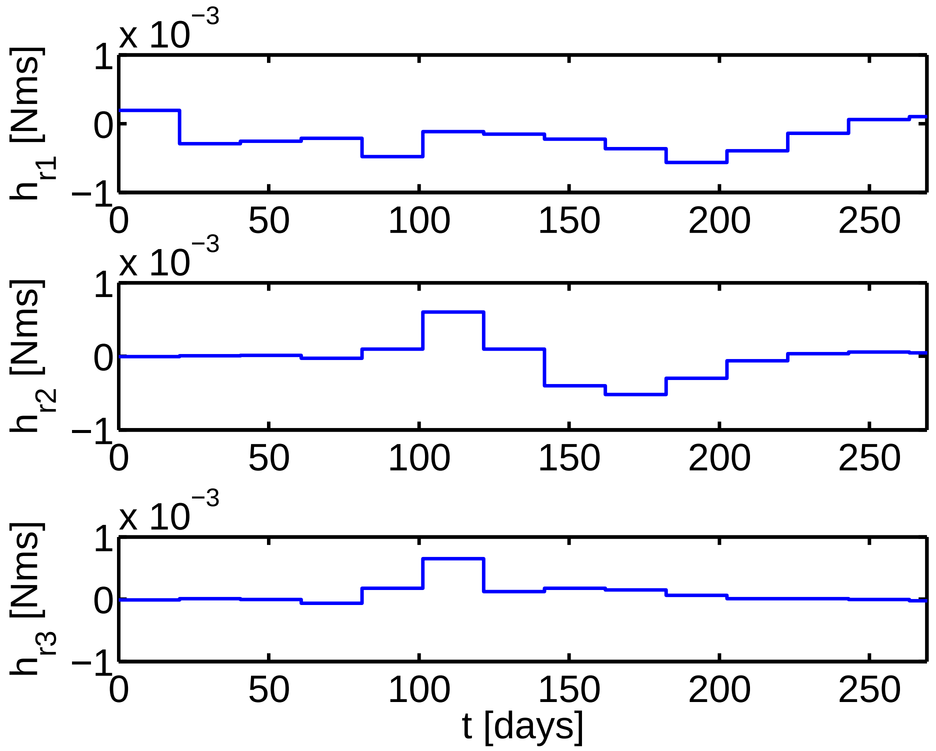

Figure 8.19. Control input for a AH guidance applied to modified, large L_1 halo orbits in the Sun-Earth system for $\beta = 0.035$.

9. CONCLUDING REMARKS

A framework is developed to explore the rotational behavior for a rigid spacecraft when it is coupled to the dynamical regime that is associated with a CR3BP periodic orbit. Two models are considered to reproduce the orbit-attitude dynamics of a vehicle: a Simplified Coupled Model (SCM), that solely includes gravity, and partially reflects the interaction between the orbit and attitude motions; a Fully Coupled Model (FCM), that incorporates gravity, and the Solar Radiation Pressure (SRP), and renders a fully coupled orbit-attitude dynamics. Relevant information in a highly sensitive regime as the CR3BP, are more easily obtained employing a straightforward description of the motion, such as the SCM or FCM, and may serve as a basis to justify further investigation. This document, first supplies a reference for the construction of a dynamical model useful to reproduce the orbit and attitude dynamics for a rigid spacecraft within a CR3BP system. The CR3BP model assists the propagation of the motion for the vehicle center of mass, and may be elaborated to include additional force models, such as SRP. Euler equations of motion and quaternion kinematics representation are used to predict the attitude evolution for the spacecraft. Practical applications may require an understanding of the response nearby a nominal solution. An analytical expression for the variational equations, which describe the motion nearby a reference, is also derived. The variational equations in analytical form facilitate the construction of the State Transition Matrix (STM), another mathematical tool that is largely beneficial in targeting or correction schemes. A transformation of the STM from inertial to rotating frame is discussed, as the reference observer may vary, accordingly to the specific problem. Within the coupled orbit-attitude framework, both the natural and controlled dynamics are explored. First, the SCM enables the delineation of some important natural dynamical structures, that are associated with the gravitational field. Within the SCM, periodic solutions are dynamical patterns that supply a valuable insight into a complex dynamical regime, and are a practical reference motion for space mission applications, as periodic solutions are a well-defined subset of bounded behaviors. Similarly to the concept of gravity gradient stabilization, that is applicable along a Keplerian orbit, periodic librations may be a means to passively establish a bounded attitude oscillation along a CR3BP orbit. Second, an analysis of the controlled dynamics for an ideal solar sail explores the application of orbit-attitude targeting schemes within the CR3BP. Strategies that implement different forms of attitude control, so to adjust the sailcraft pointing, and steer the orbital path, are developed and applied to a test station keeping scenario. This scenario requires the guidance law to correct an initial perturbation and target a final state that re-inserts the spacecraft into the nominal orbit. A simple mantainance operation is valuable to identify fundamental benefits and challenges that are associated with each guidance strategy, and preliminary to the application of a coupled orbit-attitude control scheme in a more complex and sensitive problem. Better understanding for the available natural dynamical structures, as well as for viable maneuvering techniques, may foster a coupled orbit-attitude approach in mission design.

9.1 Analysis of Bounded Solutions: Orbit-Attitude Periodic Solutions

A general approach to the construction of orbit-attitude periodic solutions that are associated with a known CR3BP reference orbit, is presented. A numerical algorithm for the precise computation of an orbit-attitude periodic solution, as well as the corresponding family, is detailed, and may be easily replicated in future applications. Although an efficient correction scheme may be available, the identification of an accurate initial guess is a principal challenge. When the behavior within an highly sensitive dynamical regime is influenced by several parameters, including the configuration at an initial epoch, the reference orbit, and the spacecraft mass distribution, the exploration of the solution space to determine dynamical structures possibly useful for a certain mission application, is non-trivial. To support the identification of a good initial guess, three different strategies are discussed, ones that involve well-established dynamical systems theory tools, i.e., Floquet theory and Poincaré map, as well as more recent instruments, specifically, grid search maps applied to attitude dynamics. This work supplies a reference for the application of Floquet theory to the coupled orbit-attitude problem, and encompasses some of the related challenges. For example, an elementary scenario that lies within the assumptions for Floquet theory, and serves as a stepping stone to the identification of more complex and interesting orbit-attitude periodic motions, is presented. Analysis of the linear stability for an orbit-attitude nominal periodic motion also contains an useful contribution to the definition of attitude modes that describe nearby rotational behaviors, and to the compact visualization of stability information across a large range of selected parameters. Poincaré maps are an additional tool to reveal important dynamical structures, such as periodic solutions. To assist the inspection of many surface of sections, ones that may reflect a variety of system configurations, a straightforward algorithm for the automatic detection of ordered patterns on the map is discussed. Such technique may be transferable from the orbit-attitude dynamics within the CR3BP to other applications. More recently, another type of map is employed to visualize resulting information for a grid search, and individuate conditions that produce bounded attitude librations. In this investigation, a linkage between periodic behaviors and regions on the grid search map that are associated with bounded attitude librations, is observed. Such understanding is successfully exploited to recognize orbit-attitude periodic solutions in a complex scenario, such as a three-dimensional motion along an halo orbit, where the direct application of Floquet theory or Poincaré mapping may be more cumbersome, especially, while lacking of any precedent insight into this regime of motion. Several families of orbit-attitude solutions are computed using Floquet theory, Poincaré mapping and grid search maps, in combination with a targeting algorithm. Initial conditions for selected sample solutions are available in this document. In general, the solution space emerges as permeated with orbit-attitude periodic solutions, which may offer an extended set of novel design options for space mission applications. Orbit-attitude periodic solutions are illustrated along different reference orbits, and exist for different stability properties (including stable or slowly diverging behaviors), as well as geometrical complexity (including three-dimensional orbits and three-dimensional rotations). The capability to identify, construct and understand periodic attitude behaviors along periodic orbits in the CR3BP is pivotal to design novel attitude modes, maneuver profiles or long-term stable configurations that leverage the natural dynamics in a multi-body system.

9.2 Investigation of Orbit-Attitude Coupling Devices: Solar Sail Orbital Maneuvering

Considering solar sail operations, orbit-attitude dynamics are incorporated into a multiple shooting algorithm that can be employed for shaping the orbital path. The main contribution is a modification of a classical Turn and Hold (TH) model to include the spacecraft attitude dynamics. The rotational and translational motion for the vehicle are simultaneously propagated. During the propagation, different means for adjusting the sail attitude configuration and steering the spacecraft along a desired path are explored, including the application of instantaneous reorientations, inertially fixed pointing directions, constant torques, or constant relative angular momentums. The simplicity for some among those forms of control is particularly interesting, and may foster more practical implementations for solar sail missions. The classic decoupled TH strategy supplies a command input solely as a sequence of sail pointing configurations, which may require fast reorientation maneuvers at certain control points along the trajectory. Additionally, the sail pointing configurations obtained within a decoupled TH guidance are artificial, and are not reproducible when the natural rotational dynamics is incorporated, unless some type of attitude control is designed and also included. First, a coupled TH guidance strategy is investigated, demonstrating the possibility to predict instantaneous sail reorientations, that naturally evolve into an attitude profile that yields the desired trajectory. Next, a Moment Hold (MH) and an Angular momentum Hold (AH) guidance strategies are developed; the command input is, accordingly, a sequence of control torques or relative angular momentum vectors, rather than a sequence of spacecraft orientation configurations. Each strategies is applied to a straightforward scenario, which requires to mitigate some initial errors relative to a nominal trajectory. Employing a coupled orbit-attitude correction scheme presents some numerically challenges, that are also discussed in this investigation. The ability to succeed in a simplification of a mission operation is preliminary to the utilization of each guidance approach in a more complex problem, and supplies an immediate and clear understanding of the main challenges that are associated with a certain control strategies.

9.3 Recommendation for Future Work

As more ambitious interplanetary missions appear on the roadmap for advancing the human presence in space, and new technologies for space exploration emerge, the understanding of spaceflight mechanics is also required to progress, and enable more efficient design solutions. Within the context of coupled orbit-attitude dynamics in a multi-body regime, the following research areas are, perhaps, an interesting continuation of this work:

- Following to the precise creation of an orbit-attitude periodic solution, the exploration of dynamical structures that are associated with the periodic motion, such as manifolds surfaces or quasi-periodic behaviors, is generally an important piece within the characterization of the solution space for a complex dynamical system, and it is potentially useful in the actual functioning for a spacecraft attitude system. Among the possible applications, manifold surfaces may supply a natural reference for reorientation maneuvers, and the existence of a set of quasi-periodic structures may assist in enabling long-term stable configurations.

- The transition of the orbit-attitude solutions for the simple coupling model presented in this document to higher fidelity models is warranted. An improved representation of the dynamical environment at an interplanetary destination may first incorporate the force and torque exerted by the Solar Radiation Pressure (SRP). Ephemeris position of the attracting bodies is also relevant for a more accurate determination of the gravity action. For certain mission scenarios, the irregular mass distribution for the primary bodies may also be significant in more precisely predicting the spacecraft orbit-attitude dynamics. Stability for the type of orbit-attitude solutions, that are presented in this work, should also be examined within an higher fidelity environment.

- Some numerical difficulties are encountered during the construction of orbit-attitude solutions for solar sailing within the current framework. Reproducing the orbit-attitude dynamics for fast spinning vehicles is one specific challenge. The direct integration for the orbit-attitude motion associated with a fast spinning spacecraft is cumbersome, because of the difference in the characteristic time-scale for the orbital and attitude response. Orbit frequencies may, in fact, be measured in months, or days, whereas, the spinning frequency is close to seconds, or fractions of a second. Techniques to average the spinning motion, and the introduction of intermediate frames to represent the spacecraft orientation, may be useful to alleviative the computational demand for simulating orbit-attitude dynamics of fast spinning bodies. The capability to reproduce a coupled fast spinning motion is particularly important in solar sail applications. A solar sail may, for example, be spinned at a high rate, as a dynamical means to grant stiffness to the sail structure. Modifications to a targeting algorithm to prevent a tangency condition within the quaternions variables, is a second continuation work of interest. Overshooting the quaternion components appears to be the currently remaining cause for the failure of the convergence process in the computation of orbit-attitude solutions for solar sails. Including additional constraint conditions to specifically avoid a tangency condition, or exploring an alternative set of kinematics variable may be options to be investigated. Reducing numerical difficulties may further consolidate a coupled orbit-attitude approach to the study and design of solar sail flight mechanics.

- Within this investigation, a guidance strategy that incorporates coupled orbit-attitude dynamics is demonstrated for a straightforward station keeping scenario. The station-keeping scenario examined includes an ideal solar sail, and constraints on the final position and velocity only. Following a simple application, it is natural to explore the implementation of a coupled orbit-attitude control scheme into a more elaborated, and higher fidelity, framework. Such framework may comprise 1) a more realistic model for the solar sail and the dynamical environment, 2) a long-term station keeping simulation, 3) a closed-loop control law, 4) a larger set of reference orbits and initial errors. Along with improving the station keeping framework, the addition of constraints for the spacecraft rotational motion should be considered. A coupled orbit-attitude approach to the construction of the guidance law fosters, in fact, the possibility to design the orbital path in combination with constraints on the attitude configuration, which may be relevant in several mission applications, such as solar sails, but also astronomical observatories, and some architectures with a limitation on the thrusting direction.

REFERENCES

REFERENCES

[1] J. Gardner, J. Mather, M. Clampin, R. Doyon, M. Greenhouse, H. Hammel, J. Hutchings, P. Jakobsen, S. Lilly, K. Long, et al. The James Webb Space Telescope. *Space Science Reviews*, 123(4):485–606, 2006.

[2] W. Traub, S. Shaklan, and P. Lawson. Prospects for Terrestrial Planet Finder (tpf-c, tpf-i, & tpf-o). In *Proceedings of the conference In the Spirit of Bernard Lyot: The Direct Detection of Planets and Circumstellar Disks in the 21st Century*, volume 1, page 36. University of California, Berkeley, 2007.

[3] M. Hechler and J. Cobos. Herchel, Planck, Gaia orbit design. In *Libration Point Orbits and Application: Proceedings of the Conference, Aiguablava, Spain, 10-14 June 2002*. World Scientific, London, 2003.

[4] J. Geffre, D. Cooke, and J. Carpenter. Lunar L1 gateway conceptual design report. Technical report, NASA Johnson Space Center, 2001.

[5] J. Brophy and B. Muirhead. Near-Earth Asteroid Retrieval Mission (ARM) study. In *Proceedings of the 33rd IEPC, October, 2013, Washington, DC, USA*, pages 2013–82. ERPS, Fairview Park, 2013.

[6] N. Strange, D. Landau, T. McElrath, G. Lantoine, T. Lam, M. McGuire, L. Burke, M. Martini, and J. Dankanich. Overview of mission design for nasa asteroid redirect robotic mission concept. In *Proceedings of the 33rd IEPC, October, 2013, Washington, DC, USA*, pages 2013–82. ERPS, Fairview Park, 2013.

[7] D. Folta, T. Pavlak, A. Haapala, K. Howell, and M. Woodard. EarthMoon libration point orbit stationkeeping: Theory, modeling, and operations. *Acta Astronautica*, 94(1):421 – 433, 2014.

[8] T. Kane and E. Marsh. Attitude stability of a symmetric satellite at the equilibrium points in the restricted three-body problem. *Celestial Mechanics*, 4:78–90, 1971.

[9] W. Robinson. Attitude stability of a rigid body placed at an equilibrium point in the restricted problem of three bodies. *Celestial Mechanics*, 10:17–33, 1974.

[10] A. Abad, M. Arribas, and A. Elipe. On the attitude of a spacecraft near a lagrangian point. *House of the Czechoslovak Academy of Sciences*, 40(1988), 1989.

[11] E. Brucker and P. Gurfil. Analysis of gravity-gradient perturbed rotational dynamics at the collinear lagrange points. *The Journal of the Astronautical Sciences*, 55(3):271–291, 2007.

[12] B. Wong, R. Patil, and A. Misra. Attitude dynamics of rigid bodies in the vicinity of lagrangian points. *Journal of Guidance, Control, and Dynamics*, 31(1):252–256, 2008.

[13] M. Sanjurjo-Rivo, F. Lucas, J. Peláez, C. Bombardelli, E. Lorenzini, D. Curreli, D. Scheeres, and M. Lara. On the dynamics of a tethered system near the collinear libration points. In *AIAA/AAS Astrodynamics Specialist Conference 2008*. AAS/AIAA, 2008.

[14] M. Lara, J. Peláez, C. Bombardelli, F. Lucas, M. Sanjurjo-Rivo, D. Curreli, E. Lorenzini, and D. Scheeres. Dynamic stabilization of L2 periodic orbits using attitude-orbit coupling effects. *Journal of Aerospace Engineering*, 4(1):73, 2012.

[15] D. Guzzetti. *Large Space Structures Dynamics in a Multi-Body Gravitational Environment*. M.S. Thesis, Politecnico di Milano, Milano, Italy, July 2012.

[16] D. Guzzetti, R. Armellin, and M. Lavagna. Coupling attitude and orbital motion of extended bodies in the restricted circular 3-body problem: A novel study on effects and possible exploitations. In *IAF 63rd International Astronautical Congress*. IAF, 2012.

[17] A. Knutson and K. Howell. Application of Kanes method to incorporate attitude dynamics into the circular restricted three body problem. In *Proceedings of the 22nd AAS/AIAA Space Flight Mechanics Meeting*. AAS/AIAA, 2012.

[18] A. Knutson and K. Howell. Coupled orbit and attitude dynamics for spacecraft comprised of multiple bodies in Earth-Moon halo orbits. In *IAF 63rd International Astronautical Congress*. IAF, 2012.

[19] A. Knutson, D. Guzzetti, K. Howell, and M. Lavagna. Attitude responses in coupled orbit-attitude dynamical model in Earth-Moon lyapunov orbits. *Journal of Guidance, Control an Dynamics*, 38:1264–1273, 2015.

[20] A. Knutson. *Application of Kane's Method to Incorporate Attitude Dynamics Into the Circular Restricted Three-Body Problem*. Ph.D. Dissertation, School of Aeronautics and Astronautics, Purdue University, West Lafayette, Indiana, December 2012.

[21] Y. Meng, R. Hao, and Q. Chen. Attitude stability analysis of a dual-spin spacecraft in halo orbits. *Acta Astronautica*, 99:318–329, 2014.

[22] H. Poincaré. Mémoire sur les courbes définies par une équation différentielle (ii). *Journal de Mathématiques pures et Appliquées*, pages 251–296, 1882.

[23] F. Moulton, D. Buchanan, T. Buck, F. Griffin, W. Longley, and W. MacMillan. Periodic orbits. *Washington, Carnegie institution of Washington*, 1, 1920.

[24] C. Goudas. Three-dimensional periodic orbits and their stability. *Icarus*, 2:1–18, 1963.

[25] M. Hénon. Numerical exploration of the restricted problem, v. *Astronomy and Astrophysics*, 1:223–238, 1969.

[26] D. Dunham and R. Farquhar. Libration point missions, 1978–2002. In *Libration Point Orbits and Applications: Proceedings of the Conference, Aiguablava, Spain, 10-14 June 2002*, pages 45–73. World Scientific, London, 2003.

[27] E. Doedel, V. Romanov, R. Paffenroth, H. Keller, D. Dichmann, J. Galán-Vioque, and A. Vanderbauwhede. Elemental periodic orbits associated with the libration points in the circular restricted 3-body problem. *International Journal of Bifurcation and Chaos*, 17(8):2625–2677, 2007.

[28] D. Folta, N. Bosanac, D. Guzzetti, and K. Howell. An Earth-Moon system trajectory design reference catalog. *Acta Astronautica*, 110:1–13, 2014.

[29] D. Guzzetti, N. Bosanac, D. Folta, and K. Howell. A framework for efficient trajectory comparisons in the Earth-Moon design space. In *AIAA/AAS Astrodynamics Specialist Conference 2014*. AAS/AIAA, 2014.

[30] D. Guzzetti, N. Bosanac, A. Haapala, K. Howell, and D. Folta. Rapid trajectory design in the Earth-Moon ephemeris system via an interactive catalog of periodic and quasi-periodic orbits. In *66th International Astronautical Congress, Jerusalem, Israel*. IAF, 2015.

[31] D. Guzzetti and K. Howell. Coupled orbit-attitude dynamics in the three-body problem: a family of orbit-attitude periodic solutions. In *AIAA/AAS Astrodynamics Specialist Conference 2014*. AAS/AIAA, 2014.

[32] D. Guzzetti and K. Howell. Natural periodic orbit-attitude behaviors for rigid bodies in three-body periodic orbits. In *IAF 66th International Astronautical Congress, Jerusalem, Israel, October 12-16*, 2015.

[33] L. Bucci and M. Lavagna. Coupled dynamics of large space structures in lagrangian points. In *6th International Conference on Astrodynamics Tools and Techniques, Darmstadt, Germany, March 14-17*, 2016.

[34] K. Howell. Three-dimensional, periodic, halo orbits. *Celestial Mechanics*, 32(1):53–71, 1984.

[35] H. Keller. *Numerical Methods for Two-Point Boundary-Value Problems*. Dover Publications, New York, 1992.

[36] D. Grebow. *Trajectory Design in the Earth-Moon System and Lunar South Pole Coverage*. Ph.D. Dissertation, School of Aeronautics and Astronautics, Purdue University, West Lafayette, Indiana, May 2010.

[37] G. Gómez, J. Masdemont, and C. Simó. Quasihalo orbits associated with libration points. *Journal of the Astronautical Sciences*, 46(2):135–176, 1998.

[38] T. Pavlak. *Mission Design Applications in the Earth-Moon System: Transfer Trajectories and Stationkeeping*. M.S. Thesis, School of Aeronautics and Astronautics, Purdue University, West Lafayette, Indiana, May 2010.

[39] K. Howell and H. Pernicka. Numerical determination of lissajous trajectories in the restricted three-body problem. *Celestial Mechanics*, 41(1-4):107–124, 1987.

[40] B. Marchand, K. Howell, and R. Wilson. Improved corrections process for constrained trajectory design in the n-body problem. *Journal of Spacecraft and Rockets*, 44(4):884–897, 2007.

[41] H. Keller. Numerical solution of bifurcation and nonlinear eigenvalue problems. *Applications of Bifurcation Theory*, 1(38):359–384, 1977.

[42] C. Sauer. Optimum solar-sail interplanetary trajectories. In *AIAA/AAS Astrodynamics Specialist Conference*, pages 76–792. AIAA, 1976.

[43] G. Mengali and A. Quarta. Optimal three-dimensional interplanetary rendezvous using non-ideal solar sail. *Journal of Guidance, Control, and Dynamics*, 28(1):173–177, 2005.

[44] T. Waters and C. McInnes. Invariant manifolds and orbit control in the solar sail three-body problem. *Journal of Guidance, Control, and Dynamics*, 31(3):554–562, 2008.

[45] M. Otten and C. McInnes. Near minimum-time trajectories for solar sails. *Journal of Guidance, Control, and Dynamics*, 24(3):632–634, 2001.

[46] G. Mengali and A. Quarta. Solar sail trajectories with piecewise-constant steering laws. *Aerospace Science and Technology*, 13(8):431–441, 2009.

[47] C. McInnes and J. Simmons. Solar sail halo orbits part ii-geocentric case. *Journal of Spacecraft and Rockets*, 29(4):472–479, 1992.

[48] C. McInnes. Solar sail mission applications for non-keplerian orbits. *Acta Astronautica*, 45(4):567–575, 1999.

[49] C. McInnes. *Solar Sailing: Technology, Dynamics and Mission Applications.* Springer, New York, 2004.

[50] C. McInnes. Passive control of displaced solar sail orbits. *Journal of Guidance, Control, and Dynamics*, 21(6):975–982, 1998.

[51] P. Gong, J. Li, and H. Baoyin. Passive stability design for solar sail on displaced orbits. *Journal of Spacecraft and Rockets*, 44(5):1071–1080, 2007.

[52] J. Bookless and C. McInnes. Dynamics and control of displaced periodic orbits using solar-sail propulsion. *Journal of Guidance, Control, and Dynamics*, 29(3):527–537, 2006.

[53] C. McInnes, A. McDonald, J. Simmons, and E. MacDonald. Solar sail parking in restricted three-body systems. *Journal of Guidance, Control, and Dynamics*, 17(2):399–406, 1994.

[54] A. Farrés and À. Jorba. Periodic and quasi-periodic motions of a solar sail close to SL1 in the Earth–Sun system. *Celestial Mechanics and Dynamical Astronomy*, 107(1-2):233–253, 2010.

[55] J. Bell. *The Impact of Solar Radiation Pressure on Sun-Earth L1 Libration Point Orbits*. M.S. Thesis, School of Aeronautics and Astronautics, Purdue University, West Lafayette, Indiana, August 1991.

[56] J. Simo and C. McInnes. Solar sail orbits at the Earth–Moon libration points. *Communications in Nonlinear Science and Numerical Simulation*, 14(12):4191–4196, 2009.

[57] G. Wawrzyniak and K. Howell. Investigating the design space for solar sail trajectories in the Earth-Moon system. *The Open Aerospace Engineering Journal*, 4:26–44, 2011.

[58] G. Wawrzyniak and K. Howell. Numerical techniques for generating and refining solar sail trajectories. *Advances in Space Research*, 48(11):1848–1857, 2011.

[59] H. Baoyin and C. Mcinnes. Solar sail halo orbits at the Sun–Earth artificial L1 point. *Celestial Mechanics and Dynamical Astronomy*, 94(2):155–171, 2006.

[60] A. Farrés and À. Jorba. Dynamics of a solar sail near a halo orbit. *Acta Astronautica*, 67(7):979–990, 2010.

[61] A. McInnes. *Strategies for Solar Sail Mission Design in the Circular Restricted Three-Body Problem.* M.S. Thesis, School of Aeronautics and Astronautics, Purdue University, West Lafayette, Indiana, August 2000.

[62] D.l Lawrence and S. Piggott. Solar sailing trajectory control for sub-L1 station-keeping. In *AIAA Guidance, Navigation, and Control Conference and Exhibit*, pages 2004 – 5014. AIAA, 2004.

[63] J. Bookless and C. McInnes. Control of lagrange point orbits using solar sail propulsion. *Acta Astronautica*, 62(2):159–176, 2008.

[64] M. Xu and S. Xu. Structure-preserving stabilization for hamiltonian system and its applications in solar sail. *Journal of Guidance, Control, and Dynamics*, 32(3):997–1004, 2009.

[65] G. Wawrzyniak and K. Howell. An adaptive, receding-horizon guidance strategy for solar sail trajectories. *The Journal of the Astronautical Sciences*, 59(4):650–675, 2012.

[66] G. Wawrzyniak and K. Howell. Look-ahead flight path control for solar sail spacecraft. *Proceedings of the Institution of Mechanical Engineers, Part G: Journal of Aerospace Engineering*, 227(12):1938–1952, 2013.

[67] L. Chen-Wan. Solar sail geostorm warning mission design. In *Proceedings of 14th AAS/AIAA Space Flight Mechanics Conference*, pages 04–107.

[68] M. Macdonald and C. McInnes. Solar sail mission applications and future advancement. pages 45–2010. ISSS 2010, New York, 2010.

[69] L. Johnson, R. Young, N. Barnes, L. Friedman, V. Lappas, and C. McInnes. Solar sails: Technology and demonstration status. *International Journal of Aeronautical and Space Science*, 13(4):421–427, 2012.

[70] O. Mori, Y. Tsuda, H. Sawada, R. Funase, T. Saiki, K. Yonekura, H. Hoshino, H. Minamino, T. Endo, J. Kawaguchi, et al. World's first demonstration of solar power sailing by IKAROS. In *The 2nd International Symposium on Solar Sailing*, pages 21–2010. ISSS 2010, New York, 2010.

[71] L. Johnson, M. Whorton, A. Heaton, R. Pinson, G. Laue, and C. Adams. Nanosail-d: a solar sail demonstration mission. *Acta Astronautica*, 68(5):571–575, 2011.

[72] J. Heiligers, B. Diedrich, B. Derbes, and C. McInnes. Sunjammer: Preliminary end-to-end mission design. In *2014 AIAA/AAS Astrodynamics Specialist Conference*, pages 2014–4127. AIAA/AAS, 2014.

[73] B. Wie. Solar sail attitude control and dynamics, part 1. *Journal of Guidance, Control, and Dynamics*, 27(4):526–535, 2004.

[74] B. Wie. Solar sail attitude control and dynamics, part 2. *Journal of Guidance, Control, and Dynamics*, 27(4):536–544, 2004.

[75] M. Macdonald. *Advances in Solar Sailing*. Springer Science & Business Media, New York, 2014.

[76] H. Curtis. *Orbital mechanics for engineering students*. A Butterworth-Heinemann Title, 2009.

[77] A. Roy. *Orbital motion*. Taylor & Francis, 2004.

[78] V. Szebehely. *Theory of Orbit: The Restricted Problem of Three Bodies*. Academic Press, New York, 1967.

[79] W. Koon, M. Lo, J. Marsden, and S. Ross. *Dynamical systems, the three-body problem and space mission design*. World Scientific, 2006.

[80] D. Guzzetti, N. Bosanac, D. Folta, and K. Howell. A framework for efficient trajectory comparisons in the Earth-Moon design space. In *Proceedings of the AAS/AIAA Astrodynamics Specialist Conference, San Diego, California*, 2014.

[81] D. Grebow. *Generating Periodic Orbits in the Circular Restricted Three-Body Problem with Applications to Lunar South Pole Coverage*. M.S. Thesis, School of Aeronautics and Astronautics, Purdue University, West Lafaette, Indiana, May 2006.

[82] T. Kane, P. Likins, and Levinson D. *Spacecraft dynamics*. McGraw-Hill, 2005.

[83] J. Wertz. *Spacecraft attitude determination and control*, volume 73. Springer Science & Business Media, 2012.

[84] R. Sood. *Solar Sail Applications for Mission Design in Sun-Planet Systems from the Perspective of the Circular Restricted Three-Body Problem*. M.S. Thesis, School of Aeronautics and Astronautics, Purdue University, West Lafayette, Indiana, 2012.

[85] C. Douskos, V. Kalantonis, and P. Markellos. Effects of resonances on the stability of retrograde satellites. *Astrophysics and Space Science*, 310(3-4):245–249, 2007.

[86] R. Farquhar, D. Dunham, Y. Guo, and J. McAdams. Utilization of libration points for human exploration in the Sun-Earth-Moon system and beyond. *Acta Astronautica*, 5(3):687–700, 2004.

[87] E. Messerschmid and Bertrand R. *Space Stations: Systems and Utilization*. 1999.

[88] G. Wawrzyniak. *The Dynamics and Control of Solar-Sail Spacecraft in Displaced Lunar Orbits*. Ph.D. Dissertation, School of Aeronautics and Astronautics, Purdue University, West Lafayette, Indiana, August 2011.

[89] David L Richardson. Halo orbit formulation for the isee-3 mission. *Journal of Guidance, Control, and Dynamics*, 3(6):543–548, 1980.

VITA

VITA

Davide Guzzetti was born to Pierino Guzzetti and Antonella Calcaterra in Casorezzo. Italy on June 16, 1987. He studied at Politecnico di Milano, Italy from 2006 to 2012, when he graduated with a M.S. in Space Engineering. During the later years at Politecnico di Milano, he was a member of the honor society Alta Scuola Politecnica. In August 2012, Davide formally joined prof. K. C. Howell's research group and began a doctoral degree at Purdue University. During the years at Purdue, Davide had the opportunity to lecture for the grad course "Advance Orbital Dynamics" and to collaborate at different projects for the NASA Goddard Space Flight Center and the NASA Johnson Space Center. In January 2016, he was awarded a Chinese National Post-doc Fellowship to continue his studies at Tsinghua University, Beijing.